SHAPE-SHIFTING BUBBLE-DRIVEN HYDROGEL MICROBOTS

by

BERK ALTUNKEYIK

A thesis submitted to
The University of Birmingham
for the degree of
DOCTOR OF PHILOSOPHY

School of Mathematics
College of Engineering and Physical Sciences
The University of Birmingham
June 10, 2024

Abstract

Microbots are artificial swimmers engineered to perform complex tasks at the microscale including drug delivery, cargo transport, and non-invasive surgery. Historically, the design of microbots has advanced from basic rigid structures to more sophisticated flexible and active particles. This transformation has been driven by the use of soft and flexible materials like hydrogels, which offer low elastic moduli and, consequently, high deformability. These soft active materials hold the potential to enable microbot navigation through shape and volume transformations.

This thesis begins by showing that hydrogel-based bubble-driven rigid microbots with I, U, and S-shapes exhibit distinct swimming characteristics: pumping, translation, and rotation. While the manufacturing and experiments of this study were conducted by our experimental collaborators, we propose a mathematical model to provide physical insight into the bubble growth mechanism at the active tips. The findings of this study inspire us to explore the use of hydrogels to control microbot dynamics through shape transformations.

We proceed by investigating the deformations of active hydrogel-based filaments in Stokes flow. For this investigation, we propose a simple numerical model incorporating a bead and spring system with the method of regularised stokeslets. The bead and spring network captures the elastic deformations, while the method of regularised stokeslets accounts for the non-local hydrodynamic interactions between different segments of the hydrogel body. Simulations of porous filaments, representing hydrogels activated by single or double-tip forces, reveal periodic oscillations and motion patterns such as corkscrew motion and run-and-tumble behaviour, reminiscent of the motility seen in sperm and bacteria.

Finally, the same framework is adapted to model the volume and shape transformations of the responsive hydrogels. By combining responsive and non-responsive sections

within the same hydrogel, we are able to control both the function and swimming characteristics of passive and active hydrogel bilayers. Additionally, we propose new smart microbot prototypes, including star-shaped structures, and suggest control mechanisms that integrate responsivity with activity. The findings of this dissertation offer guidance for designing shape-shifting active microbots, and the methodologies developed are broadly applicable to various problems in the study of artificial microswimmers and undulatory motion.

Acknowledgements

I would like to thank first my PhD supervisors, Prof Tom Montenegro-Johnson and Dr Amin Rahmat, for their guidance, valuable insight, and for introducing me to an amazing field of science. More importantly, I would like to thank them for supporting me in various aspects whenever I have needed it. I cannot write enough to express how grateful I am. I am grateful for funding support from the Leverhulme Trust Research Leadership Award RL-2019-014 Shape Transforming Active Microfluidics to Tom Montenegro-Johnson. Additionally, I express my acknowledgements for the scholarship by the School of Mathematics at the University of Birmingham. Further thanks to our collaborators, Dr Juliane Simmchen, Dr Ivan Rehor, and Dr Mostafa Safdari Shadloo, for sharing their experimental and numerical expertise with me. I would also like to thank my best friend, Koço, for talking about anything but PhD. Thanks to my parents and sisters, who were always there for me. Without them, there is no way I could have finished this thesis. And finally, I would like to thank HJM.

CONTENTS

1 Introduction to Artificial Microswimmers **1**

1.1 Artificial Microswimmers 2

1.2 Externally-Actuated Swimmers 5

1.2.1 Magnetic Fields 5

1.2.2 Acoustic Waves 7

1.2.3 Light Intensity 9

1.3 Self-Propelled Swimmers 10

1.3.1 Phoretic Microswimmers 11

1.3.2 Bubble Propelled Microswimmers 15

1.4 Microswimmer Dynamics and Stokes Flow 19

1.4.1 Properties of Stokes Flow and Fundamental Solution 22

1.5 The Method of Regularised Stokeslets 26

1.5.1 Stokes Flow Past an Impermeable Sphere 28

1.6 Overview of This Thesis 30

2 Bubble Driven Hydrogel Based I-, U-, and S-shaped Microbots **32**

2.1 Bubble Growth Mechanism 34

2.1.1 Detecting Bubbles with Image Analysis 37

2.2 Fundamental Modes of Swimming 41

2.3 Conclusions and Inspiration 43

3 Introduction to Soft Matter and Hydrogels **46**

3.1 Gels and Hydrogels . . . 49
3.1.1 Stokes Flow Through a Hydrogel . . . 50
3.2 Responsive Hydrogels . . . 53

4 Methodology **62**
4.1 The Bead and Spring System . . . 62
4.2 The Method of Regularised Stokeslets . . . 70
4.3 Numerical Algorithm . . . 72
4.4 Verification and Results . . . 77
4.4.1 Sedimentation of Porous Non-Deformable Spheres . . . 78
4.4.2 Sedimentation of Nonporous Deformable Filaments . . . 83
4.5 Sedimentation of Porous Deformable Filaments . . . 86

5 Dynamics of Active Poroelastic Filaments **91**
5.1 Clamped Filaments . . . 92
5.2 Active Janus Filaments . . . 98
5.3 Active Saturn Filaments . . . 103
5.3.1 Stationary Pumping Filaments . . . 103
5.3.2 Ballistic Motion . . . 105
5.3.3 Spiral Trajectory . . . 105
5.3.4 Run-and-Tumble . . . 106
5.3.5 Tumble Dominant Run . . . 110
5.4 Discussion . . . 112

6 Responsive Shape-Shifting Microbots **116**
6.1 Updating the Bead and Spring System for Responsive Hydrogels . . . 117
6.2 Passive Shape Shifters . . . 118
6.2.1 Rod Bilayer, also known as Pump to Translator (I to U) . . . 119
6.2.2 Pump to Rotator (I to S) . . . 124
6.2.3 Bilayer with Fixed End . . . 127

6.2.4 Self-Folding Star . . . 128
6.3 Active Shape Shifters . . . 135
6.4 Discussion . . . 139

7 Concluding Remarks **142**
7.1 Highlights of Findings . . . 142
7.2 Future Work . . . 145

A The Code **151**

B Curvature Post-Process Tool **153**

C Summary of Research Articles **157**
C.1 Published Work . . . 157
C.2 Submitted Work . . . 157

List of References **182**

LIST OF FIGURES

1.1 Eukaryotic and prokaryotic creatures propel themselves with whip-like organelles, namely cilia and flagella. In panel (a), a cilium beats around a fixed point. In panel (b), a bacterium uses flagella to perform run-and-tumble. During the "run" phase, the bacterium swims forward. Subsequently, in the "tumble" phase, flagella deform to change the direction of motion. 2

1.2 Janus particles can be designed in various shapes. For example, on the left-hand side, a traditional spherical Janus particle is demonstrated, while on the right-hand side, a cylindrical Janus rod is presented. Generally, the active face, indicated by pink, interacts with the environment, causing the swimmer to move in the opposite direction. 4

1.3 The schematic demonstrates a magnetic swimmer capable of rotating its helical tail under magnetic field gradients to propel itself. For example, Zhang et al. (197) employed a similar mechanism. 6

1.4 The schematic illustrates different applications of acoustic microswimmers. Panel (a) depicts the study of Wang et al. (182). In panel (b), the previous work of Esteban-Fernández de Ávila et al. (42) is redrawn. 8

1.5 The faces of light-propelled Janus swimmer can consist of different material pairs, such as gold (Au) and titanium dioxide (TiO_2), corresponding to pink and grey colours in the schematic. There is a transfer of H^+ and H_2O in the opposite direction to the motion. 9

1.6 The figures illustrates the working principles of diffusiophoretic, electrophoretic, and thermophoretic microbots from panel (a) to panel (c) in respective order. In each figure, the motion occurs from left to right. In panel (a), the grey face represents an inert material and the pink face triggers a catalytic reaction. In panel (b), the colours can be considered as a metal pair such as platinum (Pt) and gold (Au), and the electron transfer is in the opposite direction to the motion. In panel (c), due to the thermal gradient fluid particles at the left-hand side obtain more energy and hit the active surface, resulting in propulsion. 12

1.7 The schematic describes the working principle of a bubble-driven conical microtube. The top illustration is redrawn from the previous work by Gallino et al. (53). The inner walls trigger the catalytic reaction and also confine the growing bubble. The ejected bubble and microbot move in opposite directions. 15

1.8 As a result of a catalytic reaction, the active face of the Janus swimmer, indicated in pink, produces oxygen bubbles, causing the swimmer to move from left to right in the schematic. 17

1.9 Purcell's theoretical three-link swimmer moves with changing arm positions relative to the body (150). The key configurations of swimmer are given as states, with the green colour indicating the moving arm compared to previous position. The third state is particularly crucial for inducing non-reciprocal motion. In configuration III, the red arm shows a theoretical reciprocal deformation, hence, no motion. 23

1.10 The drag anisotropy results in a 2:1 ratio for perpendicular and parallel forces to obtain the same velocity. The schematic is redrawn from the work of Blake and Sleigh (12). 25

1.11 As spreading increases, the blob function becomes shorter. 27

1.12 The schematic demonstrates the streamlines of a creeping flow around a sphere. The drag force on the sphere is in the opposite direction of the far-field flow. 29

2.1 Swimmers are dyed to illustrate active and inactive regions. Red tips indicate active caps, while green sections represent inactive regions. 33

2.2 SFL is used to fabricate 2- and 3-component microrods. The method employs active and inactive pre-gel mixtures, producing rods consisting of parallel sections. In the schematic, green represents active tips, while blue indicates inactive sections. 34

2.3 Due to buoyancy force, swimmers operate at the air-water interface. In panel (a), a rod-shaped motor translates at the interface. Panel (b) illustrates the pumping behaviour of a 3-component microbot. 35

2.4 Frame-by-frame of a single growing bubble over an entire growth cycle. The blue circle denotes the bubble that is detected by the circular Hough transform. 37

2.5 The radius of a single bubble as a function of time over multiple growth-collapse cycles. A subregion of clean data are selected to be used for phase averaging. 38

2.6 a) The bubble growth cycles are phase-averaged to obtain a dataset. b) The flux rate Q in equation 2.7, as a single parameter, is fitted to experimental data using the method of least squares, showing good agreement. 39

2.7 Panel (a) shows the steady (linear) decay of the maximum bubble radius over time indicating degradation of the catalytic enzyme. In panel (b), period between collapses shows a steady increase. 40

2.8 I-shaped microbots swim in different modes depending on the number of poles they possess. Panels (a) and (b) show the motion of Janus and Saturn rods respectively, as captured in the experimental work. 41

2.9 Typical motion patterns of the differently shaped particles: a) pumping of I-shaped swimmers b) translating movement of U-shaped swimmers and c) rotating S-shaped swimmers. The scale bar equals 150 µm. 42
2.10 The interplay between the shape and bubble force directions determines the dynamics of the microbot. In the zeroth mode, the I-shaped microbot pumps the fluid around. The first shape mode corresponds to translation. An S-shaped microbot that represents the second mode rotates. 43
2.11 Motion patterns of the differently shaped particles caused by the influences described above: a) partial rotation, partial translation of I-shaped swimmers b) partial rotation, partial translation of U-shaped swimmers and c) rotating translation of S-shaped swimmers. The scale bar equals 150 µm. . 44

3.1 Various examples of soft matter are demonstrated. Panel (a) is the work of Paul Topham and printed under a CC BY-SA 4.0 license. Panel (e) is taken and reprinted from the work of Ju et al. (91) with permission from IOP Publishing. In panel (b), the outer region contains an aqueous fluid, while the pink-coloured droplet is an oil-based fluid. 47
3.2 Thermo-responsive hydrogels including PNIPAM expel fluid at temperatures over their LCST. Throughout the volume change, polymer chains start to tangle up, which is named coil to globule transition. 54
3.3 The schematic re-illustrates the self-folding behaviour by using responsive hydrogels as hinges in the study of Ge et al. (62). In panel (a), the responsive middle section causes an out-of-plane deformation. In panel (b), a cross-shaped rod transforms into a box, inspired by origami. 56
3.4 Menger sponges have rectangular channel profiles. Depending on the number of channels, they may expel fluid locally reaching moderate Reynolds numbers. 60

4.1 Schematic of a two-bead, one spring system is provided. Dashed lines indicate the instantaneous positions. 63
4.2 A bead and spring system is used to create porous geometries. In panel (a), a tetrahedral element is illustrated, while panel (b) demonstrates the meshed volume of the porous sphere. 64
4.3 Initially, a straight filament is illustrated on top. After bending it into a known arc, the new positions of the beads are calculated. 68
4.4 There is no significant change in spring stiffness according to variations in curvature. In figure a), three different curves as depicted as an example. In respective order blue, yellow, and orange curves labelled as I, II, and III have uniform curvatures equal to $1/10L$, $1/L$, and $5/L$. 69
4.5 The sedimentation of porous spheres are investigated. In panel (a), the numerical results are compared with equation 4.43. In panel (b), for $\phi = 0.9$, the sphere numerically reaches a steady state and translates at terminal speed. 80
4.6 The terminal speeds and flows inside the spheres are compared. In panel (a), the porosity of the sphere and sedimentation speed have an inverse correlation. Panel (b) shows that even for high porosity values, the flow inside the sphere has a much lower speed than the terminal speed of the sphere (36). 81
4.7 According to temporal and spatial resolution studies, we determine the number of beads and time step size in our system. 82
4.8 Filaments may buckle into a "U" shape. While A represents the distance between minimum and maximum points in the $z-$axis, the horizontal distance between tips is defined as B. 83

4.9 Properties of sedimentation are compared for different elastogravitational numbers. As $\mathcal{G}$ increases, the U shape of the filament becomes narrower and more pronounced. In panel (b), the sedimentation speed is normalised according to the body length per second. 85

4.10 For $\mathcal{G} = 1000$, the filament drifts away from the initial centre of mass, and also deform out-of-plane. 86

4.11 Deflection parameters are presented $\mathcal{G} = 600$ and $\mathcal{G} = 1000$, each calculated using different elastogravitational number definitions. 88

4.12 Sedimentation speeds of two sets are compared for $\mathcal{G} = 600$ and $\mathcal{G} = 1000$. The $y-$axis is normalised according to a speed of body length per second. . 89

4.13 In panel (a), the comparison of sedimentation speeds for nonporous filament and the second set with $\phi = 0.9$ are given for $\mathcal{G} = 3000$. Panels (b) and (c) show the shapes of the porous filament at different time steps. 90

5.1 A flexible filament may deform under non-conservative end forces, as demonstrated by the red arrows. The filament under the influence of a single tip force is named Janus, while the Saturn filament experiences forces at both tips. 92

5.2 The ratio of follower force to bending resistance is denoted by σ. As σ increases, decay dynamics change. In both panels, the $y-$axis plots the position of the active tip, which is normalised with respect to the length of the filament. 95

5.3 The oscillations in the third regime are captured for different σ values. . . 96

5.4 For $\sigma = 15$, the centreline of the filament is followed, and the motion remains planar. The transition from cyan to magenta colour is synced with the filament's position over time. The figure is viewed in the $xy-$plane. 97

5.5 For $\sigma = 20$, the centreline of the filament is tracked. In each figure, cyan colour indicates the initial position, which is identical to the magenta coloured final position in the previous figure. 98

5.6 For $\sigma = 30$, the filament translates along a straight trajectory. The convergence to the fixed translation speed takes 30 iterations. 99
5.7 For $\sigma = 100$, the Janus filament moves with side-to-side bending. In panel (a), the cyan-to-magenta transition represents the evolution of the filament's trajectory from from its initial to final position. The time points marked in panel (b) correspond to the filament shapes shown in panel (c). 100
5.8 For $\sigma = 130$, the filament moves in a corkscrew-like motion. In panel (a), the cyan-to-magenta transition represents the evolution of the filament's trajectory from from its initial to final position. The time points marked in panel (b) correspond to the filament shapes shown in panel (c). 101
5.9 For $\sigma = 100$ and 130, the speeds of centre of masses are compared, and the $y-$axis is normalised respect to the body length per second. It should be noted that originally the $\sigma = 100$ case run longer. However, for this figure, a section that matches the time frame of the $\sigma = 130$ case is presented. . . 102
5.10 For $\sigma = 40$, Saturn filament buckles into a "U" shape and translates ballistically. In panel (a), the cyan-to-magenta transition represents the evolution of the filament's trajectory from from its initial to final position. The time points marked in panel (b) correspond to the filament shapes shown in panel (c). 104
5.11 For $\sigma = 70$, Saturn filament rotates in a spiral trajectory. In panel (a), the cyan-to-magenta transition represents the evolution of the filament's trajectory from from its initial to final position. The time points marked in panel (b) correspond to the filament shapes shown in panel (c). 106
5.12 For $\sigma = 120$, Saturn filament moves in a run-and-tumble pattern. In panel (a), the cyan-to-magenta transition represents the evolution of the filament's trajectory from from its initial to final position. The time points marked in panel (b) correspond to the filament shapes shown in panel (c). 107

5.13 For $\sigma = 110$, tumble phase of run-and-tumble appears as a helix. In panel (a), the cyan-to-magenta transition represents the evolution of the filament's trajectory from from its initial to final position. The time points marked in panel (b) correspond to the filament shapes shown in panel (c). 109

5.14 For $\sigma = 140$, there is no directional tendency or running phase. Thus, the Saturn filament tumbles continuously. In panel (a), the cyan-to-magenta transition represents the evolution of the filament's trajectory from from its initial to final position. The time points marked in panel (b) correspond to the filament shapes shown in panel (c). 110

5.15 The speeds of the centres of mass are compared. The $y-$axis is normalised with respect to the body length per second. The $x-$axis is determined by the simulation time of $\sigma = 140$ cases because of faster dynamics. Therefore, it should be noted that the plot represents the snapshots of the other simulations instead of the full ranges. 112

6.1 The responsive region of the bilayer shrinks, which leads to a bending motion. As a result, the bilayer forms the 1^{st} mode of bending. In panel (a), blue indicates the responsive section before shrinkage. In panel (b), orange represents the final shape of the responsive section after shrinkage. In both panels, black denotes the non-responsive sections. 119

6.2 The hydrogel bilayer is constructed to have a boundary layer in the $xy-$plane. In panel (a), the final shape is demonstrated and the inset of the figure shows the initial bilayer from a side view in the $yz-$plane. In panel (b), the evolution of the curvature values over time is shown. 120

6.3 The initial configurations of bilayers are illustrated. The responsiveness ratio, Υ, increases from left to right. Each plot is viewed in the $xy-$plane. The blue regions represent the responsive areas in the bilayer, while black sections are non-responsive. 121

6.4 The quantitative data are provided for $\Upsilon = 0.25, 0.43$, and 0.75. In panel (a), Υ increases from left to right. In panel (b), the average bead speed is normalised with respect to the body length per second. Panel (c) shows the volume change for each bilayer. 122

6.5 The curvature values increase as the responsivity ratio increases from $\Upsilon \approx 0.25$ to $\Upsilon \approx 0.75$. Panels (a) to (c) correspond to the bilayers from left to right in panel (a) of figure 6.4, in respective order. 123

6.6 The homogeneous and responsive hydrogel shrinks while preserving its shape, and the dynamics are faster than heterogeneous bilayers. In panel (b), the $y-$axis is normalised with respect to a speed of body length per second. 124

6.7 The hydrogel can switch shapes between I and S in the presence of multiple responsive layers. 125

6.8 A hydrogel with four responsive regions initially shrinks and forms a wave-like shape. After recovery, it re-creates the original configuration. 126

6.9 I-shaped bilayers with clamped boundary condition deflects as Hippler et al. (72) suggested. As length increases, bending transforms into self-rolling. Previously, similar mechanisms were realised in both millimetre (168) and micrometre scale (100). 128

6.10 Numerical simulations agree with the previous study of Hippler et al. (72) and demonstrate that the direction and position of hydrogel can be navigated by changing the number of active regions. 129

6.11 Different self-folding mechanisms are suggested. Their initial configurations are shown from the $xy-$plane with elevation. The bottom halves of the bilayers are constructed by a non-responsive layer. 130

6.12 Final shapes of various designs are provided. The top row demonstrates a star with 4 equilateral triangle arms from 2 different views. The middle row depicts a star with circular arms from 2 different angles. In the bottom row, a star with isosceles triangle arms and a hexagonal star with 6 arms are shown from $30° - 30°$ azimuth and elevation angle. 131

6.13 From (a) to (c) the final shape of the bilayer is shown from $30° - 30°$, $90° - 0°$, and $0° - 90°$ azimuth and elevation angles, respectively. 132

6.14 Having non-responsive middle sections changes the shrinkage dynamics significantly. The top row demonstrates 2 different views of a star with 4 responsive arms and a non-responsive middle. In the middle row, the same views are used to show a hexagonal star with an identical configuration to the previous case. The bottom row captures how the shrinkage ratio impacts the final shape. 133

6.15 Responsive Janus bilayer deforms into a hook-like shape. The switch in the shape results in a change in trajectory. 136

6.16 Shrinkage and recovery can be used to direct the trajectory of the rod. Panels (a) and (b) are depicted at $t = 0.5$. The orange section represents the responsive area after shrinkage, while the rest of the body is non-responsive. 137

6.17 Active Janus rod with multiple responsive regions deforms and changes its direction. Figure c) is captured from a $90° - 0°$ angle. 139

7.1 The unit normal vectors $\mathbf{N}_{a12}$ and $\mathbf{N}_{a23}$ are stored for each bead in their respective triangles. As the a^{th} bead serves a common corner for both triangles, the unit normal on bead a is computed as the average of $\mathbf{N}_{a12}$ and $\mathbf{N}_{a23}$. 147

B.1 Noisy data is removed out from the function d^2x/ds^2 using algorithm 2. . . 155

CHAPTER 1

INTRODUCTION TO ARTIFICIAL MICROSWIMMERS

Movement is an essential feature of life, intrinsic to finding nutrition, reproduction, and avoiding predators. The way living organisms move differs across different length scales. At the microscale where viscous forces are dominant to inertial forces, locomotion methods are distinct from those at the macroscale. Most microscale creatures exist in a fluid. Therefore, they need to swim, which requires deformation of the body or the use of a tail-like appendage such as a cilium or flagellum (see figure 1.1). Thanks to theoretical and experimental studies in biological locomotion, how living creatures and cells propel at the microscale is thoroughly understood (104).

This understanding has inspired the engineering of artificial microswimmers. These microbots have the potential to perform intricate biomedical tasks, such as targeted drug delivery or miniaturised surgery (92). The success of these applications depends on the 'intelligence' of the microbots, which can be considered to be self-propelled, externally controlled, and multifunctional in some cases. To design a 'smart' microbot capable of accomplishing complex missions, it is essential to elaborate on their historical development.

In this chapter, different propulsion strategies and ways to control artificial microswimmers are introduced, along with a brief history of microbots. In sections 1.2 and 1.3, we compare the benchmark examples of external and self-actuation methods. In section 1.4,

(a) Cilium of an eukaryotic cell deforms as depicted.

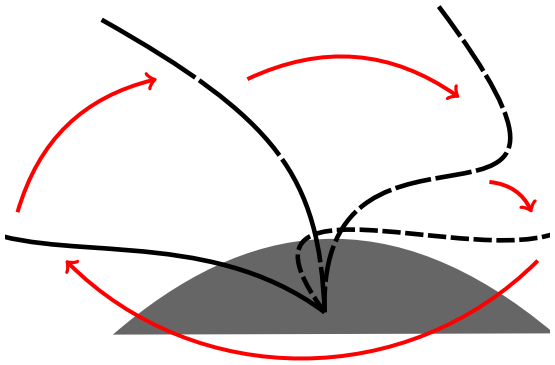

Eukaryotic Cell

(b) Some bacteria use their flagella to have a run-and-tumble motion.

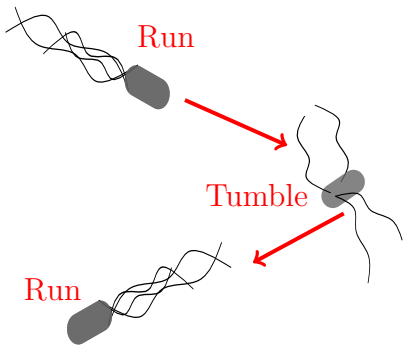

Figure 1.1: Eukaryotic and prokaryotic creatures propel themselves with whip-like organelles, namely cilia and flagella. In panel (a), a cilium beats around a fixed point. In panel (b), a bacterium uses flagella to perform run-and-tumble. During the "run" phase, the bacterium swims forward. Subsequently, in the "tumble" phase, flagella deform to change the direction of motion.

we provide the properties of viscous flows from a mathematical perspective and describe the Stokes equations. Moreover, we mention singularity-based solutions to model slender structures. We conclude this chapter with an analytical solution for the problem of Stokes flow past a sphere in section 1.5.1.

1.1 Artificial Microswimmers

Swimming in viscous fluids at the microscale is a challenging task. There is no inertia that helps the swimmer use momentum. Consequently, natural microswimmers including sperm cells, bacteria, algae and amoebae employ a variety of propulsion mechanisms. Some of these mechanisms exploit a long thin appendage to move. Periodic deformations of flagella or cilia may suffice to break symmetry in the fluid, enabling swimming. Some others such as amoebae deform their entire bodies, so they can have movement in highly

viscous fluids.

Similarly, artificial microswimmers also experience the same problem of moving in viscous fluids. However, unlike their natural counterparts, which have evolved over thousands of years, the manufacturing and development of microbots are still in the early stages. The concept of microbots as a promising field of science began to gain traction only 65 years ago, when Feynman (44) credited Albert Hibbs for the concept of "swallowing the doctor". Even after that, it took almost four decades to realise the simplest propulsion mechanisms and primary designs.

Some of these designs were biomimetic, featuring rigid or flexible tails to propel. Human spermatozoa inspired attaching a magnetic filament to red blood cell (39). In another study, a helical filament was linked to a magnetic head, resembling the motion of *Escherichia coli* (E.coli) bacteria (197). Additionally, new synthetic propulsion methods were invented as well. Diffusiophoresis, a transportation mechanism driven by chemical concentration gradients in the fluid, was used for the passive motion of particles (40). As an extension of phoretic motion, Janus particles with hydrophobic and hydrophilic halves were theoretically described (20). A Janus swimmer, named after the Roman god, has two distinct faces (30). One face is made of a material that introduces activity, while the other face is passive. The term 'activity' refers to interactions with the environment, such as catalysing a chemical reaction. Depending on the affinity of the active material for the environmental conditions, the swimmer either propels towards chemically rich areas in the fluid or moves away from them. Although the initial Janus particles were spherical, subsequent designs have included tubes, rods, filaments, and various arbitrary shapes (see figure 1.2). Over time, examples of employing other field gradients, including temperature (88) and magnetism (51) were demonstrated. Another novel artificial propulsion method was nucleating microbubbles to push the ambient fluid, thus facilitating locomotion (63). It is worth noting that most of these propulsion methods were developed not only to power the swimmer but also to control its trajectory.

This is particularly important for *in vivo* applications, where precise navigation be-

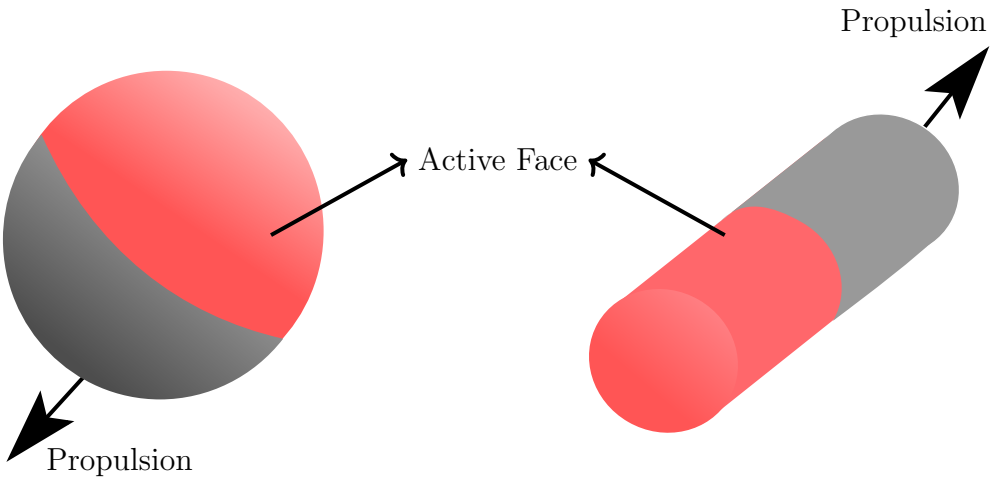

Figure 1.2: Janus particles can be designed in various shapes. For example, on the left-hand side, a traditional spherical Janus particle is demonstrated, while on the right-hand side, a cylindrical Janus rod is presented. Generally, the active face, indicated by pink, interacts with the environment, causing the swimmer to move in the opposite direction.

comes crucial. For instance, local delivery of therapeutic drugs requires different functions including translation, rotation, stopping, and drug release. Moreover, both the process and the microbot itself should be non-invasive and biodegradable. These issues can be addressed by using soft, flexible and harmless materials that can be externally tunable. However, outer control mechanisms may lack precision, especially for operations employing a swarm of microbots (129). Identifying individual swimmers in a group and avoiding collisions can be cumbersome or costly. Therefore, the ultimate goal is to engineer microbots that are biocompatible, self-sufficient for movement, spatially aware, and internally controlled.

To obtain these smart microbots, the shape, propulsion method, navigation, and corresponding applicability of artificial swimmers have been in development (164). Thanks to these improvements, intelligent microbots may perform complex tasks for biomedical and environmental purposes, including local drug delivery (56), cargo transport (191), and mixing as a microfluidic device (125).

In the next sections, we explain different propulsion methods and their associated

control mechanisms. We categorise these swimmers into two groups; externally controlled and self-actuated microbots (129). Externally-actuated microbots are directed by outside factors such as applied magnetic fields (197), acoustic waves (9), or light intensity (98). In the absence of an external stimulus, these microbots remain stationary. In contrast, self-actuated microbots are typically fuel-based microswimmers that utilise environmental conditions to move autonomously without external stimuli. (188). In some instances, a microbot may benefit from multiple mechanisms simultaneously, blurring the boundary between external and self-actuation methods. Additionally, it should be noted that there can be different ways of categorisation, such as directed and undirected motion. In such groupings, the main focus is on the presence of a control mechanism. Therefore, most examples in the following sections may be categorised under directed motion. Given this nuance, sections 1.2 and 1.3 should be considered a general review rather than a strict classification.

1.2 Externally-Actuated Swimmers

Externally-actuated swimmers are controlled by outside factors. Depending on the task, these stimuli can include magnetic fields, acoustic waves, and light signals. These swimmers rely on external actuation for navigation which means they can use different propulsion mechanisms similar to self-sufficient microbots. We will begin our review with magnetic fields for externally controlling and propelling microbots.

1.2.1 Magnetic Fields

Exerting magnetic fields is one of the most common propulsion methods in artificial microswimmer studies. The ease of implementation and compatibility with any swimmer shape (helical, spherical, or more complex designs) have placed magnetic fields in a pivotal role in the advancement of microbots. Moreover, magnetic field gradients offer remote control for the user without the need for any additional device or system.

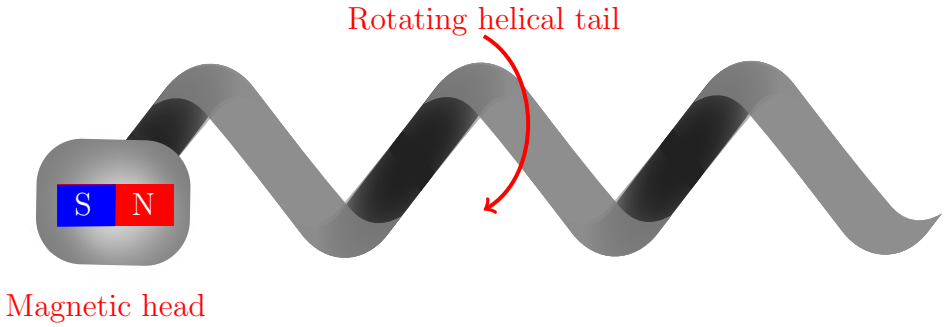

Figure 1.3: The schematic demonstrates a magnetic swimmer capable of rotating its helical tail under magnetic field gradients to propel itself. For example, Zhang et al. (197) employed a similar mechanism.

Some early studies utilised magnetic fields to control microbots, mimicking natural swimmers. At the millimetre scale, a rigid spiral connected to a magnet was turned by alternating magnetic torque (74). Later, in a landmark study, Zhang et al. (197) magnetically rotated a helical tail at the micrometre scale attached to a soft head inspired by the monotrichous bacterium. The passive tail was spun around the head by changing the magnetic gradient, resulting in a corkscrew-like motion, hence translation (see figure 1.3). In experimental studies, magnetically controlled helical swimmers were used for loading and unloading objects as microcarriers (79) and were involved in the degradation of bacterial pollution (75). Although these tasks were conducted in laboratory settings, they are crucial in demonstrating the potential of these swimmers.

As an alternative to helical swimmers, deformations of the flexible tails have been used for microscale locomotion. Dreyfus et al. (39) magnetically actuated a chain of colloids as a micrometre-scale filament. In the same study, red blood cells were transported by an artificial flagellum *in vitro*. In Gao et al.'s study (57), akin to oscillations of the prokaryotic flagellum, the rotary motion of nanowires provided both propulsion and control.

In contrast to drawing inspiration from nature, some studies have focused on virtual methods. For example, Yesin et al. (194) developed an untethered elliptical swimmer that

can be pulled via magnetic fields. Similarly, a Janus sphere was magnetically steered in the work by Chen et al. (22). This study also provided an example of using magnetic fields to trigger an effective scavenger mode for noble metals. Additionally, Jang et al. (85) employed flexibility to realise a modified version of Purcell's theoretical three-link swimmer (see 1.4.1). In the study, a three-link swimmer was magnetically deformed to exhibit planar undulation.

These examples have paved the way for more precise, efficient, and biodegradable magnetically controlled swimmers. Deformable materials have been employed to increase the functionality of microbots, offering dynamic shape transformations and different operational modes. For example, Fusco et al. (51) showcased self-folding microtubes *in-silico* and *in vitro* environments. In the research by Huang et al. (78), a thermal stimulus was used to change the morphology of a magnetically guided hydrogel bilayer. Polymer-based composites and other degradable materials have also been exploited to reduce potential harm and improve *in vivo* applicability. Peters et al. (144) fabricated a canonical helical swimmer made of poly(ethylene glycol) diacrylate (PEG-DA) for drug delivery purposes. Recently, Luan et al. (114) streamlined a micromotor by alginate hydrogel. The swimmer combined catalytic bubble propulsion (will be detailed in section 1.3.2) with magnetic navigation to demonstrate run-and-tumble motion.

For a more detailed review of recent developments and future directions of magnetically driven microswimmers, readers are referred to the study by Shen et al. (162). In the next section, we will explore the usage of acoustic waves in microbot studies.

1.2.2 Acoustic Waves

Acoustic waves and ultrasound have been used both as an energy source and a guidance mechanism in artificial microswimmers. Generally, they are regarded as safe options capable of penetrating through soft tissues (182). This feature renders acoustic waves suitable for controlling microbots carrying therapeutic payloads in biomedical applications. The direct usage of ultrasound for motion is based on the principle of inducing particle motion

(a) Acoustic microbots can follow circular trajectories.

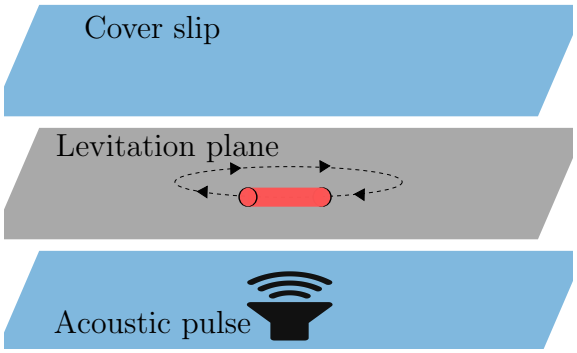

(b) Acoustic nanowires can operate extracellularly.

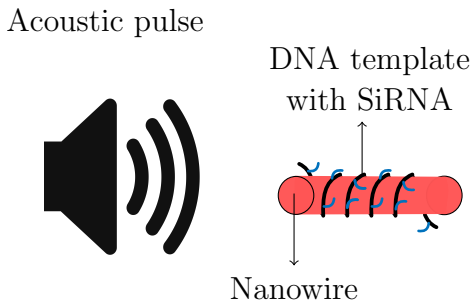

Figure 1.4: The schematic illustrates different applications of acoustic microswimmers. Panel (a) depicts the study of Wang et al. (182). In panel (b), the previous work of Esteban-Fernández de Ávila et al. (42) is redrawn.

via adsorption and reflection of acoustic radiation. A travelling or standing wave excites the swimmer in a highly biocompatible manner, and around the early 2010s, this property began to be considered as an alternative to magnetic fields.

In a landmark study, asymmetric nanorods were levitated by acoustic fields to propel in water (182) (see figure 1.4a). A similar mechanism was employed by Ding et al. (35) to manipulate microparticles with an acoustic tweezer. Later, acoustically propelled microbots were advanced on the nano-scale and used for in-cell operations. For example, Wang et al. (183) operated nanorods in two different modes, namely translation and spinning, inside living HeLa cells. In another study, small interfering RNA-loaded (siRNA) acoustic nanowires transported intracellularly (42) (see figure 1.4b).

Aside from these examples, the compatibility of acoustic waves has been combined with other propulsion mechanisms and has been used in fuel-free swimming. In the study by Valdez-Garduño et al. (179), an ultrasound-driven Janus particle was oriented by fixed magnetic fields. Another approach was experimented with by adding a metallic helical tail to a nanorod (106). The design of the micromotor offered to benefit from both acoustic waves and magnetic fields to have double propulsion. Other examples of hybrid swimmers

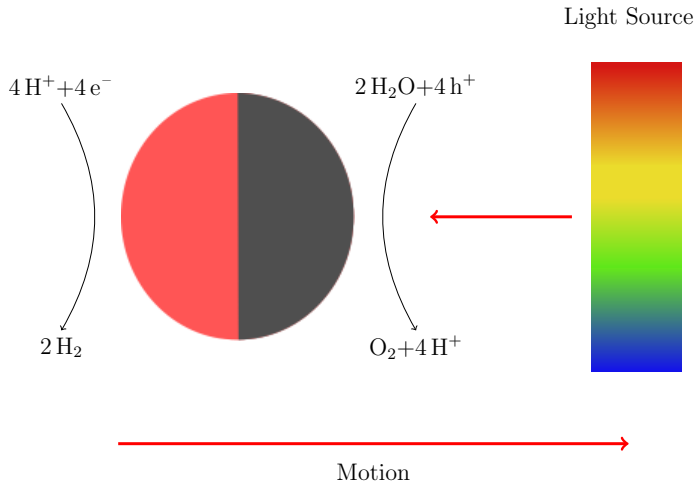

Figure 1.5: The faces of light-propelled Janus swimmer can consist of different material pairs, such as gold (Au) and titanium dioxide (TiO_2), corresponding to pink and grey colours in the schematic. There is a transfer of H^+ and H_2O in the opposite direction to the motion.

and propulsion methods, particularly acoustically controlled bubble propulsion, will be provided in section 1.3. A more detailed literature review of acoustic propulsion can be found in the study by McNeill and Mallouk (124). In the next section, we will explain light-propelled swimmers, which lie between external and self-actuation techniques.

1.2.3 Light Intensity

In light-propelled swimmers, mostly photoanodes and photocathodes are incorporated. The gradients of light around the swimmer result in an anisotropic distribution of ions, and hence propulsion (201) (see an illustration of the mechanism in figure 1.5).

An important example of exploitation of this mechanism was performed by Liu et al. (112). In that study, a nanomotor drove a disk $\mathcal{O}(10^4)$ times larger than its own body via linearly polarised light. In another investigation, a photocatalytic Janus sphere was propelled by UV light (38), suggesting a direct proportionality between swimmer speed and light intensity. A similar Janus particle was enhanced to swim in multiple wavelengths (86). Additionally, in the same study, the motion of the swimmer was manipulated to either stop or continue by toggling the light off and on.

Although these studies have demonstrated fruitful applications of light propulsion, the penetrability of light into soft tissues is more limited than that of magnetic fields and acoustic waves. As a result, these swimmers are often used near surfaces *in vitro*, and light is devised as a triggering mechanism or for navigation rather than propulsion. As an example of light-triggered thermophoresis (will be explained in 1.3.1), Wu et al. (192) produced polymer-based tubular microrockets that could reach high speeds such as 10 to 15 body lengths per second. In another study, a catalytic microtube was employed to release gas bubbles from the body by light stimulus (132). The combination of these two mechanisms promised a selective nucleation area for bubble growth. Later, the same principle was applied to Janus spheres with the aim of decomposing pollutants (109). Recently, Rey et al. (154) published a detailed review of similar uses of light intensity in the intersection of microswimmer studies and soft matter.

In this section, we complete our description of external actuation methods and pivotal studies. Research on externally-actuated microbots has significantly enhanced our understanding of the dynamics of artificial swimming at the microscale. However, due to complexity of the tasks and concerns regarding biocompatibility, external actuation mechanisms have yet to be fully commercialised. In the next section, we will delve into self-propulsion mechanisms as an alternative solution to these issues. It should be noted that hybrid methods will also be given in the same section.

1.3 Self-Propelled Swimmers

Self-propulsion is crucial to reaching the potential of smart microbots. It requires a certain level of environmental awareness, and necessary tools to exploit ambient conditions (131). Therefore, acknowledging this reliance on external factors, they may be mentioned as fuel-dependent micromachines.

This fuel for converting mechanical or chemical energy to work is mainly hydrogen peroxide H_2O_2. Although other solutions can be used to propel swimmers (83), H_2O_2

has been abundant in synthetic swimming because it can easily decompose. This ambient solution is used to start a chemical reaction resulting in either a field gradient or nucleation of gas bubbles. While the first mechanism forms the basis for phoretic motion, the latter refers to bubble propulsion. In sections 1.3.1 and 1.3.2, we will introduce these two methods in self-movement at the microscale.

1.3.1 Phoretic Microswimmers

In phoretic motion, the movement of the particles is induced by field gradients. These gradients can result from the heterogeneous distribution of chemical concentration, electric potential, or temperature field. The field gradients cause anisotropic surface reactions which result in motion. Self-phoretic or autophoretic microbots can establish these gradients themselves. Since Paxton et al. (143) experimentally performed the first example of phoretic motion, different versions of it have become ubiquitous in microbot studies.

The most common type of phoretic motion occurs due to gradients in chemical concentration. This mechanism is known as diffusiophoresis. Diffusiophoretic motion can be considered somewhat analogous to the attraction of sperm to the egg (8) or bacteria's search for nutrients (49). In general, a chemical reaction, i.e., the decomposition of hydrogen peroxide, happens on a part of the swimmer's body. Consequently, the balance between attractive and repulsive forces between the ambient fluid and particle is perturbed. This imbalance gives a push or pull, causing the swimmer to wander (see figure 1.6a).

As a theoretical benchmark study, Golestanian et al. (64) mathematically described a self-diffusiophoretic Janus particle. Following this, experimental studies realised self-diffusiophoresis for Janus particles. Howse et al. (76) investigated the relation between the directed motion of a Janus swimmer and the solute concentration. In the same study, it was observed that the long-term dynamics of Janus particles yield random walks. Later, Pavlick et al. (142) propelled a Janus sphere with chemical reaction products due to polymerisation. The study also promised precise navigation by harnessing the chemotaxis

(a) Diffusiophoretic motion is illustrated.

(b) Electrophoretic motion is demonstrated by the schematic.

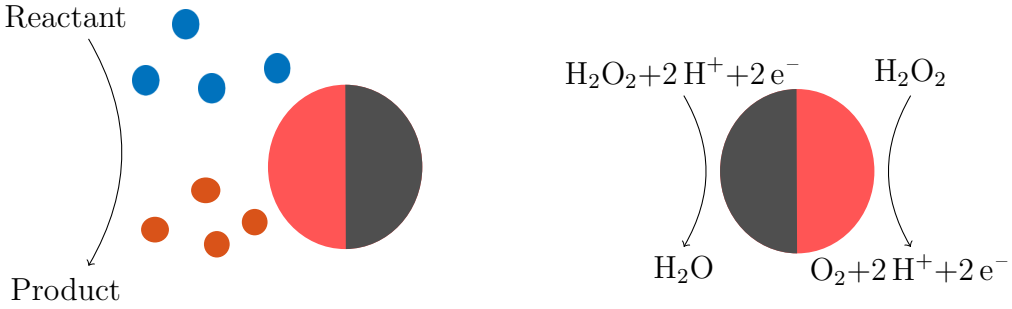

(c) Temperature gradients along the body generate motion.

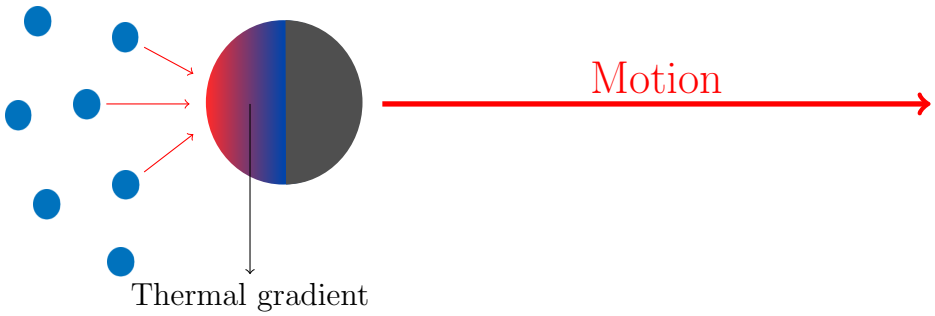

Figure 1.6: The figures illustrates the working principles of diffusiophoretic, electrophoretic, and thermophoretic microbots from panel (a) to panel (c) in respective order. In each figure, the motion occurs from left to right. In panel (a), the grey face represents an inert material and the pink face triggers a catalytic reaction. In panel (b), the colours can be considered as a metal pair such as platinum (Pt) and gold (Au), and the electron transfer is in the opposite direction to the motion. In panel (c), due to the thermal gradient fluid particles at the left-hand side obtain more energy and hit the active surface, resulting in propulsion.

behaviour through monomer concentration.

These insights have paved the way for employing diffusiophoretic swimmers for more complex tasks. For example, an autophoretic vesicle was proposed in local drug delivery across the blood-brain barrier by Joseph et al. (90). Different studies showcased spatially intelligent micromachines to sense pollution to clean (147) or solve a so-called maze (48).

While these studies illustrate the versatility of self-diffusiophoretic motion, there is another study we would like to mention. In the work by Brown and Poon (16), the swimming velocity of a self-diffusiophoretic swimmer was limited in the presence of additional surfactants. This was due to increased ionic strength and, hence, a reduction in reaction rate. This relation suggested that in most cases diffusiophoretic motion was accompanied by electrophoresis as well.

The idea of electrophoresis dates back to the 1950s. Mitchell (127) proposed that if a bacteria could pump ions asymmetrically and exchange them with the surrounding medium, it would swim without a limb. To the best of our knowledge, there is no biological example of this phenomenon (186). However, this definition can be adapted to microbots; if a gradient of electric potential exists, ions will constantly travel along the body and propel the artificial microswimmer (see figure 1.6b).

The very first experimental study of self-electrophoresis can be found in Paxton et al.'s study (143), in which bimetallic microrods consisting of gold and platinum were used to transfer protons from one end to the other end. This process resulted in a motion along the rod's long axis, hence, swimming in a hydrogen peroxide solution. Later, different metal combinations were experimented with to increase or decrease the reaction rate to control the speed of the microswimmer. In that regard, Wang et al. (185) demonstrated that as the mixed electric potential of the metal pair, higher translational speeds can be obtained.

However, some of these metal pairs were not biocompatible and could not be applied to operations in biological systems. Thus, different materials including enzymes and hydrogels have been suggested as remedies. Mano and Heller (119) designed a carbon

fibre motor that can swim at the air-solution interface via bioelectrochemical propulsion, which can be classified as the first example of enzyme usage on the millimetre scale. Over time, thanks to advancements in microfluidic technologies, the length scale of these devices has started to shrink to the microscale. In Pavel et al.'s study (141), hemoproteins capable of catalysing hydrogen peroxide were employed to establish self-electrophoresis on nanorods. However, there still remains a need for further improvement in biodegradable electrophoresis.

Thermophoresis as an independent mechanism from ionic strengths and hazardous metals, may offer a more bio-friendly option for microbots. In thermophoretic motion, a temperature gradient exists throughout the body of the swimmer. The anisotropic distribution of temperature causes more collisions with surrounding particles on the hotter side. This process causes a momentum exchange, hence, locomotion (see figure 1.6c).

A prime example of self-thermophoretic motion was given by Jiang et al. (88). In that study, a Janus particle induced by a laser beam performed self-thermophoretic motion. Later, Qian et al. (151) not only propelled the swimmer with thermophoresis but also numerically optimised a steering strategy to control the trajectory.

In terms of the external navigation of the microbot, other mechanisms have been combined with self-thermophoresis. For example, Baraban et al. (4) suggested using magnetic fields to direct self-thermophoretic Janus particles. The purpose of this hybrid approach was to have precise control over a biocompatible swimmer. With a similar motivation, Qin et al. (153) utilised asymmetric catalytic reactions on the Janus particle, creating a temperature gradient in the ambient fluid.

With these examples, we have shed light on some fundamental concepts of phoretic motion. Recent developments in this field can be found in reviews of the literature by Jang et al. (87) and Wang (181). In the next section, we will exemplify the studies on the bubble propulsion mechanism. It should be noted that section 1.3.2 will be more comprehensive than the previous sections. This is due to the fact that our collaborative study described in Chapter 2 benefited from the bubble propulsion method.

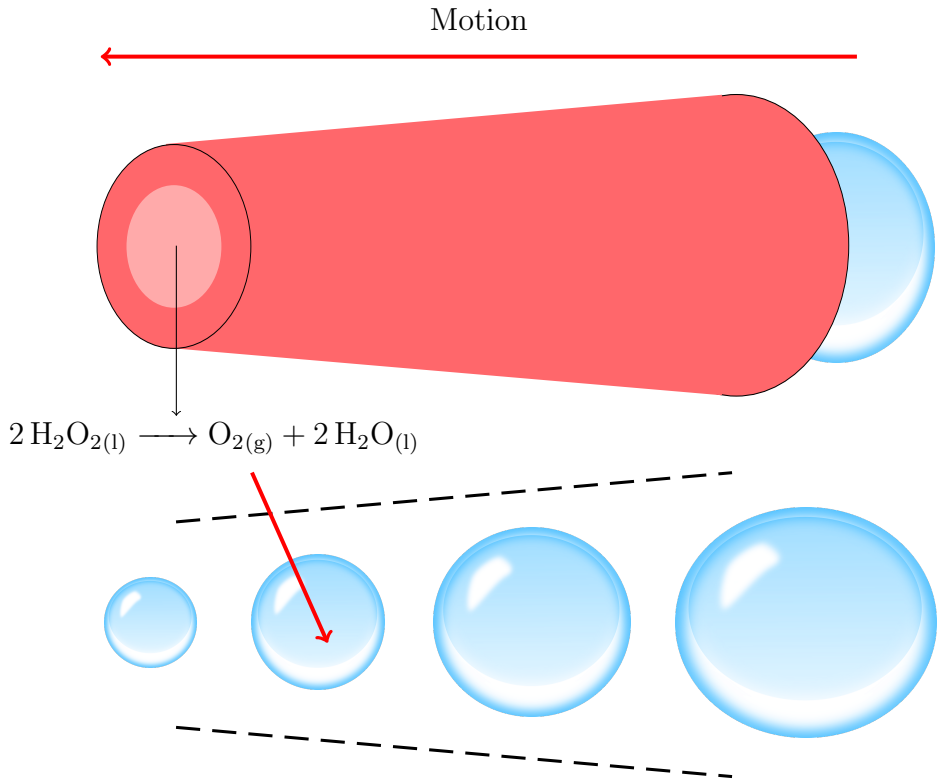

Figure 1.7: The schematic describes the working principle of a bubble-driven conical microtube. The top illustration is redrawn from the previous work by Gallino et al. (53). The inner walls trigger the catalytic reaction and also confine the growing bubble. The ejected bubble and microbot move in opposite directions.

1.3.2 Bubble Propelled Microswimmers

In the last two decades, bubble propulsion has been studied extensively as a promising method for steering microswimmers. Generally, bubble-propelled microswimmers produce gas bubbles that can either detach from the body or burst while still in contact with the microbot (84). Both the growth of the bubble and its removal can create propulsion, which raises significant interest in this mechanism.

The first example of a bubble propulsion mechanism can be found in the work of Ismagilov et al. (84). In the study, millimetre-scale circular plates were moved by the recoil of oxygen bubbles. The gas was produced as $2\,H_2O_{2(l)} \longrightarrow O_{2(g)} + 2\,H_2O_{(l)}$ catalysed by platinum. As bubbles recoiled from the body, the plates moved in the opposite direction.

Later, the decomposition of hydrogen peroxide was established by Nickel and the release of oxygen nanobubbles was used to rotate a nanorotor anchored at one end (47). In a similar study, a bubble-propelled microrocket was introduced by Mei et al. (126). This tubular jet had two openings, which were responsible for the penetration of aqueous fluid and the ejection of gas bubbles (see figure 1.7). The bubbles were formed via the silver (Ag) inner walls and detached from the body due to low adhesive forces. Following this, asymmetrically rolled up microtubes were designed to drill into biomaterials with corkscrew-like rotations (167). The mitigation of oxygen bubbles to the trailing edge resulted in thrust to move the swimmer. The same principle of detaching bubbles from the microparticle to generate a net hydrodynamic force was suggested for Janus spheres by Gibbs and Zhao (63) (see the illustration showing the motion of a bubble-driven Janus sphere in figure 1.8). In different studies, bubble-driven Janus particles have been realised for cleaning bacterial pollution(140) and targeted cargo transfer(111). Different designs including shell swimmers (81) and capsule Janus vesicles (58) have also been combined with catalytic bubble-propulsion.

In addition to catalytic bubble generation, there is also another way of exploiting gas bubbles for propulsion, which is acoustic excitement. In a landmark study, ultrasound pulses vaporised the droplets inside a microtube resulting in bubble release accompanied by a bullet-like propulsion (93). In the study by Bertin et al. (9), an experimentally manufactured bubble was placed inside an "armour". While the armour was protecting the bubble from bursting for hours, the acoustic waves periodically oscillated the bubble, causing directional motion.

Opposed to the straightforward mechanism of acoustically induced bubble propulsion, the dynamics of catalytic bubble recoil can be more ambiguous. Even though the catalytic production of gas bubbles is the dominant method for swimming, it is also possible to mention the presence of diffusiophoresis and electrophoresis. Since the decomposition equation of hydrogen peroxide may create both chemical concentration and ion gradients, phoretic motion could also contribute to propulsion. For example, Qin et al. (152) ob-

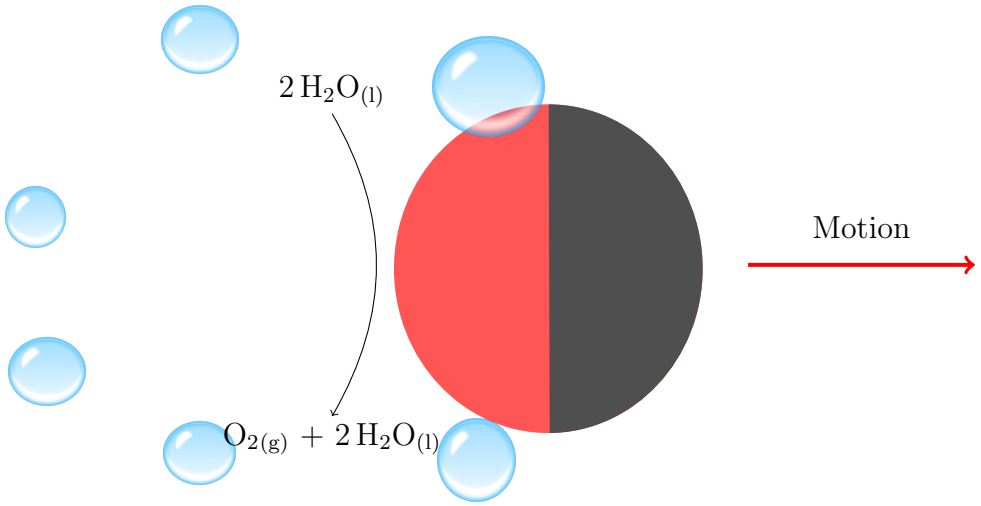

Figure 1.8: As a result of a catalytic reaction, the active face of the Janus swimmer, indicated in pink, produces oxygen bubbles, causing the swimmer to move from left to right in the schematic.

served the utilisation of both electrophoresis and bubble propulsion in catalytically driven nanorotors. To identify which mechanism governs the dynamics, Wang and Wu (180) investigated catalytic Janus dimers. In the study, it was reported that Janus swimmers with rough surfaces and higher catalytic activity tend to use bubble propulsion rather than diffusiophoresis. From a different perspective, *in-silico* study of Zhang et al. (196) numerically compared dominant mechanism according to length scale. The study suggested for Janus motors whose diameter is smaller than 5 µm to 10 µm, self-diffusiophoresis is the main propulsion mechanism. However, for larger particles, bubble propulsion dominates the motion, resulting in faster translation as well. With these valuable insights, efforts have been put into optimising the translation speed of bubble-driven microbots and improving functionality for real-life applications.

For this purpose various parameters including the material of the swimmer, concentra-

tion of solution, and applicability of multiple propulsion strategies have been tested (92). In Dey et al.'s study (34), a polymer-based bubble-propelled Janus sphere was manufactured to be sensitive to pH gradients. It was observed that as pH became more alkaline, the micromotor swam faster. In a different study, the inverse correlation between bubble radius and generation frequency was discovered for microtubes (166). The authors suggested that as the solution concentration increases, the bubble generation becomes more frequent, resulting in smaller bubbles and slower translation, which could be essential to control these microbots. In the work by Sanchez et al. (156), the usage of catalase enzyme led to the successful motion of bubble-driven microengines in low H_2O_2 concentrations. These microtubes were also rotated depending on the size of released bubble, which was a prospective application of dynamic self-steering. These results have been used to manufacture bubble-driven microbots and implement them in complex scenarios. For example, the study by Gao et al. (59) can be considered as the first *in vivo* application of bubble-propelled swimmers. The rod-shaped micromotors operated inside the stomach of mice for cargo delivery and also gradually self-destructed via gastric acid. Magnetic fields helped to control the microbot. Singh et al. (163) designed a cubic swimmer made by zeolite and able to release Ag^+ to degrade *E.coli* bacteria. The porosity of the swimmer facilitated the simultaneous release of silver ions and gas bubbles. Later, a chitosan-based Janus micromotor was employed to clean *E.coli* bacteria pollution in water (31). In that study, the magnesium-coated face triggered a chemical reaction producing hydrogen gas, while the chitosan-coated face was employed to decrease bacterial contamination.

These experimental studies have been supported by mathematical models that explain the bubble growth mechanism. Favelukis and Yablonsky (43) proposed a catalytic bubble growth model. The study focused on the generation of gas bubbles in quiescent fluids without any solid surface to attach or recoil and suggested a temperature gradient was produced as a side product of the reaction. Later, Gallino et al. (54) investigated a catalytic bubble growth mechanism inside a microrocket and described the process in three phases: spherical growth, deformation, and exit of the bubble from the cone. The study

numerically optimised the cone angle to increase the maximum displacement velocity. In Chapter 2, we will also propose a catalytic bubble growth-collapse mechanism for microrods.

The latest developments and new horizons of the bubble-propulsion mechanism can be found in Wang et al.'s study (184). With this, we complete our section on methods of artificial microswimming. In the next section, we will mathematically describe the governing equations of the motion of microbots.

1.4 Microswimmer Dynamics and Stokes Flow

Artificial microswimmers can take on different shapes and employ various propulsion mechanisms. The necessity for this broad spectrum of movement strategies arises from the fluids in which microbots operate. These microbots move in the Stokes flows. Hydrodynamics of any flow can be described with the Cauchy momentum equations, and Stokes flow is no different (5). The Cauchy momentum equations are given as:

$$\rho \frac{D\boldsymbol{u}}{Dt} = \nabla \cdot \boldsymbol{\sigma} + \boldsymbol{F} \tag{1.1}$$

$$\frac{\partial \rho}{\partial t} + \nabla \cdot (\rho \boldsymbol{u}) = 0 \tag{1.2}$$

where ρ is the fluid density, $\boldsymbol{u} := \boldsymbol{u}(\boldsymbol{x}, t)$ and $\boldsymbol{F} := \boldsymbol{F}(\boldsymbol{x}, t)$ are fluid velocity, and forces acting on the fluid, respectively. The stress tensor including the pressure field is denoted with $\boldsymbol{\sigma}$. The arguments of velocity and force are a material point in the fluid, $\boldsymbol{x}$ and time, t in respective order. Throughout this thesis, scalars will be denoted by lowercase letters, while vectors will be provided by bold lowercase letters.

In above equations, the material derivative is defined as:

$$\frac{D\boldsymbol{u}}{Dt} = \frac{\partial \boldsymbol{u}}{\partial t} + (\boldsymbol{u} \cdot \nabla)\boldsymbol{u}. \tag{1.3}$$

Since we only work on incompressible flows in this thesis, the density is not a function

of pressure. Assuming that the density is constant throughout the fluid, *mass continuity* or *continuity equation* in 1.2 can be simplified as:

$$\nabla \cdot \boldsymbol{u} = 0. \tag{1.4}$$

For Newtonian fluids such as water or aqueous solutions, the stress tensor is defined as:

$$\boldsymbol{\sigma} = -p\mathbf{I} + 2\mu\mathbf{E}(\mathbf{u}). \tag{1.5}$$

In this formulation, p and μ are the pressure and viscosity respectively. It should be noted that $\mathbf{I}$ is the identity matrix. Throughout this study, the viscosity is considered constant. The fluid strain rate is given by:

$$\mathbf{E}(\boldsymbol{u}) = \frac{1}{2}(\nabla\boldsymbol{u} + (\nabla\boldsymbol{u})^T), \tag{1.6}$$

which represents the symmetric part of the velocity gradient $\nabla\boldsymbol{u}$.

By substituting equation 1.5 into equation 1.1, we obtain the incompressible Navier-Stokes equations for a Newtonian fluid as follows:

$$\rho\left(\frac{\partial\boldsymbol{u}}{\partial t} + (\boldsymbol{u}\cdot\nabla)\boldsymbol{u}\right) = -\nabla p + \mu\nabla^2\boldsymbol{u} + \boldsymbol{F}, \qquad \nabla\cdot\boldsymbol{u} = 0. \tag{1.7}$$

For simplicity, we can express the force acting on the fluid as $\boldsymbol{F} = \rho\boldsymbol{g}$, where $\boldsymbol{g}$ is the gravitational acceleration vector (148). Then, we can non-dimensionalise equation 1.7 by introducing the following dimensionless variables:

$$\boldsymbol{u^*} = \frac{\boldsymbol{u}}{U}, \qquad \boldsymbol{x^*} = \frac{\boldsymbol{x}}{L}, \qquad t* = \frac{t}{T}, \qquad p^* = \frac{pL}{\mu U}. \tag{1.8}$$

Consequently, dimensionless Navier-Stokes equation can be written as:

$$\beta\frac{\partial\boldsymbol{u^*}}{\partial t} + Re\,(\boldsymbol{u^*}\cdot\nabla^*\boldsymbol{u^*}) = -\nabla^* p^* + \nabla^{*2}\boldsymbol{u^*} + \frac{Re}{Fr^2}\frac{\boldsymbol{g}}{g} \tag{1.9}$$

where the parameter groups

$$\beta = \frac{\rho L^2}{\mu T}, \qquad Re = \frac{\rho U L}{\mu}, \qquad Fr = \frac{U}{\sqrt{gL}}, \tag{1.10}$$

are the frequency number, the Reynolds number, and the Froude number respectively. Here, the frequency number denotes the ratio of inertial acceleration to the viscous forces. The second parameter group, the Reynolds number, provides the ratio of inertial forces to viscous forces, while the Froude number is equivalent to magnitude of inertial convective forces relative to body forces.

For microswimming studies, the Reynolds number is calculated as $Re \ll 1$ by substituting the appropriate length and velocity scales. Prime examples of low Re swimming are *E. coli* and human spermatozoon. The former swims at $Re \approx 10^{-5} - 10^{-4}$, while the latter moves at $Re \approx 10^{-2}$. By considering problems in the "zero" limit for Re, and after choosing the appropriate force scaling, we obtain the unsteady Stokes equation as follows:

$$\beta \frac{\partial \boldsymbol{u}}{\partial t} = -\nabla p + \mu \nabla^2 \boldsymbol{u} + \boldsymbol{F}. \tag{1.11}$$

Additionally, for flows where $\beta \ll 1$, the acceleration term on left-hand side of equation 1.11 may be neglected. This reduction yields the Stokes equation for creeping flows, given as:

$$-\nabla p + \mu \nabla^2 \mathbf{u} + \boldsymbol{F} = 0, \qquad \nabla \cdot \mathbf{u} = 0. \tag{1.12}$$

It should be noted that equations 1.11 and 1.12 are presented in dimensional form. Furthermore, the latter serves as the cornerstone of this thesis. Thus, it is essential to understand the distinct features of the Stokes regime, as discussed in section 1.4.1. In addition to that, in section 1.5.1, we will provide an analytical solution for the problem of a creeping flow past a sphere. The solution will be further used in Chapter 4 to determine the regularisation width.

1.4.1 Properties of Stokes Flow and Fundamental Solution

We can begin by describing one key property of the Stokes flow: *instantenity*. In creeping flows, such as those described by equation 1.12, there is no inertial term or time derivative ($\rho\frac{D\boldsymbol{u}}{Dt} \rightarrow 0$). This means the flow field is solely determined by instantaneous boundary conditions and force fields. For example, if a non-deformable sphere sediments under gravity, it reaches the terminal velocity immediately. An important implication of the absence of inertial terms is no net force on the swimmer. Thus, the sum of body forces and external forces should be always equal to zero.

The instantenity of Stokes flow also results in *kinematic reversibility.* This feature implies that if the boundary motion is reversed, then the flow field would be equal and in the opposite direction to the original flow. Consequently, periodic reversible motions would create a net zero displacement. In a short movie by Taylor (173), the kinematic reversibility was showcased by mixing and unmixing a parcel of dye and glycerine through an equal number of rotations clockwise and counterclockwise.

The same film also demonstrated that a rotating helical filament was enough to propel a body in creeping flows. The non-reversible motion of the helical filament resulted in non-zero forces on average on the body, what was later described by Purcell (150) as "Scallop Theorem". According to this theorem, a scallop cannot move in the Stokes flow by just periodically opening and closing its shell. Consequently, the swimmers in the Stokes regime are required to use non-reciprocal deformations to achieve propulsion. As an illustrative example of bypassing the kinematic reversibility, Purcell proposed a theoretical swimmer comprising three links connected by two hinges. The swimmer swings its arms in a non-reciprocal fashion in each beat cycle, as depicted in figure 1.9. Since the periodic motion of the three-link swimmer is irreversible, it generates a net flow. A similar yet simpler theoretical swimmer was suggested by Najafi and Golestanian (135), consisting of three spheres and beating in a non-reciprocal fashion.

Another important feature of the Stokes equation is its *linearity*, which means that the sum of two solutions is also a solution of the equation. In other words, if $(\boldsymbol{u}_1, p_1)$ and

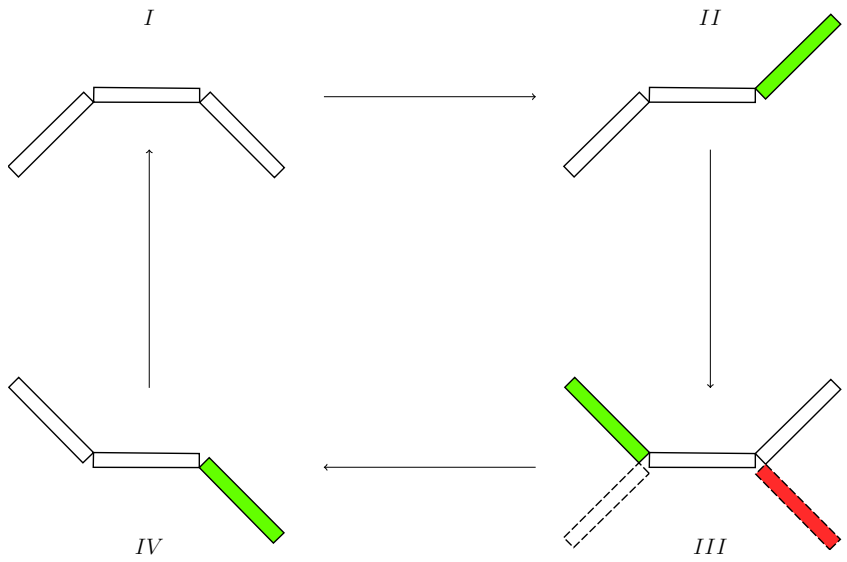

Figure 1.9: Purcell's theoretical three-link swimmer moves with changing arm positions relative to the body (150). The key configurations of swimmer are given as states, with the green colour indicating the moving arm compared to previous position. The third state is particularly crucial for inducing non-reciprocal motion. In configuration III, the red arm shows a theoretical reciprocal deformation, hence, no motion.

$(\boldsymbol{u}_1, p_2)$ are both solutions, then the following equation is satisfied as well.

$$\mu\nabla^2(\boldsymbol{u}_1 + \boldsymbol{u}_2) - \nabla(p_1 + p_2) + \boldsymbol{F} = (\mu\nabla^2\boldsymbol{u}_1 - \nabla p_1) + (\mu\nabla^2\boldsymbol{u}_2 - \nabla p_2) + \boldsymbol{F} \tag{1.13}$$

$$\nabla \cdot (\boldsymbol{u}_1 + \boldsymbol{u}_2) = \nabla \cdot \boldsymbol{u_1} + \nabla \cdot \boldsymbol{u}_2 = 0. \tag{1.14}$$

This property enables superposition, which has been essential in developing several techniques to model swimming at the microscale. By superposing fundamental solutions, it becomes possible to describe different and more complex flows in the Stokes regime. To obtain a fundamental solution, consider a Stokes flow driven by a concentrated force per unit volume, $\boldsymbol{F} = \boldsymbol{f}\delta(\boldsymbol{x} - \boldsymbol{x}_0)$. The three-dimensional Dirac delta function is centred at $\boldsymbol{x}_0$, and $\boldsymbol{x}$ represents a material point in the fluid domain. Then, by using the Green's function for equation 1.12, we can write:

$$\boldsymbol{u}(\boldsymbol{x}) = \frac{1}{8\pi\mu}\boldsymbol{S}(\boldsymbol{x}, \boldsymbol{x}_0) \cdot \boldsymbol{f}(\boldsymbol{x}_0) \tag{1.15}$$

where $\boldsymbol{S}$ is known as the *Stokeslet* or the *Oseen-Burgers* tensor (148). The stokeslet is a point force driving the flow field, given by:

$$\boldsymbol{S}(\boldsymbol{x}, \boldsymbol{x}_0) = \frac{\mathbf{I}}{r} + \frac{\boldsymbol{r}\boldsymbol{r}}{r^3}, \tag{1.16}$$

where $\boldsymbol{r} = \boldsymbol{x} - \boldsymbol{x}_0$ and $r = |\boldsymbol{r}|$. Then, the associated pressure field with this flow may be presented as (104):

$$p(\boldsymbol{x}) = \boldsymbol{H}(\boldsymbol{x}, \boldsymbol{x}_0) \cdot \boldsymbol{f}, \qquad \boldsymbol{H}(\boldsymbol{x}, \boldsymbol{x}_0) = \frac{\boldsymbol{r}}{4\pi r^3}. \tag{1.17}$$

Due to the linearity of the Stokes equation, the derivatives of the stokeslets are also fundamental solutions. The first derivative yields force dipoles, while the second derivative leads to a source dipole and force quadrupoles (104). Appropriate combinations of these fundamental solutions can describe a flow field, such as the flow past a sphere, which can be solved using a stokeslet and a source dipole.

Equation 1.16 contains an anisotropic term, which in component form can be written as $r_i r_j / r^3$. This anisotropy plays a significant role in explaining the dynamics of slender structures such as cilia or flagella in Stokes flows (128). If we consider velocities parallel and perpendicular to the exerted force, f_j (see figure 1.10), we would obtain the following result;

$$u_{\parallel} = \frac{f_j}{4\pi\mu r} \tag{1.18}$$

$$u_{\perp} = \frac{f_j}{8\pi\mu r}. \tag{1.19}$$

Equations 1.18 and 1.19 mean that the same force produces a parallel velocity twice that of the perpendicular direction, i.e., $u_{\parallel} = 2u_{\perp}$. Then, a slender cylindrical object such as a cilium or flagellum can be modelled as a line distribution of singular stokeslet forces. By summing the stokeslet solutions along the centreline of the slender body, we can approximate the velocity field. Consequently, the drag on a slender body moving

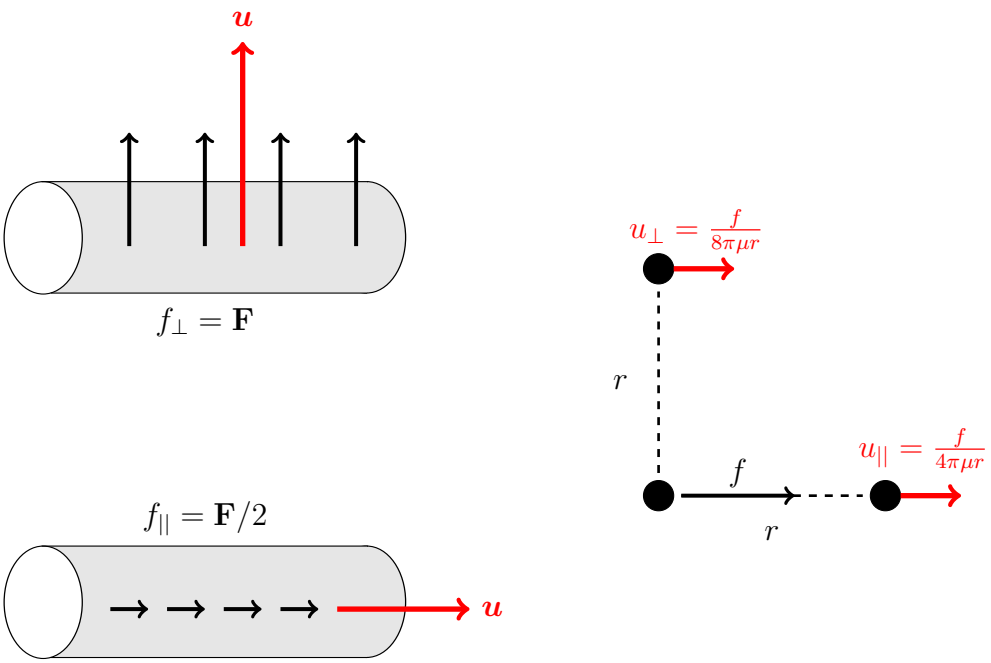

Figure 1.10: The drag anisotropy results in a 2:1 ratio for perpendicular and parallel forces to obtain the same velocity. The schematic is redrawn from the work of Blake and Sleigh (12).

along the flow direction is about half that of an equivalent body moving perpendicular to the flow.

This "two to one" ratio provides a valid approximation for exponentially thin structures, as first suggested by Gray and Hancock (65). However, over time, Lighthill (110) and Johnson (89) refined the calculation of drag coefficients, proposing more accurate models for slender bodies. The physical correspondence of these mathematical descriptions is known as *drag-based thrust*, which describes how flagellum buckles to propel sperm. Apart from this natural mechanism, equations 1.18 and 1.19 are essential to understand deformations of synthetic thin filaments. Therefore, the physical insights from this section will be employed in Chapter 4 to explain the deflections of filaments due to sedimentation.

It should be noted that the stokeslet solution in equation 1.16 is singular. However, this singularity can be addressed by regularising the driving force with a technique known as *the method of regularised Stokeslets* (25). This method smooths the point forces by distributing it over a sphere to provide pressure and velocity fields. By using the method

of regularised stokeslets, fluid-solid interactions for slender filaments or microswimmers have been modelled in a computationally efficient manner (52). Further details of this method will be discussed in the next section.

1.5 The Method of Regularised Stokeslets

The method of regularised stokeslets was developed by Cortez (25), and since then, it has become a powerful numerical tool for investigating viscous flows at the microscale. Due to simplicity of implementation, the method has been widely used to simulate flagellated locomotion (136), propulsion of artificial microswimmers (130), reproduction of pollen tubes (178), and flows in and through porous media (28).

The main purpose of the method is to offer a divergence-free exact solution by removing the singularity of stokeslet. This is achieved by smoothing the point force in equation 1.15. The point force driving the flow is distributed over a sphere in $\mathbb{R}^3$ as follows:

$$\boldsymbol{F}(\boldsymbol{x}) = \boldsymbol{f}\psi_\epsilon(\boldsymbol{x} - \boldsymbol{x}_0), \tag{1.20}$$

where ψ_ϵ is the smoothing function. The position vector $\boldsymbol{x} = [x,\ y,\ z]^T$ is the collocation point, and $\boldsymbol{x}_0$ is the location of regularised stokeslet. The radially symmetric smoothing function is a modified version of the Dirac-δ distribution and has the following property:

$$\iiint_{\mathbb{R}^3} \psi_\epsilon(\boldsymbol{x}) d\boldsymbol{x} = 1. \tag{1.21}$$

Hereafter, the terms *cut-off* and *blob* function will be used interchangeably for smoothing function.

Blob function ψ_ϵ can be defined in many different ways. However, in the original

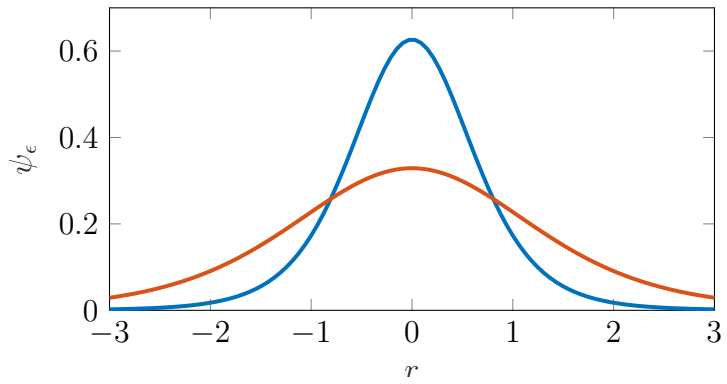

Figure 1.11: As spreading increases, the blob function becomes shorter.

studies in $\mathbb{R}^2$(25) and $\mathbb{R}^3$(26), it is given as:

$$\text{in } \mathbb{R}^2: \ \psi_\epsilon(\boldsymbol{x}) = \frac{3\epsilon^3}{2\pi(||\boldsymbol{x}||^2 + \epsilon^2)^{5/2}} \tag{1.22}$$

$$\text{in } \mathbb{R}^3: \ \psi_\epsilon(\boldsymbol{x}) = \frac{15\epsilon^4}{8\pi(r^2 + \epsilon^2)^{7/2}} = \frac{15\epsilon^4}{8\pi r_\epsilon^7}, \qquad r_\epsilon = \sqrt{r^2 + \epsilon^2} \tag{1.23}$$

where ϵ is the regularisation width known as spreading. Regularisation width is a parameter behaving like the Dirac-δ function as $\epsilon \to 0$. It is responsible for limiting the influence of regularised force. Additionally, for the same cutoff function, different values of ϵ result in wider or narrower spreading (see figure 1.11).

After substituting the regularised force into equation 1.12, we obtain:

$$-\nabla p + \mu\nabla^2\boldsymbol{u}(\boldsymbol{x}) = -\boldsymbol{f}\psi_\epsilon(\boldsymbol{x} - \boldsymbol{x}_0). \tag{1.24}$$

Equation 1.24, can be solved using the smoothed approximation of the Green's function, $G_\epsilon(\boldsymbol{x})$ as

$$\Delta G_\epsilon(\boldsymbol{x}) = \psi_\epsilon(\boldsymbol{x}) \tag{1.25}$$

$$\Delta B_\epsilon = G_\epsilon(\boldsymbol{x}). \tag{1.26}$$

Then, equation 1.15 yields to;

$$\boldsymbol{u}(\boldsymbol{x}) = \frac{1}{8\pi\mu}\boldsymbol{S}^{\epsilon}(\boldsymbol{x}, \boldsymbol{x}_0) \cdot \boldsymbol{f}(\boldsymbol{x}_0) \tag{1.27}$$

where $\boldsymbol{S}^{\epsilon}$ is the regularised stokeslet that is given as:

$$S_{ij}^{\epsilon}(\boldsymbol{x}, \boldsymbol{x}_0) = \frac{\delta_{ij}(r^2 + 2\epsilon^2) + r_i r_j}{r_{\epsilon}^3} \tag{1.28}$$

in the component form. In equation 1.28, δ_{ij} is the Kronecker-δ tensor, and $r^2 = r_i r_i$. Equations 1.27 and 1.28 will be the basis of our numerical method in Chapter 4. In the next section, we will provide an analytical solution for a problem of a Stokes flow past a sphere.

1.5.1 Stokes Flow Past an Impermeable Sphere

We consider a creeping flow past a rigid sphere with radius m (see figure 1.12). The background flow has a velocity of $\boldsymbol{U}_{\infty} = [U_{\infty}, 0, 0]$. The disturbance in the flow created by the sphere held fixed is identical with the same sphere translating with a velocity of $-\boldsymbol{U}_{\infty}$.

For equation 1.12, it is known that:

$$\nabla^2 \boldsymbol{w} = 0, \qquad \nabla^2 p = 0 \tag{1.29}$$

where $\boldsymbol{w}$ is the vorticity vector. In the axisymmetric case, by using the relationship, $\boldsymbol{w} = -\nabla^2 \Psi$, we obtain:

$$\nabla^4 \Psi = 0 \tag{1.30}$$

where $\Psi(\mathtt{r}, \Theta)$ is the stream function. In spherical coordinates, the radial and polar

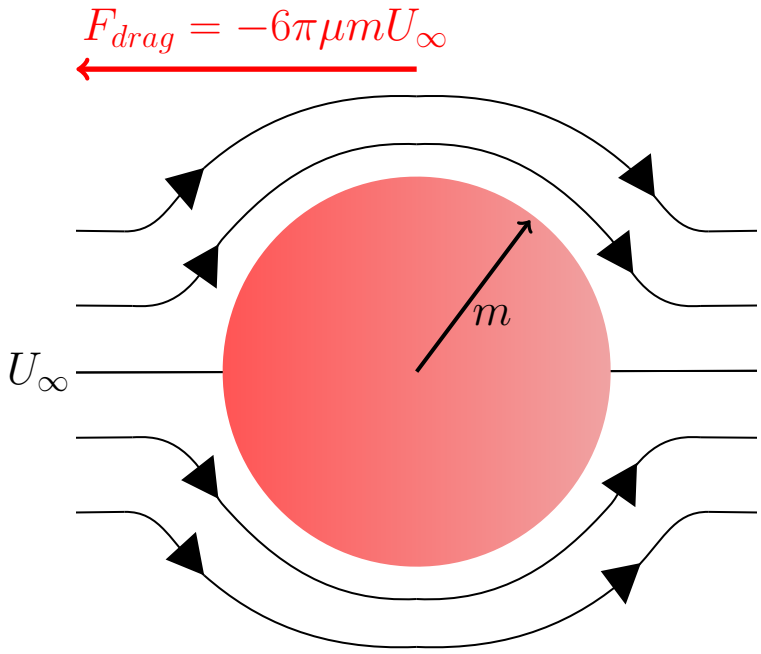

Figure 1.12: The schematic demonstrates the streamlines of a creeping flow around a sphere. The drag force on the sphere is in the opposite direction of the far-field flow.

components of the velocity can be defined as:

$$u_{\mathtt{r}} = \frac{1}{\mathtt{r}^2 \sin\Theta} \frac{\partial \Psi}{\partial \Theta} \tag{1.31}$$

$$u_{\Theta} = -\frac{1}{\mathtt{r} \sin\Theta} \frac{\partial \Psi}{\partial \mathtt{r}}. \tag{1.32}$$

In addition, equation 1.30 yields to:

$$\Lambda^4 \Psi = 0 \tag{1.33}$$

$$\Lambda^2 = \frac{\partial^2}{\partial \mathtt{r}^2} + \frac{\sin\Theta}{\mathtt{r}^2} \frac{\partial}{\partial \Theta} \left[\frac{1}{\sin\Theta} \frac{\partial}{\partial \Theta} \right] \tag{1.34}$$

and differential operator Λ^2 is different than the Laplacian operator in spherical coordinates.

By applying the no-slip, $u_{\mathtt{r}} = 0$ at $\mathtt{r} = m$, and the far-field boundary conditions where

$u_{\mathtt{r}} = U_\infty \cos\Theta,\ u_\Theta = -U_\infty \sin\Theta$, we obtain flow variables as:

$$u_{\mathtt{r}} = \frac{1}{2} U_\infty \frac{m}{\mathtt{r}} \left(\frac{m^2}{\mathtt{r}^2} - 3 \right) \cos\Theta \tag{1.35}$$

$$u_\Theta = \frac{1}{4} U_\infty \frac{m}{\mathtt{r}} \left(\frac{m^2}{\mathtt{r}^2} + 3 \right) \sin\Theta \tag{1.36}$$

$$p = -\frac{3}{2} \frac{\mu U_\infty}{m} \frac{m^2}{\mathtt{r}^2} \cos\Theta. \tag{1.37}$$

Finally, we can find the traction over the sphere and then by integrating over its surface, we can obtain the drag force exerted on the sphere (149). The traction can be find by summing the normal ($\sigma_{\mathtt{rr}}$) and tangential ($\sigma_{\mathtt{r}\Theta}$) components of stress tensor given in equation 1.5. Consequently, the drag on the sphere is:

$$F_{drag} = -6\pi\mu m U_\infty \tag{1.38}$$

The result derived in equation 1.38 will be substantial in both our implementation of regularised stokeslet framework and validation cases (Chapter 4).

1.6 Overview of This Thesis

The remainder of this thesis aims to suggest control mechanisms for hydrogel-based artificial microswimmers through analytical models, numerical methods, and physical understanding, and is organised as follows.

Chapter 2 presents the published article "Fundamental modes of swimming correspond to fundamental modes of shape: Engineering I-, U-, and S- shaped swimmers", which includes a mathematical bubble growth model, image analysis study, and comparison with experimental results.

Chapter 3 provides the necessary background information about gels and responsive hydrogels. In addition, our discrete multiphysics study for modelling hydrogel swelling, namely "Numerical modelling of heterogeneous stimuli-responsive hydrogels" is briefly

explained in the same chapter.

In Chapter 4, we propose a simple bead and spring system employing the method of regularised stokeslets to model hydrodynamics of hydrogel-based active particles. Using this methodology, we investigate the dynamics of active filaments driven by follower forces in Chapter 5. The result of that chapter was extended to an article "Dynamics of active poroelastic filaments" and submitted for publication.

In Chapter 6, the bead and spring system is adapted into the numerical simulations of the swelling and shrinking process of responsive hydrogels. Our numerical technique successfully predicts the shape evolution of hydrogel bilayers.

Finally, in Chapter 7, the findings of each chapter are discussed. and future directions are suggested. The published and unpublished works are provided in the Appendix C.

CHAPTER 2

BUBBLE DRIVEN HYDROGEL BASED I-, U-, AND S-SHAPED MICROBOTS

This chapter elaborates on the mathematical bubble growth model in the published paper "Fundamental modes of swimming correspond to fundamental modes of shape: Engineering I-, U-, and S- shaped swimmers" (161). The manufacturing and experimental work for this study were done by our collaborators Dr Juliane Simmchen and Dr Ivan Rehor's groups and relevant information is provided in Appendix C. This investigation includes a summary of the catalytic bubble growth mechanism and the relationship between the shape and swimming characteristics of rigid microbots. In addition, the findings of this chapter will serve as the primary inspiration for the rest of this thesis.

Recently, soft materials including hydrogels and gels have emerged as key components in partially reaching the avenue of smart or intelligent artificial microswimmers. Thanks to their biocompatibility, versatility, and low Young's moduli, these materials have introduced important properties such as self-assembly (116), self-folding (125), and self-organisation (80). These beneficial features have been realised through advancements in manufacturing techniques including Stop-Flow Lithography (SFL). In this study, gel-based rigid microbots produced using SFL are employed.

In terms of the geometries of microbots, we have been inspired by a previous mathematical phoretic swimmer model proposed by Montenegro-Johnson (129). In that study, phoretic swimmers reminiscing the first three bending modes were employed for different

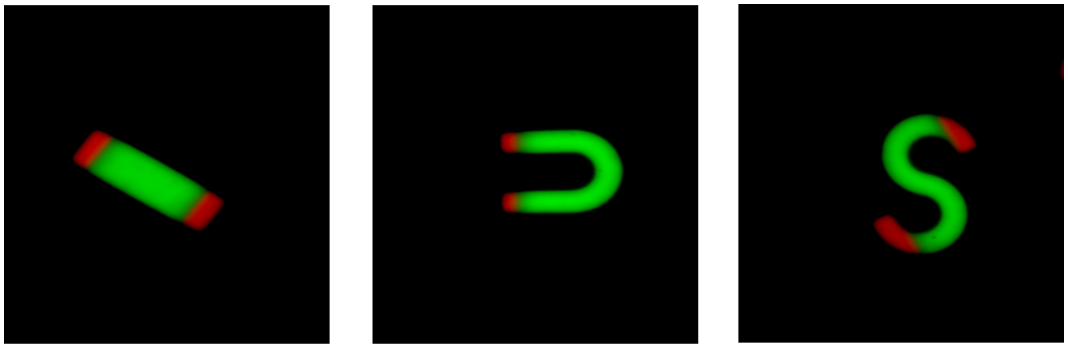

Figure 2.1: Swimmers are dyed to illustrate active and inactive regions. Red tips indicate active caps, while green sections represent inactive regions.

functions. These swimmers, characterised by their shapes, could have operated as micropumps, motors, and rotors. Here, we revisit the previous theoretical study (129) to obtain physical insight; therefore, we focus on three different shapes reminiscent of the letters I, U, and S. However, it should be noted that in this study, each microrod preserves its shape instead of undergoing dynamic shape transformations.

The activity is attributed to the presence of catalase enzyme content in the tips, which is added to the pre-gel mixtures made of Poly(ethylene glycol diacrylate) (PEGDA) in microfluidic channels at SFL manufacturing. The enzyme initiates a chemical reaction with the ambient fluid, which is a solution of hydrogen peroxide H_2O_2. The chemical reaction decomposes solution into its components, hence, the production of O_2 gas that accumulates in active regions, forming bubbles (see figure 2.1).

The bubble growth at active caps causes the displacement of the fluid, resulting in motion, which is then followed by the collapse of the bubble. The hydrodynamics of microbots are influenced by several factors, including periods of bubble growth-collapse mechanism, the shape of the swimmer, and the configuration of active and inactive regions. While we primarily focus on 3-component swimmers (1 inactive region and 2 active tips as shown in figure 2.2a), we also investigate 2-component swimmers (1 active and 1 inactive region, as seen in figure 2.2b). An I-shaped swimmer with 2 components is equivalent to a Janus rod, and a 3-component I-shaped swimmer is referred to as a Saturn rod.

In this chapter, we first present a mathematical model for the catalytic bubble growth

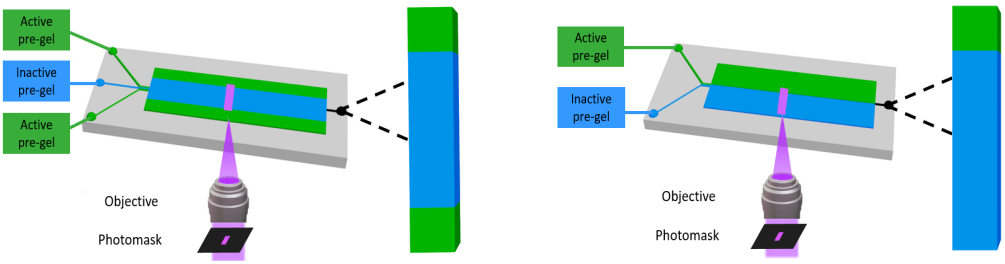

(a) (b)

Figure 2.2: SFL is used to fabricate 2- and 3-component microrods. The method employs active and inactive pre-gel mixtures, producing rods consisting of parallel sections. In the schematic, green represents active tips, while blue indicates inactive sections.

mechanism, comparing it with experimental results. Subsequently, the dynamics and motion patterns of various swimmers will be described, followed by a discussion of the results and potential outcomes.

2.1 Bubble Growth Mechanism

In our system, O_2 gas molecules nucleate at the active ends as a result of the following reaction; $2\,H_2O_2(aq) + \text{catalase} \longrightarrow 2\,H_2O\,(l) + O_2$. The growing bubbles increase the buoyancy of the gel microswimmer, causing motion to occur at the air-water interface, a common feature in bubble-driven motors (see figure 2.3). Typically, in any bubble-driven system, three main trends are observed.

Firstly, as bubbles grow, they push the ambient fluid in the vicinity of the swimmer, leading to anisotropic displacement. This displacement creates a propulsive force which may result in translation or pumping of surrounding fluid, depending on the shape design.

In the second aspect, the bubble detaches from the body depending on the strength of adhesion forces and flow properties. During ejection, the bubble and microbot move in opposite directions to preserve net zero force balance.

The last trend is the collapse of the bubbles, which can occur due to different reasons such as pressure differences or instabilities. This collapse creates a powerful microjet perpendicular to the surface to which the bubble was attached. The jet instantaneously

(a) (b)

Figure 2.3: Due to buoyancy force, swimmers operate at the air-water interface. In panel (a), a rod-shaped motor translates at the interface. Panel (b) illustrates the pumping behaviour of a 3-component microbot.

impulses the microswimmer and propels it in the opposite direction.

In our study, we only observe bubble growth and collapse. We initiate the analysis of periodic bubble growth-collapse dynamics with a general description of the Rayleigh-Plesset equation (145);

$$p - p_\infty = \frac{2\sigma}{r_b} + \frac{4\mu}{r_b}\dot{r_b} + \rho(r_b\ddot{r_b} + \frac{3}{2}\dot{r_b}^2) \tag{2.1}$$

where p corresponds to internal gas pressure, p_∞ pressure far away from the bubble, r_b bubble radius, σ surface tension, μ viscosity, and ρ density. The superscript $\dot{}$ refers to the time derivative.

For a microbubble, the capillary forces ($Ca = \mu U/\sigma \approx 10^{-5} \ll 1$ where U is the microbot velocity) are small and therefore negligible (53). Consequently, the surface tension dominates the viscous forces, and the bubble remains spherical. In addition, experimental results suggest that inertial effects are also negligible (118). Thus, we can eliminate the last two terms at the right-hand side in equation 2.1 and rearrange it to yield the Laplace Law as following;

$$p = p_\infty + 2\sigma/r_b. \tag{2.2}$$

The O_2 gas inside the bubble obeys the ideal gas law,

$$pV = nRT, \tag{2.3}$$

where $V = 4\pi r_b^3/3$ corresponds the bubble volume and n is the number moles of O_2 gas inside the bubble. The temperature is defined as $T \approx 293\,\mathrm{K}$ and the ideal gas constant equals to $R = 8.314\,\mathrm{J\,mol^{-1}\,K^{-1}}$.

After substituting these expressions into equation (2.3) and taking its derivative with respect to time, we obtain:

$$\frac{1}{RT}\frac{\mathrm{d}}{\mathrm{dt}}\left[\left(p_\infty + \frac{2\sigma}{r_b}\right)\frac{4\pi r_b^3}{3}\right] = \frac{\mathrm{d}n}{\mathrm{d}t}, \tag{2.4}$$

and after a rearrangement, the bubble growth dynamics are given by

$$\dot{r_b} = \frac{\mathrm{d}r_b}{\mathrm{d}t} = \frac{RT}{4\pi}\frac{\mathrm{d}n/\mathrm{d}t}{p_\infty r_b^2 + 4\sigma r_b/3}, \tag{2.5}$$

where $\mathrm{d}n/\mathrm{d}t$ is the molar flux of gas into the bubble.

At this point, we may assume that the gas is produced at a constant rate at the catalytic end, as the solute concentration is constant and gas molecules transfer directly into the bubble without diffusing (63). In this case, the molar flux can be written as $\mathrm{d}n/\mathrm{d}t = Q$, for some constant Q. Substituting this into equation (2.5) results in the following;

$$\dot{r_b} = \frac{RT}{4\pi}\frac{Q}{p_\infty r_b^2 + 4\sigma r_b/3}. \tag{2.6}$$

After integrating equation (2.6) with the initial condition $r_b = 0$ at $t = 0$, the final form of the bubble growth mechanism is obtained as:

$$\frac{p_\infty}{3}r_b^3 + \frac{2\sigma}{3}r_b^2 = \frac{RTQ}{4\pi}t. \tag{2.7}$$

In equation 2.7, R and T are known parameters with constant values. The bubble radius, r_b, and time, t can be obtained from experimental results. Consequently, we have a model with a single unknown parameter, Q, which can calculated using standard numerical methods such as the method of least squares. In the next section, we determine the molar flux rate by fitting the single parameter to experimental data through an image

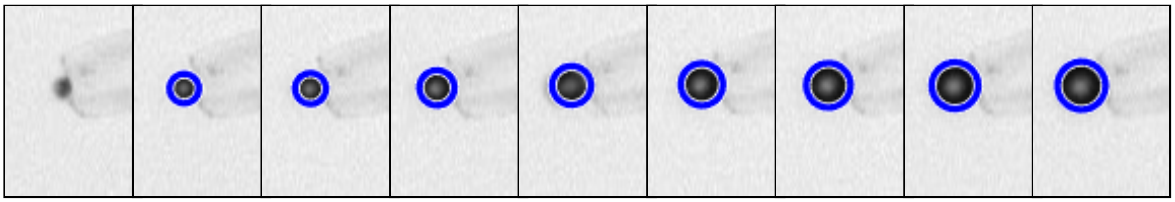

Figure 2.4: Frame-by-frame of a single growing bubble over an entire growth cycle. The blue circle denotes the bubble that is detected by the circular Hough transform.

analysis study.

2.1.1 Detecting Bubbles with Image Analysis

The image analysis is conducted by an in-house code processing the experimental data set. The process begins by importing video microscopy data into MATLAB®. The bubble detection function displays the first frame of the video to the user, who then selects a small region of interest(ROI) using ginput function which identifies the axis coordinates. Subsequently, the algorithm iterates through each frame to detect the bubble radius.

Since bubbles remain spherical, an algorithm detecting circular shapes can find the radius as a function of time, corresponding to the number of frames in this case. For this purpose, MATLAB®'s built-in function imfindcircles was employed, as shown in figure 2.4. The imfindcircles function uses Circular Hough Transform (CHT), a specific version of the Hough Transform based on the Canny edge detector algorithm. The Canny edge detector was designed to extract structural information by converting colour triplets to the grayscale (19), making it convenient for finding the intensity gradients in the filtered data. The method can be summarised in five main steps.

First, a Gaussian filter is applied to the image data to remove noise. The Gaussian filter is passed across each pixel to smooth the image, reducing the likelihood of false edge detection. In the second step, the image is filtered to determine the edges and intensity values by calculating the first derivatives in the horizontal and vertical directions.

In the third step, a gradient magnitude threshold or lower bound cutoff suppression

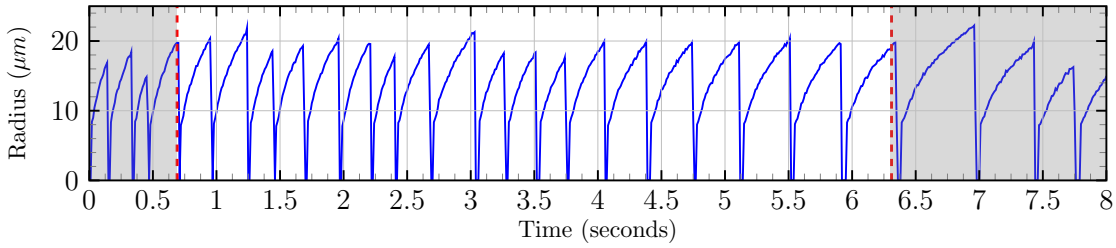

Figure 2.5: The radius of a single bubble as a function of time over multiple growth-collapse cycles. A subregion of clean data are selected to be used for phase averaging.

is employed for edge thinning process. This step aims to locate the sharpest change in intensity value. Edge strengths are compared for each pixel, and the algorithm determines whether the value should be retained or suppressed. The next step can be considered as identification of remained edge pixels due to variations in colour or noise. Pixels are categorised as strong or weak edge pixels based on predefined threshold values. As a result, smaller gradient values than the weak edge threshold are removed.

In the final step, the connection between edges in a blob is analysed. If a weak edge point is involved in the same 8-point blob (also known as an 8-point neighbourhood) with a strong edge point, it is preserved, while others are suppressed. With this, edge tracking process by hysteresis is finalised.

The CHT follows a similar process to Canny edge detector, but it specifically finds circular shapes among all the edges. For each edge, circles are drawn with the desired radius. The intersection point gives the coordinates of the centre of the real circle in the image. After distinguishing the circles, the routine eliminates some of them according to user-given parameters, which is termed as voting. The minimum radius and the object polarity are some of the user-given parameters in the CHT. The robustness of the function circumvents the possible inaccuracies due to noise.

Using the CHT, the radius over time as a periodic signal is plotted, and a region of interest is selected on the data, as depicted in figure 2.5. This region of interest is phase averaged by using the locations of the bubble collapses, and the averaged data set for bubble radius is obtained for comparison with the mathematical growth model (see

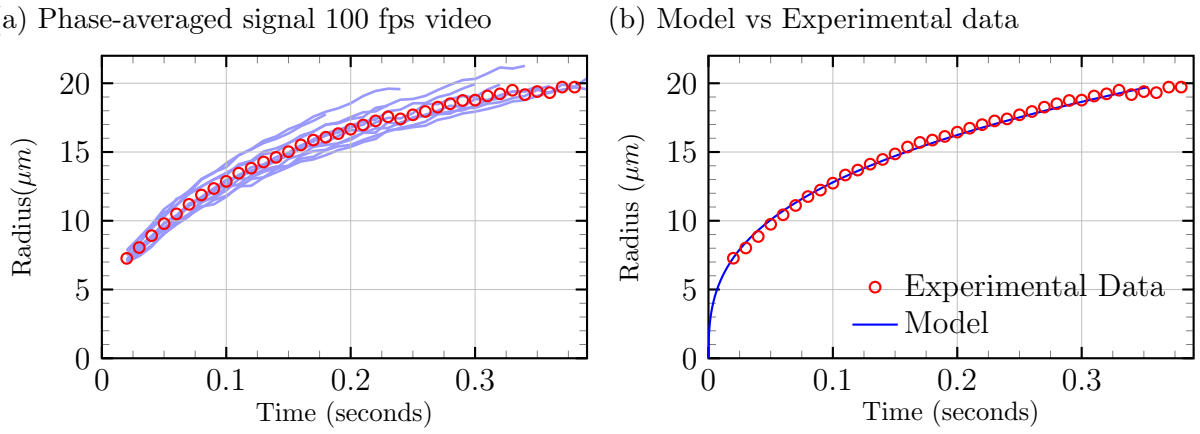

Figure 2.6: a) The bubble growth cycles are phase-averaged to obtain a dataset. b) The flux rate Q in equation 2.7, as a single parameter, is fitted to experimental data using the method of least squares, showing good agreement.

figure 2.6a).

The flux rate Q can be determined by inserting ambient pressure and surface tension into the equation 2.7. At the air-water interface $p_\infty = 1$ atm $= 101\,325\,\mathrm{N\,m^{-2}}$ and surface tension can be considered as $\sigma = 7.2 \times 10^{-2} Nm^{-1}$ for microbubbles, as reported in the literature (53). By using the method of least squares, the flux rate is found to be $Q \approx 8.45 \times 10^{-13}\,\mathrm{mol\,s^{-1}}$.

We can determine the bubble radius over time through reverse engineering by inserting Q into the same equation. The comparison between the periodic bubble growth-collapse model and the experimental data shows good agreement in figure 2.6b. It should be noted that the initial stages of bubble growth in experiments could not be captured due to the minimum radius requirement in the CHT algorithm.

In our results, we observe a considerable fluctuation in the flux rate from cycle to cycle, with $Q_{min} \approx 6 \times 10^{-13}\,\mathrm{mol\,s^{-1}}$ and $Q_{max} \approx 1.2 \times 10^{-12}\,\mathrm{mol\,s^{-1}}$. As the flux rate increases, bubbles grow faster. Although this variance occurs stochastically, a long-term trend is detected in terms of decaying maximum bubble radius and slower bubble growth.

In figure 2.7 both trends are depicted for multiple cycles. In these figures, the legend represents the bubbles at different edges of swimmers for the entire experiment. The decrease in maximum radius can be interpreted as the decay in the molar flux of gas

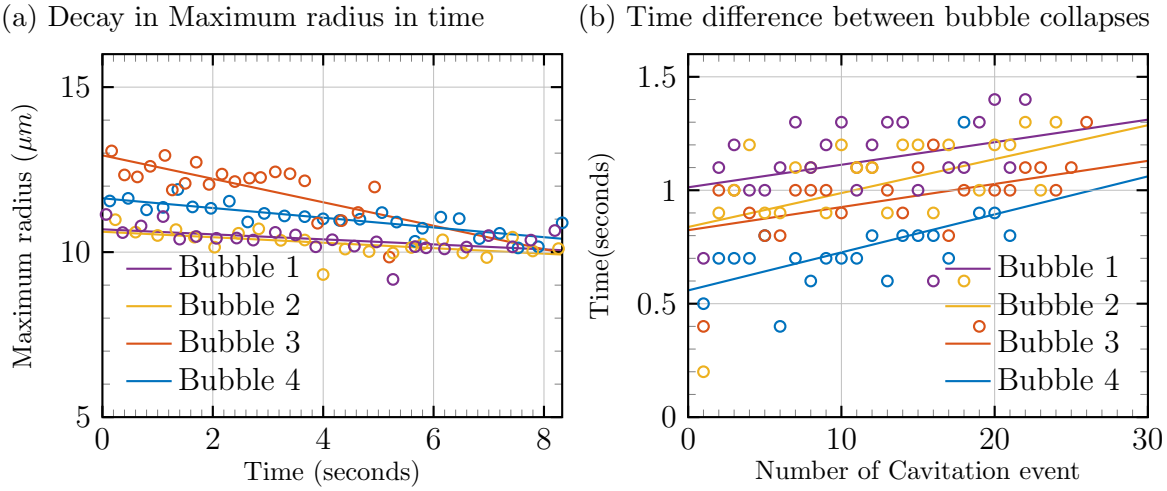

Figure 2.7: Panel (a) shows the steady (linear) decay of the maximum bubble radius over time indicating degradation of the catalytic enzyme. In panel (b), period between collapses shows a steady increase.

into the bubble. The molar flux could decline over time due to depletion of the local solute concentration, or the diminishing catalase enzyme at the active end. However, it is noteworthy that the same decay is observed for both pumps (3-component I-shaped) and translators (3-component U-shaped). The fact that 3-component U-shaped swimmers wander into areas rich with solute reduces the likelihood of the first possibility. Therefore, enzymatic degradation emerges as the main cause of decay in molar flux.

Before explaining the hydrodynamic motion of artificial microswimmers, we examine the reasons behind the collapse of bubbles. In general, during the growth period, the gas pressure inside the bubbles begins to drop to values similar to those of the surrounding liquid. Due to this pressure drop, at some point the bubble becomes unstable and even a small fluctuation may cause a violent collapse. The threshold value for the collapse mechanism is defined with Blake critical radius (69) and given as:

$$r_c = \left[\frac{9m_g RT}{8\pi\sigma}\right]^{1/2} \tag{2.8}$$

where m_g is the mass of the gas. We can estimate the mass by multiplying the average molar flux $Q \approx 8.45 \times 10^{-13}\,\mathrm{mol\,s^{-1}}$ with average collapse time $t_c \approx 0.5\,\mathrm{s}$.

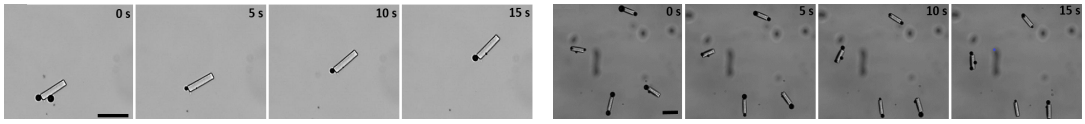

(a) (b)

Figure 2.8: I-shaped microbots swim in different modes depending on the number of poles they possess. Panels (a) and (b) show the motion of Janus and Saturn rods respectively, as captured in the experimental work.

By substituting the values of gas mass and other parameters into equation 2.8, the critical radius is found $r_c \approx 70\,\mu m$. On the other hand, the experimental data in figure 2.5 shows that bubbles collapse when the radius reaches approximately $20\,\mu m$. At the free surface, the film that covers the bubble gets thinner over time and becomes fragile (195). Thus we can suggest that the collapse occurs due to oscillations at the air-water interface that are present enough to rupture the bubble. In conclusion, while the growing bubble gives steady propulsion to the microrod, the collapse mechanism creates a secondary impulsive effect in the form of a microjet. Since the bubble growth and collapse mechanisms are fully explained, we can detail the characteristic swimming patterns of microbots thoroughly.

2.2 Fundamental Modes of Swimming

The investigation begins with I-shaped rigid rod swimmers. Ideally, for a 2-component I-shaped swimmer, the active end periodically produces bubbles. As microbot raises to the air-water interface due to increasing buoyancy, the bubbles continue to grow and collapse (see figure 2.8a). Since the 2-component I-swimmer has only one active end, the bubbles exert a single force on to the swimmer. This force is balanced by drag and consequently, the I-shaped microbot translates ballistically. On the other hand, in a 3-component I-shaped swimmer the active tips are located at each end, which creates a symmetric geometry. Consequently, the propulsive forces at the active ends are equal in magnitude but act in opposite directions, which leads to zero net force. Thus, the

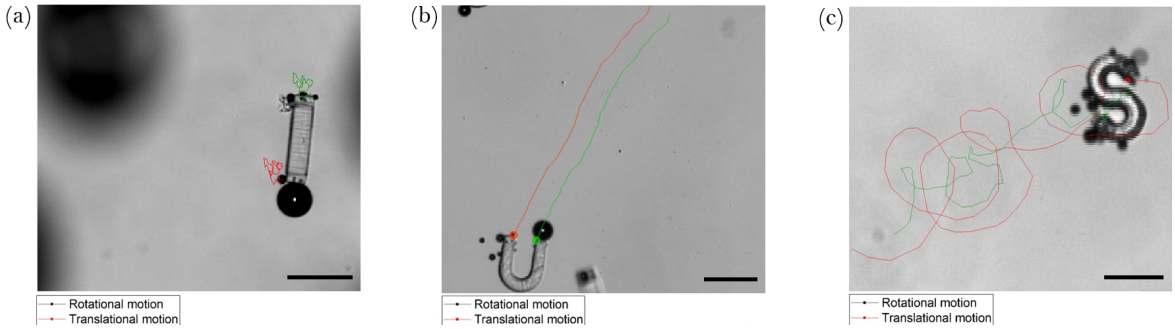

Figure 2.9: Typical motion patterns of the differently shaped particles: a) pumping of I-shaped swimmers b) translating movement of U-shaped swimmers and c) rotating S-shaped swimmers. The scale bar equals 150 µm.

swimmer pumps the fluid around, which is demonstrated in figures 2.8b and 2.9a.

In the case of a 3-component U-shaped swimmer, the propulsive forces arise in the same direction, balanced by the viscous drag, thus enabling forward movement. As a result, the microswimmer achieves ballistic locomotion (see figure 2.9b).

The 3-component "S" swimmer functions as a rotator due to its geometry. Similar to the 3-component I-shaped swimmer, the propulsive forces are equal and in opposite directions, yet the shape of the swimmer induces a torque. The torque is counteracted by the rotation, as can be seen in figure 2.9c. However, owing to the stochastic nature of the nucleation sites, the forces are not entirely opposite in direction. Consequently, the S-shaped microrod undergoes translation as well. In summary, the I-, U-, and S-shaped microbots mirror the first three modes of buckling or shape, corresponding to the first three modes of swimming: pumping, translation, and rotation (see the schematic illustrated in figure 2.10).

It is important to acknowledge that these are ideal scenarios with flawless manufacturing and simultaneous bubble production on both ends. However, when accounting for intrinsic stochasticity of locations in bubble generation, time lags between periods at opposite ends, and minor manufacturing variations, the swimmers may exhibit different behaviours. For instance, on figure 2.11a, a Saturn microrod (3-component I-shaped microbot) generates multiple nucleation sites at one of its active caps. As a result, the opposing forces are not balanced, leading to translational motion accompanied by rota-

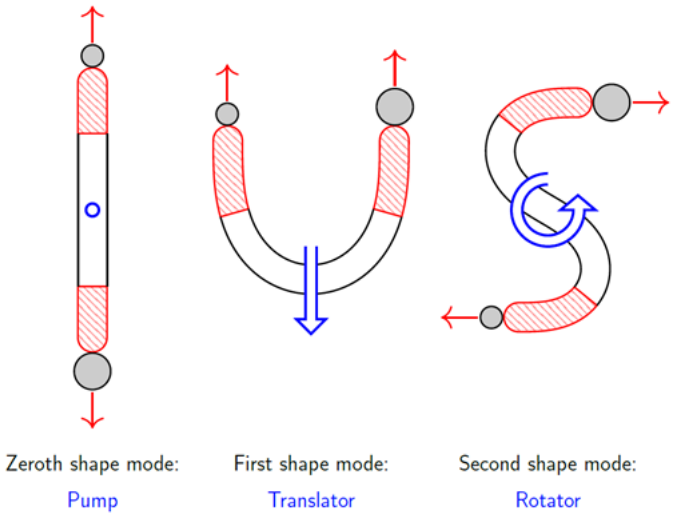

Figure 2.10: The interplay between the shape and bubble force directions determines the dynamics of the microbot. In the zeroth mode, the I-shaped microbot pumps the fluid around. The first shape mode corresponds to translation. An S-shaped microbot that represents the second mode rotates.

tion.

Furthermore, the number of active poles also changes the characteristics of the swimmer. In figure 2.11b, a U-swimmer with a single active pole performs translation accompanied by rotation. In the case of a 2-component U-swimmer, the absence of a balancing tip force results in a moment around the centre of the swimmer and subsequent rotation. In the case of asymmetric S-swimmers, there is no change in rotational behaviour because a single bubble can produce a torque around the centre (see figure 2.11c). However, the velocity and rotation periods of swimmer are affected by such change. With this, we have presented our results. In the next section, we will highlight some of the findings and explain how these results influence our research.

2.3 Conclusions and Inspiration

In conclusion, this study aims to understand the effects of shape and bubble growth mechanisms as propulsive forces in rigid microrods. The swimming modes of gel-based

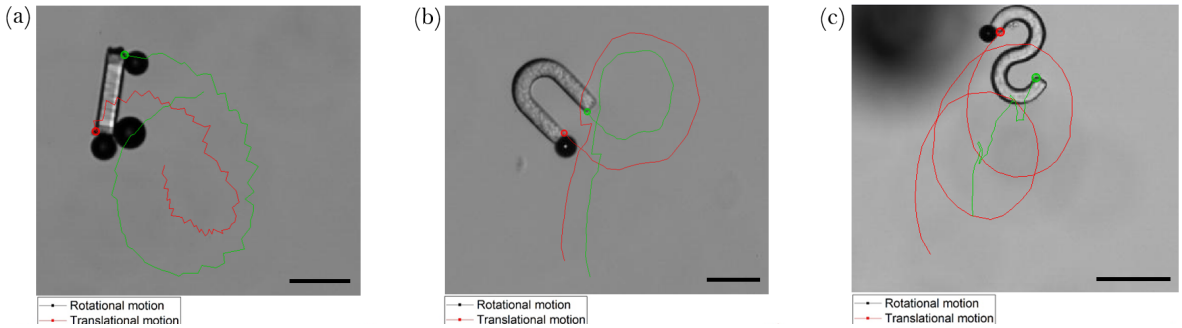

Figure 2.11: Motion patterns of the differently shaped particles caused by the influences described above: a) partial rotation, partial translation of I-shaped swimmers b) partial rotation, partial translation of U-shaped swimmers and c) rotating translation of S-shaped swimmers. The scale bar equals 150 µm.

microbots are significantly dependent on the shape, the number of active poles, manufacturing quality, and the inherent stochasticity of bubble sites. In general, it is observed that 3-component "I" swimmers pump stresslet-like flows, while "U" and "S" swimmers exhibit translation and rotation patterns, respectively. On the other hand, due to the factors mentioned, each swimmer has the potential of demonstrating other behaviours, such as translating I-swimmers, rotating U-shaped microbots, and translating S-shaped rotors.

The findings of this chapter motivate us to investigate the relationship between these shapes and swimming patterns in different setups. Our main inspiration lies in understanding the transitions between these shapes, thereby gaining control over the swimming modes. Achieving such control could facilitate navigating the swimmer to accomplish intricate missions. Having translation, rotation, and pumping behaviours within the same swimmer could help in performing complex tasks, including local drug delivery and microfluidic mixing in environments with obstacles.

The transitions between these shapes can be done through various means, such as using deformable materials or changing the volume of the microswimmer. Soft hydrogels offer both of these features. Due to their low Young's moduli, they can buckle, twist, and bend into different shapes under external forces. Another effective method of changing their shapes is by shrinking or swelling the hydrogel. Responsive hydrogels, as a special

type of gel, can absorb or release fluid when they are stimulated by external factors such as pH or temperature.

In the following chapters, background information will be provided about the characteristics and historical development of such materials, and both shape transition strategies will be showcased through numerical studies.

CHAPTER 3

INTRODUCTION TO SOFT MATTER AND HYDROGELS

Soft matter is the general name for materials that can be easily deformed under thermal or mechanical stresses, e.g., polymers, surfactants, liquid crystals, colloids, foams, and gels. The name itself was coined by de Gennes (30) who contributed to the recognition of polymers and liquid crystals, during his Nobel Prize acceptance speech. Soft matter provides a middle ground between fluid and solid phases of matter; therefore, it is also referred to as "complex fluids". This intermediate position is mainly due to the complex and unusual molecular structures of soft matter. At the molecular level, their units are individual and disordered like fluid particles, which allows them to swap positions and flow. However, on larger length scales, there is an order that forms structures. Consequently, the material responds as a whole. In other words, their subunits (macromolecules) are large enough to neglect quantum effects, but also small enough to be impacted by thermal fluctuations (37).

This interaction between the fluid and solid states results in significantly "exaggerated" responses to external stimuli such as temperature or pH. A small shift in these factors can lead to considerable changes in material properties. Furthermore, soft matter is capable of self-assembly, which plays a vital role in biopolymers such as DNA and RNA (189). These dynamic responses can be tailored for specific functions, ranging from drug delivery systems to smart actuators, depending on the type of soft matter.

(a) A cartoon schematic of a polymer chain is illustrated.

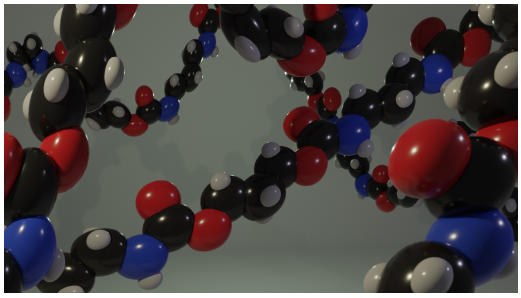

(b) Surfactants cover the surface of the fluid.

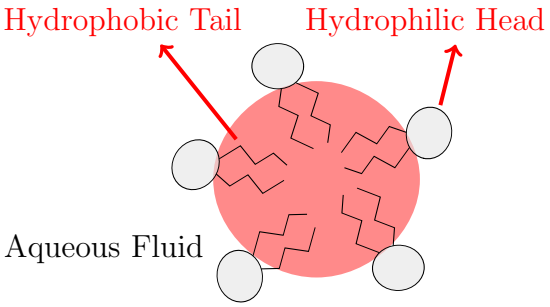

(c) Colloids are suspensions with immiscible solid granules.

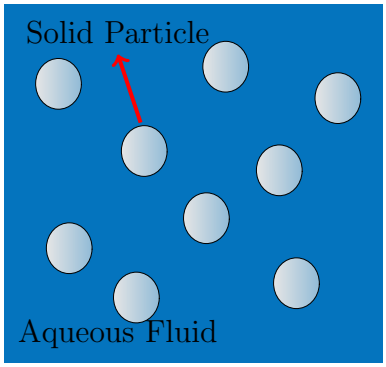

(d) Liquid crystals lie in the middle between solid and liquid states.

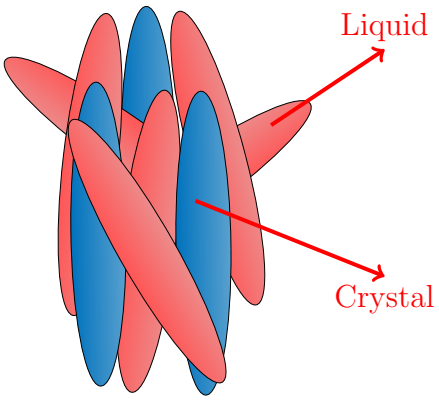

(e) A SEM image of a homogeneous gel is provided.

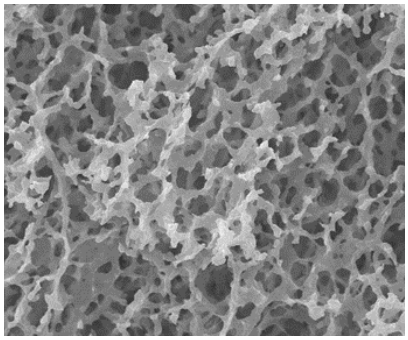

Figure 3.1: Various examples of soft matter are demonstrated. Panel (a) is the work of Paul Topham and printed under a CC BY-SA 4.0 license. Panel (e) is taken and reprinted from the work of Ju et al. (91) with permission from IOP Publishing. In panel (b), the outer region contains an aqueous fluid, while the pink-coloured droplet is an oil-based fluid.

Regarding the categorisation of soft matter, drawing distinct borders between different groups could be a difficult task, since most materials exhibit common properties. Noting this, we start classifying with polymers (see figure 3.1a). The name originates from Greek, meaning "many parts" as a reference to repeating very large macromolecules. Natural and synthetic polymers are exemplified by DNA, hemp, wool, cellulose, polyethylene, polypropylene, rubber, nylon, and silicone. The configuration of polymer chains and their repeat distance determine the material properties of the polymers (189).

Another example of soft matter is surfactants containing two parts within themselves. One part is hydrophilic, and the other is hydrophobic. When these molecules form bonds with each other in a bulk fluid, there is a tendency to cover the surface at arbitrary sizes (134). The outer face of the surface corresponds to the hydrophobic side. In this regard, it may remind a collection of Janus particles; however, it differs due to its penetrability. An aggregation of Janus particles has voids between the microspheres; therefore, it is reminiscent of human skin that is breathable. On the other hand, a surfactant-covered surface has no pores (see figure 3.1b).

Liquid crystals have molecules that can translate in any direction, similar to fluids; however, these molecules generally align in the same direction (see figure 3.1c). The molecules of liquid crystals, known as "mesogens", have a preferred direction called the director. This order in direction creates a crystalline structure. These materials have been widely used in home electronics and biotechnologies (101).

Colloids are fluids filled with granular particles, which can form distinct phases. In colloids, the scattered impermeable solid particles are suspended in a fluid; therefore, the word "suspension" is used interchangeably (134) (see figure 3.1d). Similarly, foams can be categorised as the bubble counterparts of colloids.

Another significant instance of soft matter pertains to gels (see figure 3.1e). We will numerically investigate the dynamics of gels in Chapters 5 and 6. Therefore, we will explain the general properties and some examples of gels in the next section, 3.1 in detail. In the same section, we will approach the problem of flows through a hydrogel from

a mathematical perspective. After, in section 3.2, theoretical and experimental studies about a special type of gels, responsive hydrogels are scrutinised. Hence, the sections 3.1 and 3.2 will provide the foundation for subsequent chapters.

3.1 Gels and Hydrogels

A gel is a dilute polymer or colloidal network that is present in a solvent agent. The large gaps between the subunits of the network increase the surface area of gels and allow them to have low density. Additionally, the non-solvent-solute scaffold of gels permits it to be squished under external forces. The combination of flexibility and low density makes gels ideal candidates for a plethora of applications. They have been commonly used in biomedical studies such as tissue engineering, local drug delivery, and contact lens designs, and also can be found in everyday products, including ketchup, shampoos, toothpaste, and paints (24).

Gels can be categorised according to solvent type, e.g., air, water, or other chemical solutions. When a gel is dried, it loses the fluid content and leaves a solid structure behind. Consequently, the residual porous structure has a large surface area. If the gel is ambient or freeze-dried, the material is named xerogel. During this process, shrinkage is observed. On the other hand, if the material is dried at a supercritical state, where the liquid is transformed directly into a gas without capillary stresses, an aerogel is obtained. The pores between subunits are filled with air, and almost no shrinkage occurs. The difference between drying processes leads to variations in porosity values. Aerogels are known to have larger porosity values which can be up to $\approx 95\%$, while porosity in xerogels is around 75% (77).

As another example of gels, hydrogels are swollen in water and were first discovered by Kuhn (99) and Breitenbach and Karlinger (15) independently. A polymer hydrogel is made from hydrophilic macromolecules, resulting in a great capacity for absorbing water. This property can facilitate complex tasks including retaining micro and nanoparticles, or

covering surfaces by increasing the volume of hydrogel. To maximise the effectiveness of these applications, it is essential to understand the interplay between the outside and inside fluid and the porous structure of the hydrogel. In the next section, we will investigate mathematical models for the problem of a creeping flow through a hydrogel.

3.1.1 Stokes Flow Through a Hydrogel

From a mathematical point of view, the interaction between the surrounding fluid and hydrogel is full of rich dynamics. The related understanding can be derived as simplifying the problem as a flow through a porous medium. Although such simplification may ignore the chemical mechanisms contributing to the problem, it offers an efficient description of the physics. Therefore, we review the mathematical models for flows passing through porous media.

In general, the determination of appropriate boundary conditions increases the complexity of this problem compared to flows passing a rigid object. The number of pores, their shapes and sizes, and their uniformity add extra depth. Consequently, several models have suggested approximate solutions for flow through a porous medium.

Historically, the first model of flow in a porous medium was proposed by Darcy (13). The model established a constitutive relationship between fluid velocity and porosity, based on experimental observations on flow through beds of sand. According to Darcy, the volumetric flow rate in a pore, Q can be described as:

$$Q = -\frac{\zeta A_{pore}}{\mu L_{pore}} \nabla p \tag{3.1}$$

where ζ is the permeability of the system, and A_{pore} and L_{pore} are the cross-sectional area and the length of the void, respectively. As flow passes through the pore, the pressure

drops. For an isotropic porous medium, equation 3.1 can be expressed in a local form as;

$$\mathbf{q} = -\frac{\zeta}{\mu}\nabla p = \phi \boldsymbol{u} \tag{3.2}$$

$$\boldsymbol{u} = \frac{\mathbf{q}}{\phi} \tag{3.3}$$

where ϕ is the porosity of the system and $\boldsymbol{u}$ is the velocity vector for the fluid. While the original Darcy's law in equation 3.2 was found experimentally, it can be also derived analytically (187).

At this point, we recall the problem of creeping flow past a sphere given in 1.5.1 with a modification. Now, the sphere with radius m is permeable. Therefore, the sphere can be considered as a collection of many small impermeable spherical elements. In the presence of gravity, an additional term $\rho_f \mathbf{g}$ is added to equation 3.2, resulting in:

$$\phi \boldsymbol{u} = -\frac{\zeta}{\mu}(\nabla p - \rho_f \mathbf{g}), \tag{3.4}$$

which describes the internal flow. By using the stream function in 1.31 and matching the internal and external flow conditions, the drag on the sphere is obtained as:

$$F_{drag} = 6\pi\mu m(1-\varphi)U_\infty \tag{3.5}$$

where φU_∞ is the permeation velocity inside the sphere (36). The permeation criterion, also known as the deviation parameter, is given as:

$$\varphi = \frac{3\zeta/2m^2}{1+3\zeta/2m^2}. \tag{3.6}$$

The permeability of the sphere, ζ, can be written according to Brinkman's formulation as:

$$\zeta = \frac{c^2}{18}\left(3 + \frac{4}{1-\phi} - 3\sqrt{\frac{8}{1-\phi} - 3}\right) \tag{3.7}$$

where c is the radius of each impermeable sphere (159). We will use equation 3.5 in

Chapter 4 for validation.

However, equation 3.4 is not compatible near boundaries since there is no shear term associated with it (137). As an alternative approach, the Brinkman equation suggests a mathematical formulation independent of empirical data. The equation provides a translational velocity between boundaries as follows:

$$\nabla p = -\mu \nabla^2 \boldsymbol{u} + \mu \alpha^2 \boldsymbol{u}, \qquad \nabla \cdot \boldsymbol{u} = 0 \tag{3.8}$$

where α is the resistance of the porous medium ($\alpha^2 = 1/\zeta$). The above equation is the modified version of the traditional Stokes equation with an additional resistance term. Analytical solutions of equation 3.8 have been used to describe flows in simple porous geometries including gels in equilibrium, hence, no deformation (50). However, these solutions would not be sufficient in our particular interest in shape-switching porous hydrogels.

For more complex geometries, such as the interaction between a bacterium and arbitrary domains with pores, numerical solutions could be used. Especially a fundamental solution smoothed by regularisation may handle such complicated problems (105). Similar to the method of regularised stokeslets (which will be detailed in 4.2), a regularised Brinkmanlet can efficiently solve the dynamics in a Brinkman medium (27). The only drawback of any numerical scheme associated with regularised Brinkmanlets occurs when heterogeneities are intrinsic to the domain. Such heterogeneous domains can be encountered in media where materials properties, such as permeability, are not uniform. In these cases, in addition to the loss in accuracy of regularised Brinkmanlet solutions, frequent re-meshing negatively contributes to computational cost.

To overcome the aforementioned challenges, recently Kamarapu et al. (94) proposed a new framework that represents the porous medium as a collection of regularised stokeslets. The method stemmed from the assumption that the flow inside the porous domain is a creeping flow; therefore, the regularised stokeslets correspond to the solid part of the

medium. The rest of the domain and the voids between the regularised stokeslets are fluid. The method was combined with a boundary element method (BEM) to reduce the dimension of the problems and was applied to the Couette and source flows through stationary porous domains. This solution procedure has inspired our research. Therefore, we will extend this method to dynamic and poroelastic boundaries, such as flexible and porous filaments or shape-switching smart microbots. The details of our methodology will be given in the next Chapter 4.

In this section, we have discussed the flow within and surrounding a porous medium. The respective equations provide insights for refining our model in Chapter 4 and addressing the problem presented in Chapter 5. In these chapters, the hydrophilic structure of the hydrogels will be emphasised. On the other hand, in some cases, the positive interest of hydrogels towards aqueous fluids could be reversed. In the next section, we will detail the examples of this phenomenon with responsive hydrogels.

3.2 Responsive Hydrogels

Responsive hydrogels can change their physical properties and volume in response to external conditions. Stimulating environmental factors such as temperature, pH, and light can reversibly change the affinity of the hydrogel to aqueous solutions, leading to volume changes such as swelling or contraction. Throughout the volume transition, responsive hydrogels absorb or expel a significant amount of aqueous fluids (172).

Depending on the type of actuation and cross-linking properties, the mechanics of volume transition may differ. Although these differences raise interesting questions about the dynamics, in this thesis we specifically focus on thermo-responsive hydrogels. This is due to the vast literature about their features (96; 95) and their compatibility with advanced manufacturing techniques such as stop-flow lithography (161) mentioned in Chapter 2 or two-photon polymerisation (72).

For thermo-responsive hydrogels, a critical temperature known as the volume phase

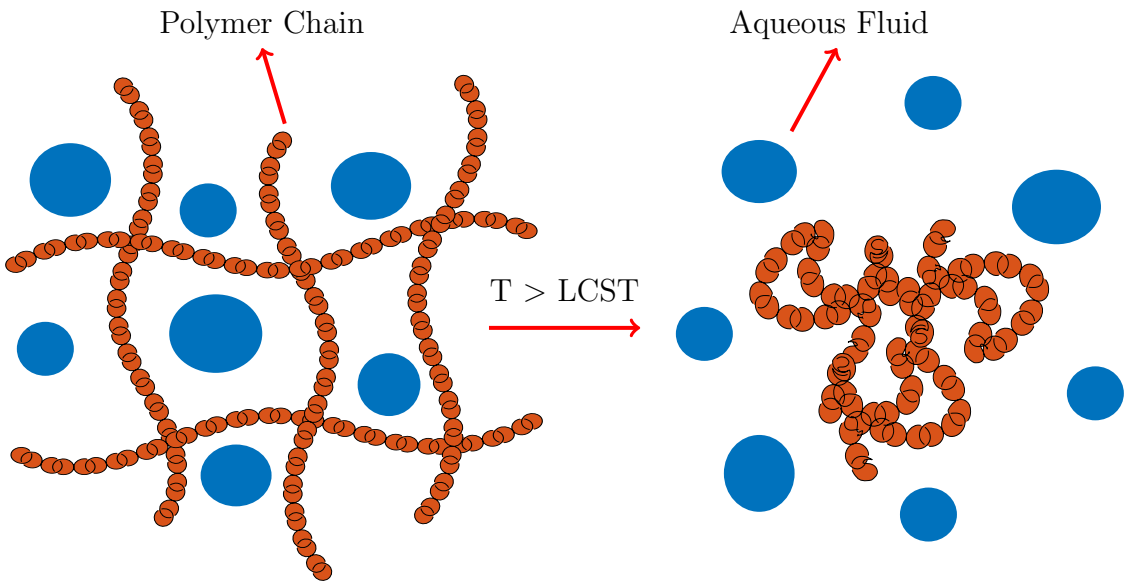

Figure 3.2: Thermo-responsive hydrogels including PNIPAM expel fluid at temperatures over their LCST. Throughout the volume change, polymer chains start to tangle up, which is named coil to globule transition.

transition temperature controls the miscibility of the solid skeleton and interstitial fluid (95). This temperature governs the swelling and shrinking characteristics, and accordingly, thermo-responsive hydrogels can be classified into two groups. The first type of thermo-responsive hydrogels has a lower critical solution temperature (LCST). At temperatures above the LCST, these hydrogels shrink significantly. Increasing the temperature weakens the hydrophilic bonds within the polymer chains, and the hydrogel becomes hydrophobic. Consequently, the hydrogel loses its affinity for the fluid. Meanwhile, the polymer chains start to form spherical structures (known as coil-to-globule transition), which decreases the pore size, hence, the release of fluid (see figure 3.2). Throughout the fluid expulsion, the material becomes stiffer, resulting in an increase in the elastic modulus (72).

An opposite process can be observed in hydrogels with upper critical solution temper-

ature (UCST). The hydrophilic bonds strengthen, so the absorbing capacity of hydrogel increases. Subsequently, the hydrogel starts to swell. Although both groups can be synthetically produced, those with LCST have been employed more often (96). In particular, poly(N-isopropyl acrylamide) (PNIPAM) has been used widely in *in vivo* applications due to its LCST $\approx 32\,^{\circ}\mathrm{C}$, which is around human body temperature (160), and it will be the main material for our numerical studies. In addition, PNIPAM can operate under different pH conditions, facilitating the performance of complex tasks in biological sites including the vagina and gastrointestinal tract (97).

This versatility allows PNIPAM to be used in diverse applications such as fabricating smart actuators (122), as devices for local drug delivery (97), filling materials for broken tissues (169), or producing micro imaging apparatus (60). Traditionally, PNIPAM and other thermo-responsive hydrogels have been used as homogeneous materials. It should be distinguished that here, homogeneity refers to a single type of material with the same features. For example, in a study by Bhattarai et al. (10), microdose drugs were immersed between the polymer chains and squeezed out during the deswelling process. Alternatively, by employing a thermoresponsive hydrogel with UCST, the drug can be diffused out as a homogeneous material swells (68). In tissue engineering, PNIPAM facilitated wound healing as a flexible scaffold that can expand or contract in response to temperature on the damaged skin (202). The flexible and biodegradable properties of PNIPAM meet the requirements of real-life implementation. In the study by Cheng et al. (23), temperature-sensitive hydrogels swelled and morphed into the letters "SOS" to signal an emergency, drawing inspiration from Morse code.

In these studies, isotropic volume change in homogeneous thermo-responsive hydrogels have been exploited. However, these materials may present new horizons. Obtaining anisotropic responses such as partial swelling/deswelling can pave the way for engineering programmable passive and active materials, thus, accomplishing more complex missions (73). Combining different behaviours in the same material can provide precise control over the shape of the hydrogel, which is the main goal of this research. As a result

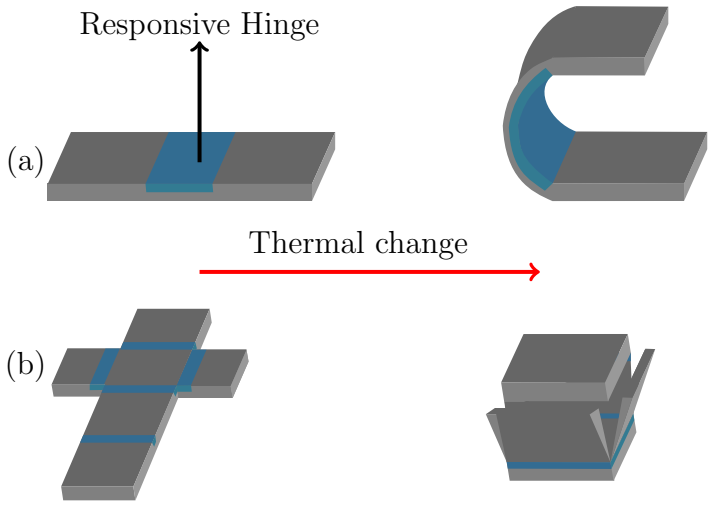

Figure 3.3: The schematic re-illustrates the self-folding behaviour by using responsive hydrogels as hinges in the study of Ge et al. (62). In panel (a), the responsive middle section causes an out-of-plane deformation. In panel (b), a cross-shaped rod transforms into a box, inspired by origami.

of alternating sensitivities, hydrogels can be forced to deform with volume transition in all three planes via bending, buckling, and twisting. Moroever, other deformation patterns such as wrinkling or creasing, or origami like programmable-folding (177) can be observed. To this degree, there has been engagement in both experimental and numerical inquiries.

The simplest mechanism would involve two materials to have a bilayer. As the materials have different responsivity, controlled deformations could been directed. This principle was followed in the work of Stoychev et al. (170). The authors fabricated a star-like shape at the micron scale by using photolithography. While one face of the star was made of thermo-responsive PNIPAM, the other face was manufactured by hydrophobic polycaprolactone. As the material heated, the faces responded differently, resulting in a closing motion that could theoretically encapsulate microloads. A different attempt realised out-of-plane deformations with a planar X-shaped hydrogel bilayer, which could serve as a soft microgripper (108).

A similar strategy would use responsive hydrogels as hinges to connect non-responsive sections (see figure 3.3). For example, Ge et al. (62) employed 4D printing to engineer

a flat cross-shape that can fold into a box under heating. The mismatched stresses at hinge sites forced the structure to bend (see figure 3.3). While both methods have led to fruitful experimental studies, the chemical attachment of two materials may face challenges in practical applications. The interface between the material is prone to damage due to repeated mechanical stresses (41). From a mathematical perspective, different materials introduce additional complexity to the modelling problem. The presence of two different materials would involve two elastic moduli and two porosity values that are not necessarily identical. Therefore, effective modulus and effective porosity would be required to determine, which can be an intriguing topic of research in itself.

However, recent efforts have been put to utilise a single hydrogel in an inhomogeneous fashion. Spatial gradients of response within the same hydrogel can overcome interfacial fractures caused by differences in material properties. The main numerical advantage of the employment of only one material is the ability to gather all the necessary information about mechanical properties without further calculation, such as elastic modulus and porosity. Therefore, simple mathematical models could efficiently predict the evolution of shape transformation.

Responsive hydrogels with spatial gradients can be manufactured by altering the monomer or cross-linker concentration (67). In their benchmark study, Hippler et al. (72) experimentally designed PNIPAM bilayers that can be induced by light. The bilayers consisted of a single material; however, hetero-responses were achieved by adapting the cross-linking density as dose exposure during manufacturing. Consequently, the bilayers performed anisotropic deformations and complex actuation patterns. In Chapter 6, we will use this study as our main inspiration and provide a qualitative comparison. It should be noted that the responsivity was mapped to a step function in the mentioned study. It is also possible to shift the response rate gradually rather than a sharp transition. Nojoomi et al. (139) manufactured spatially nonuniform rates of shrinkage along the radius of circular plates. The varying rate of deformation formed more complex 3D morphologies such as hyperbolic paraboloids.

Some other efficient strategies have also been suggested for the directional responsivity. For instance, Maslen et al. (122) introduced PNIPAM-based hexagonal platelets consisting of struts. The study achieved non-reciprocal actuation by altering the porosity of certain struts and their respective locations, which is essential for motion in low Re flows. The pores improved the fluid expulsion/absorption rate, thus a variation in the activation time. To fully utilise this feature and other heterogeneities in responsive hydrogels, it is essential to develop a numerical model capable of capturing the interplay between pores and shape transformation.

In this regard, a number of studies have focused on the development of computational models. In general, the length scale of the responsive hydrogel is the main determining factor of the variety of numerical techniques. As the length scale shifts from macro to micro, the continuum approaches are replaced by discrete models. While the method of Dissipative Particle Dynamics (DPD) is the ideal candidate for simulating the swelling and shrinking in the mesoscale (193), Molecular Dynamics (MD) (1) methods and Coarse-Grained (CG) (121) extensions are more appropriate for estimating characteristics at the micro- and nanoscale. In MD, polymers are represented as chains of computational entities; therefore, as the length scale increases, the computational cost becomes exponentially expensive (33). Using a single computational unit, such as a bead for a lattice of atoms or molecules, would reduce the cost, as in the case of CG simulations (7). Although such methods are remarkably useful for explaining the local interactions between pores and ambient fluid, the bulk dynamics of swelling and shrinking at the macroscopic scale are mostly described by theoretical mathematical models.

The initial mathematical models regarding the equilibrium dynamics and volume transition of responsive hydrogels focused on homogeneous materials. Flory and Rehner suggested a foundational theory based on entropy changes and calculating swelling behaviour by minimising the free energy density (46). The theory considers the shape transformation of the homogeneous hydrogel, the mixing of the polymer chains and interstitial fluid, and the energy expended against the osmotic pressure (45). Due to significant defor-

mations throughout the volume transition, Flory-Rehner theory has been combined with neo-Hookean expression of elastic energy and shear modulus (113). Similar works have highlighted the difference between swelling and shrinking behaviours of homogeneous hydrogels (17) and shown that shrinking is more unstable compared to swelling (157).

These studies have paved the way for investigating more complex volume transitions, such as anisotropic deformations due to responsive regions in heterogeneous hydrogels. In this regard, Tomari and Doi (174) published a landmark article proposing a mechanical model addressing the internal stresses and flow-related terms in a hydrogel bar with varying swelling ratios along its length. Later, the same approach was employed for modelling thermo-responsive spherical hydrogels (175). Based on the experimental results, Hino and Prausnitz (71) suggested a modification for classical Flory-Rehner theory taking heterogeneities into account.

Recently, we suggested a hybrid approach that can investigate both fluid-solid interactions at the local pore level and estimate shape transition during swelling and shrinking. The submitted article "Numerical modelling of heterogeneous stimuli-responsive hydrogels" can be found in Appendix C. Our numerical method embeds a Mass-Spring System (MSM) into a Smoothed-Particle Hydrodynamics (SPH) framework. Since our methodology in Chapter 4 will use a bead-spring model, the details regarding such networks will be provided in the respective chapter. Here, we will elaborate on the general technique and intriguing results.

The numerical scheme is a particle-based method that can operate in multiscale. While SPH resolves the fluid-solid interface, MSM is employed to account for elastic deformations. A distinct feature of the method is the identities of the particles. The particles stand in the middle of being computational points similar to mesh-dependent discretisation methods and material elements that are aware of physical properties. This hybrid approach brings versatility to the method, and from this perspective, it is possible to find some similarities with the developed method in the next chapter. In terms of the grid, an unstructured mesh to model a heterogeneous hydrogel cube is generated by tetrahedral

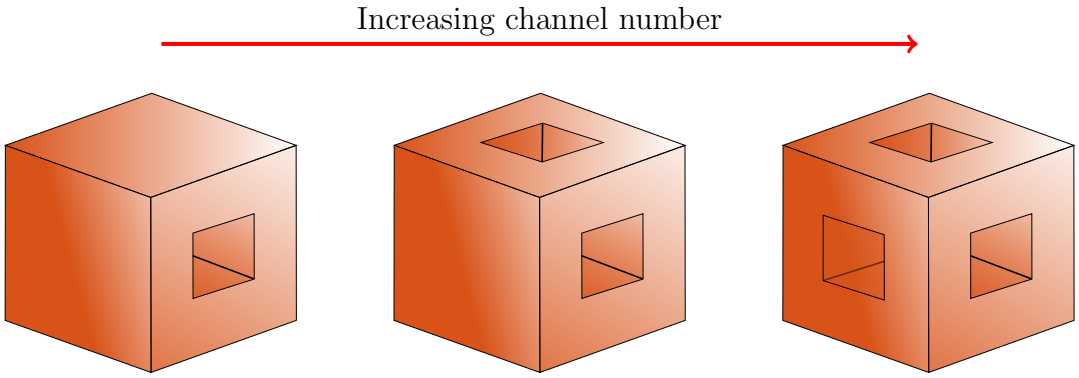

Figure 3.4: Menger sponges have rectangular channel profiles. Depending on the number of channels, they may expel fluid locally reaching moderate Reynolds numbers.

elements. Each element is a cluster of 20 elements creating a dodecahedron lattice.

The method is employed to explore the impacts of different parameters, including elastic modulus and shrinking ratio, on fluid expulsion. The numerical results suggest that depending on the parameters, deswelling may result in jet formation, which has locally finite Re, that is pushed out from the pores. These jets can facilitate local drug delivery with directional tendencies. To numerically realise this intention, we offer different Menger sponges with varying numbers of channels and directions. These channels are larger openings than the intrinsic pores of the hydrogel. In this regard, they may resemble apertures in optic lenses, fulfilling the same purpose of achieving an anisotropic response as the pores in the previous study of Maslen et al. (122). For example, the velocity profile of expelled fluid changes in the channel direction with increased circulation and diminishes in other directions for a one-hole sponge (see figure 3.4). Moreover, it is also noted that the local Re number becomes two times larger than the cases with no channels. The study provides insight in regard to design heterogeneity for responsive hydrogels, some of which will be used in Chapter 6.

To summarise, this chapter has presented examples of soft matter, in particular, focusing on hydrogels and responsive hydrogels. The material properties of gels will form the foundation of the rest of this thesis from a numerical standpoint. In the next chapter,

we will develop our numerical method for flows through porous media.

CHAPTER 4

METHODOLOGY

Here, we present a simple framework for modelling the dynamics of porous materials in Stokes flows. We develop a methodology that may be applied to simulate the motion of artificial microswimmers or active particles of arbitrary shapes. The framework employs a bead and spring system to capture elastic deformations in the forms of buckling, bending, and twisting. The method of regularised stokeslets is used to explore non-local hydrodynamic interactions.

This chapter starts with a description of the bead-spring systems and adaptation in this study in 4.1. It is followed by an elaboration of the method of regularised stokeslets in 4.2. Subsequently, both methods are coupled to develop a numerical algorithm (Section 4.3). The chapter ends with the validation of the developed methodology and a new insight regarding the sedimentation of porous filaments in section 4.4.

4.1 The Bead and Spring System

Bead and spring systems mathematically represent elastic materials. In general, a bead-spring network consists of a finite number of nodes (beads) that are connected with elastic springs. Under external forces, elastic springs can expand, compress, or rotate. Depending on the requirements of the problem, the springs can be linear, non-linear, or torsional. Additionally, extra elements such as dashpots can be introduced to the problem setup to

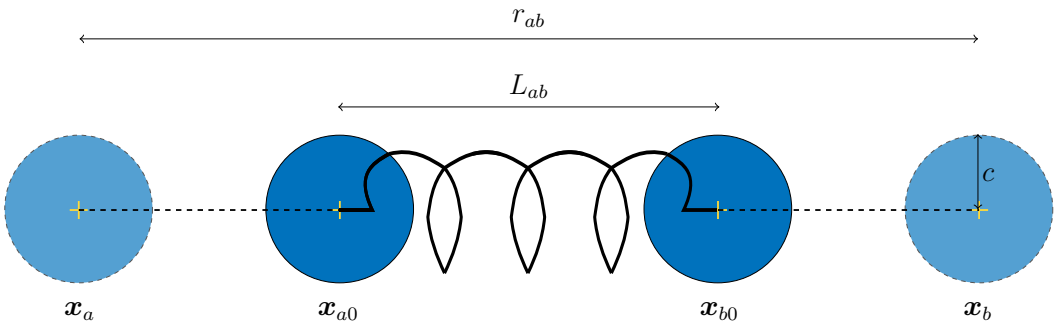

Figure 4.1: Schematic of a two-bead, one spring system is provided. Dashed lines indicate the instantaneous positions.

increase damping, thus providing a smoother response.

In the field of applied mathematics and engineering, physical phenomena can be modelled using bead or mass spring systems. These models include polymer physics (11), microswimmer motility (146), mechanics of non-Newtonian fluids (190), and dynamics of flexible filaments (32). The mesh-free nature of bead-spring networks has offered computationally cost-efficient solutions. In addition, the bead-spring networks can be easily employed for arbitrary shapes and heterogeneous materials.

On the other hand, for rod-like structures continuum approaches have been widely used as well (123). For example, inextensible cylindrical structures including flagella, cilia, and filaments can be modelled as Kirchhoff rods (3). In their landmark study, Tornberg and Shelley (176) combined the slender body theory with Kirchhoff inextensibility constraint. Although such models provide insight about the dynamics of homogeneous materials in beam shapes (107), they are not applicable to model porous structures in complex shapes with heterogeneities. Since bead-spring networks consider interactions of individual elements with each other, they provide discrete solutions which is essential for modelling heterogeneity.

These advantages of bead and spring networks have been used to simulate the dynamics of flexible materials and organisms at the nano and microscale. Previously, Gauger and Stark (61) presented a bead-spring formulation to model a magnetic swimmer attached to DNA. Similarly, Manghi et al. (117) simulated a rotating elastic nanorod. In another

(a) Edges of the tetrahedral elements may have different lengths.

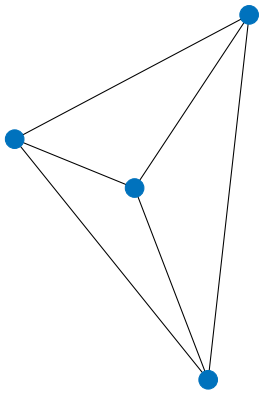

(b) Collection of tetrahedral elements creates the body.

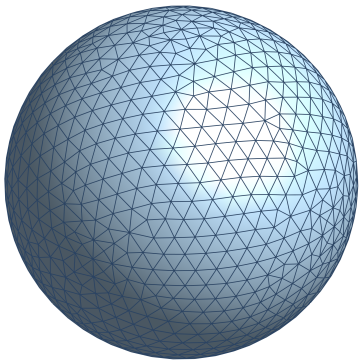

Figure 4.2: A bead and spring system is used to create porous geometries. In panel (a), a tetrahedral element is illustrated, while panel (b) demonstrates the meshed volume of the porous sphere.

landmark study, Delmotte et al. (32) provided a general bead and spring framework for elastic fibres, in addition to the joint and gear models governing the distance and contact criteria between beads.

In our model, we begin by creating a 3D geometry in GMSH® and meshing it in an unstructured grid. The nodes in the mesh are utilised as the beads in our system, while the links connecting the beads serve as harmonic springs. We create porous geometries with N_b impermeable beads by assigning each bead an identical radius. These beads correspond to solid parts or the skeleton of the porous body, while the voids between them represent the pores in the hydrogel. The radius of each bead is determined according to desired porosity, ϕ. Since the total volume of the body, V is a known parameter, we can calculate the volume of each bead as follows:

$$V_b = \frac{V(1-\phi)}{N_b} \tag{4.1}$$

where V_b is a single bead volume. In equation 4.1, the volume of each bead is identical. Then, the radius of each bead c is given by:

$$c = \sqrt[3]{\frac{3V_b}{4\pi}}. \tag{4.2}$$

With this model preference, the heterogeneities in the material are accounted for by the unstructured mesh. One might argue for different means to address heterogeneous material properties, such as assigning different bead radii. However, as we will explain later in section 4.2, our approach emphasises simplifying the model and obtaining robust results by keeping numerical parameters as constant and uniform as possible.

In the presence of external forces, the beads start to move, causing the Hookean springs to deform elastically. In our system, the beads are connected by total number of N_s springs. Then, the rest length between beads a and b, located at $\boldsymbol{x}_{a0}$ and $\boldsymbol{x}_{b0}$ respectively, is defined:

$$L_{ab} = ||\boldsymbol{x}_{b0} - \boldsymbol{x}_{a0}||, \tag{4.3}$$

as illustrated in figure 4.1. The distance between the beads during contraction or extension is given as:

$$r_{ab} = ||\boldsymbol{r}_{ab}||, \qquad \boldsymbol{r}_{ab} = \underbrace{\begin{pmatrix} x_b \\ y_b \\ z_b \end{pmatrix}}_{\boldsymbol{x}_b} - \underbrace{\begin{pmatrix} x_a \\ y_a \\ z_a \end{pmatrix}}_{\boldsymbol{x}_a} \tag{4.4}$$

where $\boldsymbol{x}_a$ and $\boldsymbol{x}_b$ are the instantaneous positions of the beads.

The unit vector pointing from the centre of bead a to the centre of bead b is defined

as:

$$\boldsymbol{e}_{r_{ab}} = \frac{\boldsymbol{r}_{ab}}{r_{ab}} = \begin{bmatrix} e_{r_{ab},x} \\ e_{r_{ab},y} \\ e_{r_{ab},z} \end{bmatrix}. \tag{4.5}$$

By inserting equations 4.4 and 4.5 into Hooke's law, we can write the elastic force on the bead a:

$$\boldsymbol{f}_{spring,ab} = -\boldsymbol{f}_{spring,ba} = k(r_{ab} - L_{ab})\boldsymbol{e}_{r_{ab}} \tag{4.6}$$

where k is the spring stiffness or spring coefficient.

In our system, the beads are connected in a manner that creates tetrahedral elements (see figure 4.2a). However, considering the heterogeneity of the material, the number of tetrahedra formed by each bead is not identical. Consequently, the number of springs linked to each bead may vary. Moreover, the deflection of these springs can differ in terms of both magnitude and direction. Therefore, the total elastic force on the a^{th} bead should be written as a sum, as follows:

$$\boldsymbol{f}_{spring,a} = \sum_{b=1}^{N_{c,a}} k(r_{ab} - L_{ab})\boldsymbol{e}_{r_{ab}}. \tag{4.7}$$

In equation 4.7, $N_{c,a}$ denotes the total number of beads connected to the a^{th} bead.

Since our model is a mathematical formulation that emulates real-life dynamics, it is necessary to relate the spring constant in the model to the macroscopic material properties, such as bending modulus. For this purpose, we adopt the spring stiffness formulation provided by LaGrone et al. (102). This method relates the elastic energy to the bending modulus $B = EI$, thereby providing a constitutive relationship for the spring coefficient (21). It should be noted that E and I represent the elastic modulus and second moment of area of the material, respectively.

Then, the elastic energy of a spring network that creates a filament-like shape can be

calculated as:

$$E_b = \frac{1}{2}\sum_{a,b}^{N_s} k\left(r_{ab} - L_{ab}\right)^2 . \tag{4.8}$$

The bending modulus can be found by bending the filament into a known curvature, κ;

$$B = \frac{2E_b}{\kappa^2 L} \tag{4.9}$$

where L is the length of the filament like spring network. For a known bending rigidity, the spring constant can be obtained by inserting equation 4.8 into equation 4.9 and solving inversely.

To bend the filament into a known curvature, we utilise arclength parameterisation ($s \in [0, L]$) for the centreline and local cylindrical coordinates for the filament as $(\mathtt{r}, \Theta, s)$. We begin with a filament with a circular cross-section with radius R and length L. Initially, the centreline of the filament is located between $x_{c0}(s) = 0$ and $x_{c0}(s) = L$ (see figure 4.3). Then, the centreline of the deformed filament can be written as follows:

$$x_c(s) = \frac{\sin(\kappa x_{c0}(s))}{\kappa} \tag{4.10}$$

$$y_c(s) = \frac{1}{\kappa} - \frac{\cos(\kappa x_{c0}(s))}{\kappa} \tag{4.11}$$

$$z_c(s) = 0 \tag{4.12}$$

The coordinates of the a^{th} bead on the arc with curvature κ is given as:

$$\boldsymbol{x_a}(\mathtt{r}, \Theta, s) = \boldsymbol{x_c}(s) + \mathtt{r}\cos\Theta\mathbf{N} + \mathtt{r}\sin\Theta\mathbf{B} \tag{4.13}$$

where $\mathbf{N}$ and $\mathbf{B}$ are the unit normal and binormal vectors respectively, given by Frenet-Serret formulation. Once the coordinates of all beads are known, the elastic energy can be calculated.

For a filament with a bending modulus of $B = EI = E\pi R^4/4$, we repeat this procedure for different curvature values $\kappa = 1/(10L), \ldots, 1/L, \ldots, 1/(L/10)$. Figure 4.4a

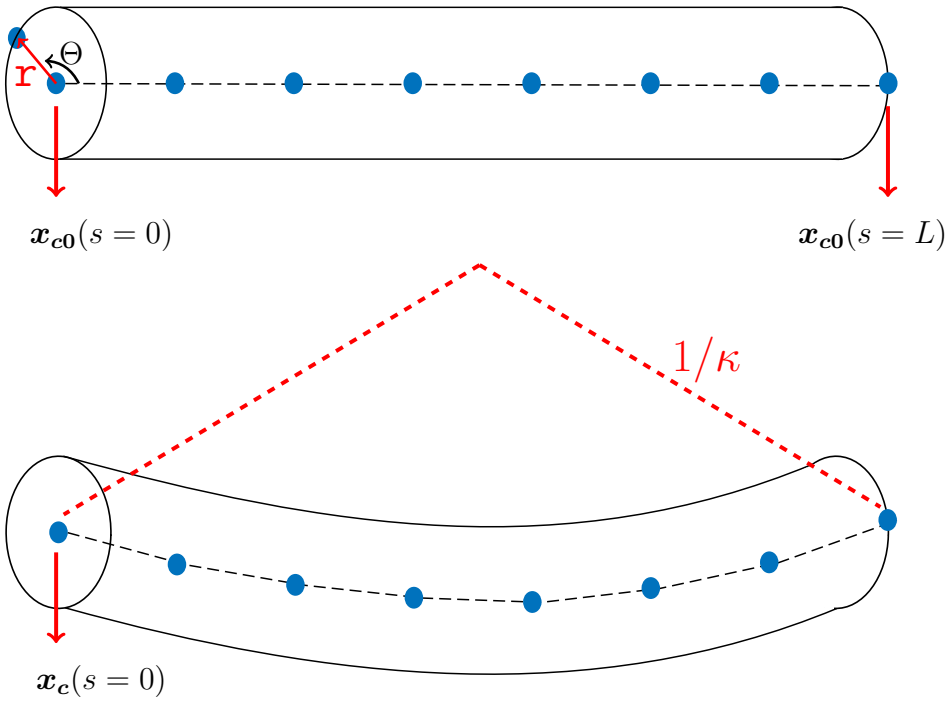

Figure 4.3: Initially, a straight filament is illustrated on top. After bending it into a known arc, the new positions of the beads are calculated.

demonstrates the bent filaments for $\kappa = 1/(L/5), 1/L$, and $1/10L$. In figure 4.4b, the $y-$axis is normalised according to the average value of spring stiffness. The figure suggests that the sensitivity of the spring constant to curvature is negligible. When $\kappa = 1/(L/2\pi)$, the filament is bent into a circle. Even for curvatures greater than this value, the spring stiffness remains approximately identical. Therefore, we will calculate spring constants for the filaments with $\kappa = 1/2L$.

This method offers an easy-to-implement solution and we will follow it for the majority of this thesis. However, equation 4.9 only holds for rod-like shapes and it is not suitable for modelling geometries like spheres or arbitrary shapes. To address this limitation, we also benefit from another formulation, namely the 3D distinct lattice spring model (DLSM).

The DLSM framework was first described by Zhao et al. (199) to relate spring stiffness with elastic modulus in unstructured bead-spring systems. Previous validation cases for cubic and spherical geometries (200) demonstrated that the method is ideal for modelling arbitrary shapes. Additionally, the DLSM formulation is specifically designed for

(a) Different curvatures are tested for calculating spring stiffness.

(b) Spring stiffness is insensitive to curvature changes in a reasonable range.

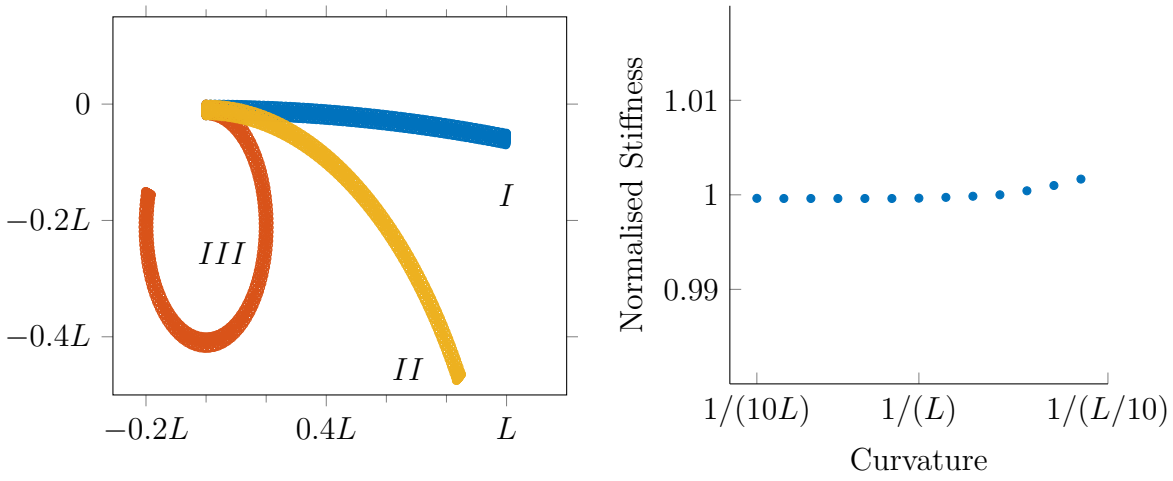

Figure 4.4: There is no significant change in spring stiffness according to variations in curvature. In figure a), three different curves as depicted as an example. In respective order blue, yellow, and orange curves labelled as I, II, and III have uniform curvatures equal to $1/10L$, $1/L$, and $5/L$.

unstructured meshes. According to the model, the spring coefficient is given by:

$$k = \frac{3E}{\alpha^{3D}(1-2\nu)} \tag{4.14}$$

where ν represents Poisson's ratio. In our method, we will assume that the Poisson's ratio is fixed at $\nu = 0.25$. The microstructure geometry coefficient α^{3D} is an effective length scaling parameter defined as:

$$\alpha^{3D} = \frac{\sum_{a,b}^{N_s} L_{ab}^2}{V}. \tag{4.15}$$

It is worth noting that the original DLSM formulation was designed for elastic materials rather than poroelastic hydrogels. As a result, it may suggest slightly different spring coefficients for the same system compared to the formulation in 4.9. Both methods can be calibrated against empirical data, which is planned as a part of further studies in

Chapter 7. However, for the remainder of this thesis, we will disregard this difference and utilise the elastic energy formulation for rod-like structures, while the DLSM formulation will be applied to the other geometries. Additionally, we use the DLSM formulation in the cases where the material either does not deform at all or is subject to internal stress rather than external force. In such problem setups, the spring stiffness does not have an impact on the dynamics, therefore, any large spring coefficient would yield to same results. In the next section, we will adopt the method of regularised stokeslets described in section 1.5 for the hydrodynamics in our numerical method.

4.2 The Method of Regularised Stokeslets

In our system, each regularised stokeslet is placed at the centre of its corresponding bead. Consequently, the number of regularised stokeslets is identical to the number of beads. With this formulation, the regularised stokeslets may effectively represent both the solid parts of the porous structure and the interstitial fluid within the pores. To accurately and robustly describe the hydrodynamics of the system, we need to determine an appropriate regularisation width, ϵ, for the regularised stokeslets.

For this purpose, we consider a simple problem setup in which the viscous drag on an impermeable sphere with a radius of m is calculated using the method of regularised stokeslet. We begin by recalling the velocity formulation with a regularised force, as given in equation 1.27 and 1.28. Then, the flow field can be described by:

$$\boldsymbol{u}(\boldsymbol{x}) = \frac{1}{8\pi\mu}\boldsymbol{S}^{\epsilon}(\boldsymbol{x}, \boldsymbol{x}_0) \cdot \boldsymbol{f}(\boldsymbol{x}_0) \tag{4.16}$$

$$S^{\epsilon}_{ij}(\boldsymbol{x}, \boldsymbol{x}_0) = \frac{\delta_{ij}(r^2 + 2\epsilon^2) + r_i r_j}{r^3_{\epsilon}}. \tag{4.17}$$

Additionally, as provided in section 1.5.1, the drag force on the sphere is given by $f_{drag} = 6\pi\mu m u$. If we consider a single regularised stokeslet with $r = 0$, implying evaluation/collocation point is identical to the centre of regularised stokeslet $\boldsymbol{x} = \boldsymbol{x}_0$,

equation 4.16 becomes:

$$u_i(\boldsymbol{x}_0) = \frac{\delta_{ij} 2\epsilon^2}{8\pi\mu\epsilon^3} f_{drag} = \frac{1}{6\pi\mu m} f_{drag} \tag{4.18}$$

$$\therefore \epsilon = \frac{3}{2} m. \tag{4.19}$$

In our study, regardless of the number of beads and hydrogel shape, we will adhere to the formulation in equation 4.19. Previously, Zhao et al. (198) compared the accuracy of different regularisation widths for the same blob function and also different blobs. We may consider a similar study for improving our methodology in the future. However, our selection of the constitutive relation between the bead radius and the regularisation width is intended to produce a system in which the porosity is user-determined. Therefore, for a prescribed body volume and desired porosity value, the radius of each bead is calculated accordingly, and the same regularisation is applied to each bead.

Additionally, the example above uses a single regularised stokeslet to describe the flow field. However, for slender filaments such as flagella or cilia, or more complex structures including porous networks, the combination of multiple regularised stokeslets can provide a more accurate solution. Since we couple the method of regularised stokeslets with our bead and spring system, for N_b regularised stokeslets, equation 4.16 results in a linear matrix system that can be written as:

$$\underbrace{\frac{1}{8\pi\mu}\begin{pmatrix} \boldsymbol{S}^\epsilon(\boldsymbol{x}_1,\boldsymbol{x}_1) & \boldsymbol{S}^\epsilon(\boldsymbol{x}_1,\boldsymbol{x}_2) & \dots & \boldsymbol{S}^\epsilon(\boldsymbol{x}_1,\boldsymbol{x}_{N_b}) \\ \boldsymbol{S}^\epsilon(\boldsymbol{x}_2,\boldsymbol{x}_1) & \boldsymbol{S}(\boldsymbol{x}_2,\boldsymbol{x}_2) & \dots & \boldsymbol{S}^\epsilon(\boldsymbol{x}_2,\boldsymbol{x}_{N_b}) \\ \vdots & \vdots & \ddots & \\ \boldsymbol{S}^\epsilon(\boldsymbol{x}_{N_b},\boldsymbol{x}_1) & \boldsymbol{S}^\epsilon(\boldsymbol{x}_{N_b},\boldsymbol{x}_2) & \dots & \boldsymbol{S}^\epsilon(\boldsymbol{x}_{N_b},\boldsymbol{x}_{N_b}) \end{pmatrix}}_{\mathcal{M}} \underbrace{\begin{pmatrix} \boldsymbol{f}_1 \\ \boldsymbol{f}_2 \\ \vdots \\ \boldsymbol{f}_{N_b} \end{pmatrix}}_{\mathcal{F}} = \underbrace{\begin{pmatrix} \boldsymbol{u}_1(\boldsymbol{x}_1) \\ \boldsymbol{u}_2(\boldsymbol{x}_2) \\ \vdots \\ \boldsymbol{u}_{N_b}(\boldsymbol{x}_{N_b}) \end{pmatrix}}_{\mathcal{U}} \tag{4.20}$$

$$\boldsymbol{S}^\epsilon(\boldsymbol{x}_a,\boldsymbol{x}_b) = \begin{pmatrix} S^\epsilon_{xx}(\boldsymbol{x}_a,\boldsymbol{x}_b) & S^\epsilon_{xy}(\boldsymbol{x}_a,\boldsymbol{x}_b) & S^\epsilon_{xz}(\boldsymbol{x}_a,\boldsymbol{x}_b) \\ S^\epsilon_{yx}(\boldsymbol{x}_a,\boldsymbol{x}_b) & S^\epsilon_{yy}(\boldsymbol{x}_a,\boldsymbol{x}_b) & S^\epsilon_{yz}(\boldsymbol{x}_a,\boldsymbol{x}_b) \\ S^\epsilon_{zx}(\boldsymbol{x}_a,\boldsymbol{x}_b) & S^\epsilon_{zy}(\boldsymbol{x}_a,\boldsymbol{x}_b) & S^\epsilon_{zz}(\boldsymbol{x}_a,\boldsymbol{x}_b) \end{pmatrix} \tag{4.21}$$

where $\mathcal{M}$ is a $3N_b \times 3N_b$ matrix, and $\mathcal{F}$ and $\mathcal{U}$ are $3N_b \times 1$ column matrices. Each element of $\mathcal{F}$ represents the force acting on the a^{th} bead and $\boldsymbol{f}_a = [f_x,\ f_y,\ f_z]_a^T$. As we will detail in the next section, this force can be a combination of gravitational force, spring forces due to elastic deformations, and external forces such as a compressive pusher force. The velocity vectors are given by $\boldsymbol{u} = [u, v, w]^T$. Now that we have elaborated on our bead-spring system and the method of regularised stokeslet, we can develop a numerical algorithm incorporating both.

4.3 Numerical Algorithm

In our methodology, the elastic deformations of the bead system are coupled with the hydrodynamic effects resulting from the creeping flow in and out of the porous hydrogels. We model the interactions involved by distributing regularised stokeslets on the solid beads. Consequently, the regularised force on each stokeslet is determined by the forces exerted by each bead onto the fluid.

The numerical algorithm begins with a force balance equation between hydrodynamic drag, body forces, and elastic deformations. Since we consider sedimentation problems under gravity for validation in this Chapter, the force balance is given by:

$$\boldsymbol{f}_{drag} + \boldsymbol{f}_{spring} + \boldsymbol{f}_{body} = 0 \tag{4.22}$$

where $\boldsymbol{f}_{body}$ represents the gravitational force.

In our model, $\boldsymbol{f}_{spring}$ and $\boldsymbol{f}_{body}$ are known parameters that depend on the dynamics of the physical system. Therefore, by using the force acting on each bead, the velocity at any arbitrary fluid parcel within the domain can be estimated. The drag force is applied by the fluid onto the bead as a resultant force in the direction opposite to the sum of the body and spring forces.

After inserting equation 4.22 into equation 4.20, the force matrix $\mathcal{F}$ becomes:

$$\mathcal{F} = \begin{pmatrix} \boldsymbol{f}_{body,1} + \boldsymbol{f}_{spring,1} \\ \boldsymbol{f}_{body,2} + \boldsymbol{f}_{spring,2} \\ \vdots \\ \boldsymbol{f}_{body,N_b} + \boldsymbol{f}_{spring,N_b} \end{pmatrix}. \tag{4.23}$$

For sedimentation cases in section 4.4, the body force on the a^{th} bead is written as:

$$\boldsymbol{f}_{body,a} = \Delta\rho \mathbf{g} V_b, \tag{4.24}$$

which is the sedimentation force resulting from gravity and buoyancy. In equation 4.24, $\Delta\rho = \rho_s - \rho_f$ is the difference between bead density and ambient fluid density, and $\mathbf{g} = [g_x,\ g_y,\ g_z]^T$.

By implementing 4.7 and the above expression 4.24 into equation 4.23, the force matrix, $\mathcal{F}$, can be written in vector form as the following:

$$\mathcal{F} = \begin{pmatrix} \Delta\rho \mathbf{g} V_b + \sum_{b=1}^{N_{c,1}} k(r_{1b} - L_{1b}) \boldsymbol{e}_{r_{1b}} \\ \Delta\rho \mathbf{g} V_b + \sum_{b=1}^{N_{c,2}} k(r_{2b} - L_{2b}) \boldsymbol{e}_{r_{2b}} \\ \vdots \\ \Delta\rho \mathbf{g} V_b + \sum_{b=1}^{N_{c,N_b}} k(r_{N_b b} - L_{N_b b}) \boldsymbol{e}_{r_{N_b b}} \end{pmatrix} \tag{4.25}$$

where each entry is a 3×1 column vectors. By updating equation 4.20 with equation 4.25, the velocity at any point in the domain can be determined at any given instant. Alternatively, if the velocities of the solid boundaries are known, the force exerted on the fluid can be calculated by inverting equation 4.20. In our simulations, we know the body forces; therefore, once the velocity is calculated, the positions of the beads can be advanced.

Time marching can be performed explicitly or implicitly. Considering a first-order

forward Euler method, the position of the a^{th} bead is given by:

$$\boldsymbol{x}_a^{n+1} = \boldsymbol{x}_a^n + \Delta t \boldsymbol{u}_a^n \tag{4.26}$$

where the superscript n denotes the time step, and Δt is the time step-size. However, the problems that we will solve in this thesis are numerically stiff. To preserve numerical stability in the presence of numerical stiffness, the explicit scheme requires the use of small time step sizes, typically on the order of $\Delta t \approx \mathcal{O}(10^{-8} - 10^{-6})$. For example, if we consider a system with $N_b = 2283$ beads which we will use in 4.4, for $\Delta t = 10^{-6}$, each time step takes approximately 1 s. Then, simulating a single second of the physical problem would take around ≈ 11 days. As Δt becomes smaller and simulation time increases, this wall time would become even more dramatic.

To avoid this expensive computational cost, we can employ a first-order implicit Euler scheme. The implicit method allows us to use larger time step sizes, thereby requiring fewer iterations. The disadvantage of the method is that a single iteration would take more time since it involves solving a system of ordinary differential equations. In addition to that, it could be cumbersome to develop an algorithm while preserving the linearity of the system.

As a remedy to the mentioned issues, we propose a semi-implicit Euler scheme. The scheme uses a force balance equation at the current time step, $n+1$, while the positions of the regularised stokeslets are estimated at the previous time step, n. A similar formulation for the locations of regularised stokeslets was previously used in the study of Bouzarth et al. (14). Consequently, the semi-implicit scheme can be written as follows:

$$\boldsymbol{x}_a^{n+1} = \boldsymbol{x}_a^n + \Delta t \boldsymbol{u}_a^{n+1} \tag{4.27}$$

$$\boldsymbol{u}_a^{n+1} = \sum_{b=1}^{N_b} \boldsymbol{S}^{\epsilon}(\boldsymbol{x}_a, \boldsymbol{x}_b)^n \cdot \left(\boldsymbol{f}_{body,b}^{n+1} + \boldsymbol{f}_{spring,b}^{n+1} \right). \tag{4.28}$$

In equation 4.28, the gravitational force is constant so it remains unchanged between time

steps. However, the elastic spring force on the a^{th} bead is adapted as:

$$\boldsymbol{f}_{spring,a}^{n+1} = \sum_{b=1}^{N_{c,a}} k(r_{ab}^{n+1} - L_{ab})\boldsymbol{e}_{r_{ab}}^{n}. \tag{4.29}$$

It should be noted that, in equation 4.29, the unit vector pointing from the a^{th} bead to the b^{th} bead, $\boldsymbol{e}_{r_{ab}}^{n}$, is calculated at the previous time step. This is done to preserve the linearity of equation 4.20. This assumption limits the rotation of the springs, however, the resulting error can be neglected by selecting small time steps. Our assumption yields to following relationship:

$$\boldsymbol{e}_{r_{ab}}^{n+1} \approx \boldsymbol{e}_{r_{ab}}^{n} \tag{4.30}$$

$$\therefore r_{ab}^{n+1}\boldsymbol{e}_{r_{ab}}^{n} \equiv r_{ab}^{n+1}\boldsymbol{e}_{r_{ab}}^{n+1} = \boldsymbol{r}_{ab}^{n+1} = \boldsymbol{x}_{b}^{n+1} - \boldsymbol{x}_{a}^{n+1} \tag{4.31}$$

$$\therefore (r_{ab}^{n+1} - L_{ab})\boldsymbol{e}_{r_{ab}}^{n} = \boldsymbol{x}_{b}^{n+1} - \boldsymbol{x}_{a}^{n+1} - L_{ab}\boldsymbol{e}_{r_{ab}}^{n}. \tag{4.32}$$

If we combine this information with equation 4.29, the semi-implicit algorithm implies;

$$\frac{\boldsymbol{x}_{a}^{n+1} - \boldsymbol{x}_{a}^{n}}{\Delta t} = \boldsymbol{u}_{a}^{n+1} = \frac{1}{8\pi\mu}\sum_{b=1}^{N_b} \boldsymbol{S}^{\epsilon}(\boldsymbol{x}_a, \boldsymbol{x}_b)^n \left(\Delta\rho\mathbf{g}V_b + \sum_{c=1}^{N_{c,b}} k\left(r_{bc}^{n+1} - L_{bc}\right)\boldsymbol{e}_{r_{bc}}^{n}\right) \tag{4.33}$$

$$= \frac{1}{8\pi\mu}\sum_{b=1}^{N_b} \boldsymbol{S}^{\epsilon}(\boldsymbol{x}_a, \boldsymbol{x}_b)^n \left(\Delta\rho\mathbf{g}V_b + \sum_{c=1}^{N_{c,b}} k\left(\boldsymbol{x}_{c}^{n+1} - \boldsymbol{x}_{b}^{n+1} - L_{bc}\boldsymbol{e}_{r_{bc}}^{n}\right)\right). \tag{4.34}$$

For the remainder of this thesis, equation 4.33 will be used to create a linear matrix system. While the second term on the right-hand side (RHS) considering elastic deflections will remain the same, the body force may be replaced by external forces or omitted entirely, depending on the problem setup.

If we collect the known terms on the n^{th} time step on the RHS, we can obtain the linear system. From equation 4.33, the RHS can be written as:

$$RHS = \boldsymbol{x}_{a}^{n} + \frac{\Delta t}{8\pi\mu}\sum_{b=1}^{N_b} \boldsymbol{S}^{\epsilon}(\boldsymbol{x}_a, \boldsymbol{x}_b)^n \left(\Delta\rho\mathbf{g}V_b - \sum_{c=1}^{N_{c,b}} k\left(L_{bc}\boldsymbol{e}_{r_{bc}}^{n}\right)\right). \tag{4.35}$$

Then, the left-hand side (LHS) of the linear system is given by:

$$LHS = \boldsymbol{x}_a^{n+1} + \frac{k\Delta t}{8\pi\mu} \sum_{b=1}^{N_b} \boldsymbol{S}(\boldsymbol{x}_a, \boldsymbol{x}_b)^n \left(\sum_{c=1}^{N_{c,b}} \boldsymbol{x}_b^{n+1} - \boldsymbol{x}_c^{n+1} \right). \tag{4.36}$$

After rearranging equations 4.35 and 4.36, we can write the following matrix system:

$$\mathcal{A}\mathcal{X}^{n+1} = \mathcal{B} \tag{4.37}$$

where $\mathcal{X}$ is a $3N_b \times 1$ column matrix of the bead positions. If we introduce $\gamma = \frac{\Delta t}{8\pi\mu}$, $\mathcal{A}$ is given as:

$$\mathcal{A} = \mathbb{I}_{3N_b \times 3N_B} + k\gamma \mathcal{M}^n \mathcal{C}_1 - k\gamma \mathcal{C}_2 \tag{4.38}$$

where

$$\mathcal{C}_1 = \begin{pmatrix} N_{c,1} & N_{c,1} & N_{c,1} & \dots & N_{c,N_b} & N_{c,N_b} & N_{c,N_b} \\ \vdots & & & & & \vdots & \\ N_{c,1} & N_{c,1} & N_{c,1} & \dots & N_{c,N_b} & N_{c,N_b} & N_{c,N_b} \end{pmatrix} \tag{4.39}$$

and

$$\mathcal{C}_2 = \begin{pmatrix} \sum_{c=1}^{N_{c,1}} S_{xx}^{\epsilon}(\boldsymbol{x}_1, \boldsymbol{x}_{c,1}) & \dots & \sum_{c=1}^{N_{c,N_b}} S_{zx}^{\epsilon}(\boldsymbol{x}_{N_b}, \boldsymbol{x}_{c,1}) \\ \sum_{c=1}^{N_{c,1}} S_{xy}^{\epsilon}(\boldsymbol{x}_1, \boldsymbol{x}_{c,1}) & \dots & \sum_{c=1}^{N_{c,N_b}} S_{zy}^{\epsilon}(\boldsymbol{x}_{N_b}, \boldsymbol{x}_{c,1}) \\ \sum_{c=1}^{N_{c,1}} S_{xz}^{\epsilon}(\boldsymbol{x}_1, \boldsymbol{x}_{c,1}) & \dots & \sum_{c=1}^{N_{c,N_b}} S_{zz}^{\epsilon}(\boldsymbol{x}_{N_b}, \boldsymbol{x}_{c,1}) \\ \vdots & & \\ \sum_{c=1}^{N_{c,1}} S_{xx}^{\epsilon}(\boldsymbol{x}_1, \boldsymbol{x}_{c,N_b}) & \dots & \sum_{c=1}^{N_{c,N_b}} S_{zx}^{\epsilon}(\boldsymbol{x}_{N_b}, \boldsymbol{x}_{c,N_b}) \\ \sum_{c=1}^{N_{c,1}} S_{xy}^{\epsilon}(\boldsymbol{x}_1, \boldsymbol{x}_{c,N_b}) & \dots & \sum_{c=1}^{N_{c,N_b}} S_{zy}^{\epsilon}(\boldsymbol{x}_{N_b}, \boldsymbol{x}_{c,N_b}) \\ \sum_{c=1}^{N_{c,1}} S_{xz}^{\epsilon}(\boldsymbol{x}_1, \boldsymbol{x}_{c,N_b}) & \dots & \sum_{c=1}^{N_{c,N_b}} S_{zz}^{\epsilon}(\boldsymbol{x}_{N_b}, \boldsymbol{x}_{c,N_b}) \end{pmatrix}^T \tag{4.40}$$

where $\mathcal{A}$, $\mathcal{C}_1$, $\mathcal{C}_2$ are $3N_b \times 3N_b$ matrices. Then, equation 4.35 is converted to a matrix as:

$$\mathcal{B} = \mathcal{X}^n + \gamma \mathcal{M}^n \mathcal{D} \tag{4.41}$$

$$\mathcal{D} = \begin{pmatrix} \Delta\rho g_x V_b - \sum_{c=1}^{N_{c,1}} kL_{1c} e_{r_{1c},x} \\ \Delta\rho g_y V_b - \sum_{c=1}^{N_{c,1}} kL_{1c} e_{r_{1c},y} \\ \Delta\rho g_z V_b - \sum_{c=1}^{N_{c,1}} kL_{1c} e_{r_{1c},z} \\ \vdots \\ \Delta\rho g_x V_b - \sum_{c=1}^{N_{c,N_b}} kL_{1c} e_{r_{N_b c},x} \\ \Delta\rho g_y V_b - \sum_{c=1}^{N_{c,N_b}} kL_{1c} e_{r_{N_b c},y} \\ \Delta\rho g_z V_b - \sum_{c=1}^{N_{c,N_b}} kL_{1c} e_{r_{N_b c},z} \end{pmatrix} \tag{4.42}$$

where $\mathcal{D}$ is a $3N_b \times 1$ column matrix. We create the above matrices in MATLAB® and solve them by using the built-in function linsolve. A pseudo-code demonstrating the MATLAB® algorithm can be found in Appendix A. In the next section, we will test our method in various validation cases.

4.4 Verification and Results

Our methodology is validated against previous theoretical and experimental studies. The comparison begins with numerical simulations of the sedimentation of porous and non-deformable spheres under gravity. Later, the developed technique is used to model sedimentation of nonporous and deformable filaments. After verifying the method, the algorithm is applied to capture the physics of sedimenting porous and deformable passive filaments.

An aqueous solution at room temperature is selected as the ambient and interstitial fluid. The density and dynamic viscosity of the fluid are given as $\rho_f = 997\,\mathrm{kg\,m^{-3}}$ and $\mu = 1 \times 10^{-3}\,\mathrm{N\,s\,m^{-2}}$ respectively. Sedimentation occurs under standard gravitational acceleration in the $-z$-direction, $g = 9.81\,\mathrm{m\,s^{-2}}$ in an infinite and quiescent fluid. There

are no wall effects. With the motivation to extend the model for responsive hydrogel studies, we consider the material properties of Poly(N-isopropylacrylamide) (PNIPAM) for the solid bodies. Thus, the density is $\rho_s = 1100\,\mathrm{kg\,m^{-3}}$ and elastic modulus is $E = 10\,\mathrm{kPa}$ (158), unless otherwise stated.

4.4.1 Sedimentation of Porous Non-Deformable Spheres

The sedimentation of porous spheres is a problem studied through theoretical, numerical, and experimental investigations. The problem can be observed in the sedimentation of suspensions (155), the movement of microbial granules (133) and the flow through fixed beds of catalyst pellets (171). In these examples, the porous sphere is typically composed of aggregates of spherical components. While the approaching flow is defined by Stokes' formulation, determining the boundary conditions and flow description inside the sphere is more complicated.

Previously, in their landmark study, D.N.Sutherland and C.T.Tan (36) suggested an analytical model for creeping flows through a permeable sphere with a radius of m. We provided the drag on the sphere in 3.5. Inserting gravitational force into the equation, the settling speed is provided as:

$$u_t = \frac{2(\rho_b - \rho_f)gm^2}{9(1-\varphi)\mu} \tag{4.43}$$

where $\rho_b = (1-\phi)\rho_s + \phi\rho_f$ is the bulk density of the porous structure. Equation 4.43 can be interpreted as that a porous sphere would sediment faster than an impermeable sphere with the same bulk density, as the denominator is smaller for the porous case. This statement has been supported by experimental studies (133).

We conduct a numerical study to compare our results with the above formulation. The sphere in our simulations has a radius $m = 10\,\mu\mathrm{m}$ and consists of N_b smaller spheres. Due to spherical geometry, DLSM formulation is used to determine spring stiffness. However, it should be noted that since the sphere is rigid and non-deformable, the elastic modulus is

chosen to be higher than $E = 10\,\text{kPa}$. Our simulations correspond to 10 s of sedimentation in physical parameters.

We begin by comparing the accuracy in terminal speed for changing porosity values. The number of beads is equal to $N_b = 2283$ which is the second-highest spatial resolution for this problem setup, and a detailed resolution study will be provided later in this section. The porosity is varied between $\phi = 0 - 0.9$ with increments of 0.1, and an additional case with $\phi = 0.95$ is considered. In all simulations, the time step size equals $\Delta t = 0.01$. Figure 4.5a plots the relative error between our numerical method and the theoretical study (36). The results show good agreement and exhibit a trend of increasing accuracy with the porosity. The reason behind this is the fact that the regularised stokeslets may overlap with each other for low porosity cases, which causes erroneous forces on the beads. In figure 4.5b, we demonstrate the number of iterations required for the convergence of the terminal speed. Because of the instantaneity of Stokes flow, a sedimenting non-deformable sphere would reach the terminal velocity immediately. With our numerical method, the settling speed is reached after 20 iterations of the simulations.

To understand the dynamics of the system, we compare the magnitudes of the terminal velocities. Terminal speed for a nonporous sphere can be found by balancing the drag force with sedimentation force, $-f_{drag} = f_{gravity} = (\rho_s - \rho_f)gV_s$ where $V_s = 4\pi m^3/3$. By using the analytical solution provided in equation 1.38, the terminal speed of a nonporous sphere can be found as the following:

$$u_t = \frac{2(\rho_s - \rho_f)gm^2}{9\mu}. \tag{4.44}$$

Thus, the terminal speed with our parameters is $u_t \approx 2.46 \times 10^{-5}\,\text{m}\,\text{s}^{-1}$, which corresponds to $Re \approx 2.45 \times 10^{-4} \ll 1$. In figure 4.6a, we normalise the terminal speeds for this value. It can be seen that with increasing porosity, the magnitude of terminal velocity decreases linearly. There may be two factors contributing to this trend. First of all, as porosity increases, the mass of the sphere decreases, therefore, the driving force becomes smaller.

(a) The relative error in terminal speed decreases as porosity increases.

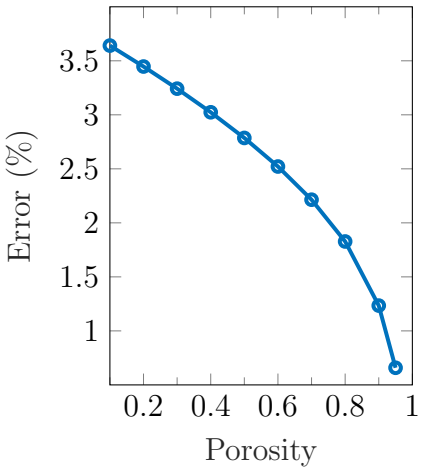

(b) The terminal speed begins to converge to a stable value after 20 iterations.

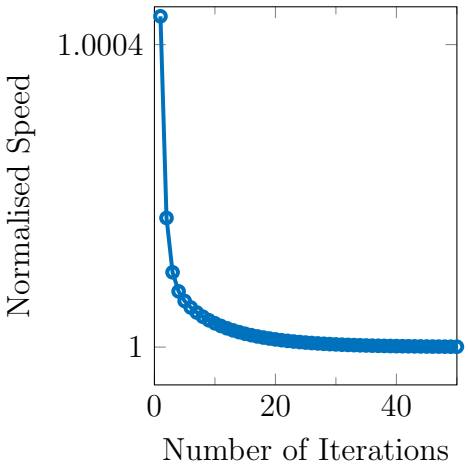

Figure 4.5: The sedimentation of porous spheres are investigated. In panel (a), the numerical results are compared with equation 4.43. In panel (b), for $\phi = 0.9$, the sphere numerically reaches a steady state and translates at terminal speed.

In addition to that, the internal flow may affect the sedimentation speed. Therefore, we investigate the flow inside the sphere.

Due to small length scales, experimentally measuring the flow inside the pores has been a challenging task. Consequently, theoretical and numerical studies have suggested different solutions to this problem. A comprehensive study of Neale et al. (138) compared extensions of Brinkman and Darcy solutions. The main difference between the two models is the magnitude of interstitial flow compared to sedimentation speed.

We estimate the speed of flow inside the sphere by using regularised stokeslets. For this purpose, we determine some fluid points on the z_{gc}^{n} plane which is the z coordinate of the geometrical centre of the sphere at the n^{th} time step. Then, we take the average of flow speed at these points.

Figure 4.6b depicts the ratio of average internal flow speed to the terminal speed of sphere u_i/u_t, in percentages. According to the figure, as porosity increases, the internal flow becomes more pronounced. However, since the ratio remains less than 1%, we conclude that the flow within the sphere is negligible, as suggested by D.N.Sutherland

(a) Terminal speed decreases as porosity increases.

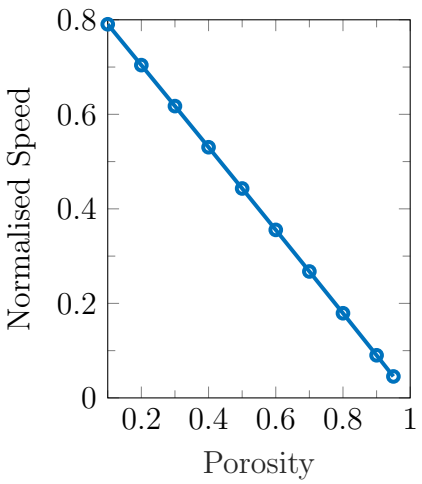

(b) Flow inside the sphere is negligible.

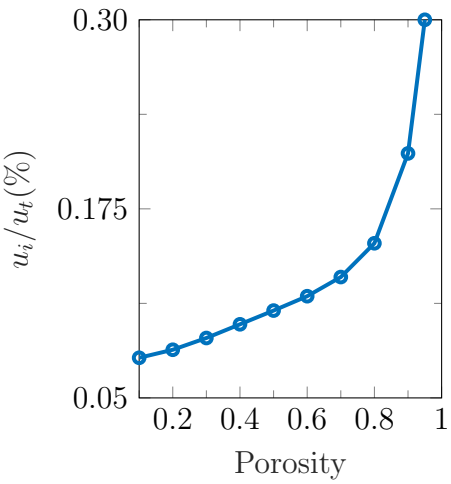

Figure 4.6: The terminal speeds and flows inside the spheres are compared. In panel (a), the porosity of the sphere and sedimentation speed have an inverse correlation. Panel (b) shows that even for high porosity values, the flow inside the sphere has a much lower speed than the terminal speed of the sphere (36).

and C.T.Tan (36). It should be added that the flow inside the sphere is parallel to the sedimentation direction unless it encounters a bead.

Finally, we conduct a resolution study for time marching and spatial discretisation. For testing the temporal resolution, we simulate the same sedimentation problem for $N_b = 2283$ and $\phi = 0.9$ with time step sizes between $\Delta t = 10^{-4}$ to 10^{-1}. In figure 4.7a, the $y-$axis is the normalised with the analytical solution. As Δt decreases, the precision of the solution increases. However, even for $\Delta t = 10^{-1}$, the error is around $\approx 2\%$. So, we can conclude that using $\Delta t = 10^{-2}$ is a safe choice for preventing stability issues. Additionally, since the end state is steady, time resolution should not significantly impact the results.

For testing the spatial resolution, the number of beads is changed for fixed $\Delta t = 10^{-2}$ and $\phi = 0.9$. In figure 4.7b, we demonstrate the relative error versus spatial resolution. Similar to temporal resolution, spatial refinement improves the accuracy of the solution. For the two finest resolutions $N_b = 2283,$ and 2859, the error is less than 1.3% and the difference between them is 0.9%. Thus, we use $N_b = 2283$, which has good accuracy with

(a) Temporal resolution does not impact the accuracy significantly.

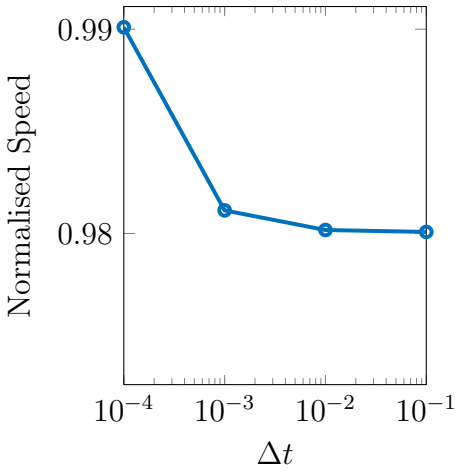

(b) As spatial resolution increases, accuracy increases as well.

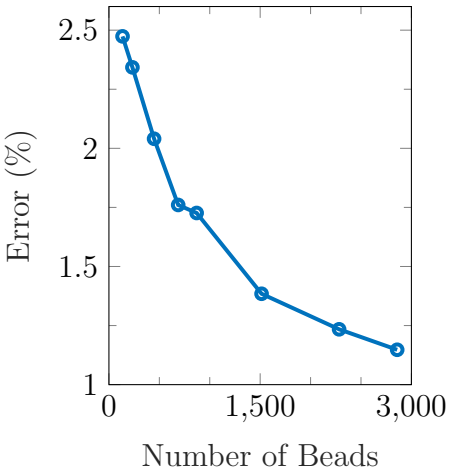

(c) As N_b changes, the deviation parameter shifts.

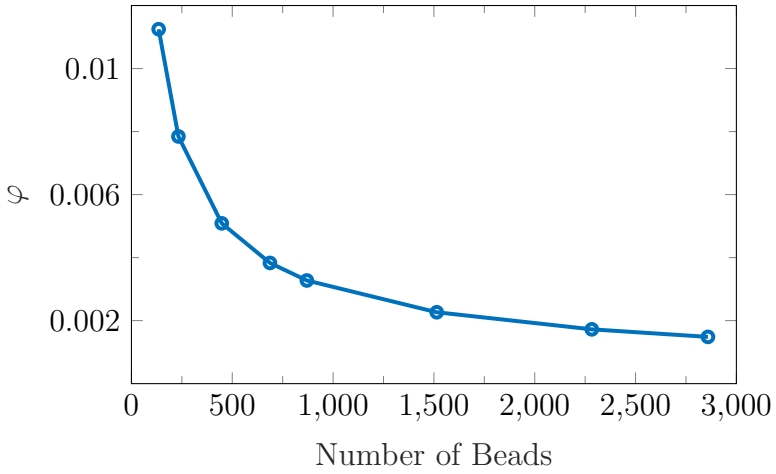

Figure 4.7: According to temporal and spatial resolution studies, we determine the number of beads and time step size in our system.

lower computational cost.

In our method, the permeability of the system is a function of the porosity and corresponding bead radius. Consequently, as the number of beads changes, the permeability of the system also alters. This is important because, during the spatial resolution study, the corresponding physical problem setup may also change slightly. Since the deviation parameter φ is a function of ζ, changes in permeability would affect the terminal speed. In figure 4.7c, φ versus N_b is presented. Because permeability has a negative correlation with the number of beads, the deviation parameter decreases as the spatial resolution

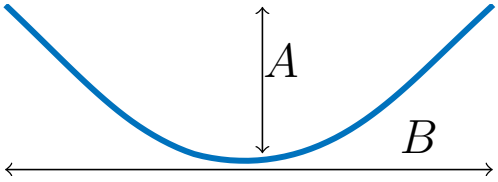

Figure 4.8: Filaments may buckle into a "U" shape. While A represents the distance between minimum and maximum points in the $z-$axis, the horizontal distance between tips is defined as B.

increases. On the other hand, for high-resolution cases, φ does not change significantly. This can be interpreted as for low spatial resolution, the number of beads may impact the problem setup up to a threshold value. After $N_b = 1514$, the number of beads only affects the accuracy but not the physical representation of the problem. With this conclusion, we finish this validation case. In the next sections, we will use our numerical technique for modelling filaments.

4.4.2 Sedimentation of Nonporous Deformable Filaments

In this section, we examine our framework for the sedimentation problem of deformable but nonporous filaments. Although we use a sedimentation force, depending on the length scale, the exerted force can be considered as any conservative force perpendicular to the long axis of the filament, such as magnetic attraction. During sedimentation, the filament or "slender body" may deform, which is coupled with the surrounding flow field. Therefore, the filament does not reach terminal velocity immediately. However, at some point, it should become stable with a fixed shape and speed.

The dynamics of this problem is governed by the elastogravitational number, $\mathcal{G}$. The elastogravitational number is defined as the ratio of gravitational forces to elastic forces and is given as:

$$\mathcal{G} = \frac{\rho g L^3}{EI} \tag{4.45}$$

where ρ is the effective mass per unit length and L is the length of the filament.

In our setup, we use a nonporous circular filament with a radius of $r = 1\,\mu\text{m}$ and an

aspect ratio of $L/r = 100$. Typically, the method of regularised stokeslets for simulating filament dynamics places one bead along the centreline of the filament. However, in this case, we consider filaments with finite thickness. Therefore, the cross-section of the filament consists of multiple beads forming a spring network, rather than a single bead. It should be noted that, due to nature of our model, there will be some pores between beads even in the $\phi = 0$ case. Therefore, a nonporous filament is an approximation used for comparing the qualitative behaviour of the filaments.

In our simulations, the nonporous filament consists of $N_b = 1548$. The long axis of the filament is aligned on the $x-$axis. The bending modulus is selected to match the elastogravitational number in equation 4.45. Once the bending modulus is found, the spring stiffness is calculated by bending the filament into an arc with a fixed curvature of $\kappa = \frac{1}{2L}$.

Our simulations investigate a range of elastogravitational numbers changing between $\mathcal{G} = 10 - 7000$. As a general trend, once filaments reach their terminal velocity, they form a "U" shape (see figure 4.8). This shape occurs due to stronger hydrodynamic interactions at the middle of the filament compared to tips, as resistive force theory approximately suggested (65).

To understand how vertical distance between the minimum and maximum points and the horizontal distance change, we normalise A and B with respect to filament length throughout the simulations for $\mathcal{G} = 600$ and 1000. In figure 4.9a, we quantitatively demonstrate that as $\mathcal{G}$ increases, the tips of the filament becomes closer to each other, and the filament creates a narrow and tall U shape. This transition of parameters A and B, depending on the elastogravitational number, shows good qualitative agreement with the previous study by Li et al. (107), in which the authors used a slender body theory based continuum approach. Additionally, for larger values of $\mathcal{G}$, the filaments reach steady state in a shorter time with a higher sedimentation speed. Figure 4.9b depicts a slight decrease in sedimentation speed for $\mathcal{G} = 1000$, where the $y-$axis is normalised with respect to a speed equal to the filament length per second.

(a) Elastogravitational number controls the deformation.

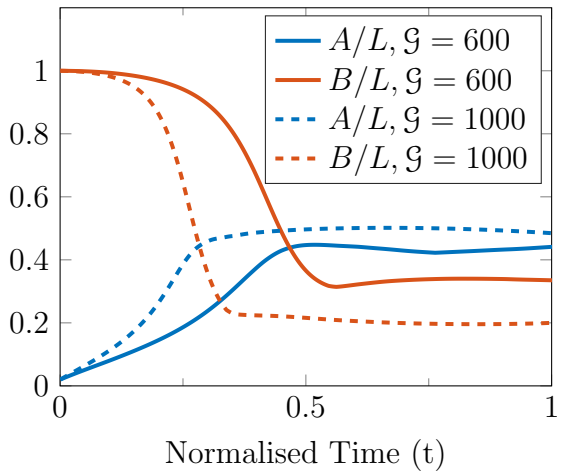

(b) As elastogravitational number increases, sedimentation speed increases.

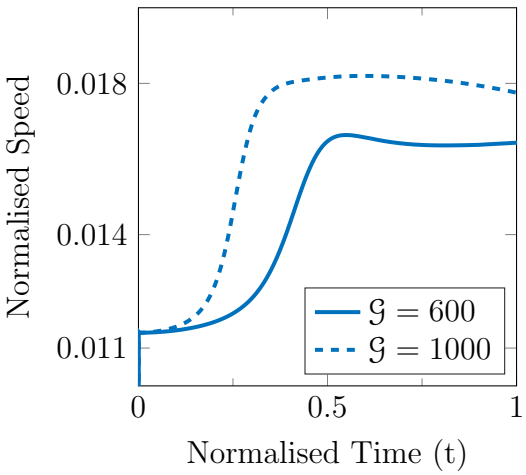

Figure 4.9: Properties of sedimentation are compared for different elastogravitational numbers. As $\mathcal{G}$ increases, the U shape of the filament becomes narrower and more pronounced. In panel (b), the sedimentation speed is normalised according to the body length per second.

In figure 4.10a, we capture the trajectory of the filament with $\mathcal{G} = 1000$ for $t > 0.5$. As it can be seen, the filament initially drifts away from the $x = 0.5L$ line. Later, it starts to come towards the centre. This behaviour happens because of an out-of-plane deformation of the filament which may due to finite thickness of the filament (see figure 4.10b). The asymmetric shape changes the drag on the filament, hence, slower sedimentation. This kind of zigzag motion pattern was reported in the previous study of Hall-McNair et al. (66), in which the authors incorporated the method of regularised stokeslets with boundary integrals formulated by the tangent angle along the centreline of the filament.

It should be noted that although there is no experimental evidence, several numerical and theoretical studies (29) suggest a metastable "W" shape for high values of $\mathcal{G}$. The limits of this regime depend on the theoretical model, with $\mathcal{G} > 3500$ in the work of Hall-McNair et al. (66) and $\mathcal{G} > 5000$ in the study by Marchetti et al. (120). In our study, we test different elastogravitational numbers up to $\mathcal{G} = 7000$. However, such deformations are not observed in our simulations, which may be attributed to the finite thickness of

(a) The filament trajectory is centred on the initial centre of mass.

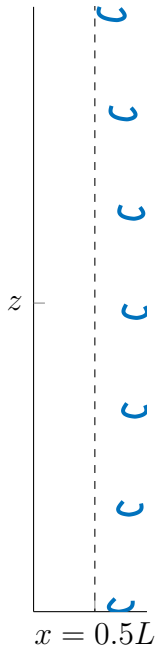

(b) An out-of-plane deformation is captured for $\mathcal{G} = 1000$.

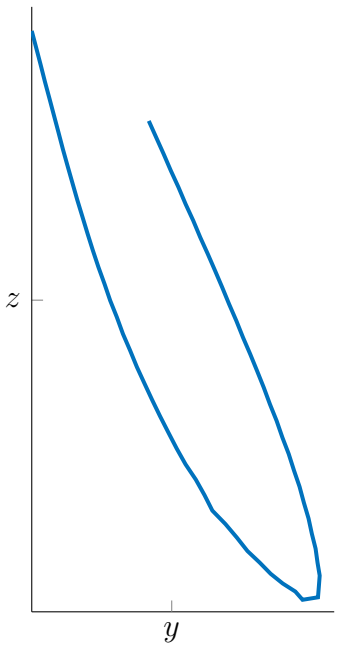

Figure 4.10: For $\mathcal{G} = 1000$, the filament drifts away from the initial centre of mass, and also deform out-of-plane.

our filaments. In conclusion, this section demonstrated the validity of our numerical algorithm for handling hydrodynamic problems coupled with elastic deformations. With this established, we can use our method to explore interesting dynamics.

4.5 Sedimentation of Porous Deformable Filaments

So far, our methodology has been tested with porous non-deformable and nonporous deformable materials. We now apply this technique to describe the sedimentation of porous and deformable filaments. To the best of our knowledge, the sedimentation of poroelastic filaments remains understudied, and we aim to address this gap. While some studies have analysed flow through porous media composed of fibres, attention to an individual permeable filament is lacking.

Compared to the original problem, the presence of pores may have two important

impacts on the physics. Firstly, it can be ambiguous in determining the elastogravitational number. Normally, the effective mass density per length for a circular filament is defined as:

$$\rho = (\rho_s - \rho_f)\pi r^2. \tag{4.46}$$

Equation 4.46 ensures that each bead has the same solid density ρ_s. However, for a porous material, using the above equation would result in a smaller force per bead due to the smaller bead volume in equation 4.24. Conversely, exerting the same force per bead implies a higher effective mass density, hence, a larger $\mathcal{G}$ according to its traditional definition.

The second effect pertains to how porosity changes the flow inside the filament. Previously, we demonstrated that flow inside a porous sphere is negligible. However, in the case of filament, geometrically non-linear deformations may be coupled with porosity. To detect the importance of both factors, we start our simulations.

We use the identical filament described in 4.4.2 with a porosity value of $\phi = 0.9$. To address the aforementioned issues, we have two sets of simulations with $\mathcal{G} = 600$ and 1000. In the first set, $\mathcal{G}$ is determined by inserting equation 4.46 into equation 4.45. Therefore, porosity only changes the radius of the bead and the corresponding regularisation width. In the second set, we match the effective mass per length with that of a nonporous filament.

In figures 4.11a and 4.11b, horizontal and vertical distances are estimated for these two sets. For the first set of simulations, there is no considerable deformation. The filaments mostly preserve their straight shape and sediment without negligible deformation at the tips. On the other, when we match the effective mass density per bead, the filaments deform in a similar fashion to nonporous filaments for $\mathcal{G} = 600$ and 1000.

When comparing sedimentation speeds for these cases, the results reveal a significant difference between each case (see figure 4.12). Terminal speeds in the second set are approximately 20 times faster than those of the first set. Moreover, these speeds surpass even the nonporous cases provided in figure 4.9. Additionally, there is a trend of subtle

(a) Two sets are compared for $\mathcal{G} = 600$.

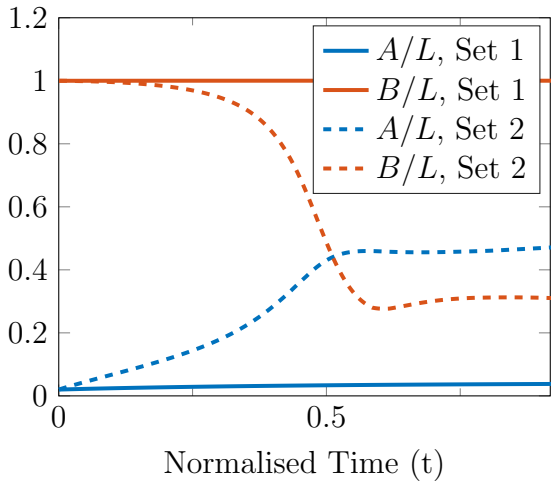

(b) Two sets are compared for $\mathcal{G} = 1000$.

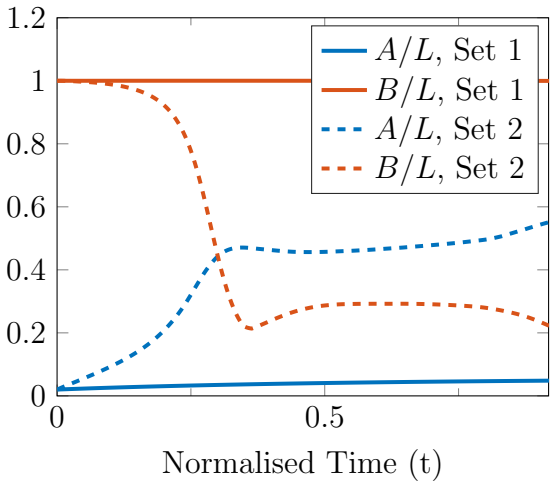

Figure 4.11: Deflection parameters are presented $\mathcal{G} = 600$ and $\mathcal{G} = 1000$, each calculated using different elastogravitational number definitions.

decrease in terminal speed once it reaches the maximum value. This little "hump" is more apparent in figure 4.9b), just before $t = 0.5$. The decline in speed implies more rotation of the filament in all three planes. In addition to rotation, the tips of the filament slightly open up as the filament relaxes.

This behaviour becomes more dramatic as $\mathcal{G}$ increases. In figure 4.13a, terminal speeds of a nonporous filament and the second set are plotted for $\mathcal{G} = 3000$. For the nonporous filament, there are some fluctuations in the speed; however, the filament settles steadily after $t > 0.5$. Even though the filament leans to one side as a whole, this does not disrupt the U shape. In the same figure, the dashed line shows the speed of the porous filament from the second set. Sedimentation occurs in an unstable form, causing fluctuations in speed. This is due to the extreme shapes of the filament. In figures 4.13b and c, the centreline of the porous filament is presented for $t = 0.9$ and $t = 1$ respectively. The filament bends into an asymmetric shape reminiscent of a hook. This shape initially occurs in the $yz-$plane with a minimum point close to the distal edge. Over time, the minimum point turns into a minimum section, therefore, the deflection spreads into the $xy-$plane. Consequently, the filament unzips itself.

(a) Two sets are compared for $\mathcal{G} = 600$.

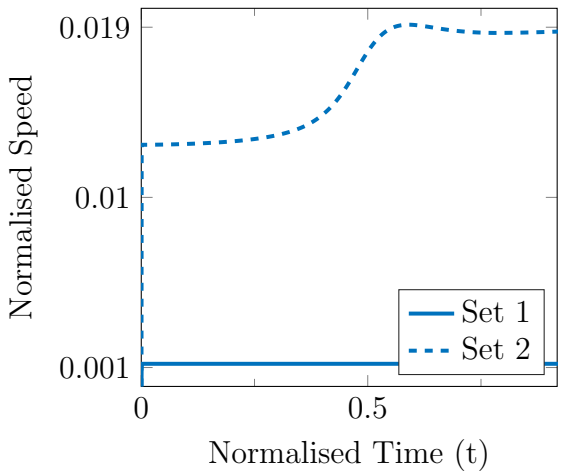

(b) Two sets are compared for $\mathcal{G} = 1000$.

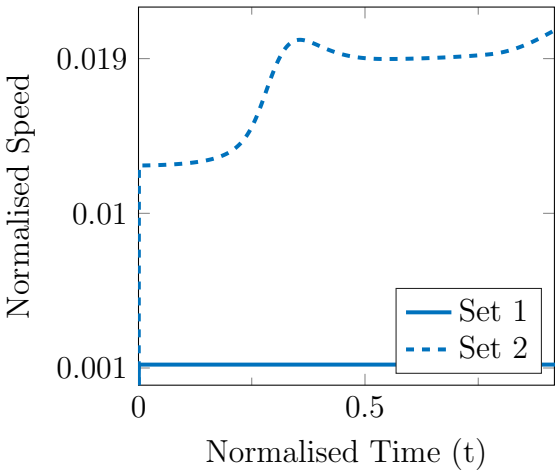

Figure 4.12: Sedimentation speeds of two sets are compared for $\mathcal{G} = 600$ and $\mathcal{G} = 1000$. The $y-$axis is normalised according to a speed of body length per second.

We can summarise the findings of this section as follows: for porous materials, the original elastogravitational number results in considerably slower sedimentation. Thus, it may be necessary to reconsider the definition of $\mathcal{G}$ or introduce a new dimensionless group. When the mass per bead is matched, the results are similar to those of nonporous filaments, and the effects of porosity become more pronounced. We observe that for the same effective mass, porous filaments tend to become more unstable. This is due to higher sedimentation velocities and possibly additional flows passing through pores. It is worth mentioning that having faster sedimentation agrees with the results of nondeformable porous sphere simulations in section 4.4.1. With these insights, our Methodology chapter ends. In the next chapter, we will investigate the dynamics of hydrogel-based active filaments by using our numerical method.

(a) The sedimentation speeds are compared. (b) $t = 0.9$. (c) $t = 1$.

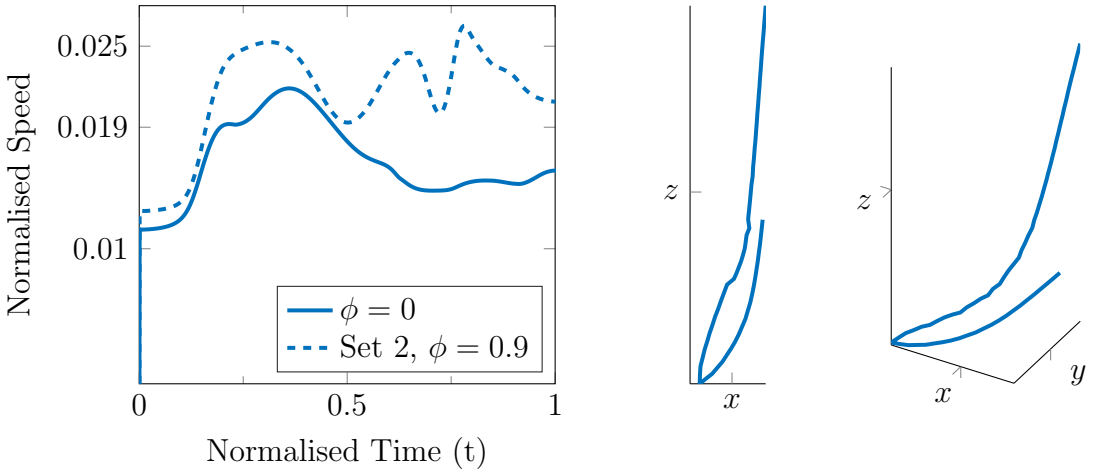

Figure 4.13: In panel (a), the comparison of sedimentation speeds for nonporous filament and the second set with $\phi = 0.9$ are given for $\mathcal{G} = 3000$. Panels (b) and (c) show the shapes of the porous filament at different time steps.

CHAPTER 5

DYNAMICS OF ACTIVE POROELASTIC FILAMENTS

In this chapter, we employ the developed methodology to simulate the dynamics of active Janus and Saturn filaments (see figure 5.1). The focus of this chapter is on the impact of non-conservative tip forces on the mobility of the filaments. In the realm of soft active particles, this problem serves as a model for understanding the motion of bubble-driven or phoretic hydrogel-based filaments. Consequently, the flexible filament can be conceptualised as a chain of beads attached to an active element at the tip. From a mathematical perspective, this is a "follower force" problem which essentially exerts a tangential force with a fixed magnitude to the tip of a filament or rod (70). It differs from classical "Euler" buckling instability since the direction of force changes according to the shape of the filament.

We will investigate the follower force problems in three different setups, in the following order: a clamped filament with one tip force (5.1), a free filament with a single tip force (5.2), and a free filament with two tip forces (5.3). While the first numerical test serves as a comparison with the literature (18), the following cases are methods for achieving dynamic shape transformations that may play a significant role in controlling flexible artificial microbots.

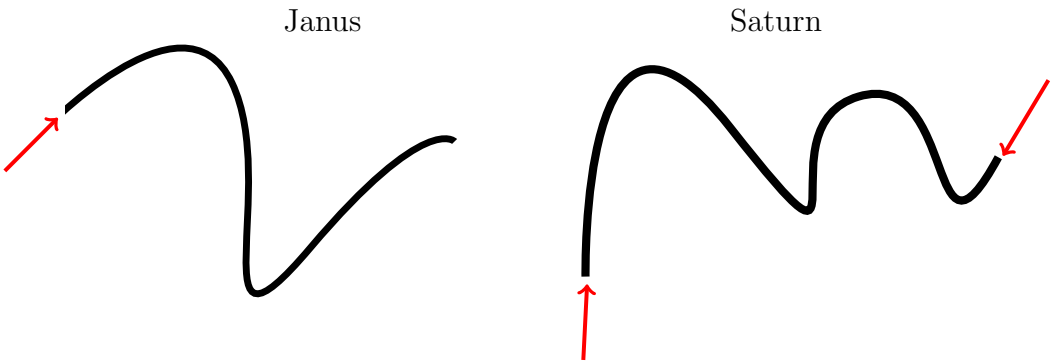

Figure 5.1: A flexible filament may deform under non-conservative end forces, as demonstrated by the red arrows. The filament under the influence of a single tip force is named Janus, while the Saturn filament experiences forces at both tips.

5.1 Clamped Filaments

Although the number of experimental studies is limited due to the challenging nature of the problem setup, the follower force problems have been examined in a number of studies, both theoretically and numerically. Previously, Canio et al. (18) modelled cytoplasmic streaming as a filament that is pinned at one end and exposed to a point force at the other end. The dynamics of the follower force problem were governed by a dimensionless parameter that was given as:

$$\sigma \equiv \frac{\Gamma L^2}{EI} \tag{5.1}$$

where $\Gamma > 0$ is the magnitude of the compressive end force. For the rest of this chapter, we will use σ for describing our problems.

In the study of Canio et al. (18), initially straight filaments were exposed to a small perturbation. Following this, a follower force was continuously exerted to observe the behaviour perturbation. According to the value of σ, filaments exhibited three different behaviours. These regimes are monotonic straightening, straightening with decaying oscillations, and growing perturbations that leading to periodic oscillations. It should be noted that in Canio et al. (18), the motion of the filaments was restricted to the $z = 0$

plane, and also the filaments had infinitesimal thickness. These factors reduce the problem to 2 dimensions.

We replicate the above problem to gain insights into our method and also validate the technique in a different setup. This comparison is essential for detecting the limits of σ in our numerical model and for assessing the impact of the finite thickness of the filaments. In our simulations, we use a filament with a circular cross section of radius r. The filament has a unit length and an aspect ratio of $L/r = 100$. By assigning the bending modulus to $EI = 1$, we ensure that $\sigma = \Gamma$. To calculate the spring constant, the filament is bent in an arc with constant curvature, $\kappa = 1/2L$. Since the study of Canio et al. (18) considered biological fluids, the viscosity was $\mu = 1\,\mathrm{Pa\,s}$, and the same value is also used in our simulations.

From a numerical standpoint, our base code needs updating for boundary conditions. The nodes at $x = 0$ are identified as the clamped end. The clamped boundary condition implies the following:

$$\boldsymbol{u}\,|_{x=0} = 0. \tag{5.2}$$

In addition to this, to account for the follower nature of the force, we need to calculate the surface normal at the other tip, $x = L$. By assuming that there is no deformation at the force tip, we can calculate the normal vector as the cross product of two vectors on the plane. For this purpose, we determine the coordinates of 3 beads out of a total of N_{tip} beads at $x = L$. Then, the unit normal vector for the plane can be expressed as:

$$\mathbf{N} = \frac{\boldsymbol{r}_{12} \times \boldsymbol{r}_{13}}{||\boldsymbol{r}_{12} \times \boldsymbol{r}_{13}||} \tag{5.3}$$

where numbers in the subscript indicate the direction of the vector. Once the normal vector is determined, the follower force is evenly distributed on each bead at the tip as $\boldsymbol{f}_{tip} = \frac{\Gamma}{N_{tip}}\mathbf{N}$. Consequently, our semi-implicit algorithm provided in equation 4.34 is

updated as:

$$\frac{\boldsymbol{x}_a^{n+1} - \boldsymbol{x}_a^n}{\Delta t} = \frac{1}{8\pi\mu} \sum_{b=1}^{N_b} \boldsymbol{S}^{\epsilon}(\boldsymbol{x}_a, \boldsymbol{x}_b)^n \left(\frac{\Gamma}{N_{tip}} \mathbf{N}^n + \sum_{c=1}^{N_c, b} k \left(\boldsymbol{x}_c^{n+1} - \boldsymbol{x}_b^{n+1} - L_{bc} \boldsymbol{e}_{r_{bc}}^n \right) \right) \tag{5.4}$$

where the first term at the RHS, considering the external force, is only applied to the beads on the tip.

Then, we introduce a small perturbation to the filament. From a numerical perspective, we employ filaments with $N_b = 1548$, and $\phi = 0.9$. Given that the dynamics vary in speed according to σ, each simulation is run for as long as needed.

Similar to the study that we stem from, we observe three phases. For $\sigma < 7.5$, the filament monotonically moves to the horizontal position (see figure 5.2a). In the range between $7.5 < \sigma < 15$, oscillations begin to appear but decay back to the straight configuration. Initially, the filament passes through the horizontally straight position and goes vertically. Subsequently, at each oscillation the tip becomes closer to $y = 0$. An important aspect of this regime is the number of oscillations and maximum tip position. As it can be seen in figure 5.2b, there is a positive correlation between the number of oscillations and σ. This trend is accompanied by an increase in the maximum tip position along the $y-$axis. These changes in dynamics result in a longer period for the filament to reach a steady state.

As we apply larger forces, the transition to the third regime occurs. The primary characteristic of this regime is the oscillation of the filament. In figure 5.3, the $y-$positions of active tips are shown for $\sigma = 15,\ 17,\ 20,$ and 25. For each value, a small initial perturbation amplifies, leading to periodic oscillations. The filament does not stop at the horizontal position but continues moving. While the oscillations in $\sigma = 15$ and 25 have constant amplitude, irregularities can be captured for intermediate values. This is due to the trajectory of the filament.

In figure 5.4, we track the centreline of the filament for $\sigma = 15$. The dots in the figure represent beads passing through the centreline. The initial position of the filament

(a) Monotonic decay is given for $\sigma = 5$.

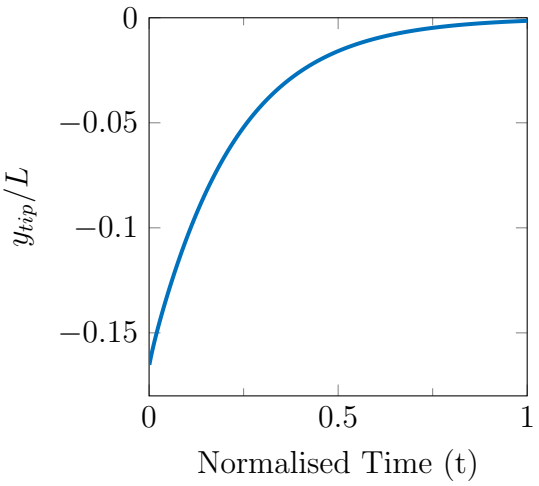

(b) Oscillatory decay is shown.

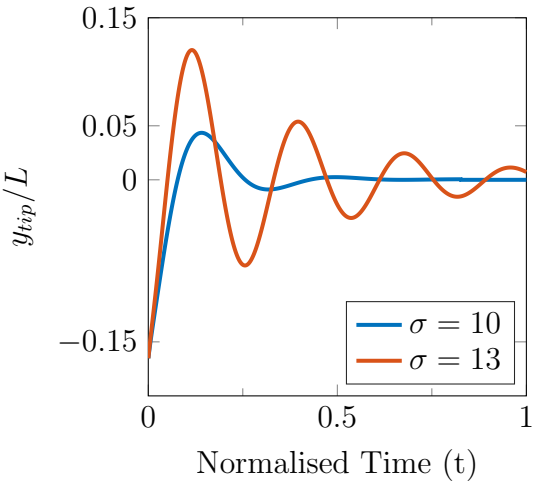

Figure 5.2: The ratio of follower force to bending resistance is denoted by σ. As σ increases, decay dynamics change. In both panels, the $y-$axis plots the position of the active tip, which is normalised with respect to the length of the filament.

is given by cyan colour, and as it moves, the colour shifts towards magenta. Following a growth phase, the tip moves vertically up and down in the $xy-$plane, which we can refer to as side-to-side bending. This result is consistent with the literature (18; 103).

On the other hand, as the exerted force increases, the whirling motion becomes more apparent, and we can capture the actual 3D dynamics. Figure 5.5 displays the trajectory of the filament for $\sigma = 20$. The early phases of the motion are similar to those of $\sigma = 15$, with oscillations in the $xy-$plane. However, after that the filament starts to translate out-of-plane. It rotates around the fixed end with a constant radius, creating the circular trajectory visible in figure 5.5. For larger values of force, i.e., $\sigma = 25$, the angle between the $xy-$plane and the plane where the circular path is followed shifts. Meanwhile, the amplitude of oscillations remains unchanged. This trend indicates an increase in the curvature towards the fixed end.

Previously, similar patterns were observed in the numerical work of Laskar and Adhikari (103). In the same study, a chain of passive beads was activated by an active bead at its terminus, serving as a theoretical actuation mechanism at the microscale. The study

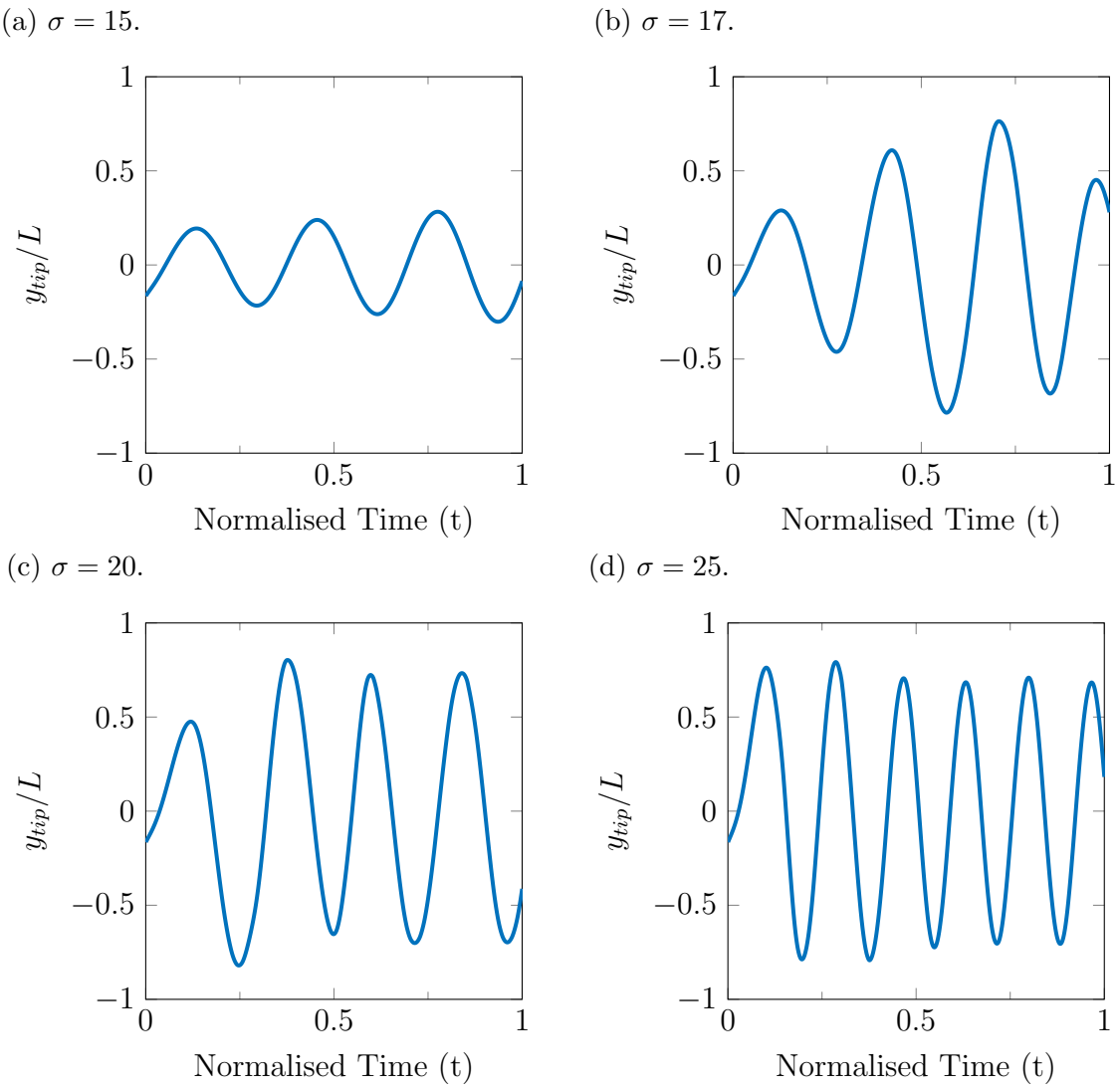

Figure 5.3: The oscillations in the third regime are captured for different σ values.

suggested another regime after the whirling motion, which is a windscreen wipers-like planar motion. However, we do not capture this behaviour. In our study, the dimensionless parameter is restricted to $\sigma < 30$. Consequently, the range of distinct phases is smaller compared to the previous studies. There could be multiple reasons for the differences between our study and the results of Canio et al. (18) and Laskar and Adhikari (103).

In Chapter 4, we demonstrated the need for modifying the definition of elastogravitational number for porous filaments. Similarly, one may suggest the same here. The tendency of porous filaments to become unstable may narrow the working range for σ. Another possible reason for slightly different dynamics is the finite thickness of our fila-

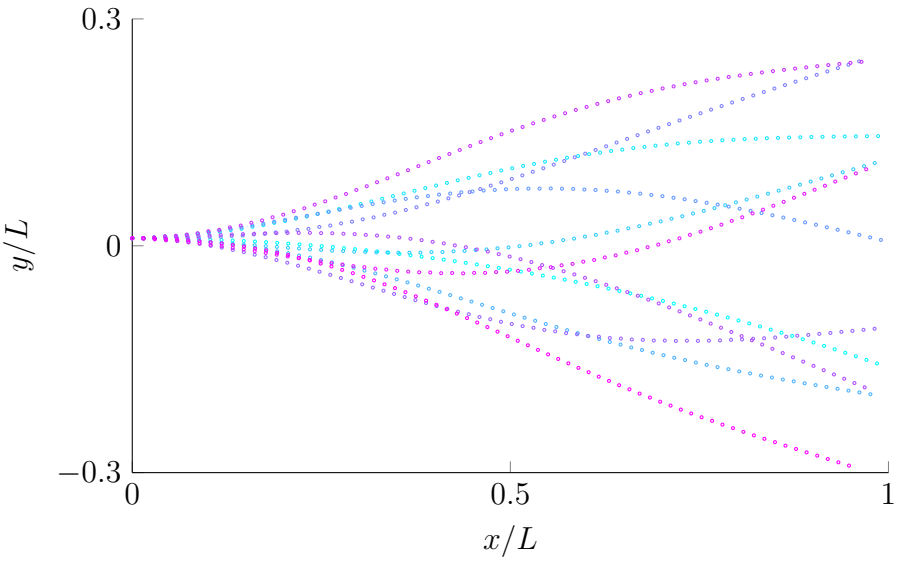

Figure 5.4: For $\sigma = 15$, the centreline of the filament is followed, and the motion remains planar. The transition from cyan to magenta colour is synced with the filament's position over time. The figure is viewed in the $xy-$plane.

ments, which was ignored in both comparison studies. In our study, the filament thickness is correlated with the bead radius and, consequently, the surface area. However, we apply force to each bead as a point force rather than distributing it over the bead surface. This may also lower the upper bounds for the regimes in our study. Additionally, and more importantly, the finite thickness of the filaments in our simulations impacts the non-local hydrodynamic contributions due to the method of regularised stokeslets, leading to different dynamics.

Now, we are motivated to extend this follower force problem to the different boundary conditions. In section 5.2, the fixed boundary condition is replaced with a free end, allowing the filament to translate. Since the filament has only one active tip, it will be referred to as a Janus filament for the rest of this thesis. After exploring the motion of Janus filaments under different values of σ, non-conservative end forces are exerted on both ends in section 5.3. The filaments with two active tips are named Saturn. To the best of our knowledge, exerting end forces at both tips is a new problem setup and will shed light on a gap in the literature.

(a) Planar trajectory occurs between $t = 0$ to $t = 0.2$.

(b) Between $t = 0.2$ and $t = 0.4$, out-of-plane deformation begins.

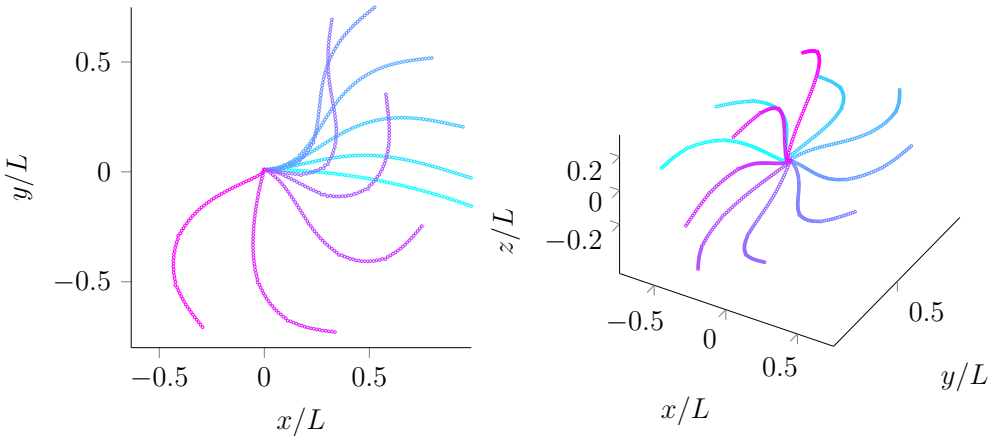

(c) After $t = 0.4$, filament rotates around a fix point.

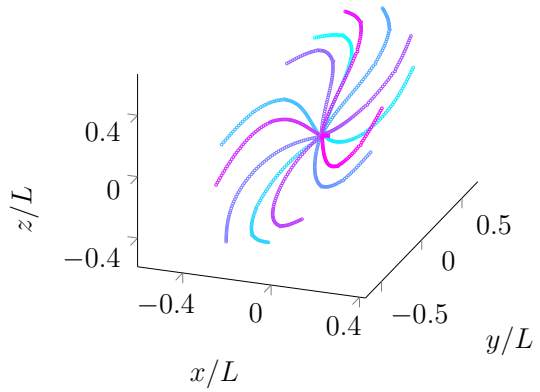

Figure 5.5: For $\sigma = 20$, the centreline of the filament is tracked. In each figure, cyan colour indicates the initial position, which is identical to the magenta coloured final position in the previous figure.

5.2 Active Janus Filaments

For active Janus filaments, we utilise a filament with $L = 10\,\mu\text{m}$ and $L/r = 100$. In all cases, the filament has a porosity of $\phi = 0.9$ and is positioned between $x = 0$ and $x = L$ as a straight line. The follower force is exerted at the $x = L$ end, and initially, the inward normal equals $\mathbf{N} = [-1, 0, 0]$. The filament has $N_b = 1548$, and the spring stiffness is calculated for bending the filament into an arc with $\kappa = 1/2L$. The bending modulus is determined as $E = 10\,\text{kPa}$, which is consistent with PNIPAM. For the viscosity of the ambient fluid, $\mu = 0.001\,\text{Pa}\,\text{s}$ is used.

(a) The filament follows a straight path.

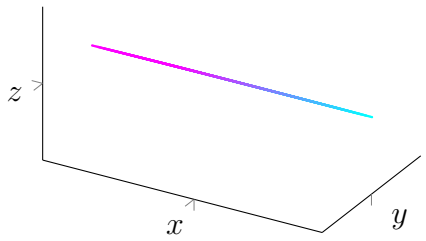

(b) The speed converges to steady state after 30 iterations.

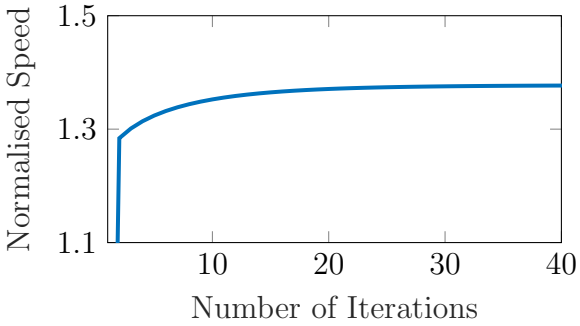

Figure 5.6: For $\sigma = 30$, the filament translates along a straight trajectory. The convergence to the fixed translation speed takes 30 iterations.

In Janus pusher filaments, 2 main characteristics are observed; pure translation and translation with oscillatory motion. Pure translation is captured for $\sigma < 90$, which is a relatively large range compared to the fixed boundary condition. In this regime, the filament exhibits no deformation and translates as a straight rod. Consequently, the filament moves in a straight trajectory (see figure 5.6a). Since there is no deflection in the geometry, the filament should move at a constant speed in a fixed direction. In our simulations, after 30 iterations, the solution converges to a constant translation speed. In figure 5.6b, the translation speed is normalised with a speed corresponding to a filament length per second.

In the second regime, where $\sigma > 90$, the filament performs both translation and deformation. The motion begins with an initial translation whose duration depends on σ. Similar to the first regime, the centre of mass of the filament follows a straight path. Subsequent to this pure translation period, the filament starts to deform and buckle. The deflection of the filament grows over time. This is followed by the deformation of the filament in the $xy-$plane initiated by the active tip. The deflection propagates as a wave towards the free end and buckles the filament in an asymmetric 1^{st} bending mode. Figures 5.7 and 5.8 show that the periodic oscillations of the filament in $\sigma = 100$ and $\sigma = 130$ are accompanied by translation.

(a) The trajectory of the filament is illustrated.

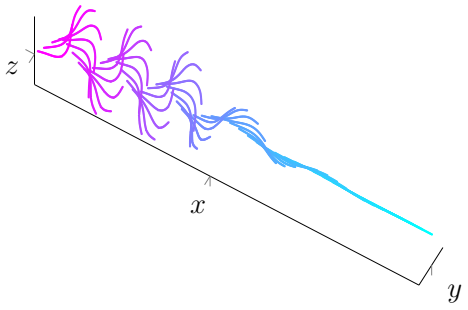

(b) Time versus distance from the initial position is plotted.

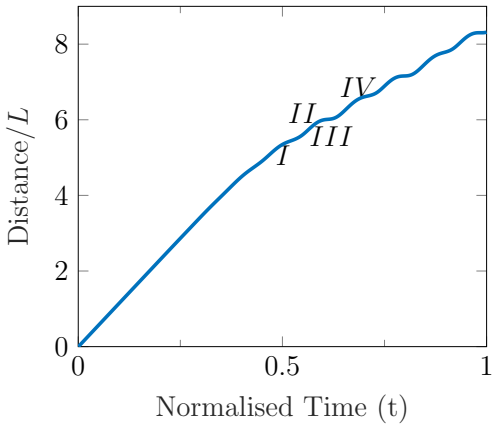

(c) Shapes of the filament are depicted.

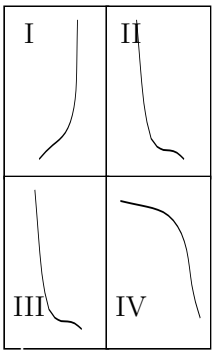

(d) The curvature values of the filament are shown as a heatmap.

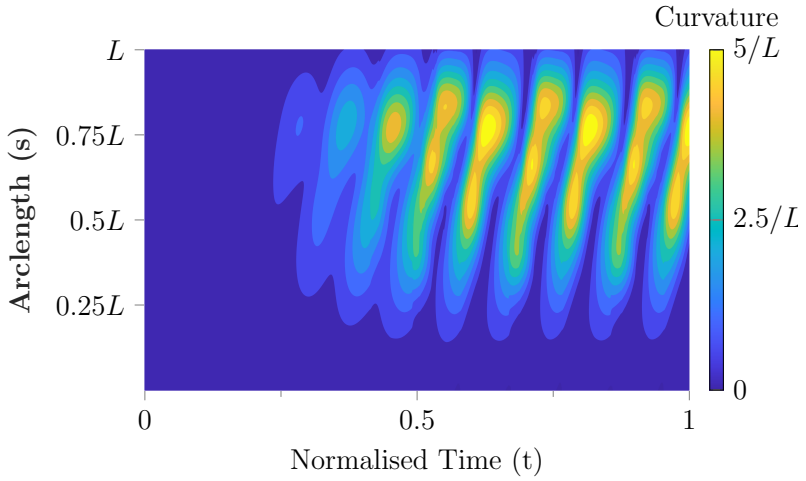

Figure 5.7: For $\sigma = 100$, the Janus filament moves with side-to-side bending. In panel (a), the cyan-to-magenta transition represents the evolution of the filament's trajectory from from its initial to final position. The time points marked in panel (b) correspond to the filament shapes shown in panel (c).

It is observed that the speed of the centre of mass decreases after the initial pure translation phase. The exerted force is converted into both elastic energy through deflection and kinetic energy due to translation.

Although the general characteristics of $\sigma = 100$ and $\sigma = 130$ are similar, they differ in the dynamics of oscillations.

(a) The trajectory of the filament is illustrated.

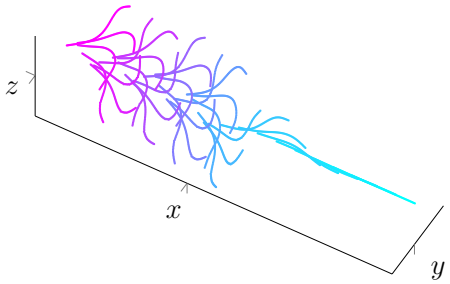

(b) Time versus distance from the initial position is plotted.

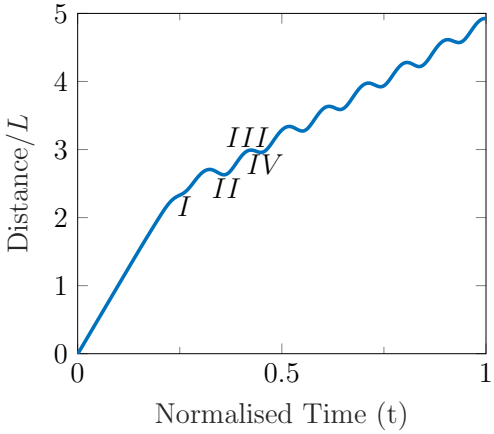

(c) Shapes of the filament are depicted.

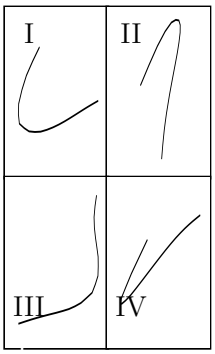

(d) The curvature values of the filament are shown as a heatmap.

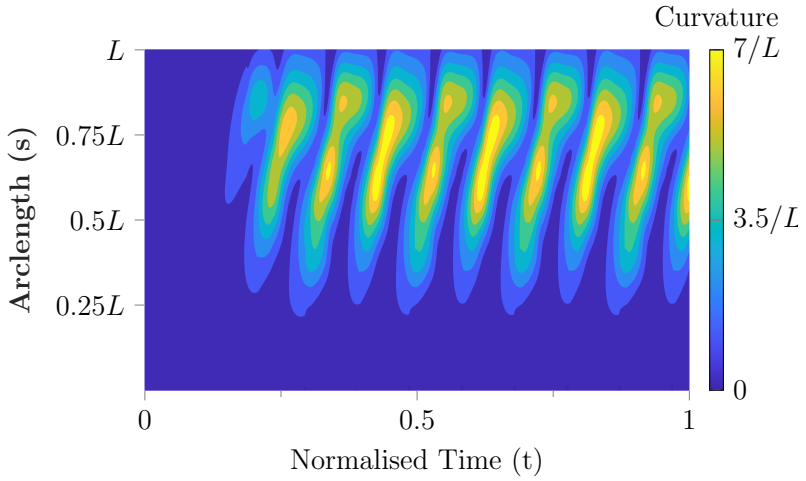

Figure 5.8: For $\sigma = 130$, the filament moves in a corkscrew-like motion. In panel (a), the cyan-to-magenta transition represents the evolution of the filament's trajectory from from its initial to final position. The time points marked in panel (b) correspond to the filament shapes shown in panel (c).

Due to the larger exerted force, the duration of the initial translation is shorter for $\sigma = 130$. Similarly, the frequency of the oscillations for $\sigma = 130$ is higher than $\sigma = 100$. This trend is accompanied by larger curvature values, implying more buckling (see figures 5.7d and 5.8d).

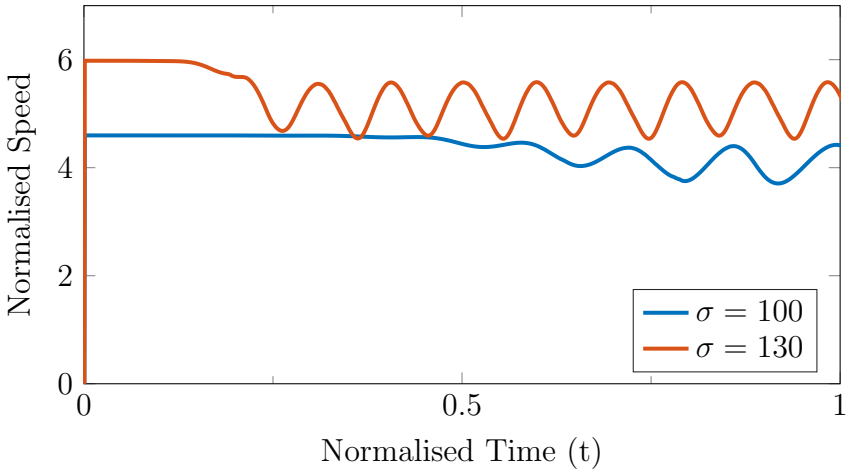

Figure 5.9: For $\sigma = 100$ and 130, the speeds of centre of masses are compared, and the $y-$axis is normalised respect to the body length per second. It should be noted that originally the $\sigma = 100$ case run longer. However, for this figure, a section that matches the time frame of the $\sigma = 130$ case is presented.

The curvature, κ values in these figures are calculated using the Frenet-Serret formulation for arclength (s). In addition, to obtain a smooth visualisation of curvature and torsion values, a post-processing tool is developed in MATLAB®. Due to the unstructured nature of our bead-spring network, the beads are not positioned along the geometrical centreline of the filament. Therefore, we require to numerically extract the geometrical quantities. Consequently, we design this in-house computational algorithm to provide quantitative insight into the deflection of filaments and flagella, as detailed in the Appendix B.

This change in deformation affects the trajectory of the filament. For smaller values of σ, the Janus filament moves side-to-side, reminiscent of in-plane deformations observed in the eukaryotic flagellum (see figure 5.7a). On the other hand, as σ increases, the filament periodically deflects in circular patterns and exhibits a whirlingcorkscrew motion, akin to oscillations of the prokaryotic flagellum (see figure 5.8a). In circular motion, the active tip covers a larger distance. However, due to larger speed, the period of oscillations becomes smaller as well (see figure 5.9).

An interesting common feature in both motions is the drift of the trajectory from a straight line. The asymmetric "U" shapes formed in figures 5.7c and 5.8c contribute to the drag anisotropy of the filaments. Consequently, Janus swimmers drift in the $xy-$plane. This kind of directional preference can be beneficial for developing biomedical tools in the microscale. What determines the direction of the drift is the initial buckling of the filament, which is intrinsically stochastic. However, the findings of this section are important to encourage investigation into the controlled buckling of these filaments. With these results, we complete our examination of Janus filaments. In the next section, we will exert follower forces on both tips.

5.3 Active Saturn Filaments

In this set of simulations, two follower forces are applied to each end of the filament. The magnitude of the forces is identical, and each of them is defined by σ. So, when σ is given for a set of simulations, it indicates the individual forces at the tips. The material properties and dimensions of the filaments are completely identical to the Janus filaments in the previous section.

As non-conservative forces are exerted onto Saturn filaments, five main regimes are observed: "pumping", "ballistic translation", "spiral trajectory", "run-and-tumble", and "tumble dominant run", sorted according to increasing σ. It should be noted that these regimes lack strict parameter boundaries *per se*. Instead, we observe a combination of behaviours, such as run-tumble-and-helical swimming, between the third and fourth regimes.

5.3.1 Stationary Pumping Filaments

For $\sigma < 30$, the follower forces do not overcome elastic forces. Therefore, no deformation or motion is observed. The filament preserves its straight shape and position between $x = 0$ and $x = L$. In addition, no torsion occurs as well. In this regard, stationary filaments can be considered as replicas of I-shaped microrods with double poles in Chapter 2.

(a) The trajectory of the filament is illustrated.

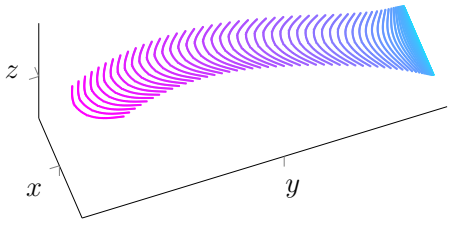

(b) Time versus distance from the initial position is plotted.

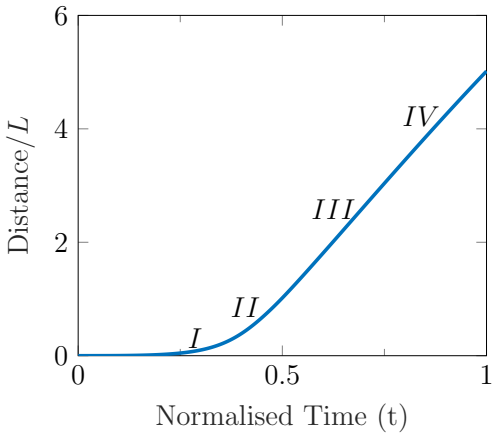

(c) Shapes of the filament are depicted.

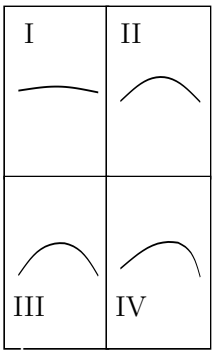

(d) The curvature values of the filament are shown as a heatmap.

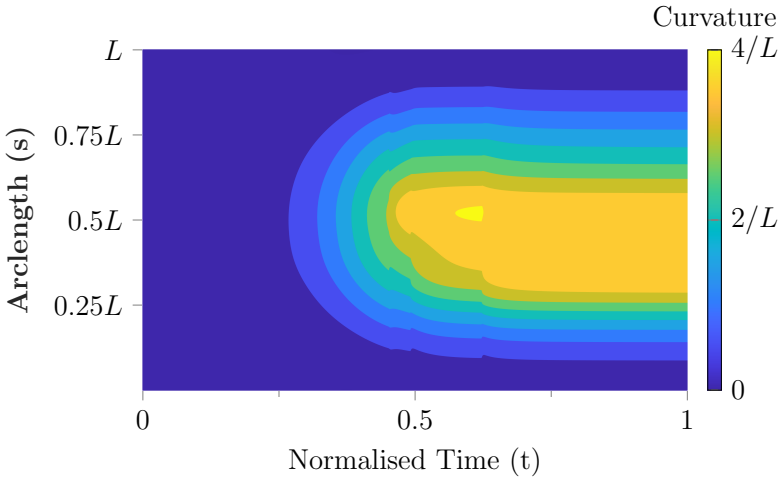

Figure 5.10: For $\sigma = 40$, Saturn filament buckles into a "U" shape and translates ballistically. In panel (a), the cyan-to-magenta transition represents the evolution of the filament's trajectory from from its initial to final position. The time points marked in panel (b) correspond to the filament shapes shown in panel (c).

However, in our simulations, forces are located completely symmetrically and are constant rather than stochastic, thus, no rotation or drift occurs.

5.3.2 Ballistic Motion

As σ increases, new dynamics begin to be observed. This regime is bounded between $30 < \sigma < 60$. Here, we present a case in this regime with $\sigma = 40$ (see figure 5.10). Initially, the filament stays in its original shape. After a while, $t \approx 0.25$, the filament deflects. The initial deformation occurs around the middle of the arclength. Over time, the magnitude of buckling increases, and the filament forms a U shape, representing the 1^{st} buckling mode. The magnitude of the exerted force determines the symmetry of the shape, hence, the trajectory.

In figure 5.10, the quantitative results are given for $\sigma = 40$. As can be seen in figure 5.10b, the filament translates ballistically. There is a minor asymmetry in the curvature values that leads to a small rotation in the $xy-$plane which can be neglected. Additionally, it is observed that the initial deflection of the filament occurs out-of-plane, as is intrinsic to any buckling problem. Since this 1^{st} buckling mode is not in the plane, the trajectory of the filament initially shows an elevation along the $z-$axis. However, over time this elevation diminishes, and the filament moves within a constant plane.

5.3.3 Spiral Trajectory

For $60 < \sigma < 100$ values, the characteristics of ballistic regime alter. In figure 5.11a, the spiral trajectory of the filament is presented for $\sigma = 70$. After translating in a straight path, the rotation begins and directs the path of the filament. In figure 5.11d, following the initial deflection, the filament begins to relax around $t \approx 0.125$. As a result of this relaxation phase, the filament reaches a steady state with an asymmetric U shape. It should be noted that the curvature values are also considerably larger than in the $\sigma = 40$ case. In terms of displacement, a bell-like shape is depicted in figure 5.11b. Following this, periodic rotation starts again.

(a) The trajectory of the filament is illustrated.

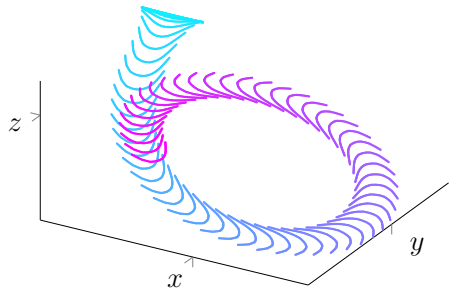

(b) Time versus distance from the initial position is plotted.

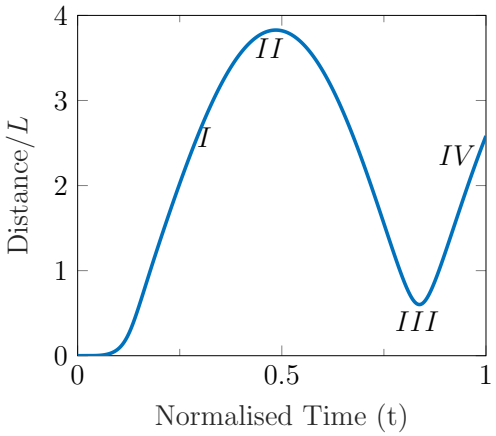

(c) Shapes of the filament are depicted.

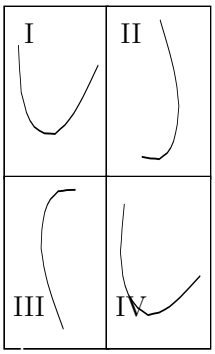

(d) The curvature values of the filament are shown as a heatmap.

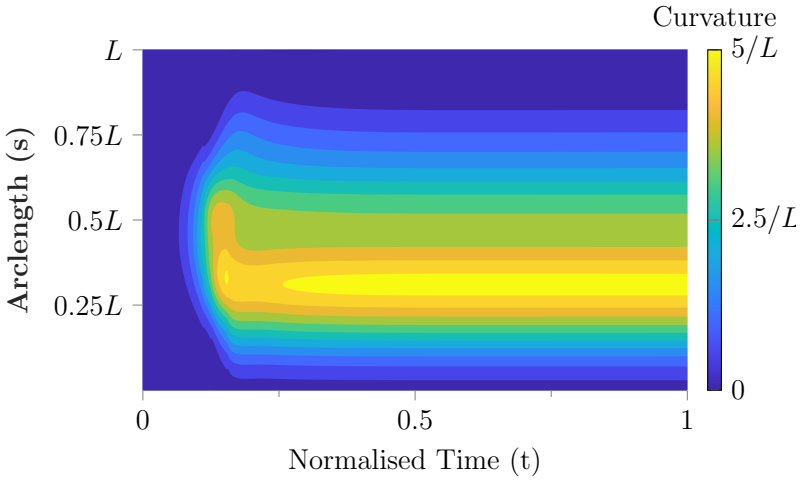

Figure 5.11: For $\sigma = 70$, Saturn filament rotates in a spiral trajectory. In panel (a), the cyan-to-magenta transition represents the evolution of the filament's trajectory from from its initial to final position. The time points marked in panel (b) correspond to the filament shapes shown in panel (c).

5.3.4 Run-and-Tumble

The fourth regime, between $100 < \sigma < 125$, consists of two phases: run and tumble, resembling the bacterial swimming pattern. In natural run-and-tumble motion, a bacterium translates in a certain direction with flagellated propulsion, which is known as

(a) The trajectory of the filament is illustrated.

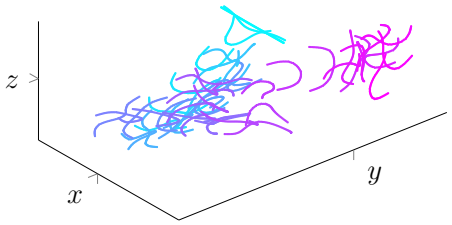

(b) Time versus distance from the initial position is plotted.

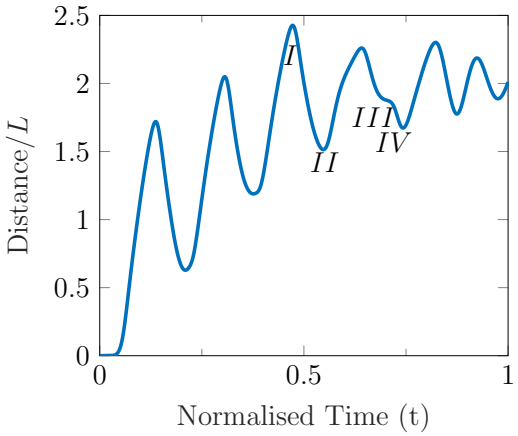

(c) Shapes of the filament are depicted.

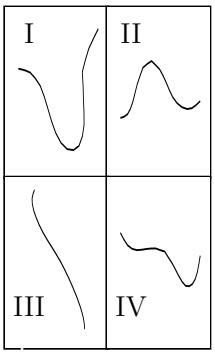

(d) The curvature values of the filament are shown as a heatmap.

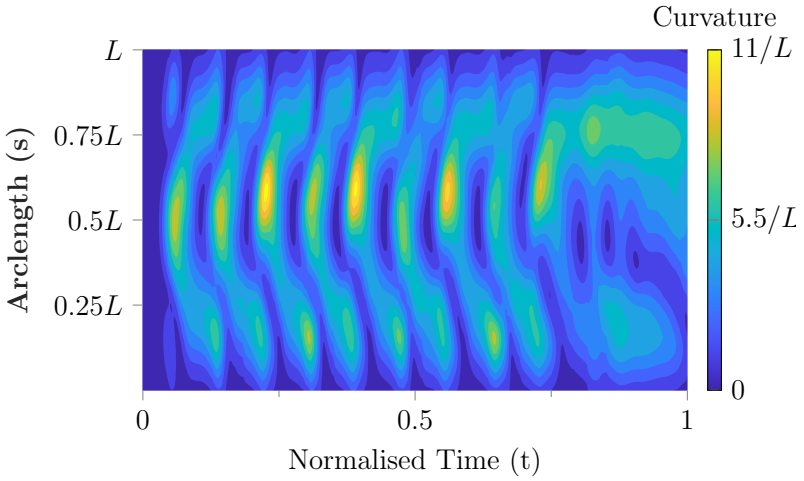

Figure 5.12: For $\sigma = 120$, Saturn filament moves in a run-and-tumble pattern. In panel (a), the cyan-to-magenta transition represents the evolution of the filament's trajectory from from its initial to final position. The time points marked in panel (b) correspond to the filament shapes shown in panel (c).

"running" phase. However, after a while, due to different reasons including finding nutrition or affinity to a light source, the bacterium needs to change its direction. At that point, the bacterium bends its flagella to reorient itself, which is the "tumbling" phase (see the schematic in 1.1).

In this regime, the filament starts running similarly to the previous regime. During

the run, the filament moves ballistically (see displacement figure 5.12b for $\sigma = 120$). However, it differs from the previous regime in terms of curvature. Although the run is initiated by the 1^{st} bending mode with a maximum curvature around the centre, over time, this changes. As the U-shaped filament moves through the fluid, the middle portion with high curvature values is exposed to larger drag. Consequently, that section bends in the opposite direction, and the filament forms the 3^{rd} buckling mode (see figure 5.12d).

This constant shape-switch disturbs the spiral trajectory. Therefore, instead of a spiral trajectory, the filament changes direction and creates a zigzag pattern. In this regard, it resembles run-and-tumble patterns. The 1^{st} buckling mode creates runs, and the 3^{rd} mode leads to direction changes, hence, tumbling.

The filament continues to follow these patterns until $t \approx 0.75$. Following this, a self-reorientation can be captured. This reorientation is a longer and more effective tumble, resulting in a decline in displacement and a trajectory without a recognisable pattern (see the magenta filaments in figure 5.12a). Meanwhile, the filament transitions into higher modes of buckling, as shown in figure 5.12c-IV. Over time this tumbling phase decays, and one side becomes dominant again.

The position of the maximum curvature value has a significant role in the trajectory of the filament in this phase. Depending on the value of σ, the tumbling phase can be more transient. In figure 5.13a, the curvature of $\sigma = 110$ case is given. The filament starts running as usual. However, instead of following a zigzag trajectory determined by the periodicity of tumbling, an interesting behaviour emerges. The 1^{st} mode propagates towards one tip, creating a hook-like shape. Subsequently, the filament changes direction by tumbling, leading to a relaxation in the filament that forms the 1^{st} mode of buckling with smaller curvature values. As a result, the filament settles in a helical orbit in the $yz-$plane with an outward directionality, which appears to be stable. This behaviour can be considered as a hybrid mixture of the third and the fourth regimes. Therefore, it may be named run-tumble-helical.

(a) The trajectory of the filament is illustrated.

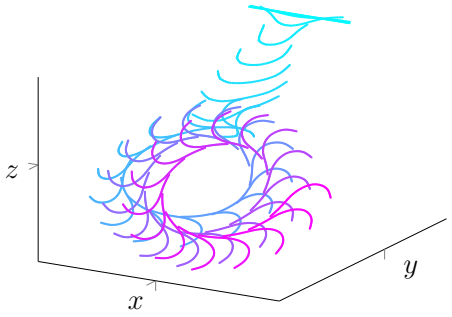

(b) Time versus distance from the initial position is plotted.

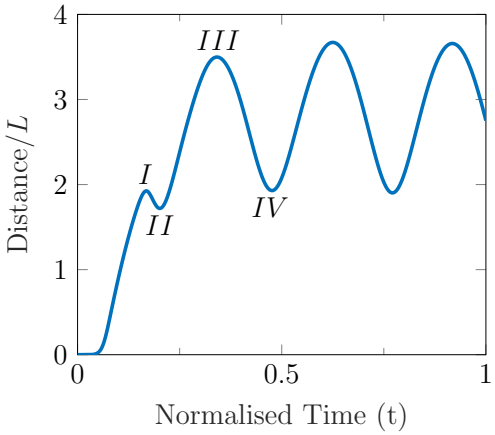

(c) Shapes of the filament are depicted.

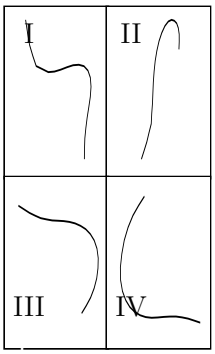

(d) The curvature values of the filament are shown as a heatmap.

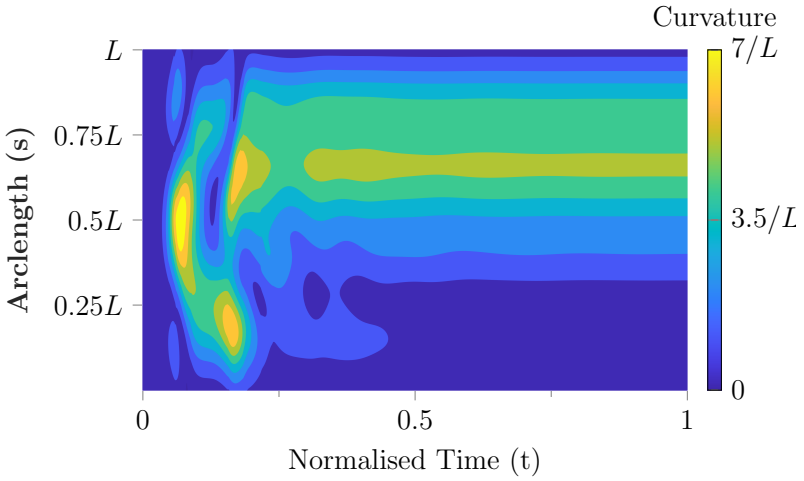

Figure 5.13: For $\sigma = 110$, tumble phase of run-and-tumble appears as a helix. In panel (a), the cyan-to-magenta transition represents the evolution of the filament's trajectory from from its initial to final position. The time points marked in panel (b) correspond to the filament shapes shown in panel (c).

However, it is not certain what makes a filament with the highest curvature off-centre more stable and move in an orbit. At this stage, it is difficult to provide a fulfilling explanation behind the physics, but we plan to investigate this phenomenon in detail in the future.

(a) The trajectory of the filament is illustrated.

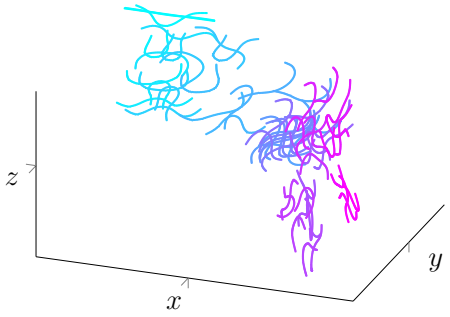

(b) Time versus distance from the initial position is plotted.

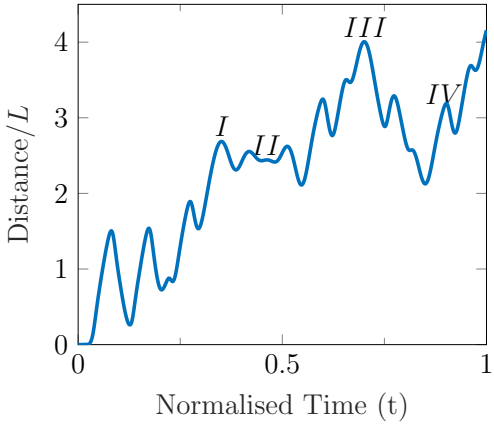

(c) Shapes of the filament are depicted.

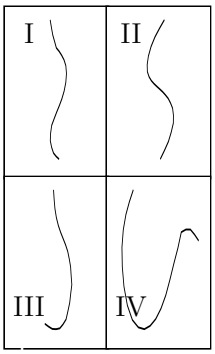

(d) The curvature values of the filament are shown as a heatmap.

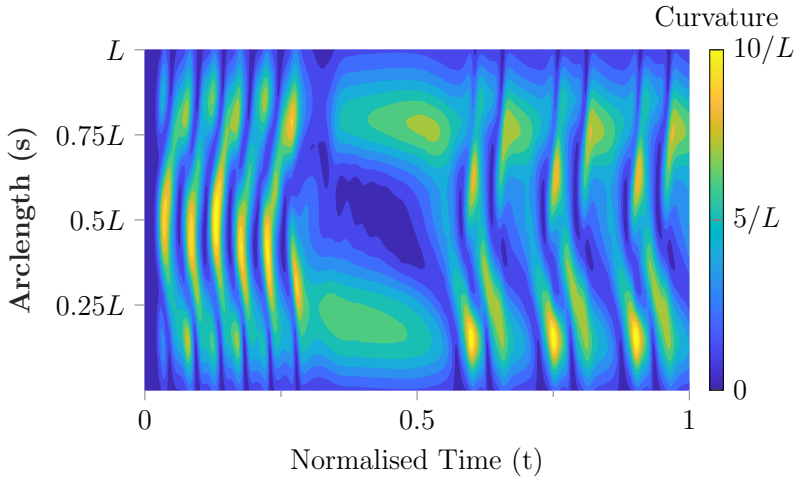

Figure 5.14: For $\sigma = 140$, there is no directional tendency or running phase. Thus, the Saturn filament tumbles continuously. In panel (a), the cyan-to-magenta transition represents the evolution of the filament's trajectory from from its initial to final position. The time points marked in panel (b) correspond to the filament shapes shown in panel (c).

5.3.5 Tumble Dominant Run

The fifth and last regime is captured for $\sigma > 125$ and it can be distinguished by the continuous tumbling of the filament. In the scarcity of a running phase, the filament constantly buckles into various modes: therefore, the filament follows a more chaotic

trajectory. Figure 5.14a shows the path of a filament with $\sigma = 140$, which does not resemble any pattern. The tumbling phase fully dominates the dynamics.

In terms of quantitative data, curvature values in figure 5.14d can provide more insight. Before $t = 0.25$, the filament deforms similarly to the early stages of the $\sigma = 120$ case. However, the transition between modes occurs more frequently, resulting in shorter durations of translation. Consequently, the zigzag pattern fades out and transforms into sudden direction changes. As $t > 0.25$, the filament relaxes into a one-side dominant 1^{st} mode briefly, which is followed by a 4^{th} buckling mode. In terms of displacement, this coincides with a plateau in figure 5.14b. At the end of the plateau, a different periodic deformation happens. The filament creates a hook-like shape, which is a 2^{nd} mode heavily dominated by one side (see figure 5.14c-IV). This shape preserves itself, thus, the filament rotates around. Consequently, the filament forms scattered clusters of tumbling (see figure 5.14a).

In figure 5.15, the speeds of the centres of mass are given for all of the mentioned regimes and normalised with respect to a speed of body length per second. The figure is rich in terms of providing physical insight. First of all, it shows that in the ballistic and spiral trajectory regimes, the Saturn filament may reach similar speeds to Janus filaments. The presence of forces at both tips provides enough thrust to hold a steady speed of up to 5 body lengths per second.

Another notable finding is the constant speed of the centre of mass in the run-tumble-helical trend. Once the filament transforms into helical phase, the speed does not fluctuate at all. This feature can be beneficial for having directional control over the trajectory of the filament without any external mechanism.

For $\sigma = 120$ and $\sigma = 140$ which are labelled with dashed and straight orange lines respectively, the impact of tumbling is illustrated. During the running phase, both filaments reach speeds exceeding 10 body lengths per second. However, these high speeds are followed by abrupt declines. These minimum speed values coincide with tumbling phases and fall within the range of $0.5 - 1$ body length per second. For $\sigma = 140$, the impact of

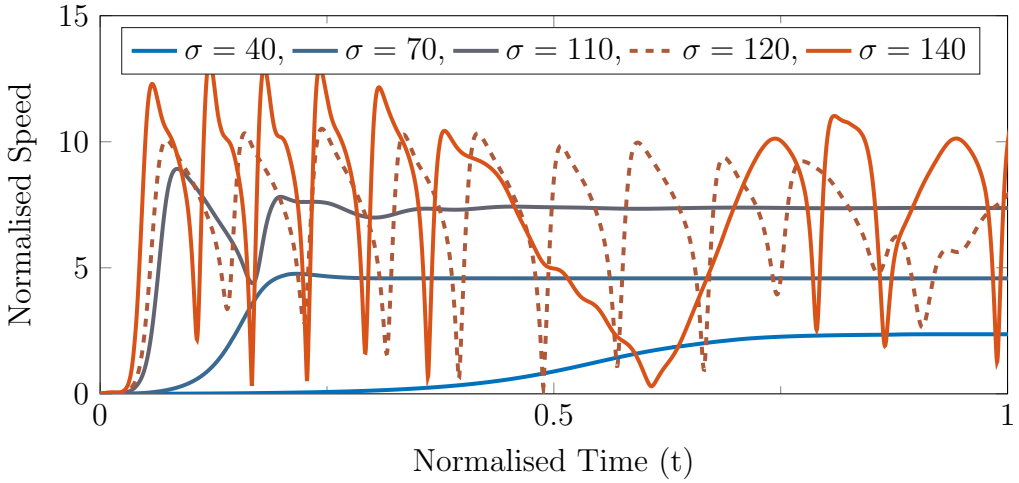

Figure 5.15: The speeds of the centres of mass are compared. The $y-$axis is normalised with respect to the body length per second. The $x-$axis is determined by the simulation time of $\sigma = 140$ cases because of faster dynamics. Therefore, it should be noted that the plot represents the snapshots of the other simulations instead of the full ranges.

relaxation around $t = 0.5$ is evident. Finishing our numerical investigation on Janus and Saturn filaments, in the next section we will delve into our findings.

5.4 Discussion

We simulate active Janus pusher filaments with free ends, employing the dimensionless group σ to describe the problem. The setup resembles the description of a passive tail excited by an active motor, as outlined by Machin (115) for sperm motility. Two distinctive trends are observed for Janus pusher filaments: pure translation and periodic oscillations involving the 1^{st} and 2^{nd} modes of buckling. In the first regime, the filament reaches the terminal speed in a short time and follows a straight path. The transition from pure translation to deformations correlates with the increase of σ. The parameter not only determines the distinctive regimes but also controls the frequency and periods in the second trend.

In the second regime, the swimming trends evolve from side-to-side motion into

corkscrew-like deformation. This is akin to the flapping-to-whirling transition observed in follower force models with fixed bases.

Another insight into this trend is the oscillations of the filament around a fixed point. Although the filament continues translating, the viscous drag at the free end puts the filament under compression. From this perspective, it is similar to the results of the study by Laskar and Adhikari (103). However, our problem and the mentioned study differ in terms of the definition of activity and consequent force balance, ensuring 0 net force in Stokes flow. In this thesis, this is secured by employing regularised stokeslets to balance viscous drag. On the other hand, the mentioned study used stresslets for the same purpose.

In terms of physics, we observed a directional preference in the trajectory of the oscillating filaments. This feature is a function of the initial buckling problem. Therefore, the idea of guiding the buckling can be fruitful in microswimmer studies. Such navigation systems can be achieved either using joints or employing stimuli-responsive hydrogels. In the next Chapter, we will explore the latter option.

We continue by exerting another non-conservative end force to obtain Saturn filaments. The results offer potential for future applications. As a function of σ, five regimes are identified; stationary pumping, ballistic motion, spiral trajectory, run and tumble, and tumble. Moreover, at the boundaries between regimes, some transient characteristics are captured including run-tumble-helical behaviour.

The significance of the first regime lies in highlighting the impact of symmetry and its real-life implications. The tip forces remain in balance and the filament does not deform. Consequently, the filament acts like a microfluidic device, pumping the fluid at both ends, resembling the I-shaped micropumps in Chapter 2. However, the filaments are more slender compared to I-shaped microrods and do not suffer from intrinsic randomness of the locations of bubble nucleation points observed in the experimental study (161).

In the second regime, the filament deforms into the 1^{st} buckling mode with an asymmetric shape and small curvature values. With equal forces at both ends, the U-shaped

filament acts as a pure translator, moving along a straight path. We numerically show how to harness the deformability of the active particles to have control over their locomotion. Such swimmers demonstrate the ability of shifting from an I-shape to a U-shape solely through the exertion of a follower force with constant magnitude and non-conservative direction. Thus, this mechanism can facilitate operations such as locally pumping a drug with an I-shaped flexible microbot and then leaving the site via pure ballistic translation as it transforms into a U-shape.

As σ increases, due to the heterogeneity of the filament, the 1^{st} mode may occur more asymmetrically with larger curvature values. Consequently, the filament follows a spiral trajectory. From this perspective, the combined translation with rotation of the filament is similar to the U-shaped microbots with double poles in Chapter 2.

While these two regimes serve as design guides, the fourth and fifth regimes introduce novel dynamics. The fourth regime is named run-and-tumble due to its similarity to bacterial motion. Throughout this regime, the filament experiences periodic buckling between the first and third modes. Depending on parameter σ, the periods of run and tumble phases can be extended or become more frequent.

A similar motion trend was experimentally observed for bubble-propelled micromotors by Luan et al. (114). However, the previous study relied on the design heterogeneity and the placements of catalysts to have distinct run-and-tumble motions. In this study, we demonstrate it is possible to have a run-and-tumble pattern by only exerting identical end forces on the filament. These periodic runs and tumbles enable the filament to translate and reorient itself. Therefore, this behaviour could be exploited for autonomously escaping from a maze. In biomedical applications, this feature could aid in navigating through media with obstacles, like turning corners.

Another finding of this regime is the helical trajectory. Under certain conditions of porosity, σ, and filament shape, a unique equilibrium occurs, leading to a stable shape. The run phase of the regime is followed by a single tumbling, and then, the filament adopts the helical trajectory. The speed of the filament remains constant and the filament

performs a drilling-like motion in a helix with a constant radius.

In the last identified regime, the filament only undergoes tumbling motion, and shifts between the first four modes with high frequency. The main difference from the other regimes is the small amount of net motion. The filament performs no running behaviour and only drifts along as it deforms. Moreover, the speed of the centre of mass fluctuates considerably, ranging between extreme values. The filament demonstrates unpredictable out-of-plane deformations inherent in the buckling instability. One possible application of this regime could be the self-orientation of the filament. By harnessing the tumbling pattern, the filament might have the ability to transition into various modes and directions as needed.

In conclusion, this chapter explores the manipulation of smart hydrogel-based microbots via deformations induced by non-conservative end forces. In the next chapter, we will offer an alternative strategy to change the shape of a microbot, which involves the use of thermo-responsive hydrogels.

CHAPTER 6

RESPONSIVE SHAPE-SHIFTING MICROBOTS

Responsive hydrogels are capable of changing their shapes by absorbing or releasing substantial amounts of aqueous fluids. This property can be harvested to control the swimming dynamics of a microbot (122). With this inspiration, we suggest a simple mathematical model that can effectively capture the foundations of shape-transformations in responsive hydrogels. The numerical simulations are constructed on the bead and spring system described in Chapter 4. It should be noted that the method differs from the SPH-based computational tool mentioned in Chapter 3. The SPH method provides an understanding regarding both the local fluid interactions and bulk dynamics in depth, which comes with a computational cost. On the other hand, our methodology in this chapter is a more flexible technique which is primarily targeting the acquisition of core dynamics. Although it is a relatively simple model, it is versatile and applicable to arbitrary shapes.

This chapter is organised as follows. In section 6.1, we begin by updating the bead and spring framework for responsive hydrogels. Later, in section 6.2, passive hydrogel bilayers are simulated to demonstrate transitions between different shapes, including self-folding and twisting behaviours for unconventional designs. In section 6.3, responsive hydrogels are utilised to navigate active Janus microbots. The chapter concludes with a brief discussion about the findings in 6.4.

6.1 Updating the Bead and Spring System for Responsive Hydrogels

Here, we employ our mathematical model, which combines a bead and spring system with regularised stokeslets. However, the main algorithm is adapted to incorporate isotropic responses in selected regions of the hydrogel, leading to anistropic deflections. This feature allows for the estimation of complex responses in single-material hydrogels with differing cross-linking densities, similar to the previous study of Hippler et al. (72). The volume and shape transitions resulting from responsive swelling and deswelling dynamics are achieved by adjusting the natural lengths of elastic springs within the system while maintaining homogeneity across all physical parameters within the material.

To implement this numerical update, we initialise a geometry and use an indicator function that distinguishes between responsive and non-responsive beads, assigning values of 1 and 0, respectively. This indicator function stores the indices of all beads whose centres lie within the user-defined region of interest, designating them as responsive beads. Subsequently, we adjust the rest lengths of springs connected to responsive beads, either contracting or extending them accordingly. The revised rest lengths would deviate from those in the initial shape.

Such modification would induce internal stresses, which would be balanced by hydrodynamic drag and elastic deformations, hence causing shape change. Consequently, our semi-implicit algorithm is given by:

$$\frac{\boldsymbol{x}_a^{n+1} - \boldsymbol{x}_a^n}{\Delta t} = \frac{1}{8\pi\mu} \sum_{b=1}^{N_b} \boldsymbol{S}^{\epsilon}(\boldsymbol{x}_a, \boldsymbol{x}_b)^n \left(\sum_{c=1}^{N_c, b} k \left(\boldsymbol{x}_c^{n+1} - \boldsymbol{x}_b^{n+1} - L_{bc} \boldsymbol{e}_{r_{bc}}^n \right) \right). \tag{6.1}$$

By adjusting the spring lengths in this manner, we would obtain deflections as sudden impulses rather than gradual changes. This modelling approach would better suit to the length scale that we are interested in. It has been generally observed that the thermal diffusion in thermo-responsive hydrogel studies occurs more rapidly than shape changes caused by fluid expulsion (17). Consequently, the rapid dynamics of thermal changes

lead to instantaneous internal state transitions in the gel.

In responsive behaviour, the volume change is accompanied by shifts in elastic modulus. As demonstrated by Hippler et al. (72), the elastic modulus of the material can increase several folds with shrinkage. This means that as the material shrinks, it becomes more difficult to deform. To represent this transition, the elastic modulus is updated along the spring lengths, which impacts the spring stiffness. Consequently, the spring stiffness becomes a function of time and the responsiveness of the beads as follows:

$$k = k_{ab}(t) \tag{6.2}$$

where the subscript indicates the connected beads.

It is worth noting that Poisson's ratio remains constant throughout our simulations. Temperature variations directly influence the Poisson's ratio, thereby impacting our 3D DLSM formulation and spring stiffness. However, thermoresponsive hydrogels are capable of shrinking and swelling immediately just over their LCST. Therefore, we can assume that transition occurs in a narrow range between 30 °C to 33 °C. In this regime, changes in Poisson's ratio are negligible. Now, we can use the modified algorithm to explore shape transformations of passive heterogeneous hydrogels.

6.2 Passive Shape Shifters

Our simulations begin by examining passive shape-shifters consisting of responsive and non-responsive layers, fully immersed in aqueous fluids. In our test cases, the shrinking behaviour of responsive hydrogels is modelled in particular. This is due to the availability of the extensive literature on PNIPAM and other responsive hydrogels with LCST.

Unless otherwise stated, the shrinkage is imposed by contracting the springs to 70% of their initial lengths. While this value could be as low as $20 - 30\%$, we opt for a relatively higher percentage to ensure a sufficient distance between regularised Stokeslets.

(a) The bilayer initially has a rod-like shape.

(b) The bilayer bends into a U-shape.

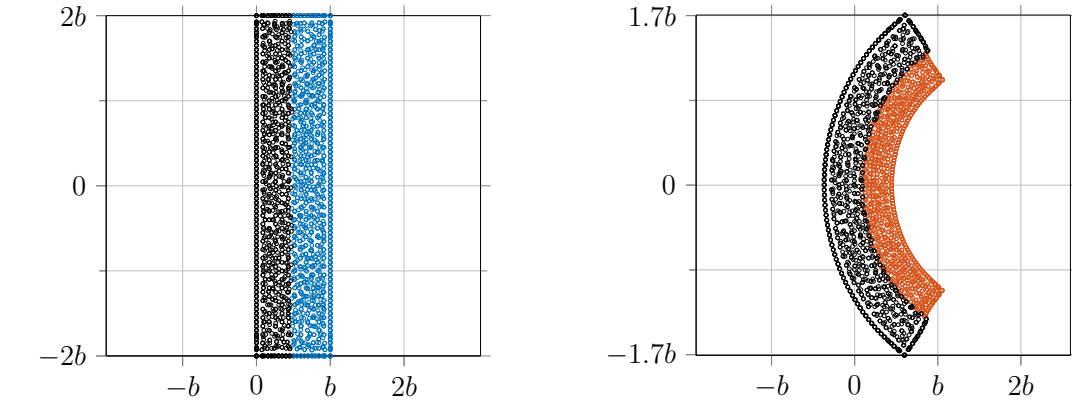

(c) Curvature values are presented.

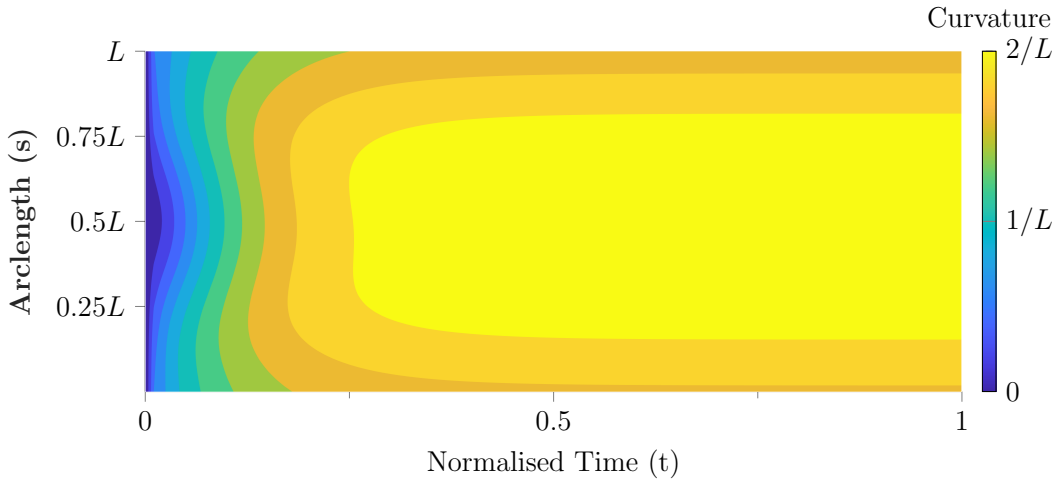

Figure 6.1: The responsive region of the bilayer shrinks, which leads to a bending motion. As a result, the bilayer forms the 1^{st} mode of bending. In panel (a), blue indicates the responsive section before shrinkage. In panel (b), orange represents the final shape of the responsive section after shrinkage. In both panels, black denotes the non-responsive sections.

The time step size is selected as $\Delta t = 1 \times 10^{-5}$, and the simulations run for as long as necessary.

6.2.1 Rod Bilayer, also known as Pump to Translator (I to U)

The first test case involves a rod-shaped passive bilayer. We examine the effects of different parameters on the shrinkage ratio and final shape of the hydrogel.

The bilayer has the dimensions of $10\,\mu m \times 5\,\mu m \times 40\,\mu m$ as $b \times h \times L$. I-shaped bilayer

(a) Final shape of the bilayer is given.

(b) The curvature values of the bilayer are provided.

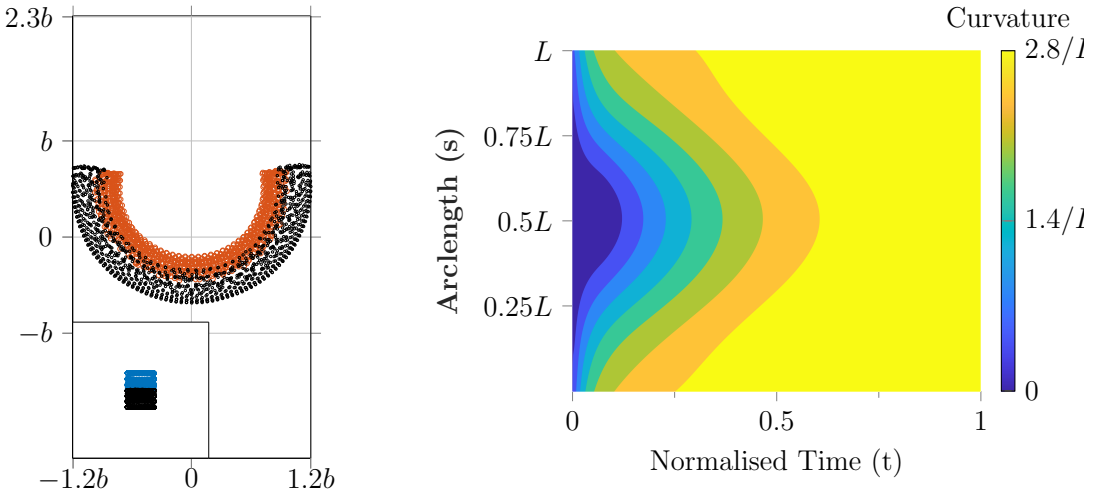

Figure 6.2: The hydrogel bilayer is constructed to have a boundary layer in the $xy-$plane. In panel (a), the final shape is demonstrated and the inset of the figure shows the initial bilayer from a side view in the $yz-$plane. In panel (b), the evolution of the curvature values over time is shown.

comprises $N_{rb} = 1295$ responsive beads out of a total of $N_b = 2466$, which corresponds to a responsiveness ratio of $\Upsilon = \frac{N_{rb}}{N_b} \approx 0.52$. An interface in the $yz-$plane determines the anisotropy in response.

In figure 6.1a, the initial configuration of the bilayer is provided as its long axis aligned between $y = -2b$ and $y = 2b$. Here, black beads represent the non-responsive layer, while the blue colour indicates the responsive section. As the thermal stimulus is applied to the bilayer rod, the responsive beads start to come closer, causing that section to shrink. Conversely, the beads in the non-responsive layer strive to maintain their original position. Consequently, the system reaches equilibrium with deformation. In figure 6.1b, the final configuration of the bilayer is shown, in which the orange colour marking the responsive section after the thermal shift. The final shape reminds the letter U, rotated 90° clockwise.

In figure 6.1c, the curvature contour of the bilayer is illustrated. The bilayer mostly undergoes symmetric deformation, reaching maximum curvature values of up to $2/L$. In the next section, we will test the impact of responsive surface area on the dynamics.

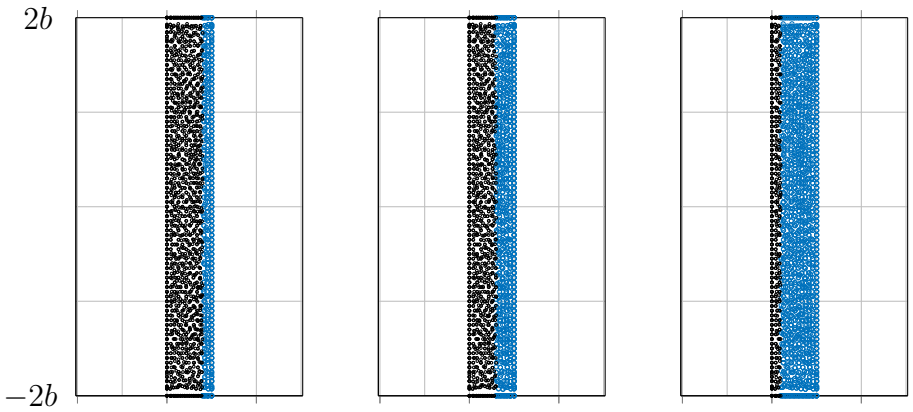

Figure 6.3: The initial configurations of bilayers are illustrated. The responsiveness ratio, Υ, increases from left to right. Each plot is viewed in the $xy-$plane. The blue regions represent the responsive areas in the bilayer, while black sections are non-responsive.

Effect of the Surface Area of Responsive Layer

To comprehend the influence of surface area, we alter the orientation of the responsive layer. Consequently, an identical hydrogel to the previous study has an interface between responsive and non-responsive beads in the $xy-$plane. The ratio of responsive beads to the whole system is approximately$\Upsilon \approx 0.5$ which ensures isolating the effects of surface area.

Figure 6.2 displays the final shape of the responsive hydrogel and the evolution of the curvature over time. Panel (b) highlights a significant difference in the curvature values compared to the previous simulation. While both simulations share similar characteristics, the curvature values are higher for the bilayer with interface in the $xy-$plane. Furthermore, the curvature becomes uniform in the same simulation. These findings suggest that as the surface area of the responsive layer increases, the bilayers tend to buckle more. This aspect can be exploited to control the buckling of a given bilayer. To gain full control over these dynamics, as part of our future studies, we plan to define a dimensionless parameter group that provides the ratio of thermal stress to both bending resistance and hydrodynamic resistance. In the next section, we will offer another way to control buckling by altering the responsiveness ratio, Υ.

(a) As Υ increases bilayer bends more.

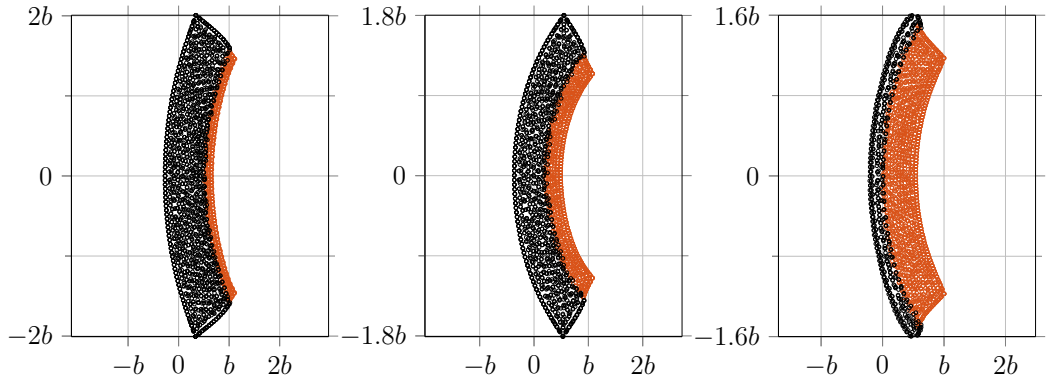

(b) Average bead speed is plotted for different Υ values.

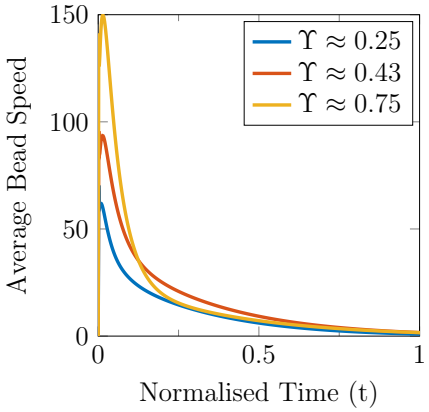

(c) Volume transition is plotted for different Υ values.

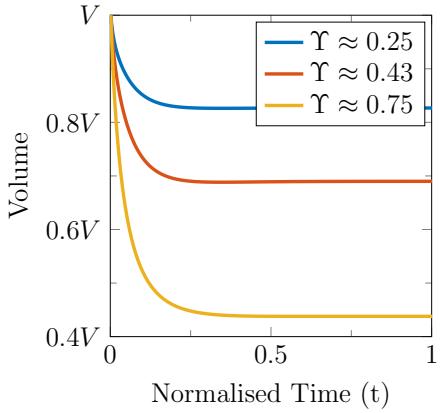

Figure 6.4: The quantitative data are provided for $\Upsilon = 0.25, 0.43$, and 0.75. In panel (a), Υ increases from left to right. In panel (b), the average bead speed is normalised with respect to the body length per second. Panel (c) shows the volume change for each bilayer.

Effect of Responsiveness Ratio

The ratio of responsive beads to non-responsive beads may govern the deformation of the bilayer. To understand this relationship, we assign $\Upsilon \approx 0.25, 0.43$ and 0.75 for the hydrogels whose initial configurations are provided in figure 6.3.

In figure 6.4a, we present the final configurations of the hydrogels after volume transition, illustrating an increasing bending trend with Υ (see figure 6.5). In figure 6.4b, the average bead speed over time is depicted. The $y-$axis is normalised with respect to the speed of body length per second. During volume transition, deformation occurs due to

(a) The curvature is plotted for $\Upsilon \approx 0.25$.

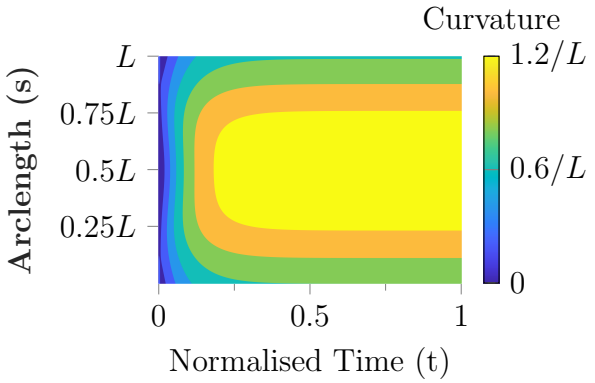

(b) The curvature is plotted for $\Upsilon \approx 0.43$.

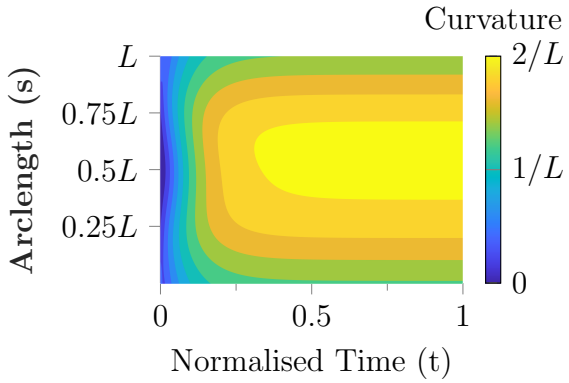

(c) The curvature is plotted for $\Upsilon \approx 0.75$.

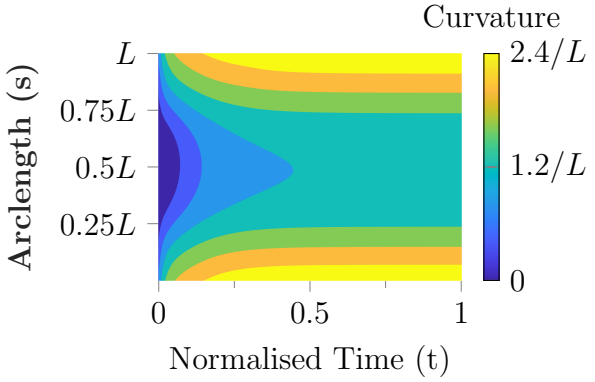

Figure 6.5: The curvature values increase as the responsivity ratio increases from $\Upsilon \approx 0.25$ to $\Upsilon \approx 0.75$. Panels (a) to (c) correspond to the bilayers from left to right in panel (a) of figure 6.4, in respective order.

internal stresses. As a result, in cases such as shrinkage or swelling of a homogeneous thermo-responsive hydrogel, the centre of mass may maintain its position while the bulk structure moves. Therefore, the average bead speed may better represent the dynamics compared to the speed of the centre of mass.

Figure 6.4b reveals a positive correlation between Υ and average bead speed, accompanying the increasing bending. As Υ increases, internal stresses become larger and conversely, there is less resistance from non-responsive beads towards shrinkage, hence, greater bead speeds.

Finally, we would like to compare the deswelling of a homogeneous hydrogel with the

(a) The homogeneous hydrogel maintains its rod-shaped structure without bending after deswelling.

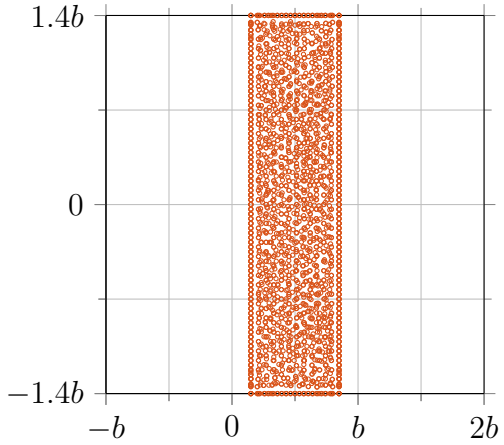

(b) Average bead speeds are compared for homogeneous and heterogeneous hydrogels.

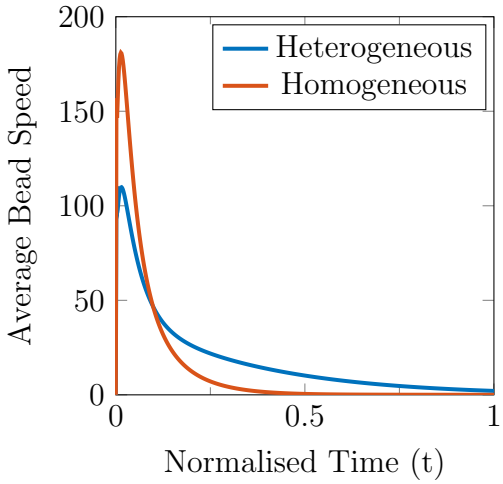

Figure 6.6: The homogeneous and responsive hydrogel shrinks while preserving its shape, and the dynamics are faster than heterogeneous bilayers. In panel (b), the $y-$axis is normalised with respect to a speed of body length per second.

initial deswelling case in figure 6.1. In the case of the entire hydrogel being responsive, the deformation is uniform and isotropic (see figure 6.6a). Thus, there is no bending throughout the volume change. However, the dynamics are considerably faster compared to the heteregeneous hydrogels (see figure 6.6b). With these results, we conclude our investigation of the parameter impacts. In the next section 6.2.2, we will introduce multiple responsive areas to initiate more complex bending forms.

6.2.2 Pump to Rotator (I to S)

So far, we have demonstrated how a single responsive region can transform the shape of a hydrogel. In this section, we employ multiple thermo-sensitive regions. To distribute these layers, we first determine the geometrical centre. Then, as shown in figure 6.7a, the body is divided into four quadrants, and responsive layers are added diagonally. The responsiveness ratio is equal to $\Upsilon \approx 0.5$.

After the thermal stimulus, both responsive regions start to shrink simultaneously.

(a) Initial configuration of hydrogel is viewed in $yz-$plane.

(b) The final shape of the hydrogel reminds S shape.

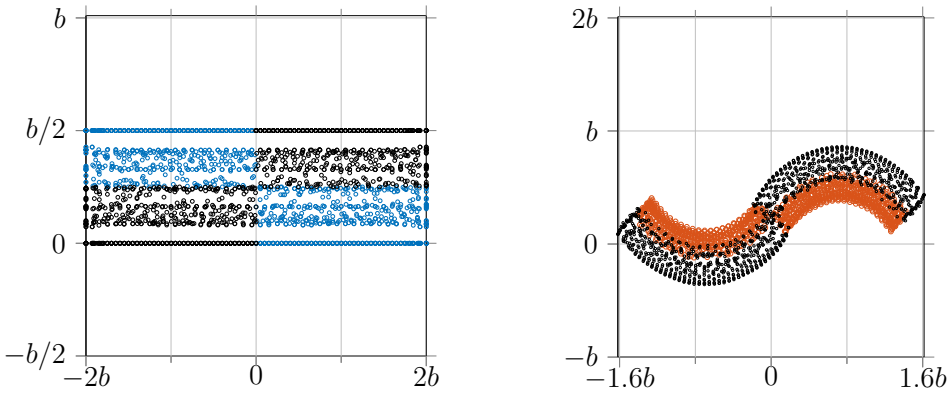

Figure 6.7: The hydrogel can switch shapes between I and S in the presence of multiple responsive layers.

As these layers are located in opposite halves along the $z-$axis, they bend in opposite directions. Consequently, the hydrogel adopts the second buckling mode, forming an S shape (see figure 6.7b). We continue by doubling the number of responsive regions. Similar to the previous simulation, the sensitive regions are arranged in a zigzag pattern (see figure 6.8a). After deformation, the hydrogel creates a wave-like shape in figure 6.8b. Interestingly, the tip-to-tip length of the hydrogel on the $y-$axis is similar to the previous case.

Although these cases have the same Υ as the original test case given in figure 6.2, the original bilayer bends significantly more. On the other hand, the difference between deswelling times and average bead velocities between these three simulations are negligible. As long as the bilayer preserves the total responsive surface area, the mentioned parameters remain unaffected.

Figure 6.8c, depicts the final shape after recovery for the thermo-responsive hydrogel with four responsive areas. Once the deswelling ceases, we reassign the rest lengths. Consequently, the responsive beads tend to move away from each other, resulting in elastic forces acting on all beads. Subsequently, the hydrogel re-swells and straightens, forming a rod-like shape identical to the initial configuration and volume (see figure 6.8d). This

(a) The initial configuration of the hydrogel is viewed in the $yz-$plane.

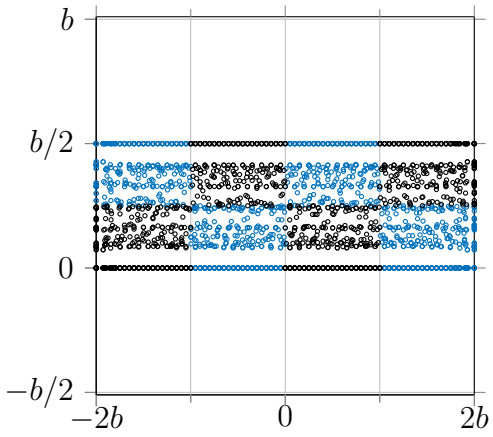

(b) The final shape of the hydrogel with four responsive regions reminds a wave.

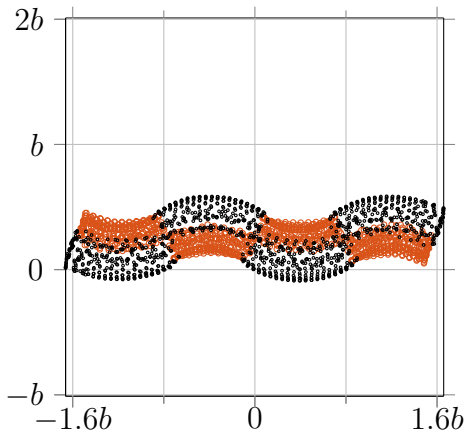

(c) The hydrogel recovers to the initial shape after re-swelling.

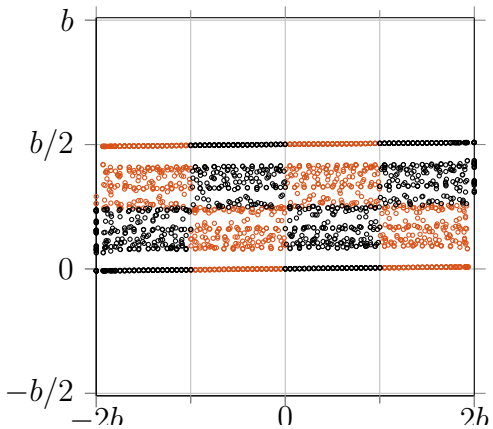

(d) The hydrogel maintains its original volume after recovery.

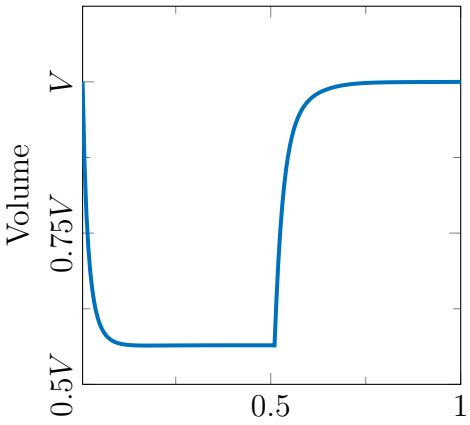

Figure 6.8: A hydrogel with four responsive regions initially shrinks and forms a wave-like shape. After recovery, it re-creates the original configuration.

result shows a good agreement with the previous study of Hippler et al. (72), considering the minor measurement errors in experimental study. Regarding the time scales of deswelling and swelling, it is difficult to draw definitive conclusions with our method. Since the method of regularised stokeslets does not enforce the no-slip boundary condition on the surface of beads, we will consider alternative methods to address this issue in the future studies.

This section has presented a method for transitioning from an I to an S shape by adding multiple responsive regions. Thus, we have demonstrated transitions from one

fundamental shape to another, as outlined in Chapter 2 (161). Utilising the self-recovery process, these shape switches can also be reversed. Moreover, by varying the number and locations of responsive areas, we have controlled the deflection of the hydrogels. Another way of obtaining complex responses is to change boundary conditions. In section 6.2.3, we will further explore this restricting motion at one end and comparing our results with those of Hippler et al. (72).

6.2.3 Bilayer with Fixed End

The introduction of a clamped boundary condition may impact the final shape and dynamics of the bilayer (72). Here, we limit the displacement of the beads at $y = -2b$, effectively creating a fixed end. The responsive interface is identical to the bilayer in 6.1. With clamped boundary condition, we simulate three different hydrogels with lengths of $L, 1.5L$, and $2L$.

In figure 6.9, the final shapes of these bilayers are illustrated. The figure suggests that the length has an impact on the curvature, which aligns the findings of Hippler et al. (72). As the length increases, bending may extend into a rolling motion. Consequently, the bilayer with a length of $2L$ forms a semi-circle on the $xy-$plane. For longer bilayers, this motion can result in a full circle. Such a bilayer configuration may facilitate grasping, holding, and releasing microobjects (100).

Additionally, we simulate the same problem with multiple responsive layers, motivated by the previous experimental study of Hippler et al. (72). After deformation, multiple curves form with centres at opposite halves of the $x = b/2$ line (see figures 6.10a and 6.10b). The main difference from the free-end problem is the preferred direction of the structure. In the free-end simulations, we observed that the centreline of the hydrogel maintains its position. However, with a clamped boundary condition, the centreline has an angle with the initial origin of symmetry. This angle depends on the number of responsive layers and exhibits a negative correlation.

Figure 6.10c plots the angle between the $x = b/2$ line and the line passing through

(a) Bilayer with length L bends.

(b) Bilayer with length $1.5L$ curves.

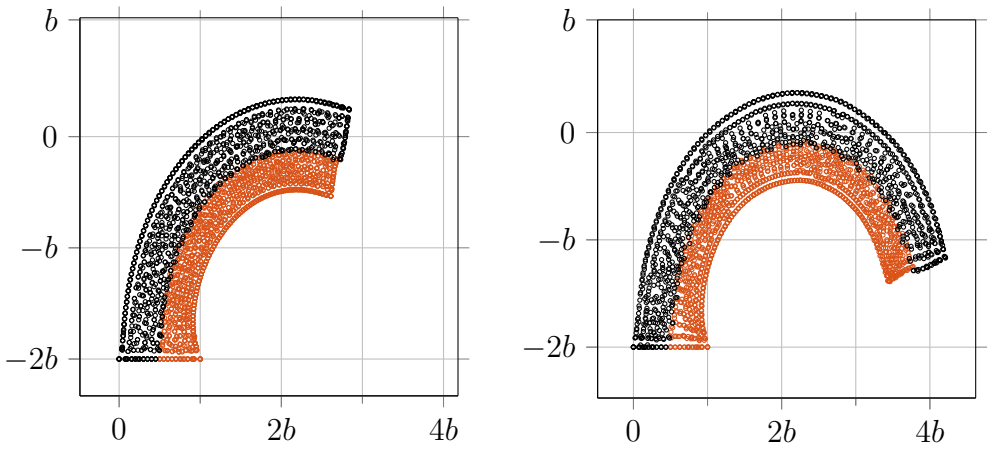

(c) Bilayer with length $2L$ rolls.

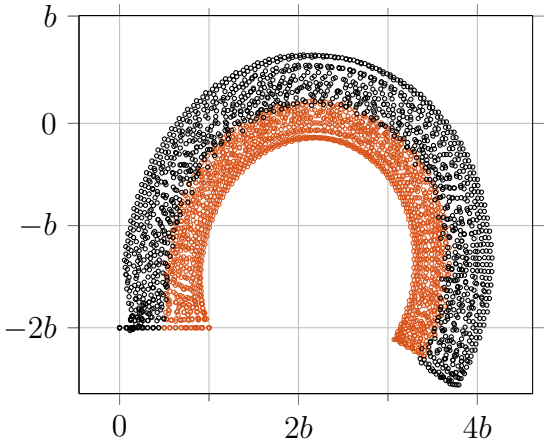

Figure 6.9: I-shaped bilayers with clamped boundary condition deflects as Hippler et al. (72) suggested. As length increases, bending transforms into self-rolling. Previously, similar mechanisms were realised in both millimetre (168) and micrometre scale (100).

the centres of both tips for two and four responsive region cases. The angles are equal to $\alpha_1 \approx 22.3$ and $\alpha_2 \approx 8.9$. In this example, we showcase how hydrogel bilayers can perform complex responses. In the next section, we will use the information collected from previous simulations to propose a smart microbot design for microdelivery.

6.2.4 Self-Folding Star

An important potential application of responsive hydrogel bilayers lies in their ability to create self-folding structures, which could revolutionise various fields such as biomedi-

(a) The final shape of the bilayer with two responsive regions is plotted.

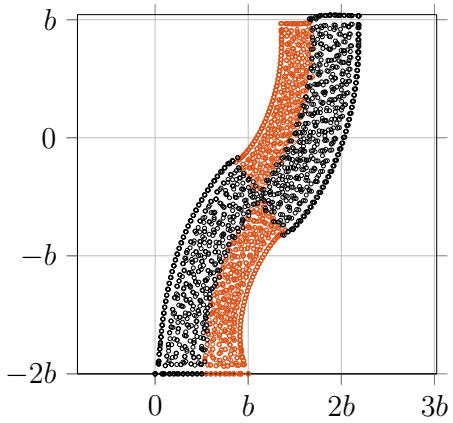

(b) The final shape of the bilayer with four responsive regions is plotted.

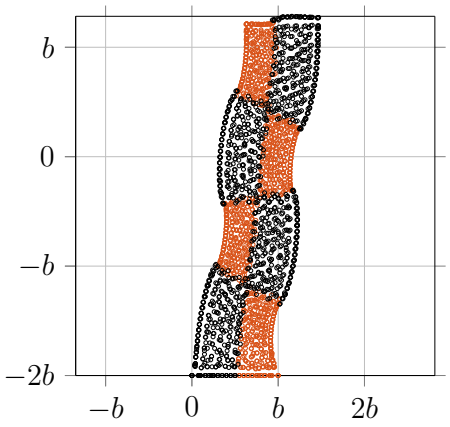

(c) As number of responsive regions increases tip-to-tip vector makes less angle with the $x = b/2$ line.

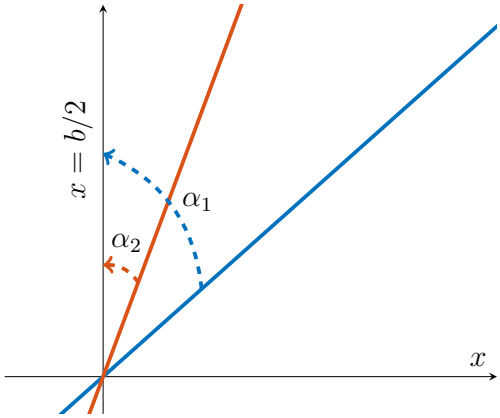

Figure 6.10: Numerical simulations agree with the previous study of Hippler et al. (72) and demonstrate that the direction and position of hydrogel can be navigated by changing the number of active regions.

cal engineering, robotics, and microfabrication. These microbots could encapsulate and release therapeutic drugs on command, as well as perform complex operations such as collecting objects. In nature, self-folding behaviour is observed in the hunting routine of the Venus flytrap (2). When triggered by a target touching it, the plant closes its mouth-shaped leaves to catch its prey. A similar mechanism can be replicated in microbots for loading, carrying, and unloading cargo. Previously, Stoychev et al. (170) manufactured thermo-responsive PNIPAM-based star-shaped microcapsules. Motivated by the results of that study, we propose a self-folding bilayer. In addition to showcasing self-encapsulation,

(a) Star with 4 equilateral triangle arms.

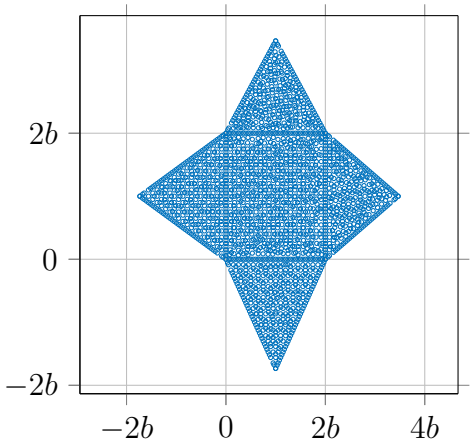

(b) Star with 4 isosceles triangle arms.

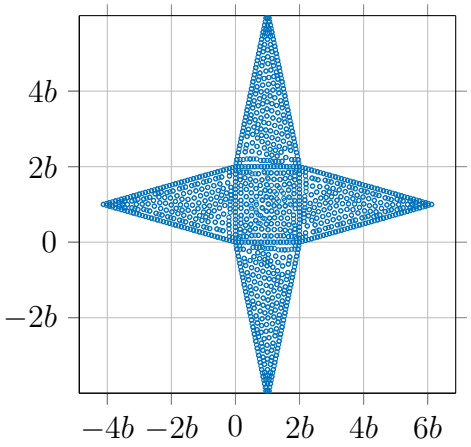

(c) Star with 4 circular arms.

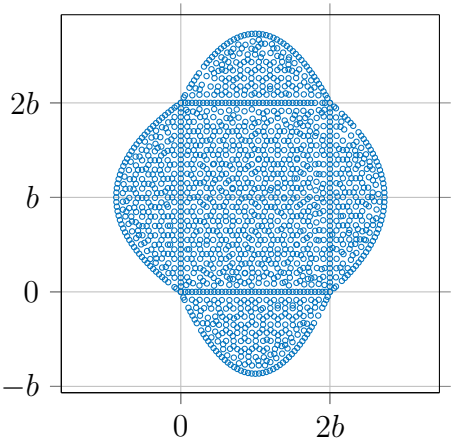

(d) Hexagonal star with 6 equilateral triangle arms.

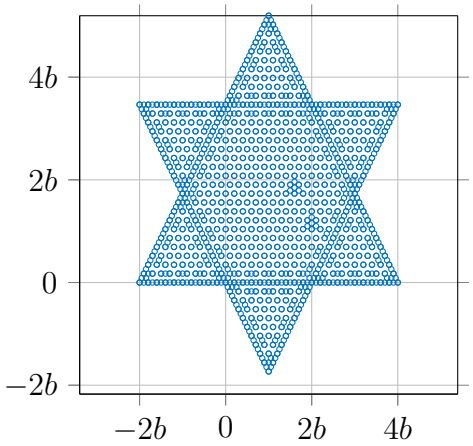

Figure 6.11: Different self-folding mechanisms are suggested. Their initial configurations are shown from the $xy-$plane with elevation. The bottom halves of the bilayers are constructed by a non-responsive layer.

we compare geometrical parameters for optimisation purposes.

In our numerical examination, we utilise star-like geometries with distinguishable arm shapes including isosceles triangles, equilateral triangles, and semicircles, and varying number of arms. In figure 6.11, the initial configurations of various self-folding stars are provided. In all of these stars, the edges of the arms connecting them to the main body have a length of 20 µm. The thickness of the stars is equal to 2 µm.

In figure 6.12, the final configurations are presented. To visualise these simulations, we create surface plots with triangulation. A common feature in all stars with triangular

(a) Star with 4 arms folds itself.

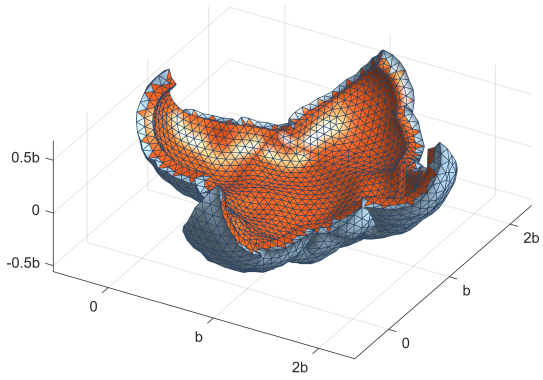

(b) Elevated view in $xy-$plane is given.

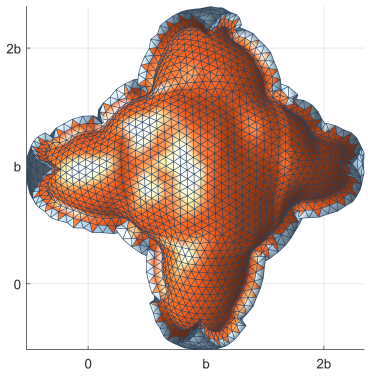

(c) Star with circular arms serves as a bowl.

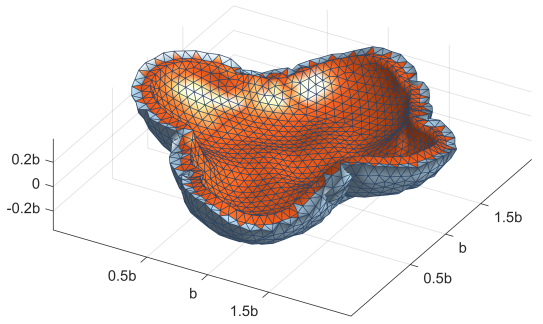

(d) Elevated view in $xy-$plane is given.

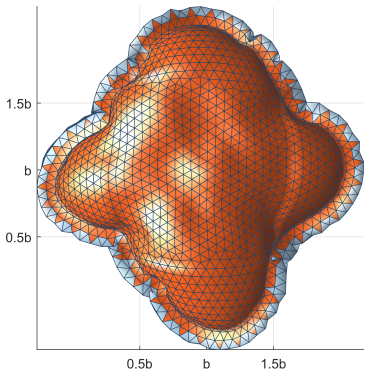

(e) Isosceles arms may grasp larger objects.

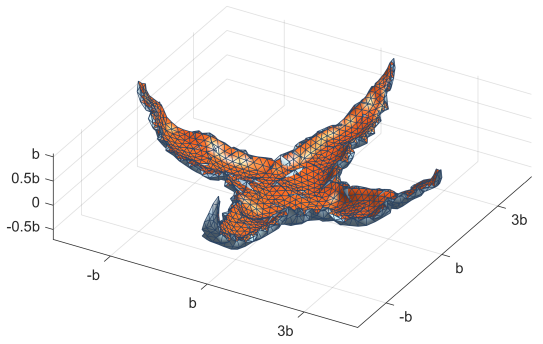

(f) Hexagonal star may hold objects stable.

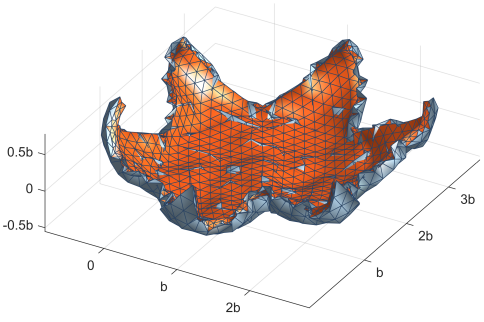

Figure 6.12: Final shapes of various designs are provided. The top row demonstrates a star with 4 equilateral triangle arms from 2 different views. The middle row depicts a star with circular arms from 2 different angles. In the bottom row, a star with isosceles triangle arms and a hexagonal star with 6 arms are shown from $30° - 30°$ azimuth and elevation angle.

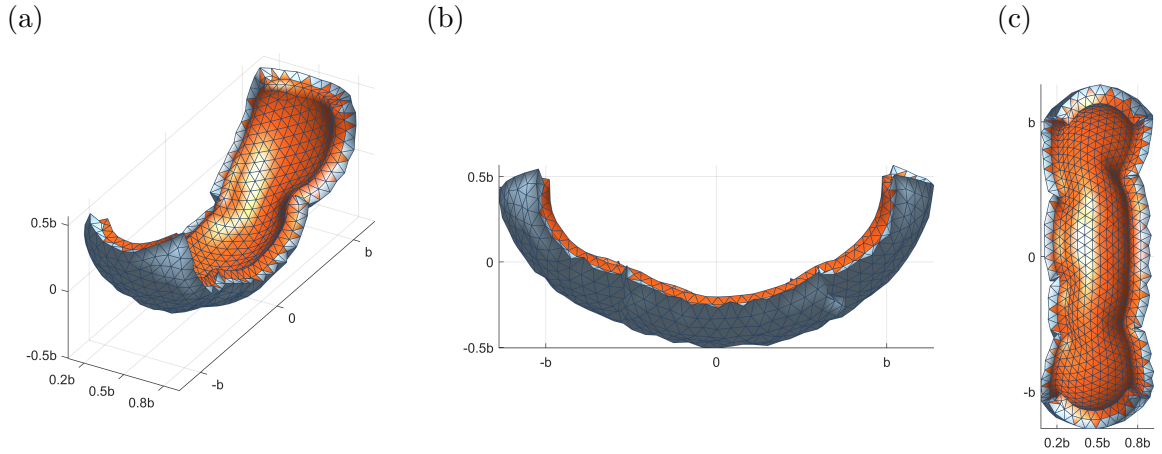

Figure 6.13: From (a) to (c) the final shape of the bilayer is shown from $30° - 30°$, $90° - 0°$, and $0° - 90°$ azimuth and elevation angles, respectively.

arms is the rolling at the tips. For circular arms, self-folding occurs more smoothly. Additionally, as the ratio of the height of the arm to thickness increases, creases can be observed at the edges (see figure 6.12e). This property suggests that elongated shapes with a high surface area-to-thickness ratio, such as ribbons, can offer additional dynamics. For example, a thinner version of the bilayer given in figure 6.1 may exhibit twists and extra curvatures on the edges. To validate this, we employ the mentioned bilayer and halve its thickness. After deswelling, a U-shape is formed. However, the edges of the bilayer have irregularities indicating self-folding towards the centreline. When we investigate the edges parallel to the $y-$axis, multiple bending modes can be seen. Thus, we may qualitatively conclude that the results support our suggestion regarding thickness and shape formation.

In figure 6.12, the bottom row contains a four-arm star with isosceles triangles and a six-arm star with equilateral triangles. These designs may expand the operational range of microcapsules. The isosceles triangles have more elongated shapes, making them suitable for grasping larger objects. On the other hand, the hexagonal star can provide better stability for holding objects steady.

We continue exploring the impact of the number of active regions in the self-folding stars by assigning non-responsive beads to middle sections. In this iteration, non-responsive beads are assigned to the middle sections, leaving only the arms thermo-responsive.

(a) Star with 4 responsive regions.

(b) Side view in $xz-$plane is given.

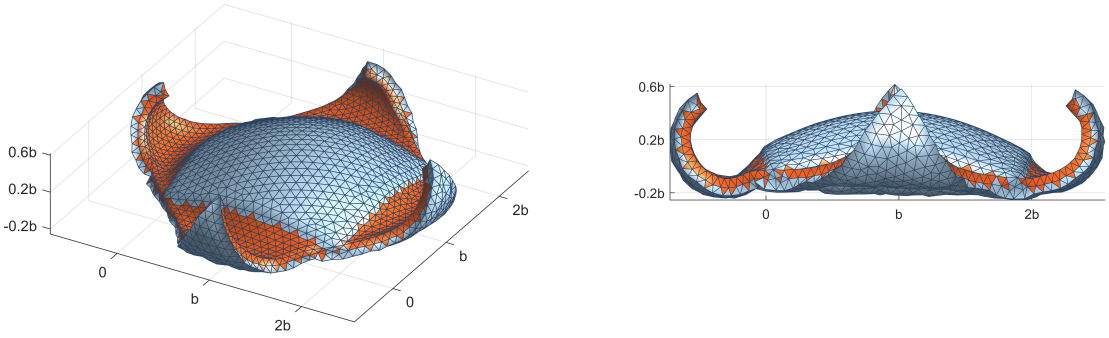

(c) Hexagonal star with 6 responsive regions.

(d) Side view in $xz-$plane is given.

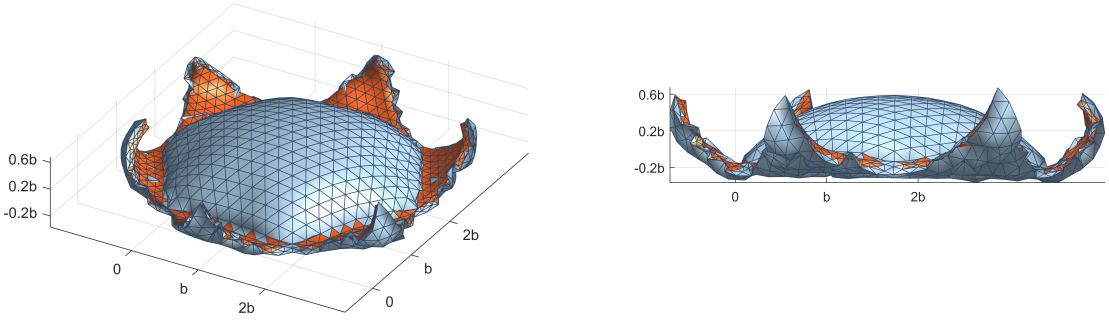

(e) Shrinking ratio affects the final shape dramatically.

(f) Side view in $xz-$plane is given.

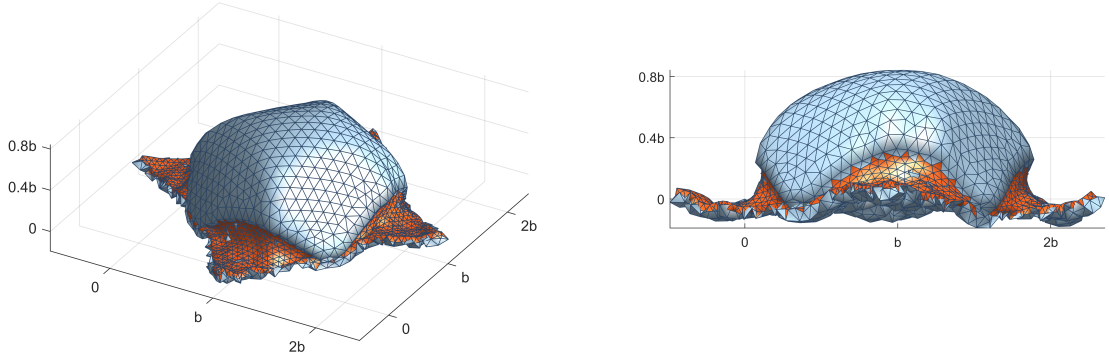

Figure 6.14: Having non-responsive middle sections changes the shrinkage dynamics significantly. The top row demonstrates 2 different views of a star with 4 responsive arms and a non-responsive middle. In the middle row, the same views are used to show a hexagonal star with an identical configuration to the previous case. The bottom row captures how the shrinkage ratio impacts the final shape.

Figure 6.14 displays the final shapes of four-equilateral arm and six-equilateral arm stars are shown. The left column provides views from a $30° - 30°$ angle, while the right column shows views in the $xz-$plane.

Figures 6.14a) to d) highlight notable differences from the previous examples. The shrinkage of arms is counteracted by a deflection in the middle section. This deformation occurs as an elevation in the $z-$axis, and the middle section of stars creates a dome-like shape. Since the hexagonal star has a larger area in the middle section, it elevates higher compared to the four-arm star.

The bottom row of the figure illustrates another intriguing deformation. Previously, a shrinkage ratio of 70% was employed. In figure 6.14e) and f), the ratio is set to 50%. With this ratio, the shrinkage does not result in self-folding. The rolling behaviour becomes less visible at the arms, and the tip of each arm remains in the $z \approx 0$ plane. This is accompanied by a higher elevation at the middle section, attributed to the production of larger elastic forces. In addition to the increased forces, the absence of self-rolling redirects this energy into mechanical work at the middle section, causing it to rise. Hence, one may suggest parametrising the middle section elevation and arms position based on the surface area of the middle section and the shrinkage ratio.

This design offers two potential theoretical applications. The first involves using it as a microvacuum. The elevation of the middle layer can create a vacuum. Thus, given the small time scale of the dynamics, these devices can instantly eject objects from the surfaces. A possible real-life application can be surface cleaning, particularly in scenarios involving bacterial pollution.

Another possible extension is utilising stars as the surface beaters. Leveraging the recovery of the bilayers, a dome-like middle section can hit a surface periodically. When the bilayer is heated, only the arms stay in contact with the surface. However, an instant cooling would lead to swelling back to its original configuration, hence, a strike to the surface. These periodic beats to the surface can be employed to smooth surface roughness or break down microobjects. Although both of these applications are theoretical at the

moment, we hope that advanced studies in the field will realise them soon.

To this point, we have provided examples of passive shape-switchers. In the next section, we will fulfil our promise of demonstrating active shape-shifters using a simple design.

6.3 Active Shape Shifters

In this section, we integrate the shape-shifting feature into active microbots. The mobility of the microbots is provided by a follower force, as defined in Chapter 5. Here, we focus on thick Janus microbots with responsive segments instead of thin, flexible filaments. Although it is feasible to examine a combination of active components, passive flexibility, and responsive bending, the main objective here is to isolate these effects and concentrate on how responsive shape changes can control trajectory. Therefore, we opt for I-shaped rods, as discussed in Section 6.2.2.

In the active rod, the responsive beads are limited by $y < 0$ and $z < 0.25b$ (see figure 6.15a). This design ensures that there is no deformation at the active tip. The shape of the active tip's surface must be preserved to correctly apply non-conservative force with the formulation in 5.3. In the event of tip deformations, calculation of the surface normal should be modified, which will be addressed in Chapter 7 as part of the further studies. In terms of tip force, $\sigma = 30$ is used and exerted to tip at $y = 2b$. In the simulation, between $t = 0$ to $t = 0.2$, there is no thermal fluctuation; therefore, the Janus rod purely translates in a straight trajectory. However, as the responsive section starts to shrink, the free end of the Janus rod starts to bend and reaches a final shape resembling a hook (see figures 6.15b and c).

This bending impacts the total drag force on the bilayer. As a result, the Janus microbot alters its trajectory and descends in the $z-$axis. The overall trajectory can be seen in figure 6.15d with a minor drift in the $xy-$plane. In figure 6.15a, the left edge of the bilayer is positioned along the $y-$axis passing through $x = 0$. However, the final

(a) Initial position of active Janus rod is given.

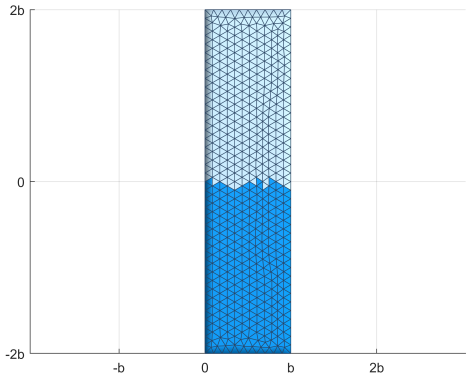

(b) Final configuration of the Janus rod is viewed in $yz-$plane.

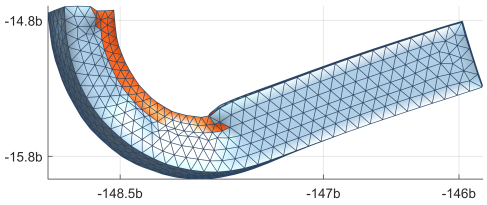

(c) Final configuration of the Janus rod is shown from $30° - 30°$ angle.

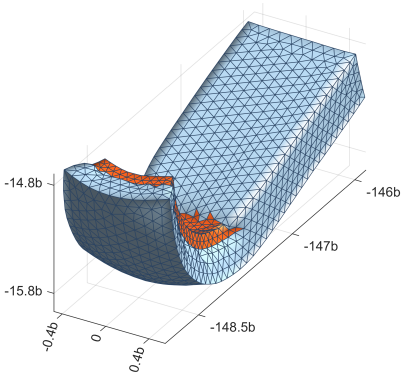

(d) Trajectory of the active tip is given in $yz-$plane.

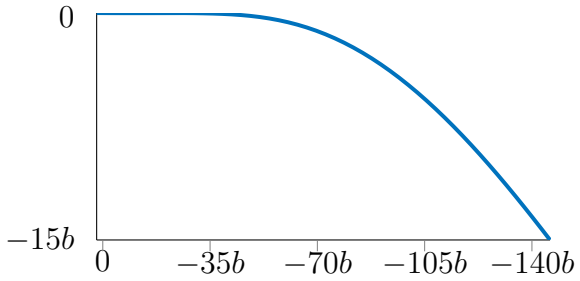

Figure 6.15: Responsive Janus bilayer deforms into a hook-like shape. The switch in the shape results in a change in trajectory.

shape in 6.15c shows that the left edge is drifted towards the $-x-$axis.

A characteristic of active and responsive Janus rods is the opposite directions in deflection and trajectory. This correlation could potentially enable smart navigation for turning corners. Recently, Ganguly and Gupta (55) theoretically suggested similar dynamics for asymmetric bent Janus rods using phoretic motion. The same study numerically showed that, in the presence of a bent section near one of the tips, the Janus particle follows a trajectory that can be described by a circle equation, with which our results qualitatively agree.

(a) Deformation of the rod is captured in the middle of the simulation.

(b) The shape is drawn in the $yz-$plane.

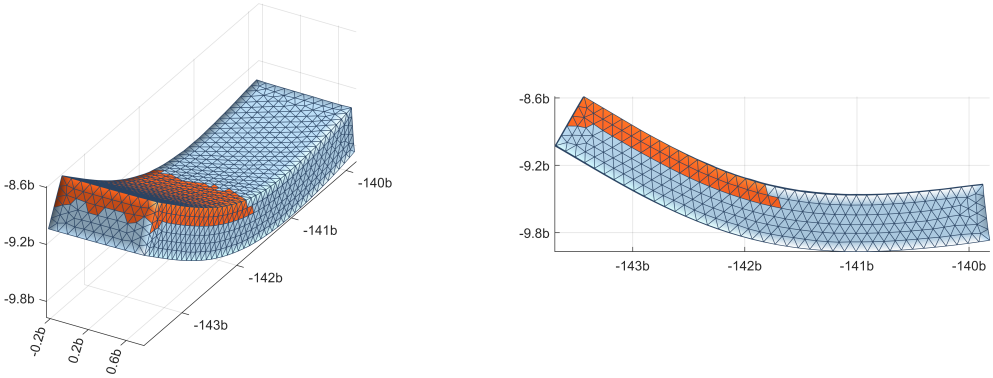

(c) Deformation of the rod is captured at the end of the simulation.

(d) The final shape is drawn in the $yz-$plane.

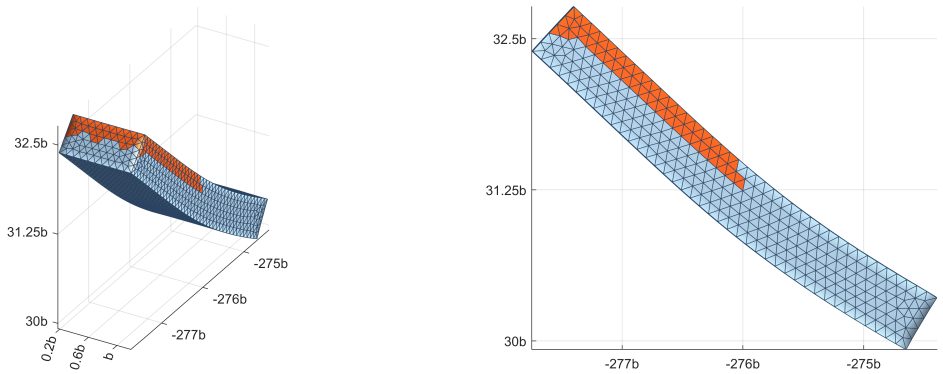

(e) The trajectory of the rod is provided.

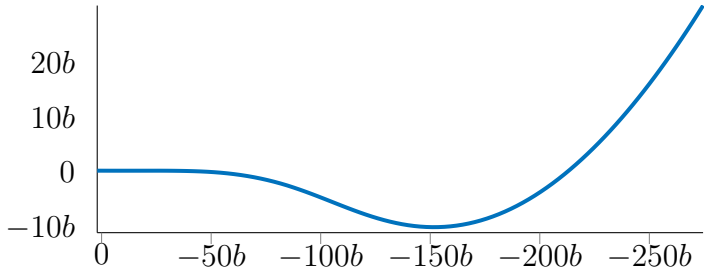

Figure 6.16: Shrinkage and recovery can be used to direct the trajectory of the rod. Panels (a) and (b) are depicted at $t = 0.5$. The orange section represents the responsive area after shrinkage, while the rest of the body is non-responsive.

To guide the trajectory of the rod, a combination of deswelling and swelling may be the ideal strategy. While shrinkage initiates the descent in the $z-$axis, the recovery phase should conclude this period and lead to a change in trajectory.

To verify this, we simulate a two-pulse system. The first pulse triggers the shrinkage at $t = 0.1$, and the second pulse begins the recovery at $t = 0.3$, corresponding to instant heating and cooling, respectively. Until the second pulse, all dynamics are identical to the previous case. However, after triggering the recovery process, the responsive layer swells. This is accompanied by relaxation at the active tip, which corresponds to a descending motion (see figures 6.16a to d). Eventually, the Janus microbot returns to its original straight rod shape. However, its orientation differs from the initial one. As shown in figure 6.16d, the final shape after recovery makes an angle with the $y-$axis instead of being parallel.

The impact of this shape and angle transformation is evident on the trajectory in figure 6.16e. Following the descending motion in the $z-$direction, the motion reaches a plateau. The plateau phase ends quickly, and the Janus rod ascends. The dynamics of this double-pulse system suggest the possibility of the fine-tuning the trajectory of active swimmers. We demonstrate that by exerting a follower force and employing responsive hydrogels, the motion in one axis can be controlled. In addition, this control mechanism comes with a negligible drawback, as the drift in the $x-$axis is minimal compared to the displacement in the $yz-$plane.

We proceed by suggesting another method for trajectory navigation. In our final simulation setup, we introduce multiple responsive regions to the active Janus rod. The design incorporates responsive beads positioned diagonally between $y < -b$ and $z > 0.25b$, and $-b < y < 0$ and $z < 0.25b$. After deflection, the free tip forms an S-shaped pointing towards $-z$-direction (see figure 6.17a and b). Consequently, the hydrogel ascends in the $z-$axis (see figure 6.17c).

The primary difference from the previous single responsive layer case is the elevation in the $z-$axis due to a change in tip-to-tip distance. The Janus rod with multiple re-

(a) Multiple active regions result in an asymmetric shape.

(b) Final configuration of the Janus rod is viewed in $yz-$plane.

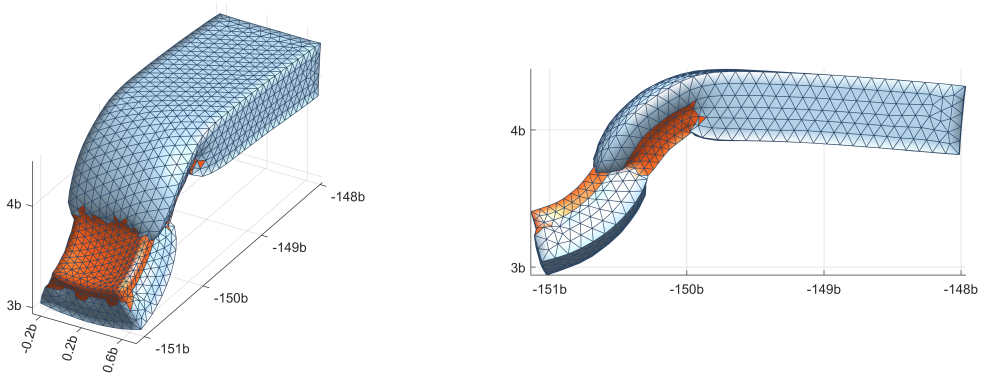

(c) Trajectory of the active tip is given.

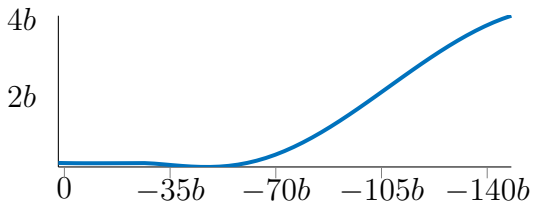

Figure 6.17: Active Janus rod with multiple responsive regions deforms and changes its direction. Figure c) is captured from a $90° - 0°$ angle.

sponsive areas exhibits a more elongated shape, which aligns parallel to the exerted force. Therefore, the angle between the tip force and the $y-$axis is reduced, leading to a smaller perpendicular component of the drag. Thus, the number of active regions may influence and control the trajectory of the active Janus rods by exploiting drag anisotropy.

With these results, we complete our numerical examination. In the next section, we will briefly discuss the findings of this chapter.

6.4 Discussion

In this chapter, we have presented shape-shifting microbot designs. The microbots have sensitive regions which can actuate anisotropic responses, thus enabling behaviours like bending, rotating, and non-reciprocal swimming.

We begin by demonstrating the shape switches between fundamental bending modes.

Inspired by the microbots in Chapter 2, we transform straight rod-shaped hydrogels into U- and S-shaped bilayers. The first transformation is achieved by utilising a single responsive layer covering half of the material, while the latter occurs due to the presence of multiple responsive areas positioned diagonally. Throughout these shape changes, we have examined the impact of different parameters including the ratio of responsive beads to the total number of beads and the surface area of the responsive layer.

An important observation is the faster dynamics as the ratio of responsive beads increases. This is due to increasing elastic stresses in the hydrogel. Regarding the effect of surface area on the dynamics, we have noted that the bending becomes more pronounced with the increase in the surface area of the responsive layer.

In addition to U and S shapes, we have introduced more complex geometries. By increasing the number of sensitive areas, a wave-like curvy structure has been obtained. For these structures, we have investigated the recovery dynamics. As the material cools down, it swells and returns to its original configuration and volume.

We have replicated the previous experimental study conducted by Hippler et al. (72), focusing on bilayers attached to a fixed surface. Our findings reveal that as the length of the bilayer increases, the deflection begins to create a rolled-up shape. Subsequently, we have examined microrods with multiple responsive sections and demonstrated that as the number of responsive layers increases, the hydrogels exhibit less planar motion. These results have inspired us to propose more practical designs for artificial microswimming studies.

Initially, we have provided a self-folding structure with a responsive face. This star-shaped structure holds the potential for loading and carrying microcargo. By exploiting the shrinking dynamics, a planar shape deforms and folds towards the centre of mass, creating a bowl-like shape. In the same numerical experiment, we have explored different designs by increasing the number of arms or altering the shape of arms. These variations offer benefits such as increased holding stability or the ability to grasp objects of different sizes.

Subsequently, we have numerically engineered stars with responsive arms only. The presence of a non-responsive layer at the centre has changed the dynamics dramatically. The middle section ascends in one direction. This shape can be used for vacuuming and protecting objects, or generating a periodic beat.

Finally, we have integrated the follower force problem from Chapter 5 with shape-shifting microbots. A simple design involving a Janus rod with a single layer of responsive PNIPAM at the free tip has been employed. The Janus swimmer is propelled by a non-conservative force at the other end. Upon shrinkage, the trajectory of the rod points in the opposite direction to the deformation.

We have combined this feature with the recovery phase in a double-pulse mechanism. The first pulse initiates the shrinkage, hence, an alteration in the followed path. With the second pulse, the route of the swimmer shifts to the opposite direction. Additionally, an extra responsive layer is added to the Janus rod. The active swimmer with multiple sensitive sections performs similar but slower dynamics compared to the first model. Thus, we have demonstrated two different methods of controlling the trajectory for active and responsive Janus microbots.

This chapter has served as a mostly qualitative description of proof-of-concept shape-shifting microswimmers. In the next chapter, this thesis will be concluded by sharing the key findings and future work.

CHAPTER 7

CONCLUDING REMARKS

This thesis commenced with an exploration of the catalytic bubble growth mechanism on bubble-propelled microswimmers. Following this, it presented a versatile numerical approach for modelling the dynamics of hydrogel-based microbots. The numerical technique integrated an elastic bead-spring system and the method of regularised Stokeslets. The method was used not only to obtain physical insights concerning theoretical and experimental studies but also to propose future designs for intelligent microbots intended for biomedical applications.

7.1 Highlights of Findings

We began our study by investigating the effects of shape on the swimming dynamics of hydrogel microbots in a collaboration with Dr Juliane Simmchen and Dr Ivan Rehor. I-, U-, and S-shaped microswimmers used catalase enzyme to decompose the H_2O_2 solution into O_2 gas, thereby facilitating the bubble propulsion. It was observed that the bubble growth mechanism causes two types of translation. During the initial growth phase, the bubbles push the surrounding fluid, which gives the microbot a steady slow translation. Our mathematical model and experimental data indicated that the bubble growth occurs with a constant molar flux at each cycle, however, the flux diminishes over time. This reduction is attributed to the degradation of the catalase enzyme at the active tip, resulting in slower

growth and decay in the maximum bubble radius.

Following this, the film covering the bubbles gets thinner and ruptures due to oscillations at the air-water interface. The bursting of bubbles generates a jet; therefore, the microbot moves forward with an impulse. Later, we captured different swimming characteristics stemming from variations in shape and symmetry. Depending on the number of active tips, I-shaped swimmers either pumped the fluid around without any movement or underwent ballistic translation. U-shaped swimmers exhibited pure translation or translation with rotation, contingent upon symmetry in nucleation sites. S-shaped swimmers demonstrated rotation with varying frequencies according to the number of active tips. In addition, it was shown that the randomness in the location of bubbles and minor flaws in the manufacturing process influenced the swimming characteristics. The study, published in the Journal of Advanced Intelligent Systems, motivated us to devise a mechanism for transitioning between the I, U, and S shapes. These shape changes could effectively control the trajectory of the microbot.

To achieve this objective, we focused on hydrogel microbots, whose flexibility could be harnessed for shifting their shapes. To understand the dynamics of deformation in these materials, we developed a numerical framework that couples a bead-spring system with the method of regularised stokeslets. Our methodology emulated the flow through the poroelastic medium by distributing regularised stokeslets on the beads. Following the validation of the method, we delved into the physics of active hydrogel filaments.

The filaments were exposed to non-conservative end forces at one end or both ends. The problem was defined by a dimensionless parameter, σ which is effectively the ratio of tip force to the elastic forces on the filament. Depending on this parameter, the regimes of the motion of Janus filaments were categorised as pure translation and translation accompanied periodic oscillations. In the second regime, deformations changed the trajectory of the filaments. As σ increased, the filaments transitioned from side to side bending to corkscrew-like rotations.

For Saturn filaments, more complex dynamics were detected. Small values of end

forces were unable to break the symmetry; therefore, filaments remained stationary and functioned as micropumps. With increasing force, deformations began to occur in four different regimes.

First, filaments formed a stable U shape and translated ballistically. Then as σ increased, filaments buckled into an asymmetric 1^{st} bending mode, which leads to a spiral trajectory with an increasing radius of rotation. With larger tip forces, the filament performed a run-and-tumble motion. Following brief intervals of propulsion or running, the viscous drag became more pronounced at the middle section of the filament, prompting a change in direction, known as tumbling. In the final regime, the motion was governed by an unstable buckling problem, making it more challenging to discern distinct patterns amidst shifts between higher buckling modes. With this part of the study, we demonstrated that the presence of non-conservative end forces alone is sufficient to induce periodic changes in the shape of filaments.

Another way of controlling the deformations of microbots involves using responsive hydrogels capable of swelling or shrinking based on external factors such as changes in temperature or pH. By adjusting the cross-linking density, it is possible to obtain nonuniform responses along the hydrogel body. To exploit this mechanism to execute complex tasks, we modified our numerical bead-spring system. This updated method was designed to contract the springs in response to thermal fluctuations and create internal stresses. Initially, we demonstrated transitions between passive microbots in the shapes of I, U, and S. The shrinkage was observed to occur almost immediately. Additionally, for passive bilayers attached at one end, the length of the structure impacted the dynamics. As the bilayers became longer, they started to roll more. Following this, we proposed star-shaped microcarriers, which are able to self-fold for loading and unloading objects.

Lastly, we combined the shape-shifting concept with the follower force problem. The resulting design was a steerable translator, essentially a Janus rod with a responsive region. Initially, the microbot was propelled by a force that allowed it to translate without deformation. However, as the responsive layer shrank, the microbot bent at the free end.

This shape led to a different trajectory from that of pure translators. Later, the same swimmer was modified with a recovery mode. This mechanism enabled us to control the trajectory of the rod. Following recovery, the rod altered its direction. Overall, we offered simple designs for controlling the trajectory of the microbots, which could be useful to accomplish complex tasks.

In summary, this thesis has advanced our understanding of hydrogel-based microbots and the bubble propulsion mechanism. Moreover, it has introduced two numerical tools for modelling flows through porous structures and estimating the radius of curvature for slender bodies such as flagella. However, there is still plenty of room to improve the developed methodology and explore the intriguing areas of artificial swimming. In the following section, we will outline planned future work.

7.2 Future Work

A number of extensions are possible to increase the accuracy and versatility of the developed methodology. Here, we begin with the bubble growth model.

Chapter 2 provides a mathematical model explaining how bubbles grow at the catalytic end and what swimming characteristics occur. However, the model does not delve deeply into the properties of the exerted force on the nucleation sites. To gain a better understanding of this aspect, a numerical model could be beneficial. The interplay between growing bubbles, ambient fluid, and porous hydrogel structure can be considered as a three-phase fluid-solid interaction problem. Therefore, the numerical method should be robust and reliable.

For this purpose, previously we collaborated with Dr Mostafa Safdari Shadloo, who is also a co-author of the submitted article "Numerical modelling of heterogeneous stimuli-responsive hydrogels". In our collaborative work, the objective was to develop a simulation based on the Lattice-Boltzmann method (LBM). A similar numerical method can be developed by using a hybrid approach combining the Immersed Boundary and Front-

Tracking methods; however, the selection of the Lattice-Boltzmann scheme is due to our collaborator's expertise in the technique. Although the numerical model is yet to be completed, it holds the promise of physical insight into the nature of forces exerted by growing bubbles, such as magnitudes of forces as a function of time and the damage on active tips due to the bubble collapse mechanism. Access to such knowledge would come along with another prospective extension.

So far, we have modelled follower forces as non-conservative in direction, but constant in magnitude as a simplification. However, this is not necessarily the case in general. Factors including the depletion of local solution concentration or cycle-to-cycle fluctuations in the molar flux of O_2 gas can introduce time-dependent forces. Implementation of this feature in the bead-spring model is straightforward. Similar to the varying spring stiffness in double-pulse mechanism in 6.3, the follower force can be defined as an array rather than a constant value. The presence of time-dependent tip forces could alter the overall dynamics for active Janus and Saturn filaments. The controlled exertion of follower forces in a timely manner can offer new swimming characteristics and means that could hold the key to novel treatment strategies. For example, ceasing force implementation after the running phase might bypass the tumbling mode, leading to filament relaxation.

In terms of follower forces, the final modification would be proposing a general mathematical model capable of calculating the local tangent vectors in arbitrary points on curved surfaces. In our current methodology, we assume that the tip surfaces are planar and remain undeformed under external forces. Therefore, a uniformly distributed force acts on the plane over every bead on the tip surface. However, our aim is to extend our methodology to more complex shapes including hyperbolic paraboloids. Additionally, we have observed that active tips may deform and bend in heterogeneous responsive hydrogels. In these cases, the normal vectors would vary across the surface.

This issue can be tackled by using connectivity information of tetrahedra. Meshing with tetrahedral elements ensures that each bead on the tip surface is connected with at least two other surface beads, and at least one bead in the interior volume (see figure 7.1).

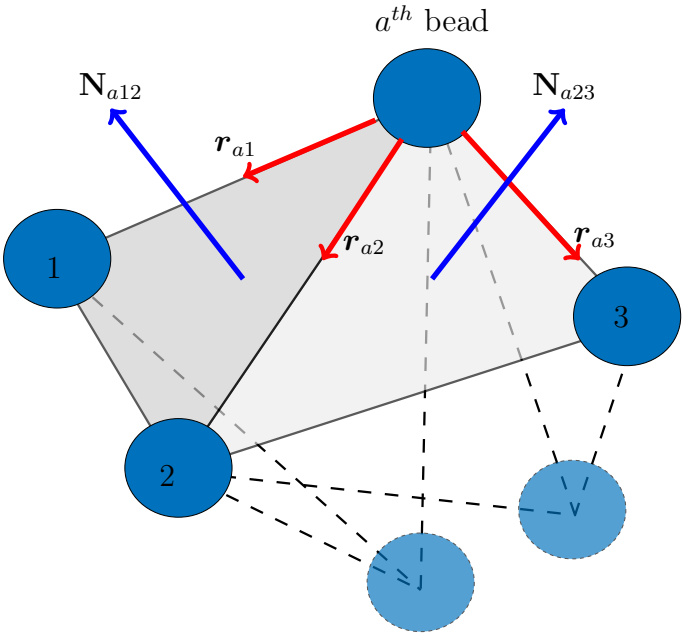

Figure 7.1: The unit normal vectors $\mathbf{N}_{a12}$ and $\mathbf{N}_{a23}$ are stored for each bead in their respective triangles. As the a^{th} bead serves a common corner for both triangles, the unit normal on bead a is computed as the average of $\mathbf{N}_{a12}$ and $\mathbf{N}_{a23}$.

By using the equation 5.3, we can calculate the surface normal for each triangle on the surface. Then, the same unit vector is stored for each bead on the corners of the triangle. At this point, the interior beads are essential to sense the direction of the unit normal vector, and ensure that the compressive (tensile) tip force is always exerted in the inward (outward) direction as suggested by Smith et al. (165). In terms of the magnitude of the force in each time step, we would adhere to distributing the force equally among each bead. By implementing such an algorithm, we can enhance the accuracy of our numerical methodology.

Apart from the method used to determine forces, there is scope for refinement in determining spring stiffness for arbitrary shapes. The 3D DLSM formulation is designed for rigid elastic materials with unstructured meshes, thus, it does not account for pores when relating spring stiffness with real-life parameters. Consequently, the simulations in Chapter 6 may not fully represent the dynamics of PNIPAM-based shape-shifters. To address this limitation, we intend to modify the 3D DLSM formulation by comparing it

with experimental data. For this purpose, we may collaborate with experimental experts, such as Prof Anne Juel of the University of Manchester. In such collaborative efforts, the sedimentation problem of disc-shaped microplates could serve as an initial focal point.

The mentioned problem offers a fine-tuning opportunity for the 3D DLSM formulation since it has a constant force exerted on all beads for a circular shape. Consequently, for a deforming disc, the impact of spring stiffness can be isolated. Throughout the tuning process, we will also investigate the regularisation width and blob function to improve the accuracy of our solution. These parameters directly affect the drag on the material; hence, they may considerably change the dynamics. Additionally, a "shell" model will be considered for the regularised stokeslets. With the shell model, we restrain the impact of regularised stokeslets on each other based on the distance. This approach is commonly practised in both SPH and LBM, effectively assigning a lattice or a threshold distance for the impact.

Once the aforementioned modifications are implemented, we will utilise the findings of this thesis to propose alternative control strategies for microbots. For example, section 6.2.1 showed an I-to-U transition for passive and responsive hydrogels. After being capable of calculating the normal vector for a deformed tip surface, this transition can be achieved for an active microbot. Therefore, a scenario where a micropump bends into a symmetric U-shaped swimmer, translates ballistically in a straight path as long as desired, and then reverts pumping in the new location by recovering back to its original shape could be realised.

Another prospective implementation could involve controlling a run-and-tumble motion. Transitioning from an S-shaped to an I-shaped swimmer may halt the tumbling phase. This could be achieved with a fully responsive hydrogel. Taking advantage of increasing stiffness during shrinkage, we can effectively reduce the σ parameter in addition to shape change. Consequently, the hydrogel adopts a rod-like shape and pumps fluid around after running.

Another theoretical design concept could revolve around responsive microribbons. Sec-

tion 6.2.4 showcased that the thickness-to-length ratio plays a significant role in the folding behaviour. By incorporating responsive layers to a microribbon, twisting and curling behaviours can be triggered in addition to rolling. These out-of-plane deformations would bring additional functionality, such as twining around an object like a vine. One practical application would be capturing the rod-shaped viruses. Alternatively, a more innovative approach could use these ribbons as joints for self-assembly purposes, enabling the tying knots to attach microobjects.

Before discussing future comparison studies, we would like to explore one final simulation case. In Chapter 5, we reported a run-tumble-helical behaviour for certain Saturn filaments. This transient regime shares some common features with the motion of active and responsive Janus particles. In both simulations, we have observed a helical or circular orbit that swimmers follow. From this perspective, our numerical studies align with the findings of the previous study of Ganguly and Gupta (55), suggesting that rigid Janus particles with bent sections would rotate in circles. However, in the case of active Saturn filaments, we are required to explore the dynamics in more detail. For this purpose, we plan to conduct more extensive simulations in this regime.

Throughout this thesis, we have mentioned some alternative formulations for different components of the numerical model. A notable example is the beam theories for modelling the buckling and bending of filaments, that we used in Chapter 4 for a qualitative comparison with the literature (107). While we employed a bead and spring formulation to address the elastic deformations for arbitrary shapes, beam theories such as Euler-Bernoulli (6) and Timoshenko-Ehrenfest (82) models have been widely used for modelling slender filaments and flagellated motion. The difference between the two models is the consideration of shear forces acting on the beams and rotational effects. Consequently, a direct comparison with one or more of these models would improve the precision of the numerical method.

Finally, we will validate our responsive hydrogel simulations against the poroelastic model proposed by Butler and Montenegro-Johnson (17). While our model is capable of

estimating the bulk dynamics, there is potential for enhancement through such comparative analyses. For instance, since regularised stokeslets do not enforce no-slip boundary conditions on the bead surfaces, we were unable to conclusively determine the time scales of swelling and deswelling. The theoretical model of Butler and Montenegro-Johnson (17) would provide this information, therefore, we can improve the accuracy of our bead and spring system. With suggested modifications and comparisons, we would have a robust and adaptable numerical tool that can aid in designing novel artificial microswimmers for biomedical applications in the near future.

APPENDIX A

THE CODE

Here, we present the numerical algorithm that is used in Chapters 5 and 6. The main body of the method is structured as the following:

Algorithm 1 Algorithm for simulating porous and flexible hydrogels

Procedure:

1. Initialise material properties
2. Upload geometry and mesh: *filament.m*
3. Parse geometry: *tet_mesh_to_bead_spring.m*
4. Initialise time parameters
5. If necessary, bend filament into a curve: *bending.m*
6. If necessary;
   (a) find end points and create follower force
   (b) perturb initial position: *start_perturbed.m*
7. If necessary; add responsivity: *responsivity.m*
8. Time loop for solving algorithm: *gel_dynamics_full_nonlocal_hydro_implicit.m*
9. Store results in a folder: *folder_creator.m.*

In above algorithm, italic names with "*.m*" extension denotes the in-house functions build for specific routines.

APPENDIX B

CURVATURE POST-PROCESS TOOL

The curvature, κ, and torsion,τ, are determined by the Frenet-Serret formulas as follows:

$$\frac{d\mathbf{T}}{ds} = \kappa\mathbf{N}, \tag{B.1}$$

$$\frac{d\mathbf{N}}{ds} = -\kappa\mathbf{T} + \tau\mathbf{B}, \tag{B.2}$$

$$\frac{d\mathbf{B}}{ds} = -\tau\mathbf{N} \tag{B.3}$$

where $\mathbf{T}$, $\mathbf{N}$, and $\mathbf{B}$ are the unit tangent, normal, and binormal vectors, respectively. The above equations are parametrised with respect to the arclength s.

The curvature post-process tool is designed to eliminate noisy data and provide a smooth evolution of the curvature along the arclength over time by using equations B.1 to B.3. The algorithm in the tool begins with finding the arclength.

This is achieved by calculating the tip-to-tip distances in each direction. Subsequently, the algorithm identifies which direction has the longest edge. Once the direction of the long axis and the arclength are determined, the algorithm proceeds to sort it out the points in ascending order along that direction. This sorting is necessary due to mesh generation on *GMSH*. In the geometry creation process, we first assign the corners of a 2D shape, followed by extruding it as translation in the 3^{rd} axis. Moreover, Delaunay triangulation follows a process of creating the neighbours and then neighbours of neighbours, rather than moving and assigning points in one direction. As a result, the data points should be

sorted, and the built-in function sort is used for this purpose.

Following this, we select a line on the filament, which is not necessarily the centre-line. Depending on our interest, the straight line can be an edge for a rectangular beam or similarly a line on the surface of a circular filament. For instance, in the case of a responsive hydrogel, it might be necessary to check the curvature of both responsive and non-responsive layers. Therefore, the centreline would not provide the required information.

The straight line is determined as checking the values in a range in one direction. To accomplish this, a small tolerance is assigned due to concerns about the computer precision. Let the tolerance value be δ, and suppose the long axis of the filament is in the $y-$ direction. Then, the indices of the edge can be detected as the intersection of points in the x and z directions:

$$x_1 - \delta < x < x_1 + \delta, \qquad z_1 - \delta < z < z_1 + \delta \tag{B.4}$$

where x_1 and z_1 are the arbitrary values. The intersection in equation B.4 is stored in an array, namely *ind*. Following this, the variables are initialised. An important variable is the smoothing parameter, *sp*, which satisfies $0 < sp < 1$. The lower bound corresponds a fully smoothed function, while the upper bound represents no smoothing at all. After initialisation, the curvature post-process algorithm operates in loop over time. The pseudo-code is provided in algorithm 2 for only one direction, therefore, it should be noted that the original algorithm repeats the same steps for all three directions within the same loop.

The built-in function csaps computes the cubic smoothing spline of any given function. The first argument of the function is the data points provided by the user, and the second argument is the values aimed to be fit. The third argument is the smoothing parameter, *sp*. In line 1a, $sp = 1$ since we are only changing the data form of the original function rather than interpolation. Following this, we use unmkpp and mkpp functions of

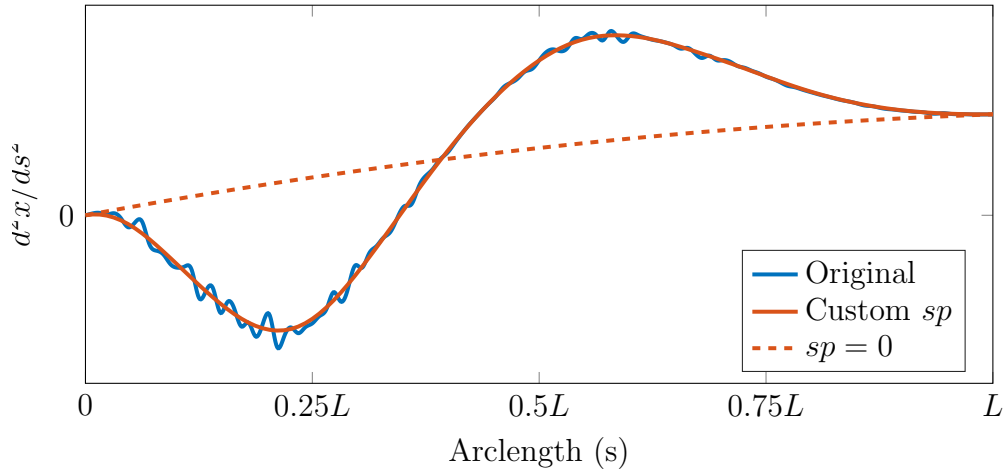

Figure B.1: Noisy data is removed out from the function d^2x/ds^2 using algorithm 2.

MATLAB®. The former extracts the polynomial details as breaks, coefficients, number of intervals, order, and dimension of target as the outputs in line 1b. With the latter function, we reconstruct the piecewise polynomial with a modification. The second argument, repmat, manipulates the coefficients of the interpolated function. Therefore, we reduce the polynomial by one order. Finally, line 1d completes the procedure by creating a piecewise polynomial for $dx(s)$ using the ppval function, where the second argument specifies the query points.

After that, the same procedure is followed for the second derivatives between lines 1e to 1h. In figure B.1, we demonstrate the original function and the smoothed versions with different sp values for $d^2x(s)$ at an arbitrary time point. The algorithm significantly smooths the initial data. The rest of the code obtains tangent, normal, and binormal vectors as given in equations B.1, B.2, and B.3. Similarly, we unwrap and reconstruct those functions to store smoothed curvature and torsion data. Finally, both data sets are plotted as contours over time and arclength.

Algorithm 2 Curvature smoothing algorithm

Procedure:

1. For $j = 1$ to t_{max} do
   (a) Evaluate points of $x(s)$: $pp\_x = csaps(y(ind), p\_xs(j, ind), 1)$
   (b) Extract the polynomial details: $[breaks, coefs, l, k, d] = unmkpp(pp\_x)$
   (c) Build the piecewise polynomial for the 1^{st} derivative: $p\_dx = mkpp(breaks, repmat(k-1:-1:1, d*l, 1). * coefs(:, 1:k-1), d)$
   (d) Compute $dx(s)$: $dxds = ppval(p\_dx, y(ind))$
   (e) Evaluate points of $dx(s)$: $pp\_dx = csaps(y(ind), dxds, sp)$
   (f) Extract the polynomial details: $[breaks, coefs, l, k, d] = unmkpp(pp\_dx)$
   (g) Build the piecewise polynomial for the 2^{nd} derivative: $p\_ddx = mkpp(breaks, repmat(k-1:-1:1, d*l, 1). * coefs(:, 1:k-1), d)$
   (h) Compute $d^2x(s)$: $ddxds = ppval(p\_ddx, y(ind))$
   (i) Obtain curvature: $curvature = \sqrt{ddxds.^2 + ddyds.^2 + ddzds.^2}$
   (j) Evaluate points of curvature: $pp\_curv = csaps(y(ind), curvature, sp)$
   (k) Store curvature: $Curv\_mat(:, j) = ppval(pp\_curv, ds)$
   (l) Compute normal vector: $n\_x = ddxds./curvature$
   (m) Compute binormal vector: $A = [dxds(:), dyds(:), dzds(:)]$, $N = [n\_x(:), n\_y(:), n\_z(:)]$, $B = cross(A, N)$
   (n) Evaluate points of binormal vector: $B_x = csaps(y(ind), B(:, 1), sp)$
   (o) Store binormal vector components: $Bi\_mat\_x(:, j) = ppval(B\_x, ds)$
   (p) Extract the polynomial details: $[breaks, coefs, l, k, d] = unmkpp(B\_x)$
   (q) Build the piecewise polynomial for the 1^{st} derivative of binormal vector: $p\_Bx = mkpp(breaks, repmat(k-1:-1:1, d*l, 1). * coefs(:, 1:k-1), d)$
   (r) Compute $dB_x(s)$: $dBxds = ppval(p\_Bx, y(ind))$
   (s) Evaluate points of $dB_x(s)$: $pp\_dbx = csaps(y(ind), dBxds, sp)$
   (t) Compute dot product for torsion: $B\_der = [dBxds(:), dByds(:), dBzds(:)]$, $tor\_mat = dot(-N', B\_der')$
   (u) Evaluate points of torsion: $pp\_tor = csaps(y(ind), tor\_mat, sp)$
   (v) Store torsion: $tau(:, j) = ppval(pp\_tor, ds)$
2. Plot curvature contour: $contourf(tt, ds, Curv\_mat(:, tt))$
3. Plot torsion contour: $contourf(tt, ds, tau(:, tt))$

APPENDIX C

SUMMARY OF RESEARCH ARTICLES

C.1 Published Work

Fundamental Modes of Swimming Correspond to Fundamental Modes of Shape: Engineering I-, U-, and S-Shaped Swimmers - *Priyanka Sharan, Charlie Maslen, Berk Altunkeyik, Ivan Rehor, Juliane Simmchen, Thomas D. Montenegro-Johnson*

This study introduces a straightforward approach to incorporating multiple swimming modes into catalase-propelled hydrogel structures, produced using stop-flow lithography (SFL). The research investigates the dynamics resulting from bubble expulsion and identifies that in "Saturn" rods, characterised by active poles and an inert midpiece, the primary swimming modes align with the first three fundamental shape modes achievable through buckling elastic filaments: I, U, and S-shapes. The paper was published in the Journal of Advanced Intelligent Systems.

C.2 Submitted Work

Numerical modelling of heterogeneous stimuli- responsive hydrogels - *Amin Rahmat, Berk Altunkeyik, Mostafa Safdari Shadloo, and Tom Montenegro- Johnson*

This paper presents a computational approach for modelling heterogeneous thermo-

responsive hydrogels, focusing on resolving local fluid-solid interactions within hydrogel pores during the deswelling process. The technique employed is a Lagrangian particle-based method, utilising computational grids to represent polymer beads within the hydrogel scaffolds. The study demonstrates that mechanical properties such as shrinkage ratio and elastic modulus directly influence the advancement of the fluid expulsion front during deswelling. Furthermore, the paper explores the impact of design heterogeneity on directional release through the development of simple heterogeneous designs inspired by Menger Sponge shapes. The article was submitted to Journal of Physical Review E.

Dynamics of Active Poroelastic Filaments in Stokes Flow - *Berk Altunkeyik, Tom Montenegro-Johnson, Amin Rahmat*

This paper starts with a brief literature review of soft matter and its applications in active microbot studies. Drawing inspiration from previous work simulating follower force problems, we propose a bead and spring method to investigate the dynamics of active poroelastic filaments. Focusing on exerted tip forces, our study suggests that flexible "Janus pusher" filaments may display oscillatory dynamics as they propel forward. Additionally, under specific conditions, "Saturn" filaments may exhibit "Run and Tumble" dynamics akin to bacteria, solely through elastohydrodynamic interactions. These findings highlight the potential role of flexibility in enhancing the functionality of active particles. The article was submitted to Journal of Physical Review E.

RESEARCH ARTICLE

ADVANCED INTELLIGENT SYSTEMS Open Access

www.advintellsyst.com

Fundamental Modes of Swimming Correspond to Fundamental Modes of Shape: Engineering I-, U-, and S-Shaped Swimmers

Priyanka Sharan, Charlie Maslen, Berk Altunkeyik, Ivan Rehor, Juliane Simmchen, and Thomas D. Montenegro-Johnson*

Hydrogels have received increased attention due to their biocompatible material properties, adjustable porosity, ease of functionalization, tuneable shape, and Young's moduli. Initial work has recognized the potential that conferring out-of-equilibrium properties to these on the microscale holds and envisions a broad range of biomedical applications. Herein, a simple strategy to integrate multiple swimming modes into catalase-propelled hydrogel bodies, produced via stop-flow lithography (SFL), is presented and the different dynamics that result from bubble expulsion are studied. It is found that for "Saturn" filaments, with active poles and an inert midpiece, the fundamental swimming modes correspond to the first three fundamental shape modes that can be obtained by buckling elastic filaments, namely, I, U, and S-shapes.

1. Introduction

Nanomotors and micromotors are self-propelling artificial machines that harvest energy from their environment (chemical, light, heat) and transform it into motion. The propulsion of motors originates from exploiting various phenomena, including bubble propulsion, diffusiophoresis, electrophoresis, and Marangoni flow, among others. Some of the earliest researched artificial micromotors were bubble-driven, where gas bubbles are released from the micromotor body due to decomposition of H_2O_2.[1–5] More recently, interest in bubble propulsion has declined due, in part, to the rise of novel phoretic propulsion mechanisms,[6–8] but also because existing manufacturing techniques are able to produce few adaptable properties, such as programmability of trajectories, or complex shape designs. Indeed, the geometries of bubble-driven micromotors have been largely restricted to tubes, or spherical particles, with notable exceptions including the stomatocytes, presented by the Wilson group, as one of the smallest bubble-driven micromotors.[9] Larger swimmers include cartridge-shaped polymer structures[10] and spherical micromotors,[11] while other complex geometries include spindle, drum, zigzag, and bilayer shapes[12] and helical motor bodies;[13] the performance of serrated swimmers, for example, was shown to depend significantly on geometry.[14] However, the previously used fabrication techniques including colloidal synthesis[9] and roll-up technology[2,15] are not capable of producing major shape variations or material composition of microswimmers, on-demand, to comply to a large variety of theoretically proposed designs.

From a hydrodynamical perspective, there are three aspects to bubble propulsion, which may be present in any given system. In the first stage, bubble growth causes the displacement of fluid. Due to the proximity of the swimmer to the bubble, this displacement is anisotropic, yielding a propulsive flow. This bubble may then eject from the swimmer, as in the propulsion of tubular microjets, and the swimmer is propelled forward at a velocity such that the net force on the bubble and swimmer is zero.[16] Alternatively, the growing bubble may violently collapse, creating a microjet of fluid perpendicular to the surface of the swimmer that impulsively propels the swimmer in the opposite direction over a very short interval.[17]

Gibbs et al.[18] presented a simple model based on the formation and release of oxygen bubbles that leads to a change in momentum, and used this model to describe the motion of spherical swimmers. Fomin et al.[19] fitted both ejection and

P. Sharan, J. Simmchen
Chair of Physical Chemistry
TU Dresden
01062 Dresden, Germany
E-mail: juliane.simmchen@tu-dresden.de

C. Maslen, I. Rehor
Department of Chemical Engineering
University of Chemistry and Technology
Prague, Czech Republic

B. Altunkeyik, T. D. Montenegro-Johnson
School of Mathematics
University of Birmingham
Edgbaston, Birmingham B15 2TT, UK

I. Rehor
Institute of Organic Chemistry and Biochemistry of the
Czech Academy of Sciences
Flemingovo nam. 2, 160 00 Prague, Czech Republic

The ORCID identification number(s) for the author(s) of this article can be found under https://doi.org/10.1002/aisy.202100068.

DOI: 10.1002/aisy.202100068

growth models to experimental results, and found that they did not fully account for the propulsive force, as the swimming speeds and bubble ejection frequencies are underpredicted by these models. An explanation for this was found in the capillary force induced through the asymmetry of the tube shape; this asymmetry led to a momentum transfer, which is counteracted by a jet force yielding higher velocities. In a later study, the same author extended their considerations to the mixing effect from the bubble ejection.[15] Other approaches include considering bubble geometric asymmetry and buoyancy force; Li et al.[20] found that the buoyancy force deforms the bubble, and therefore influences bubble release. In contrast to these methodologies, Gallino et al.[21] assumed that bubbles in tubular microjets remain spherical while passing through the inside of the tube, due to the predominance of capillary effects. Working in the zero Péclet number limit, Boundary Element Methods were used to sequentially provide the gas concentration via solution of Laplace's equation, and use the resulting bubble growth as boundary conditions for solving the Stokes flow equations.

In this article, we introduce chemically driven, hydrogel microswimmers produced using stop-flow lithography (SFL),[22,23] a high throughput microfluidic technique for the production of micrometer scale (~10–1000 μm) hydrogels (microgels) of arbitrary 2D shapes. Exploiting laminar flow of multiple streams in microfluidic channels allows the production of microgels with discretely variable composition. The method allows the production of poly(ethylene glycol) diacrylate (PEGDA) microgels with active regions (containing catalase enzyme) and inactive regions (composed of pure PEGDA). The spatial location of the active and inactive regions, coupled with the shape design of the microgels, leads to different motion behaviors—stationary, ballistic, and rotation. These three modes of propulsion correspond to the first three shape/bending modes of an elastic filament: a zeroth mode filament (straight, I-shape) with two active caps is stationary by symmetry, a filament bent into the first mode (one bend, U-shape) will translate but not rotate (by symmetry), and a filament bent in the second mode (two bends, S-shape) will rotate, as suggested in recent theoretical work on autophoretic swimmers.[24] It is expected, therefore, that this behavior may be recovered for a variety of propulsion mechanisms—modification of swimmer geometry, ultimately in an adaptable or programmable manner, may be used to control and modulate swimming behavior.

2. Results

A representative scheme of the production process in the SFL technique is shown in **Figure 1**a,b. The achieved structures are tens of micrometers in size (the size can be tuned by changing the magnification in Figure 1a,b). The successful incorporation of fluorescently labeled catalase in the hydrogel structure was proven by means of fluorescent microscopy, as well as by active bubble production after exposing the particles to peroxide fuel. The created bubbles increase the buoyancy of the hydrogel structures, so the motion is observed to be at the air–water interface, as commonly observed for bubble-driven motors.[25] A fraction of the particles with decreased to no activity were routinely observed sedimenting to the bottom surface, and are out of the focal plane and so unseen in the images. The active motility depends on the shape and enzyme distribution within the swimmers: two-component swimmers in a simple rod shape move ballistically (Figure 1c, e), while their three-component equivalents remain static while producing bubbles, which leads to fluid pumping instead, due to the higher symmetry of the system (Figure 1d,f). We found the catalase activity to be long lasting: when stored in the fridge (−20 °C), the particles could swim for about 14 days after fabrication, after which the activity declined noticeably.

The versatility of the SFL to flexibly change shapes during particle production was confirmed by exchanging the photomasks,

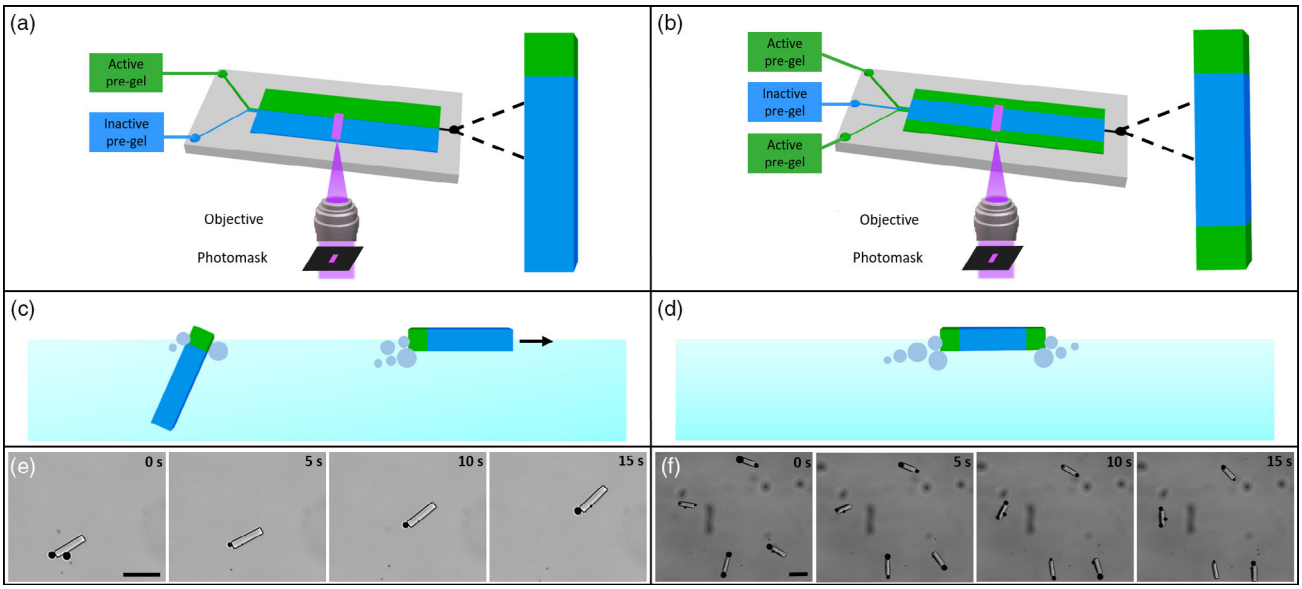

Figure 1. a) Fabrication principle of two component swimmers (further explanation in the text); b) fabrication principle of three component swimmers. c,d) Swimming principle at the air water interface of two and three component swimmers, respectively. e,f) Image sequence of bubble release versus motility, depending on the composition of the micromotors. Scale bar equals 100 μm.

and producing letters in the shape of U, I, and S (see **Figure 2** for the smaller microgel sizes and Figure S1, Supporting Information, for greater sizes). The shape in 3D is confirmed by means of scanning electron microscopy (SEM) images of freeze-dried microgels (Figure 2). The active and inactive regions in the swimmer body were indicated using dye labeling. Rhodamine-labeled catalase was used to label the enzyme-loaded region (active region) in the swimmer (indicated in red in Figure 2) and Fluorescein-*o*-acrylate was used to indicate the inactive regions of the enzyme (indicated in green in Figure 2). The thickness of the active region can be tuned easily by changing the flow rates of the active and inactive component with respect to each other. The active regions were kept small to control the position of bubbles effectively. A higher concentration of inactive component was chosen to increase the cross-linking density, which helped in preventing the diffusion of gas bubbles inside the inactive component, to an extent. Due to a two times lower PEGDA concentration in the active pregel composition, as compared with the inactive component, a slightly higher shrinkage at the edges of the fabricated letters was observed in the freeze-dried SEM samples.

We now analyze the periodic growth-collapse dynamics of the propulsive gas bubbles. This analysis comprises automated capture of the bubble radii as a function of time using custom routines (**Figure 3**a–c), together with a mathematical model for the bubble growth and a qualitative description of the collapse. The dynamics of microbubbles is dominated by surface tension[17] (i.e., the capillary number is small), and so the gas pressure P inside the bubble may be well approximated by the Laplace law $P = P_\infty + 2\sigma/r_\mathrm{b}$, for bubble radius r_b, and surface tension σ, and ambient pressure P_∞. The gas inside the bubble obeys the ideal gas law

$$PV = nRT \tag{1}$$

where n is the number of moles of gas present in the bubble, T is the temperature in Kelvin (assumed constant), and R is the ideal gas constant. We assume that the bubble remains spherical, so that $V = 4\pi r_\mathrm{b}^3/3$. Substituting these expressions into the ideal gas equation and taking the derivative with respect to time yields

$$\frac{1}{RT}\frac{\mathrm{d}}{\mathrm{d}t}\left[\left(P_\infty + \frac{2\sigma}{r_\mathrm{b}}\right)\frac{4\pi r_\mathrm{b}^3}{3}\right] = \frac{\mathrm{d}n}{\mathrm{d}t} \tag{2}$$

so that the bubble growth dynamics are given by

$$\dot{r}_\mathrm{b} = \frac{RT}{4\pi}\frac{\mathrm{d}n/\mathrm{d}t}{P_\infty r_\mathrm{b}^2 + 4\sigma r_\mathrm{b}/3} \tag{3}$$

where $\mathrm{d}n/\mathrm{d}t$ is the molar flux of gas into the bubble.

Under the simplest assumption, gas is produced at the catalytic surface at a constant rate, and moves immediately into the bubble, rather than diffusing through the surrounding solute—i.e., the flux of gas into the bubble is confined to a thin region at the catalytic surface. In this case, the molar flux $\mathrm{d}n/\mathrm{d}t = Q$, for some constant Q. Substituting Equation (3), we find

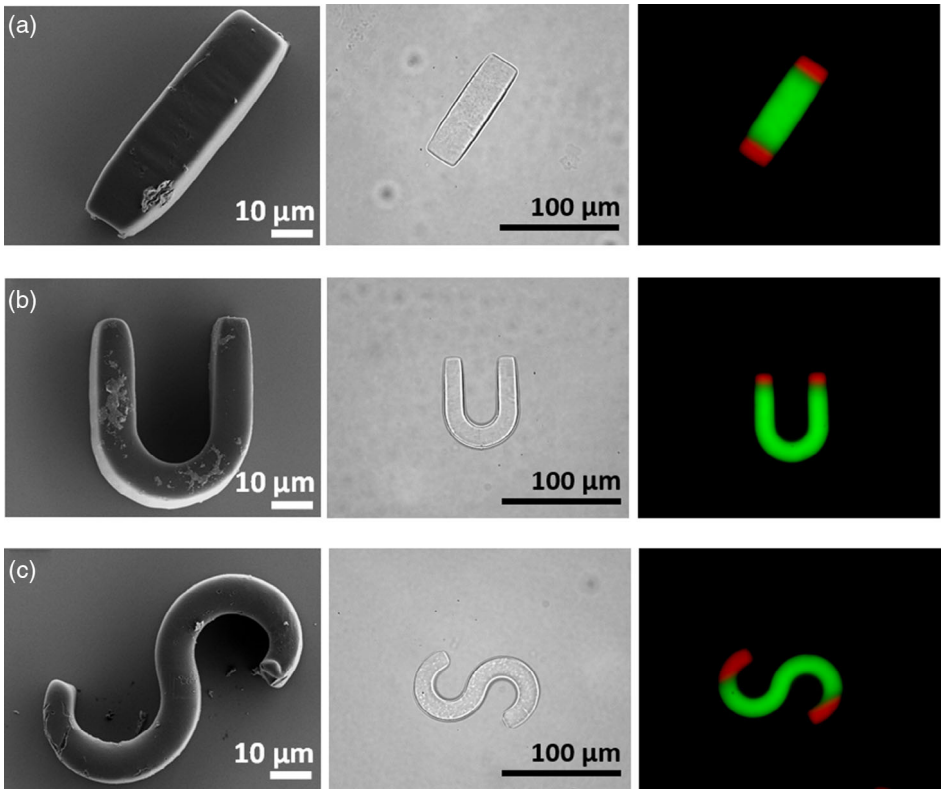

Figure 2. SEM micrograph, optical micrograph, and overlaid micrograph of different fluorescent channels, indicating the passive swimmer body (green) and the active, enzyme incorporating regions (red), respective of a) I-shaped swimmers, b) U-shaped swimmers, and c) S-shaped swimmers.

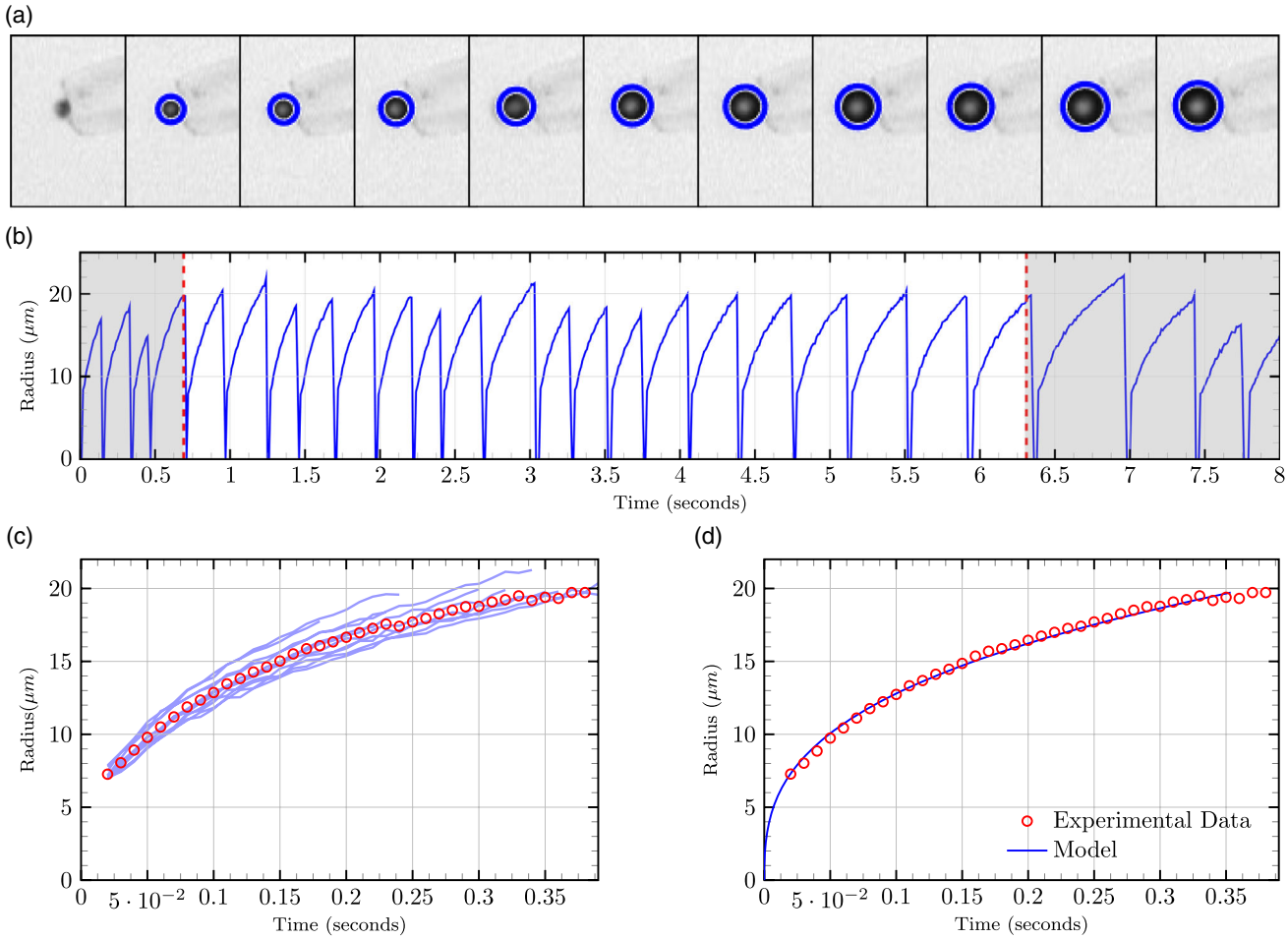

Figure 3. Analysis of the growth of a single bubble. a) Frame-by-frame of a single growing bubble over an entire growth cycle. The blue circle denotes the extent of the bubble, found via circular Hough transform. b) The radius of a single bubble as a function of time over multiple growth/collapse cycles. A subregion of clean data is selected to be used for phase averaging. c) Phase-averaged growth of the bubble, to be compared with modeling results. d) Model with a single parameter, the constant molar flux, fitted to experimental data, showing good agreement.

$$\dot{r}_b = \frac{RT}{4\pi}\frac{Q}{P_\infty r_b^2 + 4\sigma r_b/3} \Rightarrow \frac{P_\infty}{3} r_b^3 + \frac{2\sigma}{3} r_b^2 = \frac{RTQ}{4\pi} t \tag{4}$$

for time t, where we have used the initial condition $r = 0$ at $t = 0$. While this equation is not analytically invertible, it is a simple matter to numerically find $r_{b(t)}$ for a given Q. Taking values of $R = 8.314\,\mathrm{J\,mol^{-1}K^{-1}}$, $T = 293\,\mathrm{K}$, $\sigma = 7.2 \times 10^{-2}\,\mathrm{Nm^{-1}}$, and $P_\infty = 1$ atmosphere $= 101\,325\,\mathrm{Nm^{-2}}$, we find a value of $Q \approx 8.45 \times 10^{-13}\,\mathrm{mol\,s^{-1}}$, fitting our model well to phase-averaged experimental data (Figure 3d). There is significant variance in this fitted parameter from cycle to cycle, with slower growth phases typically having $Q \approx 6 \times 10^{-13}\,\mathrm{mol\,s^{-1}}$ and faster growing bubbles around $Q \approx 1.2 \times 10^{-12}\,\mathrm{mol\,s^{-1}}$.

This variation in the flux occurs from one cycle to the next stochastically, although we note a long-time (multicycle) trend of decreasing maximum bubble radius (**Figure 4**a) and slower bubble growth (Figure 4b). This long-time trend indicates that the molar flux of gas into the bubble decays slowly over time. Possible explanations for this include local depletion of solute near the swimmer and degradation of the catalytic enzyme. As this is true for both pumps and translators, which can move into areas replete with solute, we conclude that this decay is at least, in part, due to enzymatic degradation.

Finally, we examine the cause of the bubble collapse. As the bubble grows, the gas pressure lowers until it is similar to the pressure of the liquid, whereupon fluctuations can provide enough of a kick for collapse.[17] This point can be estimated via the Blake critical radius[26]

$$R_c = \left[\frac{9 m_g RT}{8\pi\sigma}\right]^{1/2} \tag{5}$$

The mass of gas m_g is approximated by the average flux in one of our bubbles $Q \approx 8.45 \times 10^{-13}\,\mathrm{mol\,s^{-1}}$ multiplied by the average time of a growth-collapse cycle $\approx 0.5\,\mathrm{s}$ using the data in Figure 3b. The critical radius is thus around 70 µm, while we see our bubbles collapsing at around 20 µm. Thus, it is likely that the cause of collapse in our case is interaction between the bubble and the air–water interface.

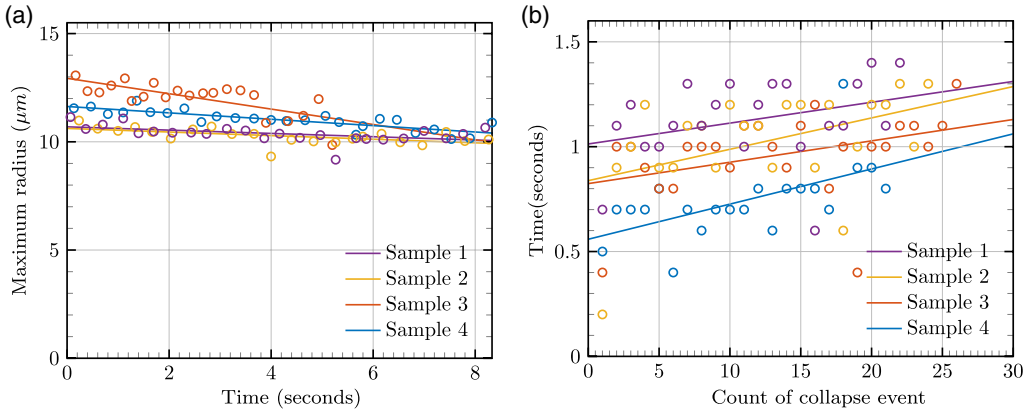

Figure 4. Multicycle analysis of four bubbles at different locations. a) Steady (linear) decay of the maximum bubble radius over time, indicating decay of the catalytic enzyme, or local depletion of solute. b) Period between collapse events, showing a steady increase.

We conclude with the observation that the effect of a collapsing bubble near a solid body is well documented, and results in a small jet of fluid that provides an impulsive force to the swimmer.[27] Thus, the bubble growth phase provides a steady propulsive force, while the collapse provides a sudden impulse from the ensuing microjet. We now characterize these dynamics more thoroughly.

When swimmers in the "I," "U," and "S" shapes were dispersed in H_2O_2 fuel, the observed swimmer dynamics was highly shape dependent (Figure S2, Supporting Information). In the "I" configuration, enzyme is located at both poles, and by symmetry the propulsive forces arising from the bubbles are equal and opposite, resulting in no net motion and a pumping "stresslet"-like flow (**Figure 5**a and Figure S9, Supporting Information, for theta and displacement vs time plot of Figure 5 particles, more examples in Figure S3 and S4, Video S1, S2, Supporting Information). Typically, a U-shaped swimmer prefers to propel ballistically, owing to its geometry (Figure 5b, and more examples in Figure S5, S6, Supporting Information). The gas bubbles located at the two poles of the "U" configuration impart a propulsive force in the same direction as each other, which is balanced by the drag force of the swimmer moving forward.

In the case of a perfectly manufactured S-shaped swimmer, propulsive forces are again equal and opposite, so that no net force is exerted on the fluid that needs to be balanced by drag

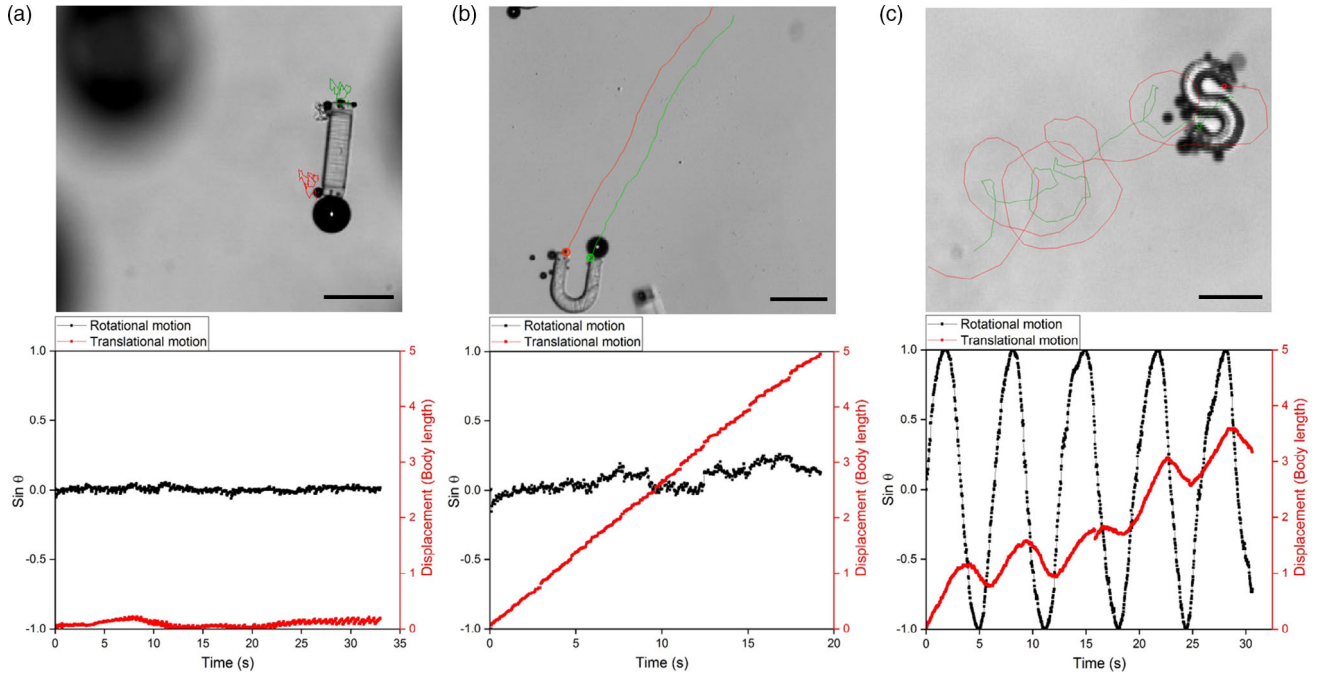

Figure 5. Typical motion patterns of the differently shaped particles: micrographs and corresponding analysis [sin Θ and displacement plotted versus time] of a) pumping of I-shaped swimmers, b) translating movement of U-shaped swimmers, and c) rotating S-shaped swimmers. Scale bar equals 150 μm.

arising from translation. However, the displacement of the forces about the center results in a torque that is balanced by the rotation of the swimmer. In addition, small differences in manufacturing and indeed inherent randomness in the bubble nucleation sites will almost always lead to a slight rotational asymmetry, in which case the S-shaped swimmer will also translate while rotating (Figure 5c, more examples in Figure S7 and S8, Supporting Information). In summary, a U-shape behaves as a propeller, an I-shape as a pump, and a S-shape as a moving rotor.

Localization of the bubbles on the microgel surfaces varies between the individual microgels. We ascribe this to the stochasticity of the bubble nucleation and growth, and the fact that surface irregularities, some small local defects, may foster the bubble nucleation at a particular spot. These nucleation spots on the active microgel surface remain unchanged over the course of the experiment involving hundreds/thousands bubbles formed. Different localizations of the bubble nucleation sites result in different microgel modes of motion. For example, in the "I" configuration, if additional bubbles are located at the sides of the swimmer body, in addition to the gas bubbles at the poles, the swimmer rotates and translates (**Figure 6**a, Figure S10, Supporting Information, for theta and displacement versus time plot of Figure 6 particles and Video S3, Supporting Information). The interplay of bubble growth and collapse at different locations results in a different motion pattern in this case. It is observed that a "U" configuration in which only a single pole is active can force the fabricated structure to rotate, in addition to translation (Figure 6b). The location of the gas bubble only at one pole results in unbalancing of the propulsive force (which is acting on only one side in this case as compared to when both the poles are active), producing a moment about the swimmer's center of drag that results in rotation. The ballistic motion of the U-shaped swimmer is compromised due to additional rotation of the swimmer; the rotation observed, however, was not as fast as that observed in the case of the "S" configuration. Since the motion of an S-shaped swimmer already has a translational and rotational component, the qualitative dynamics of its trajectory remain unaffected by imperfections, such as having only a single active cap (Figure 6c); even if gas bubbles are only produced from one of the poles, the rotating motion pattern is conserved (due to the moment of the force about the swimmer's center of drag), and merely the pivotal point and the periodicity are shifted.

3. Discussion

A considerable body of research has focused on the fabrication of micromotors with controllable shapes and sizes. Here, we used SFL as a high throughput microfluidic technique to engineer micromotors. This technique provides an edge over other methods in terms of freedom in shape selection and in controlling the active regions in the fabricated geometries. Exploiting the laminar flow in the low Reynolds number regime in the microfluidics channels, we fabricated I-, U-, and S-shaped configuration with active regions confined at the two poles of the shapes. The spatial confinement of the active component was confirmed by labeling the enzyme with a fluorescent dye. The active motion pattern of these configurations was witnessed after mixing them with H_2O_2. Oxygen bubbles generated due to decomposition of H_2O_2 result in efficient bubble propulsion.

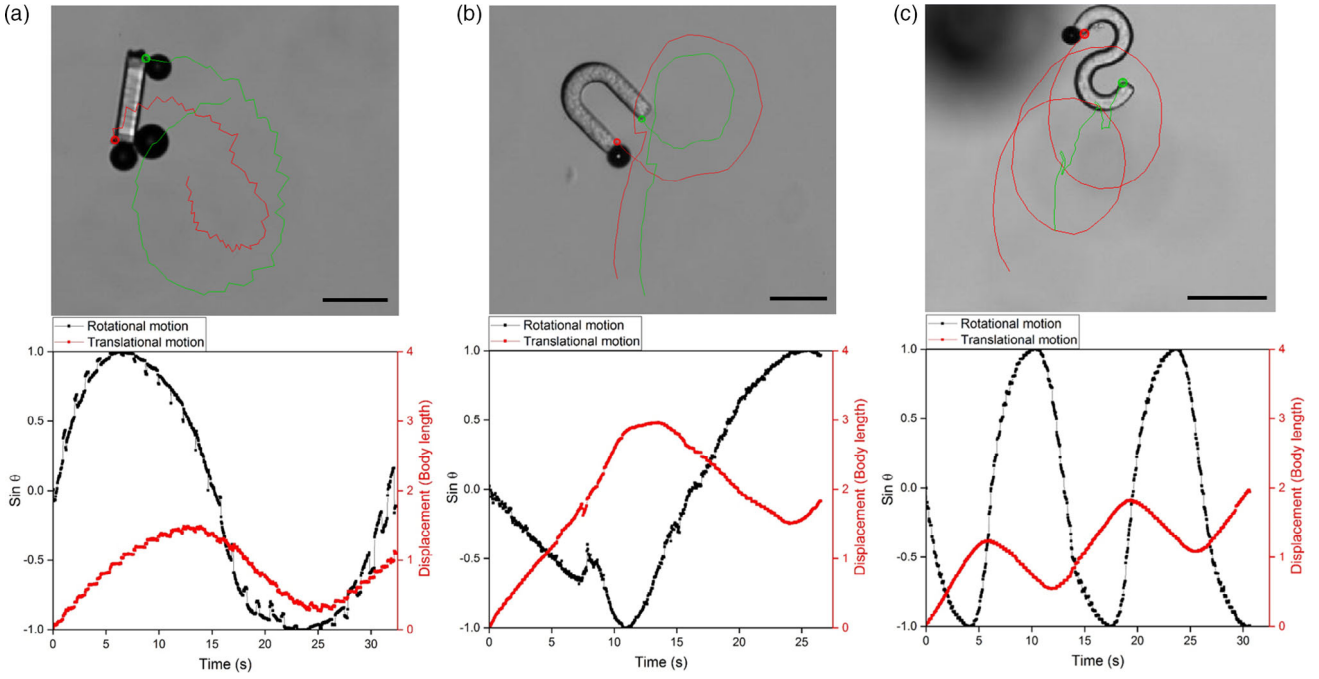

Figure 6. Motion patterns of the differently shaped particles caused by the influences described earlier: micrographs and corresponding analysis [sin Θ and displacement plotted versus time] of a) partial rotation, partial translation of I-shaped swimmers, b) partial rotation, partial translation of U-shaped swimmers, and c) rotating translation of S-shaped swimmers. Scale bar equals 150 µm.

The interplay of shape, catalytic decomposition of solute, and resultant bubble growth and collapse driving propulsive fluid flows determines the trajectories of the fabricated configurations. Bubbles collapsing at the two poles of an U-shaped configuration contribute to ballistic motion, while the higher symmetry of the I-shaped swimmer leads to these propulsive forces on the swimmer cancelling so that the shape functions as a pump. In the S-shaped microgel, although rotational symmetry means that the forces are equal and opposite, cancelling ballistic motion, their displacement allows them to exert a couple on the swimmer, which results in rotation. This rotational symmetry is not perfect, and as a result the S-shape also exhibits some translation, resulting in a moving rotor that may be able to act as an excellent microscale mixer.

4. Conclusion

In this work, we could show that different configurations of hydrogel microswimmers can achieve a set of swimming behaviors dependent on their geometries. As predicted theoretically,[24] a straight I-shaped geometry can either act as a pump or as a ballistic swimmer, having two or only a single catalytic patch, respectively. U-shaped hydrogels are dominantly translators, while S-shapes are commonly rotating. As bubble propulsion is strongly dependent on the local surface properties (e.g., cavities, or nucleation points), we find a rather large proportion of microswimmers deviating from the expected swimming modes, resulting in a broad spectrum of swimming behaviors. In the future, the implementation of shape changing materials can lead to the development of multifunctional actuators that respond to different stimuli and perform specific tasks depending on their environment. In addition, the use of hydrogels will facilitate the use of a variety of enzymes operating on base of different substrates and therefore enable the use of different fuels, which might lead to a platform technology.

5. Experimental Section

Materials: PEGDA ($M_n = 700$), Lithium phenyl-2,4,6-trimethylbenzoylphosphinate (LAP), Catalase from bovine liver (lyophilized powder) $\geq$10 000 units mg^{-1} protein, Fluorescein *o*-acrylate, Rhodamine B isothiocyanate (RITC) Tween 20, Glycerol, and Hydrogen peroxide were purchased from Sigma-Aldrich. SYLGARD 184 Silicone Elastomer Kit was purchased from Dow-Corning.

Labeling Catalase with RITC: Catalase (1 mg) was dissolved in phosphate-buffered saline (PBS) (1 mL) and a solution of RITC (2 µL of stock solution of concentration 0.2 mg mL^{-1}) was added. The mixture was gently stirred for 4 h and subsequently dialyzed against 200 mL PBS (three times, buffer was exchanged every 6 h). The final volume of the solution was 1.2 mL. The solution was divided into 150 µL aliquots and stored at −20 °C for subsequent use.

Pregel Compositions: Active pregel: LAP (10 mg) was dissolved in 650 µL of PBS buffer. Catalase (12.5 mg) was added to the mixture and dissolved by vortexing, followed by PEGDA (200 µL) addition. Then the solution of Rhodamine-labeled catalase, as received in the labeling step was added (150 µL). The resulting mixture was vortexed and spinned down (10 000 g, 5 min) to remove dispersed dirt. Fresh compositions were prepared before each use.

Inactive pregel: Similar to active pregel composition, LAP (10 mg) was dissolved in 550 µL of PBS buffer followed by PEGDA (400 µL) addition. Then, 50 µL of Fluorescein *o*-acrylate (8 mg mL^{-1} in DMSO) was added. This mixture was sonicated well and centrifuged for 5 min before use. Fresh mixtures were prepared before each use.

Microfluidic Channel Production: Polydimethylsiloxane (PDMS) microfluidic (depth = 30 µm) channels were produced as follows. Silicon wafers with SU-8 photoresist positive relief channels (Michrochem) were used as masters, having lateral dimensions of 300 µm × 15 000 µm and the height 30 and 50 µm for production of microgels of corresponding thickness. Silicone elastomer base (35 g) and curing agent (5 g) from the Elastomer Kit were mixed well and centrifuged at 15 000 *g* for 20 min. The mixture was then poured over the silicon wafer and degassed under vacuum (40 mbar, 20 min). The PDMS was cured by storing the wafer at 70 °C overnight after which it was cut and removed from the wafer and divided into individual pieces, each containing one channel. Using a biopsy needle, a 1 mm hole was punctured through the PDMS pieces at the end of each inlet channel and at the opposite, outlet, end of the main channel. Separately, glass slides were spin-coated with PDMS with a 10:1 ratio of elastomer:base. The glass slides were partially cured by storing them at 70 °C for 35 min. After partial curing, the PDMS pieces were placed, channel side down, on the PDMS side of the slides and these were then cured at 70 °C overnight. Three inlet adapters were made using flattened 1 mm diameter syringe needles with Luer adaptors and inserted in the inlet holes. A 1 mm diameter capillary was inserted into the outlet and fed into a polymerase chain reaction (PCR) tube containing 1 wt% Tween 20.

SFL: The SFL method is adapted from that presented by Dendukuri et al.[22] The active pregel solution (50 µL) was loaded into each of the two outer inlets and 50 µL of the inactive pregel was loaded into the inner inlet. The pregels were pumped into the channel using compressed N_2, regulated to 0.4–0.6 psi using a pressure regulator. One pressure regulator was used for the outer inlets and another for the central inlet. This allowed the dimensions of the outer, sheath, flows to be regulated manually. Both regulator outputs were connected to synchronized three-way solenoid valves which allowed rapid switching between input atmospheric pressure. The channels were placed on the stage of an inverted microscope (Nikon Ti-U). UV light passed through a photomask in the focal plane of the microscope objective such that it illuminated the channel in the shape given by the photomask. The shutter of the UV source and the solenoid valves were controlled by a Raspberry Pi, programmed to cycle in the following progression: flow—pregel is pumped through the channel, stop—the flow is stopped, print—UV light illuminates the channel. The UV light induced polymerization and cross-linking of the pregel in the illuminated region, producing microgels with shapes defined by the photomask and a depth slightly less than the depth of the channel (≈27 µm). By controlling the dimensions of the sheath flow and the position of the illuminated area, the active and inactive compositions were localized to predesigned regions of the microgel. The stop–print–flow cycle could be repeated up to 4 Hz and, with 50 µL of pregel in each inlet, was used to produce some 14 000 microgels within an hour. The photomasks and collection PCR tubes were exchanged within the synthesis, providing separate samples from the same set of pregel. After synthesis, the microgels were sedimented (10 min) washed five times with PBS (220 µL concentrated to 20 µL), to remove the excess of catalase. Washed microgels were stored at −20 °C for subsequent use.

Motion Studies and Analysis: Motion studies were performed in specifically designed wells. Typically, plastic washers of 2 mm height and 10 mm inner diameter were stuck on to glass slides using spin-coated PDMS as an inert glue, to render the system optically transparent. This entire assembly was then cured at 70 °C for 12 h. The fabricated wells were filled with an aqueous 2.5 wt% H_2O_2 solution containing 7.5 wt% Glycerol and subsequently swimmers were added. The motion and bubbling of microswimmers was recorded using an attached camera to an inverted Nikon (Ti-U) microscope. The recordings were generated at 30 frames per second. The videos were analyzed using Tracker software.

SEM: Droplets of water containing fabricated microswimmers were cast on silicon wafer and shock frozen using liquid N_2. Afterward, these frozen droplets were subjected to freeze drying. SEM images were obtained after sputtering a 5 nm thin Au–Pd layer on the silicon sample holders, using a Zeiss Gemini SEM 300 instrument using a 3 kV electron beam.

Fluorescence Imaging: Fluorescence images were captured on an inverted Nikon (Ti-U) microscope using green and red channels of light. The obtained images (one in green channel and the other in red channel) were subsequently overlayed in ImageJ to obtain the final images.

Image Analysis of Bubbles: Videomicroscopy data were first imported into Matlab, whereupon we selected a small region of interest (ROI) containing a single bubble. We then performed a frame-by-frame analysis on this ROI to find the radius of the bubble for each frame. A circular Hough Transform was used within the built-in function imfindcircles to give the bubble radius (Figure 3a). As the interior of the bubble appears consistently darker than the surroundings, erroneous results (most common when the bubble is small or has just collapsed) were removed by ensuring that the standard deviation of the pixels inside the circle is below a threshold. The radius as a function of time was then plotted as a periodic signal (Figure 3b). A region of interest of clean data was selected from the periodic signal (Figure 3b, between the red dashed lines), and the locations of the collapse event (to the nearest frame) were used to "phase-average" the signal (Figure 3c), to give an averaged data set against which to compare our model.

Supporting Information

Supporting Information is available from the Wiley Online Library or from the author.

Acknowledgements

P.S., C.M., and B.A. contributed equally to this work. J.S. and P.S. acknowledge a Freigeist grant (no. 91619) from Volkswagen foundation. P.S. also acknowledges Erasmus+ Staff Mobility program. B.A. and T.D.M.-J. gratefully acknowledge support from a Leverhulme Trust Research Leadership Award to T.D.M.-J., and B.A. also acknowledges support from the EPSRC for funding via a Ph.D. scholarship (grant no. EP/N509590/1). I.R. acknowledges the UCT Prague D. Prochazkova Iniciation Grant and the Czech Academy of Sciences J.E. Purkyne Fellowship. C.M. acknowledges the UCT Prague grant of Specific University Research (grant no. A1_FCHI_2020_005).

Correction added on 23 August 2022, after first online publication: Projekt DEAL funding statement has been added.

Open Access funding enabled and organized by Projekt DEAL.

Conflict of Interest

The authors declare no conflict of interest.

Data Availability Statement

Raw data is available from the authors upon request.

Keywords

active matter, bubble-driven micromotors, enzymes, microswimmers, stop-flow lithography

Received: April 20, 2021
Revised: June 21, 2021
Published online: July 28, 2021

[1] R. F. Ismagilov, A. Schwartz, N. Bowden, G. M. Whitesides, *Angew. Chem. Int. Ed.* **2002**, *41*, 652.
[2] S. Sanchez, A. A. Solovev, S. M. Harazim, O. G. Schmidt, *J. Am. Chem. Soc.* **2011**, *133*, 701.
[3] W. Gao, S. Sattayasamitsathit, A. Uygun, A. Pei, A. Ponedal, J. Wang, *Nanoscale* **2012**, *4*, 2447.
[4] J. Simmchen, V. Magdanz, S. Sanchez, S. Chokmaviroj, D. Ruiz-Molina, A. Baeza, O. Schmidt, *RSC Adv.* **2014**, *4*, 20334.
[5] P. Sharan, A. Nsamela, S. C. Lesher-Perez, J. Simmchen, *Small* **2021**, *17*, 2007403.
[6] M. Kuron, P. Kreissl, C. Holm, *Acc. Chem. Res.* **2018**, *51*, 2998.
[7] J. Bastos-Arrieta, C. Bauer, A. Eychmuller, J. Simmchen, *J. Chem. Phys.* **2019**, *150*, 144902.
[8] L. Xu, F. Mou, H. Gong, M. Luo, J. Guan, *Chem. Soc. Rev.* **2017**, *46*, 6905.
[9] L. K. Abdelmohsen, M. Nijemeisland, G. M. Pawar, G.-J. A. Janssen, R. J. Nolte, J. C. van Hest, D. A. Wilson, *ACS Nano* **2016**, *10*, 2652.
[10] Y. Su, Y. Ge, L. Liu, L. Zhang, M. Liu, Y. Sun, H. Zhang, B. Dong, *ACS Appl. Mater. Interfaces* **2016**, *8*, 4250.
[11] S. J. Ebbens, J. R. Howse, *Langmuir* **2011**, *27*, 12293.
[12] C. Zhou, P. Zhu, Y. Tian, M. Xu, L. Wang, *ACS Nano* **2019**, *13*, 6319.
[13] Y. Yu, L. Shang, W. Gao, Z. Zhao, H. Wang, Y. Zhao, *Angew. Chem. Int. Ed.* **2017**, *129*, 12295.
[14] D. Li, Y. Liu, Y. Yang, Y. Shen, *Nanoscale* **2018**, *10*, 19673.
[15] L. Soler, V. Magdanz, V. M. Fomin, S. Sanchez, O. G. Schmidt, *ACS Nano* **2013**, *7*, 9611.
[16] J. Li, G. Huang, M. Ye, M. Li, R. Liu, Y. Mei, *Nanoscale* **2011**, *3*, 5083.
[17] J. Zhang, X. Zheng, H. Cui, Z. Silber-Li, *Micromachines* **2017**, *8*, 123.
[18] J. G. Gibbs, Y.-P. Zhao, *Appl. Phys. Lett.* **2009**, *94*, 163104.
[19] V. M. Fomin, M. Hippler, V. Magdanz, L. Soler, S. Sanchez, O. G. Schmidt, *IEEE Trans. Robot.* **2014**, *30*, 40.
[20] L. Li, J. Wang, T. Li, W. Song, G. Zhang, *Soft Matter* **2014**, *10*, 7511.
[21] G. Gallino, F. Gallaire, E. Lauga, S. Michelin, *Adv. Funct. Mater.* **2018**, *28*, 1800686.
[22] D. Dendukuri, S. S. Gu, D. C. Pregibon, T. A. Hatton, P. S. Doyle, *Lab Chip* **2007**, *7*, 818.
[23] I. Rehor, C. Maslen, P. G. Moerman, B. G. Van Ravensteijn, R. Van Alst, J. Groenewold, H. B. Eral, W. K. Kegel, *Soft Robotics* **2021**, *8*, 10.
[24] T. D. Montenegro-Johnson, *Phys. Rev. Fluids* **2018**, *3*, 062201.
[25] J. Simmchen, A. Baeza, D. Ruiz-Molina, M. Vallet-Regi, *Nanoscale* **2014**, *6*, 8907.
[26] F. Hegedus, *Ultrasonics* **2014**, *54*, 1113.
[27] J. R. Blake, D. M. Leppinen, Q. Wang, *Interface Focus* **2015**, *5*, 20150017.

Numerical modelling of heterogeneous stimuli-responsive hydrogels*

Amin Rahmat†
School of Chemical Engineering, University of Birmingham, UK

Berk Altunkeyik
School of Mathematics, University of Birmingham, UK.

Mostafa Safdari Shadloo
CORIA lab., Normandie University, CNRS & INSA of Rouen, France.

Tom Montenegro-Johnson
School of Mathematics, University of Warwick, UK.

(Dated: June 6, 2024)

In this paper, we introduce a computational technique for modelling heterogeneous thermo-responsive hydrogels. The model resolves local fluid-solid interactions in hydrogel pores during the deswelling process. The model is a Lagrangian particle-based technique, which benefits from computational grids that represent polymer beads inside hydrogel scaffolds. The hydrogel shrinkage is triggered via instantaneous step-changes in spring properties, i.e. natural length and stiffness. The results show that the mechanical properties of hydrogels during deswelling, e.g. shrinkage ratio and elastic modulus, have a direct effect on the development of the front of expelled fluid. It is also observed that in certain parameter regimes the hydrogel may generate inertial fluid jets at the early stages of deswelling. Finally, simple heterogeneous designs are developed using Menger Sponge-inspired shapes to investigate the effect of design heterogeneity on promoting directional release.

I. INTRODUCTION

Hydrogels are soft porous materials with a great capacity to absorb fluids. A hydrogel comprises entangled polymer chains and the pores between them, which are loaded with aqueous fluids e.g., water and chemical solutions. Stimuli-responsive hydrogels are hydrogels that react to applied environmental stimuli, such as light [1, 2], pH [3, 4], and temperature[5, 6], losing their affinity for water and expelling interstitial fluid, thereby shrinking. Such stimuli-responsive hydrogels are suitable for applications in soft robotics [7, 8], tissue engineering [9–11], and drug delivery [12–14].

Among these various stimuli, temperature is widely employed, particularly in biomedical applications [15, 16], because it is nontoxic and easy to control. In thermo-responsive materials, a Lower Critical Solution Temperature (LCST) exists above which the polymer chains undergo a reversible conformation transition by switching from a hydrophilic state into a hydrophobic one [17]. During this process, the hydrogel expels the absorbed aqueous fluids following the shrinkage of the hydrogel structure. Poly N-isopropylacrylamide (PNIPAM) is one of the most commonly studied thermo-responsive materials [18, 19] with a LCST of $\sim 32°C$, making it suitable for various biomedical applications. It has been shown that the PNIPAM active shrinkage/swelling range, its mechanical properties, and volume shrinkage ratio can be adjusted by varying the polymerisation parameters [20, 21], the concentration of NIPAM and other co-polymers [22–24], and cross-linker type and concentration [25, 26].

Numerical simulations of thermo-responsive hydrogels have been greatly dominated by Molecular Dynamics [27, 28] and coarse-grained models such as Coarse-Grained Molecular Dynamics [29], Coarse-Grained Multi-Blob [30, 31] and Dissipative Particle Dynamics [32, 33] techniques. All-Atom Molecular Dynamics simulations in which monomers and single polymer chains are simulated at very small timescales (nano and picoseconds) and lengthscales ($\leq$ 100 nm), have been developed to study the effect of the solution and cross-linker types [28], arrangement of model components and molecules [27, 34], and polymer structural characterisation [35] for PNIPAM-based and other thermo-responsive hydrogels. At larger time and length scales, coarse-grained models have been developed to model the formation and assembly of hydrogels from crystalline lattices [36, 37], randomly distributed cross-linkers [32, 38], functionalised polymer chains [39, 40], and self-assembly of gel networks [41]. Coarse-grained models have also unfolded the kinetics and dynamics of swelling and deswelling processes [32, 42] for PNIPAM and other thermo-responsive hydrogels. The development of multiscale computational models for simulating the topological dynamics and geometrical deformations of thermo-responsive materials is pivotal in designing future smart technologies at the much larger time and length scales. However, numerical stud-

* A footnote to the article title
† a.rahmat@bham.ac.uk

ies in the literature have mainly focused on internal interactions of hydrogel components, and modelling of the macroscopic bulk dynamics of hydrogels has been unattended except in a few notable studies. Hippler *et al.* [43] studied the dynamics of heterogeneous PNIPAM thermo-responsive structures in microfluidic systems aiming to design microscale actuators for which they developed a multiphysics model to complement their experimental data. Their COMSOL multiphysics model has resolved the swelling and shrinkage mechanisms of bilayer beams in multiple cycles, and showed good agreement with experiments. Similarly, Wang *et al.* [44] developed a COMSOL multiphysics model aiming to design soft thermo-sensors and predict their deformation at different temperatures. More recently, Tanasijevic et al. [45] studied the non-reciprocal dynamics and jet-driven viscous locomotion of thermo-responsive, PNIPAM ribbons in which they used COMSOL multiphysics to model the Stokes flow for a disk under free-force locomotion.

These studies provide good geometrical and topological agreement with the experiments and are good design tools for geometrical optimisation and modelling topological variations. However, there are other knowledge gaps in the dynamics of stimuli-responsive hydrogels that are missing but crucially needed. Hydrogels are heterogeneous materials with an irregular pore structure, which is neglected in homogenised numerical/mathematical models. Such inherent heterogeneity plays a key role in fluid-solid interactions at local pore-scale dynamics. These local interactions are particularly important in biomedical applications e.g., targeted drug delivery, wound dressing, and skin regeneration, where fluid expulsion regime, directional release profile, and species transport are key objectives that need to be optimised.

In this paper, we present a hybrid multiscale computational model for thermo-responsive PNIPAM hydrogels. The model combines two particle-based methods i.e., the Smoothed Particle Hydrodynamics and Mass Spring Model, and has a continuum Lagrangian approach, which explicitly resolves the interfaces between fluid and solid phases. Similar to other homogenised models, the proposed technique captures topological variations and geometrical dynamics of stimuli-responsive hydrogels during the deswelling process. In addition, it offers modelling heterogeneous stimuli-responsive hydrogels and simulates the local fluid dynamics in hydrogel pores and around the hydrogel. These features enable us to investigate the dynamics of loaded fluid front during expulsion and directionality of released fluid by incorporating simple design heterogeneity.

II. METHODOLOGY

We have proposed a hybrid particle-based numerical model to simulate the dynamics of stimuli-responsive hydrogels. The model is extended based on the Discrete MultiPhysics model [46, 47] which has been developed for the interactions of fluid-solid systems under large deformations. In this model, both fluid and solid phases are modelled under continuum mechanics assumptions, for which computational particles are employed to discretise both phases. The proposed technique combines the Smoothed Particle Hydrodynamics (SPH) for modelling the fluid flow and a modified version of the Mass Spring Model which accounts for the deformation of compliant materials.

Within the framework of particle-based techniques, there are two distinct approaches regarding particle *"identity"*. In the first approach, particles are solely considered as *computational* particles, which are used to discretise the governing equations. Although they have physical properties, they serve as representative discrete Lagrangian points in space with no real physical dimensions. One may relate this approach to mesh-dependant discretisation techniques and the definition of points/grids, elements, and volumes in Finite Difference, Finite Element, and Finite Volume methods, respectively. In the second approach, particles have a *material* identity by holding physical properties and physical dimensions, thus the distance between particles is the void/spacing between the constructing elements of the material. The latter approach is a common practice in computational chemistry and material sciences, and is applied to the problems at the atomic, coarse-grained, and mesoscopic lengthscales where the interactions and potential dynamics between atoms/beads are considered. The SPH method, which we utilise to model the fluid phase, relies on the former approach, so we mainly consider particles as computationally-discretised Lagrangian points. However, since some dynamics of the proposed model fall at the interface between mesoscale and continuum-scale mechanics, we have adopted some characteristics of the second approach in our hybridised technique. We will refer to this discussion in the following sections wherever appropriate.

A. Smoothed Particle Hydrodynamics (SPH)

SPH is a particle-based numerical method initially developed for astrophysical purposes [48], but it soon became a popular technique due to its characteristics for modelling large deformations in fluid dynamics including free surface flows [49, 50], multiphase systems [51, 52], flow instabilities [53, 54], and fluid-solid interactions [55, 56]. The governing equations of a laminar incompressible Newtonian fluid may be written

$$\frac{\mathrm{D}\rho}{\mathrm{D}t} = -\rho \boldsymbol{\nabla} \cdot \mathbf{u}, \tag{1}$$

$$\frac{\mathrm{D}\mathbf{u}}{\mathrm{D}t} = \frac{-\boldsymbol{\nabla} p}{\rho} + \frac{1}{\rho}(\boldsymbol{\nabla} \cdot \mu \boldsymbol{\nabla} \mathbf{u}) + \mathbf{F}, \tag{2}$$

where $\mathbf{u}$ is the velocity vector, and ρ, μ, and p are density, kinematic viscosity, and pressure, respectively. Time is represented by t, $\frac{\mathrm{D}}{\mathrm{D}t}$ is the material derivative, and $\mathbf{F}$ is the volumetric body force.

SPH solves equations 1 and 2 over spatially distributed particles in the solution domain using a smoothing kernel function, $W(\mathbf{r}_{ij}, h)$ or in its concise form, W_{ij}. The kernel function relates the particle i with its surrounding neighbour particles j, based on the relative distance between these particles $\mathbf{r}_{ij} = |\mathbf{r}_i - \mathbf{r}_j|$, and the smoothing length, h. In this study, we have used the Lucy kernel function [57] due to its suitability for parallel simulations. In SPH, any arbitrary variable f can be approximated as a summation over discrete particles as

$$f_i \simeq \sum_{j=1}^{J_i} \frac{m_j}{\rho_j} f_j W_{ij}, \tag{3}$$

where m_j is the mass of the discrete neighbouring particles, and J_i is the number of neighbouring particles for particle i. It should be noted here that in SPH (and in other particle-based techniques in general) mass is automatically conserved since each computational particle has a specific mass, which remains constant throughout the simulation. Equations 1 and 2 can be written in discretised forms as

$$\dot{\rho}_i = -\sum_{j=1}^{J_i} m_j \mathbf{u}_{ij} \frac{\partial W_{ij}}{\partial \mathbf{x}_i}, \tag{4}$$

$$\begin{aligned} \mathbf{f}_i = \quad & -\textstyle\sum_{j=1}^{J_i} m_i m_j \left(\frac{p_i}{\rho_i^2} + \frac{p_j}{\rho_j^2}\right) \frac{\partial W_{ij}}{\partial \mathbf{x}_i} \\ & + \textstyle\sum_{j=1}^{J_i} \frac{m_i m_j (\mu_i + \mu_j)}{\rho_i \rho_j} \mathbf{u}_{ij} \frac{\partial W_{ij}}{\partial \mathbf{x}_i} + \mathbf{F}_i. \end{aligned} \tag{5}$$

In equation 5, the first term is the pressure gradient and the second one is the dissipation term known as the laminar viscosity model [58]. In SPH, there are two distinct approaches to evaluate pressure: (i) the incompressible SPH method which requires solving a pressure Poisson equation [59]; and (ii) the Weakly Compressible SPH (WCSPH) method [60], in which the pressure is evaluated from density variations via an equation Of state. In this paper, we employed the WCSPH technique using the so-called Tait equation Of state [61]:

$$p = \frac{c_0^2 \rho_0}{\gamma} \left[\left(\frac{\rho}{\rho_0} \right)^{\gamma} - 1 \right]. \tag{6}$$

where c_0 is a reference speed of sound. To keep the density variations below 1% in incompressible flows, it is recommended to set the reference speed of sound at least one order of magnitude larger than the maximum velocity in the domain [62]. ρ_0 is the reference density set equal to 1000 kgm^{-3} and γ is a coefficient taken equal to 7 [63]. Similar to our previous studies [47, 64], different particle types are defined to mark different fluid phases, which automatically resolve the interface between different material phases.

B. The MSM

The Mass Spring Model (MSM) [46, 65] is a particle-based model which represents deformable elastic materials using a network of interconnected springs. In the MSM [66], deformable solid material is discretised into computational particles and a network of harmonic bonds connecting these particles allows them to move according to the Newtonian equations of motion under the effect of external forces. These harmonic bonds are used to account for Hookean elasticity between solid particles by

$$\mathbf{F}_{i,bond} = k_b \left(\mathbf{r}_{ij} - \mathbf{r}_0 \right) \tag{7}$$

where k_b is the Hookean bond coefficient and r_0 is the equilibrium distance. Depending on the structure of MSM grids (e.g., tetrahedral, hexahedral, random, etc.) and the connectivity between springs and particles (i.e., structured vs unstructured, 2D vs 3D), one may correlate the model spring stiffness to the macroscopic properties such as elastic and shear moduli. For a three dimensional unstructured system, the relationship between the elastic modulus and the spring coefficient is evaluated by [67],

$$k_b = \frac{3E}{\alpha^{3D}(1 - 2\nu)} \tag{8}$$

where ν is the Poisson ratio, and α^{3D} is the microstructure geometry coefficient and is calculated as

$$k_b = \frac{\Sigma l_s^2}{V} \tag{9}$$

where l_s is the original length of the s-th bond and V is the volume of the modelling material.

We have modified the MSM to model stimuli-responsive materials such as thermo-responsive PNIPAM hydrogels, which change their volume in response to temperature variations [15, 16]. To account for the conformational changes and hydrophobicity of PNIPAM when heated, we present a simple model where the natural length of springs is adjusted in response to temperature variations, which consequently reduces the size of the hydrogel as temperature exceeds the LCST.

C. Coupling of SPH and MSM

The interaction between the solid (MSM particles) and the fluid (SPH particles) is defined by boundary conditions which relate to the behaviour of two adjacent materials at the common interface. There are three types

of boundary conditions that must be taken into consideration [68], no-penetration, no-slip, and continuity of stresses. In continuum mechanics, these conditions are often, respectively, represented as

$$\left(\frac{\partial}{\partial t}\mathbf{u}_f - \mathbf{u}_s\right)\cdot\mathbf{n} = 0, \tag{10}$$

$$\left(\frac{\partial}{\partial t}\mathbf{u}_f - \mathbf{u}_s\right)\times\mathbf{n} = 0, \tag{11}$$

and

$$\sigma_s\mathbf{n} = \sigma_f\left(-\mathbf{n}\right), \tag{12}$$

where $\mathbf{n}$ is the unit vector normal to the boundary, $\mathbf{u}_s$ and $\mathbf{u}_f$ are the displacement of the solid and the velocity of the fluid, respectively; the stress is represented by σ_s and σ_f for the solid and fluid, respectively. The proposed approach follows the principles of the ghost particle approach in particle-based techniques, in which ghost fluid particles are assigned to solid particles (herein MSM particles) at the fluid-solid interface to interact with SPH particles of the fluid.

D. Numerical algorithm

The time integration is employed using the Velocity Verlet (VV) algorithm with a first-order Euler approach and variable timestep according to the stability condition, $\Delta t = \zeta h^2/\nu$, where ν is the dynamic viscosity equal to $\nu = \rho/\mu$ and ζ is taken to be equal to 0.125 [46]. Using the VV algorithm, particles velocities are calculated at the intermediate stage

$$\mathbf{u}_{\mathrm{i}}^{*} = \mathbf{u}_{\mathrm{i}}^{(n)} + \frac{\Delta t}{2m_{\mathrm{i}}}\mathbf{f}_{\mathrm{i}}^{(n)}. \tag{13}$$

Here, the superscript $(*)$ represents an intermediate value and the superscript (n) denotes values at the n-th time step. Then, the density of the particles is updated according to

$$\rho_{\mathrm{i}}^{*} = \rho_{\mathrm{i}}^{(n)} + \frac{\Delta t}{2}\dot{\rho}_{\mathrm{i}}^{(n)}, \tag{14}$$

where the density variations $\dot{\rho}$ is calculated according to equation 4. In equation 4, the density should be updated based on the velocity difference between particles $\mathbf{u}_{\mathrm{ij}}$. To prevent poor conservation of total mass due to the lag of the velocity in the VV algorithm, an extrapolated velocity is introduced here as

$$\overline{\mathbf{u}}_{\mathrm{i}} = \mathbf{u}_{\mathrm{i}}^{(n)} + \frac{\Delta t}{m_{\mathrm{i}}}\mathbf{f}_{\mathrm{i}}^{(n)}, \tag{15}$$

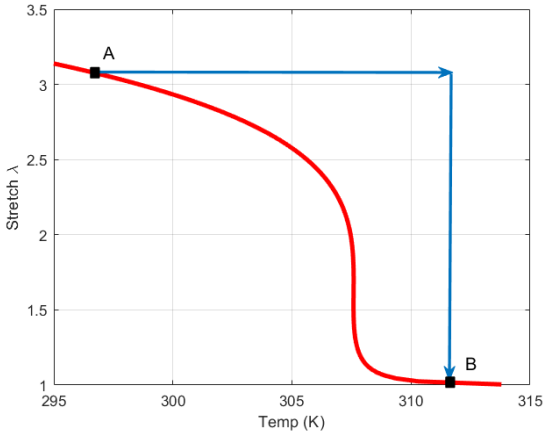

FIG. 1. The equilibrium curve as a function of temperature for thermo-responsive hydrogels [69].

where the velocity difference is now calculated based on $\mathbf{u}_{\mathrm{ij}} = (\overline{\mathbf{u}}_{\mathrm{i}} - \overline{\mathbf{u}}_{\mathrm{j}})$. The next step is to move particles to their new positions by means of

$$\mathbf{x}_{\mathrm{i}}^{(n+1)} = \mathbf{x}_{\mathrm{i}}^{(n)} + \Delta t\mathbf{u}_{\mathrm{i}}^{*}. \tag{16}$$

At this stage, $\dot{\rho}_{\mathrm{i}}^{(n+1)}$, and $\mathbf{f}_{\mathrm{i}}^{(n+1)}$ are calculated for the new time step using equations 4 and 5, respectively. Finally, the true velocity and density are calculated respectively as

$$\mathbf{u}_{\mathrm{i}}^{(n+1)} = \mathbf{u}_{\mathrm{i}}^{*} + \frac{\Delta t}{2m_{\mathrm{i}}}\mathbf{f}_{\mathrm{i}}^{(n+1)}, \tag{17}$$

and,

$$\rho_{\mathrm{i}}^{(n+1)} = \rho_{\mathrm{i}}^{*} + \frac{\Delta t}{2}\dot{\rho}_{\mathrm{i}}^{(n+1)}. \tag{18}$$

There are two approaches available for the deswelling of stimuli-responsive hydrogels. In one approach, the hydrogels follow a quasi-static deformation in which the hydrogel deforms incrementally under the effect of temperature variations to maintain equilibrium state during the deswelling process. This can be considered by following small increments in the red equilibrium curve in figure 1. In the other approach, the temperature increases instantaneously and the hydrogel undergoes a sudden change in its characteristic length-scale along the horizontal arrow in figure 1. Subsequently, the hydrogel requires to reach equilibrium which results in shrinkage. In both approaches, the underlying fact is that the hydrodynamic timescale, which describes the hydrodynamic diffusion and fluid expulsion, generally occurs at much larger timescales in comparison to the thermal timescale. Tanaka and Philmore [70] suggest that the hydrodynamic diffusivity is about four orders of magnitude

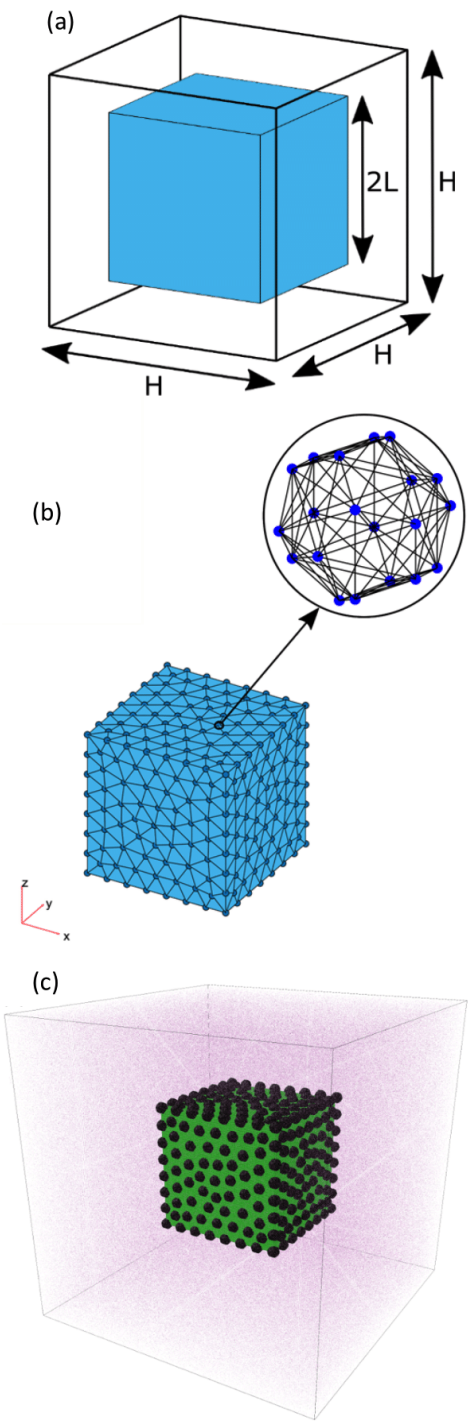

FIG. 2. A 3D representation of the computational domain; (a) a schematic view of the hydrogel with the size of 2L at the centre of the domain with a size of H = 5L, (b) hydrogel discretisation via unstructured tetrahedral mesh and the allocation of dodecahedron grids on each node, and (c) computational domain showing different particle types i.e., polymer particles (black) loaded aqueous fluid shown (green), and surrounding fluid (magenta). It should be noted that particle sizes have been changed for illustration purposes only.

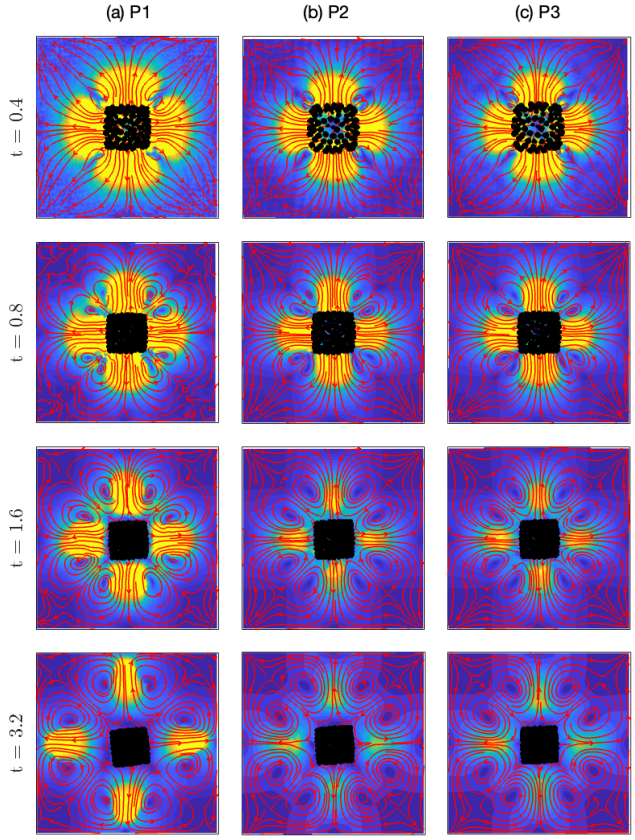

FIG. 3. Particle resolution study for three different resolutions: (a) P1 = 160Π, (b) P2 = 180Π, and (c) P3 = 200Π on a thin slice at z = H/2 ± ϵ, where ϵ is equal to H/100, shown at four different times: t = 0.4, t = 0.8, t = 1.6, and t = 3.2. Velocity contours are represented within the range of $0 \leq v \leq 2$ and velocity streamlines are shown by solid red lines while black particles illustrate hydrogel beads.

smaller than the thermal diffusivity of water, suggesting that the swelling takes 100 times slower than the heat diffusion [69, 71]. However, these two approaches differ in the hydrogel length-scale. It has been shown in literature [69, 71] that the shrinkage time is proportional to the second power of the hydrogel length-scale. Thus, the former approach is more appropriate for length-scales above 1 mm where temperature gradients are observed while the latter is more suitable for micro-scale materials, where small temperature changes occur almost instantaneously at small length-scales. In this study, we restrict ourselves to the second approach.

III. PROBLEM SETUP

Figure 2 represents the simulation domain, which is a cube with the size of H = 5L and a hydrogel cube is placed with a size of 2L at the centre. The characteristic length L = 40 μm, while the other characteristic

parameter is the shrinkage time T, calculated as the time required for the hydrogel to shrink up to 90 % of its initial volume, and the velocity is scaled by V = L/T. In figure 2, there are three different fluid types which are shown by different colours: (i) black particles represent the thermo-responsive hydrogel, (ii) green particles represent the loaded aqueous fluid, and (iii) magenta particles indicate surrounding fluid. It should be noted that the particle sizes in figure 2 do not imply any physical or numerical meaning and they are used for illustration purposes only. In all simulations, other physical properties such as fluid density and viscosity are taken as $\rho = 1000$ Kg/m^3 and $\mu = 5$ mPa.s, unless stated otherwise.

There are numerous experiments in the literature studying the PNIPAM hydrogels and their microscopic pore formation [72, 73]. It has been observed that depending on the polymerisation technique and constructing elements e.g., co-polymers and cross-linkers, unstructured PNIPAM porous structures are formed with an average pore size ranging from ~ 2 μm to a few hundreds. Detailed electron microscopy images further demonstrate the hydrogel structure as interconnected polymer clusters via linking legs. In such unstructured elasto-porous medium, the local fluid-solid interactions plays a significant role in the hydrodynamics of the hydrogel and fluid expulsion during the swelling/deswelling process. However, computational techniques ignore these microdynamics and consider assumptions that do not provide useful information about local interactions. To resolve the local fluid-solid interactions, we have developed a novel hybrid computational approach by using particle grids to represent polymer clusters. As mentioned before, computational particles do not have any physical dimensions, so it is not practical to apply no-slip boundary condition, which is required for resolving local interactions. Further, individual particles cannot represent polymer clusters and the unstructured pore formation. To overcome these limitations, we have used a MATLAB routine to generate tetrahedral unstructured mesh, which discretises the hydrogel cube into points on the vertices of tetrahedrons. Then, we have allocated a dodecahedron particle grid on each of these vertices. Each dodecahedron consists of 20 SPH particles which are interconnected via stiff springs to represent hydrogel beads as shown in figure 2-b. These grids that are shown as black packs of particles in figure 2-c, can effectively introduce no-slip surfaces for local fluid-solid interactions. Considering the size of the hydrogel, we have discretised the cube such that the pore size is approximately 8 μm at the swollen state before the initiation of the shrinkage process, while each dodecahedron has a diameter of approximately 2.5 μm. During the deswelling, there is no external control and/or enforcement on the pore size and it is governed by the competition between hydrodynamics and elastic forces.

The deswelling is implemented by updating both spring natural length and stiffness as being suggested in experiments [43]. As shown in equation 8, the spring coefficient relates with the elastic modulus, so we have set the spring coefficient to match with E = 25kPa before the shrinkage and E = 100kPa after the shrinkage, respectively. The spring natural length is further updated to 40 % of their original length. Nonetheless, it should be noted that some of these values are varied for some test-cases to test the effect of elastic modulus and shrinkage ratio.

The numerical code is modelled and implemented in LAMMPS, an open-source package developed for particle-based techniques. The computational domain contains more that 5.8 million computational particles. Simulations are performed on different available High-Performance Computing facilities and take an average wall-time of 19.5k cpu.h to run. In-house MATLAB codes are used to design computational domain during pre-processing stage, while Ovito and in-house MATLAB codes are used for post-processing purposes.

IV. RESULTS

A. Deswelling dynamics and particle resolution study

Before investigating the effect of various parameters on the hydrogel deswelling, the model is checked to remove any dependency on number of computational particles. Thus, we have compared the shrinkage dynamics of the hydrogel for three different resolution cases: P1 = 160 Π, P2 = 180 Π, and P3 = 200 Π, where Π indicates the number of particle along the side of the simulation domain. Figure 3 represents the velocity streamlines and contours as well as hydrogel beads (shown by black particles) at four different times for P1, P2, and P3. The results are shown on a thin slice at z = H/2 $\pm$ ϵ where ϵ is equal to H/200. As the shrinkage is triggered, the hydrogel beads are contracted towards the centre which causes the loaded fluid to expel out in the surrounding. Subsequently, fluid jets are diffused from the hydrogel sides and flow streamlines indicate the formation of flow circulations around the hydrogel. Flow streamlines also reveal that there are reverse flows from the hydrogel corners towards the centre, which is deemed to occur due to a combination of two effects: (a) asymmetric hydrogel structure that generates higher resisting drag for loaded fluid expulsion along the diagonals and makes the fluid diffusion faster from the sides and (b) the domain periodic boundary conditions that amplifies these circulations. These flow circulations are developed at early stages at the vicinity of the solid front and they seem to move in the outward direction. Comparing the velocity contours and streamlines, it can be qualitatively concluded that increasing particle resolution improves the results from P1 to P2, while no significant improvement is observed between P2 and P3 cases.

Figures 4 and 5 provide further quantitative comparisons for the particle resolution study of P1, P2, and

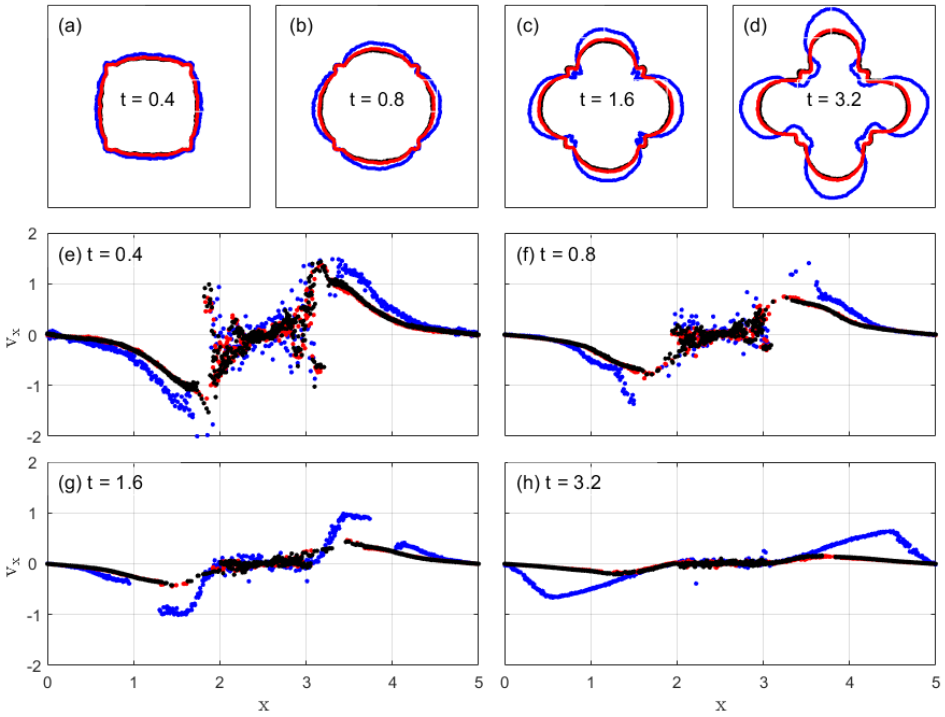

FIG. 4. Contours of fluid front on the xy-plane on a thin slice at z = H/2 ± ϵ at four different times (a-d) and x-velocity profiles along x direction at four different times (e-h) for P1 = 160Π, P2 = 180Π, and P3 = 200Π represented by blue, red, and black colours, respectively.

P3 cases. Figure 4 illustrates the interface (hereafter referred to as the 'front') between the loaded fluid and the surrounding fluid (a-d) and velocity profiles along the x-axis (e-h) at four different times on the same slice as shown in figure 3. In all sub-figures, P1, P2, and P3 are represented by blue, red, and black colours, respectively. Figure 4 (a-d) represents the fluid front which develops during the deswelling towards domain boundaries. The fluid front is developed faster from the hydrogel sides creating a total number of six spikes (two along each axis) which four are shown in the figure. Figure 4 (e-h) further demonstrates the velocity profiles, i.e. v_x along the x-axis passing through the hydrogel centre. The sudden deswelling of the hydrogel generates velocity peaks in the expelled fluid that travels towards the domain boundaries as deswelling develops. It should be noted that the velocity magnitude of the loaded fluid particles inside the hydrogel structure are noisy, which is due to the local forces exerted on individual fluid particles at the proximity of hydrogel beads, which might drag them in the opposite direction of the expulsion.

Figure 5 represents the time evolution of the front development for both fluid (solid lines) and solid (dashed lines) phases along x direction for P1, P2, and P3 cases shown by blue, red and black colours, respectively. The solid front reaches its terminal state much faster that the fluid front, due to the effect of elastic force between hydrogel beads. In other words, the difference in the rate of

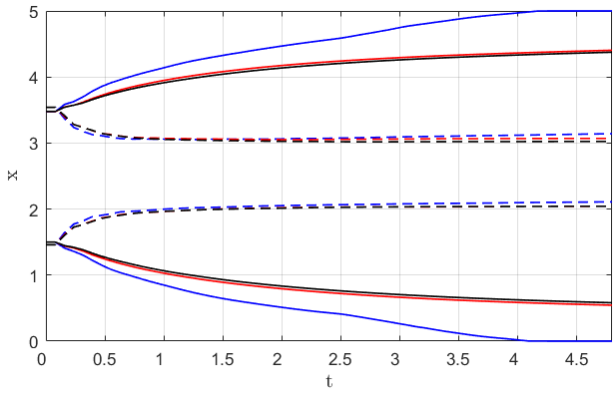

FIG. 5. Effect of particle resolution on the temporal evolution on the fluid (solid lines) and solid (dashed lines) fronts along the x direction for three different resolutions: (a) P1 = 160Π (blue), (b) P2 = 180Π (red), and (c) P3 = 200Π (black).

front development for fluid and solid phases relies on the difference between the viscoelastic response of the hydrogel in contrast to the viscous dynamics of the loaded fluid during expulsion, which develops steadily while gradually being damped due to viscous effects.

As discussed, figures 4 and 5 provide quantitative comparison between P1, P2, and P3 cases during the

deswelling process. It is observed that increasing particle resolution leads to the convergence of results such that increasing particle resolution from P1 to P2 improves numerical accuracy. However, increasing particle resolution from P2 to P3 does not seem to improve numerical results significantly, thus we have used the resolution of P2 as the baseline for the rest of the simulations in this study.

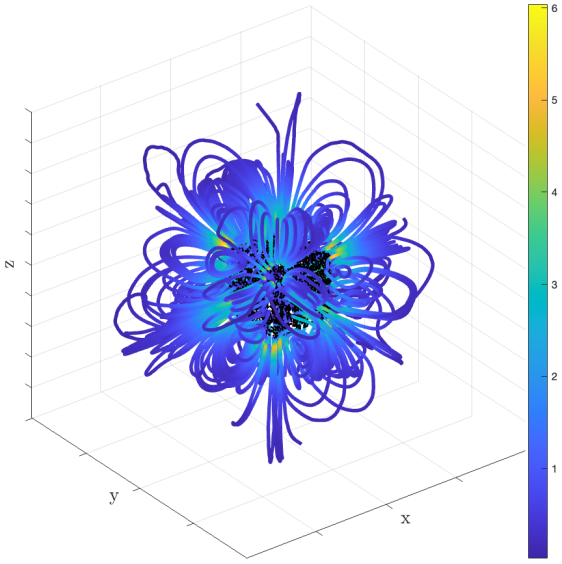

FIG. 6. Three-dimensional streamtubes around the hydrogel during the deswelling process at t = 0.8 for P2; fluid velocities are illustrated using different colours on individual tubes.

As previously mentioned, the conformational change of the hydrogel structure is implemented as an instantaneous change to the springs' "preferred" length, thus it is important to study the time scale of the deswelling dynamics. In our simulations, the deswelling of the hydrogels is occurs very quickly as it takes place in 60 μs. Other researchers including Tanasijevic et al. [45] and Zhang et al. [74] who have investigated the dynamics and swimming characteristics of microscale bi-layer thermo-responsive PNIPAM hydrogels, have reported larger (though still small) time-scales in their experiments. Tanasijevic et al. [45], for instance, studied the swimming dynamics of 80 micron bi-layer ribbons and reported that a full actuation cycle occurs within about 12 milliseconds. Their measured actuation time is clearly larger than our findings, but other factors should be taken into account. First, our numerical model simulates a hydrogel cube in a quiescent fluid, which experiences no drag from the surrounding environment during the deswelling process. In contrast, their bi-layer ribbons are resisted by the ambient fluid during the course of actuation. Second, we have modelled a homogeneous cube representing a uniform shrinkage, while the actuation dynamics of bi-layer ribbons is temporally restrained by the resisting elastic force exerted by the non-responsive layer, which seems to have a significant effect on the actuation response time. Finally, differences may arise since the formalism we have used to calculate the spring stiffness in our model was derived for elastic, rather than poroelastic materials. Therefore, the deswelling time in our numerical simulations is significantly smaller than those in experiments. While it would be possible to further fit the stiffnesses to match specific experimental data, for the purposes of this study, which focuses on methodology and the effect on the flow of adding structured mesopores - and given the wide range variation hydrogel material properties - this is not necessary to understand qualitative dynamics (as shown in Fig. 7b).

TABLE I. Simulation test cases and their properties to examine the effect of elastic modulus (E) and shrinkage ratio (δ).

Test-case	E (kPa)	δ (%)
S1	100	60
S2	100	50
S3	100	40
S4	50	60
S5	25	60

Figure 6 illustrates three-dimensional streamtubes around the hydrogel during the deswelling at t = 0.8 for P2. In this figure, streamtubes depict flow streamlines on which velocity magnitudes are locally represented using a spectrum of colours. Further, hydrogel beads are shown in black to mark the hydrogel front. It is observed that fluid jets stream out of the hydrogel side faces showing a relatively large velocity magnitudes. These jets split into four currents which generate flow circulations towards the four adjacent corners of the hydrogel side. Therefore, each corner attracts three streams of circulating fluid from its constructing faces. It might be possible and interesting to reconstruct the above flow circulations using force dipoles and singular flows at the Stokes regime for less stiff hydrogels. As the front of the hydrogel is shrinking towards the centre, however, the magnitude of these circulating streams and the amount of displaced fluid are marginal from corners compared to the expelled fluid from the sides.

B. Effect of shrinkage ratio and elastic modulus

Polymerisation parameters such as the concentration of PNIPAM, other co-polymers and cross-linkers can significantly impact the responsive dynamics and properties of hydrogels by changing the elastic modulus and shrinkage ratio. Subsequently, these two factors can affect the hydrodynamics of the deswelling. In fact, the elastic modulus contributes to the viscoelastic properties of hydrogels and the shrinkage ratio affects the fluid expulsion by changing the amount of the fluid being displaced. In this section, we investigate the local and overall deswelling dynamics by modelling five test-cases as shown in table I where S1 is the base case and identical

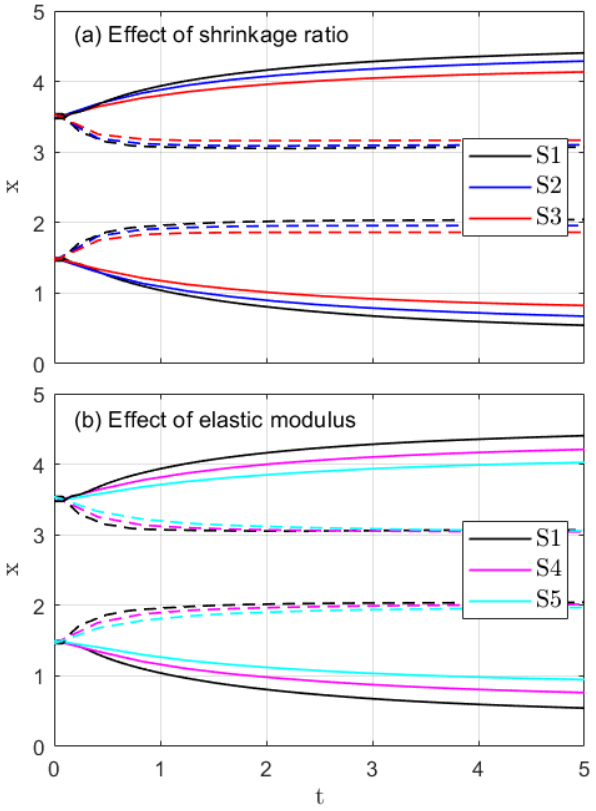

FIG. 7. Temporal evolution and development of fluid (solid lines) and solid (dashed lines) for S1, S2, S3, S4, and S5; Subfigure compare the effect of (a) shrinkage ratio and (b) elastic modulus.

to P2 in the previous section and S2-S3 and S4-S5 are introduced to examine the effect of shrinkage ratio (δ) and elastic modulus (E), respectively.

Figure 7 represents the effect of (a) shrinkage ratio and (b) elastic modulus by comparing the temporal development of fluid and solid fronts for S1, S2, S3, S4, and S5 cases. In figure 7-a, it is shown that decreasing the shrinkage ratio affects the development of both solid and fluid fronts such that decreasing the shrinkage ratio results in a slower development. It should be noted that shrinkage ratio does not affect the rate of development for the solid front and all cases reach their plateau almost at the same time. This is in contrary with the effect of the elastic modulus for the solid front in figure 7-b in which the solid front reaches the plateau at later times for smaller elastic cases (S5). The reason lies behind the fact that changing elastic modulus would affect the viscoelastic properties of the hydrogel and enhances the viscous component, thus the hydrogel represents a slower response compared to larger elastic modulus cases. On the other hand, both shrinkage ratio and elastic modulus represent similar influence on the development of the fluid front derived from various causes. Changing the shrinkage ratio impacts the amount of expelled fluid and the expulsion hydrodynamics, while the rate of front development seems unaffected. Changing the elastic modulus, however, results in a change in the rate of development but the amount of displaced fluid remains the same. Thus, it can be concluded that decreasing the elastic modulus/response rate decreases the penetration of the expelled fluid while forming a more spread front.

Figure 8 represents the v_x velocity profiles along the x-axis on a line passing the hydrogel centre for S1, S2, S3, S4, and S5 cases at four different times. As expected, velocity profiles are generally symmetric around the hydrogel centre for all cases. A detailed observation, however, reveals that there are noisy fluctuations especially at early times of the deswelling and at the proximity of the hydrogel centre. These fluctuations arise from local interactions between fluid particles and hydrogel beads, which influence fluid dynamics in their proximity. Comparing the effect of shrinkage ratio and elastic modulus, it is observed that peak velocities monotonically decrease with decreasing the shrinkage ratio and elastic modulus at all simulation times. The magnitude of the fluid velocities has a direct relationship with the development of fluid fronts, and we expect the same physics influence both. Considering the relationship between the fluid front and maximum peak velocity, it is observed that the maximum peak velocities are approximately 0.6 unit length behind the fluid front at all times and for all cases.

The dynamics of microscale swimmers and devices including stimuli-responsive hydrogels are often considered to occur in the Stokes regime where inertia is negligible. Although it is true for many natural phenomena and engineering applications, we noticed that inertial fluid jets may formed during the deswelling process, if it is sufficiently rapid. As described in previous section, these fluid jets develop in the outward direction and from the faces of the hydrogel. We herein introduce the local Reynolds number ($\mathrm{Re_L}$), which is calculated by measuring the width of the jet fluid at the location of the maximum velocity ($\mathrm{u_{max}}$) as

$$Re_L = \frac{\rho \mathrm{u_{max}} \mathcal{D}}{\mu}, \tag{19}$$

where $\mathcal{D}$ is the measured width of the jet.

Figure 9 presents the local Reynolds numbers for S1, S2, S3, S4, and S5 cases at different times during the deswelling process. The results indicate that the expelled jets are within the finite Reynolds regime and the local Reynolds number decreases as deswelling progresses in time. By comparing the solid front development and the local Reynolds number, we can conclude that the inertia limit of the expulsion ends when the solid front reaches a plateau at $t \approx 2$. Viscous dissipation is the main cause of the decay of the Reynolds number. In fact, the local Reynolds number decreases due to (a) decreasing the maximum velocity as discussed in figure 8 and (b) thin-

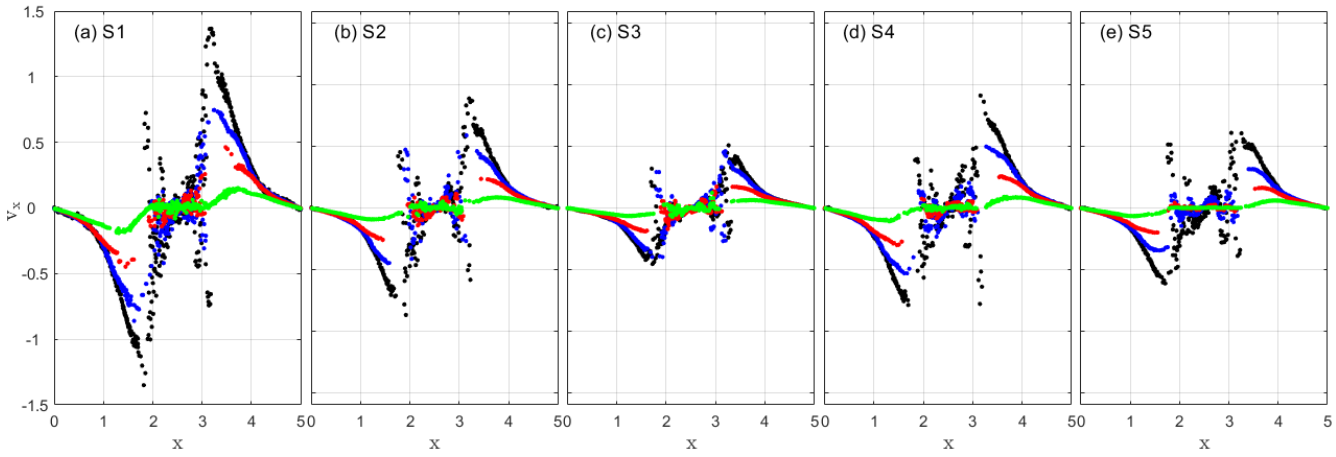

FIG. 8. Velocity profile along the x direction passing the centre of the hydrogel at four different times (black at t = 0.4, blue at t = 0.8, red at t = 1.6, and green at t = 3.2) for S1, S2, S3, S4, and S5.

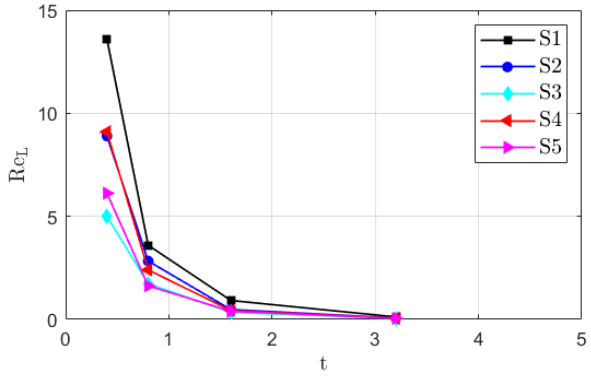

FIG. 9. Local Reynolds number for S1, S2, S3, S4, S5 cases.

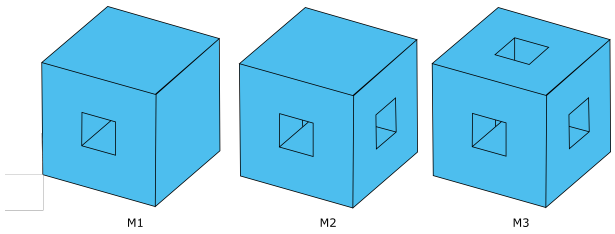

FIG. 10. Schematic views for the M1, M2, and M3 cases; the size of the openings are a third of the hydrogel size i.e., 2L/3.

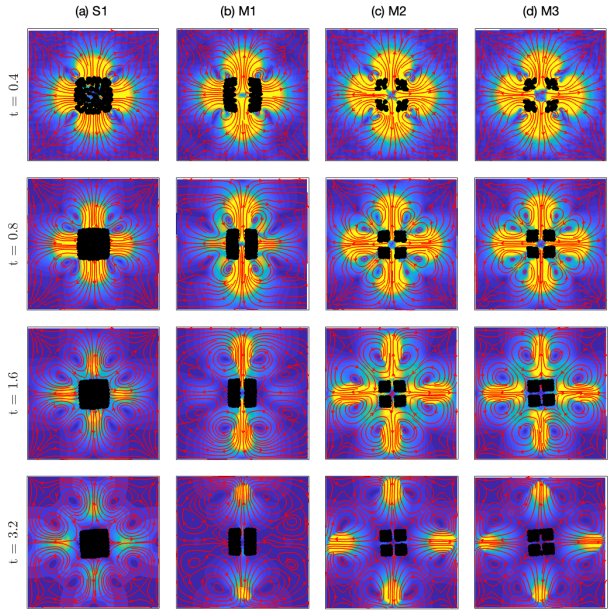

FIG. 11. Velocity contours and flow streamlines for S1, M1, M2, and M3 cases on a thin slice at z = H/2 ± ϵ, which ϵ is equal to H/100, shown at four different times: t = 0.4, t = 0.8, t = 1.6, and t = 3.2; velocity streamlines are shown by solid red lines while black particles illustrate hydrogel grids.

ning of the jet stream as it penetrates in the surrounding.

C. Effect of design heterogeneity

So far, we have investigated the dynamics of shrinkage and fluid expulsion for a solid cube. However, thermo-responsive hydrogels can be exploited for developing more sophisticated designs, which provide additional features that can be used in many applications such as targeted drug delivery. One of these features is the directional release of the loaded material, which can be achieved by different techniques including design heterogeneity. Design heterogeneity can be introduced using various approaches such as hybrid polymerisation and advanced geometrical designs. Here, we make use of Menger Sponge-inspired structures to develop simple geometrical

designs to promote directional expulsion in homogeneous hydrogels, inspired from experiments on anisotropic dynamics of non-reciprocal actuators [75]. These structures are motivated by Menger Sponges as fractal objects [76]. Figure 10 illustrates three Menger-inspired designs i.e. M1, M2, M3 cases, in which Menger channels (hollow spaces within the hydrogel structure) are introduced in one, two, and three directions, respectively. The size of the Menger channels are one third of the width of the hydrogels. All physical properties of these test-cases are similar to S1 including elastic modulus, shrinkage ratio and properties of the loaded fluid.

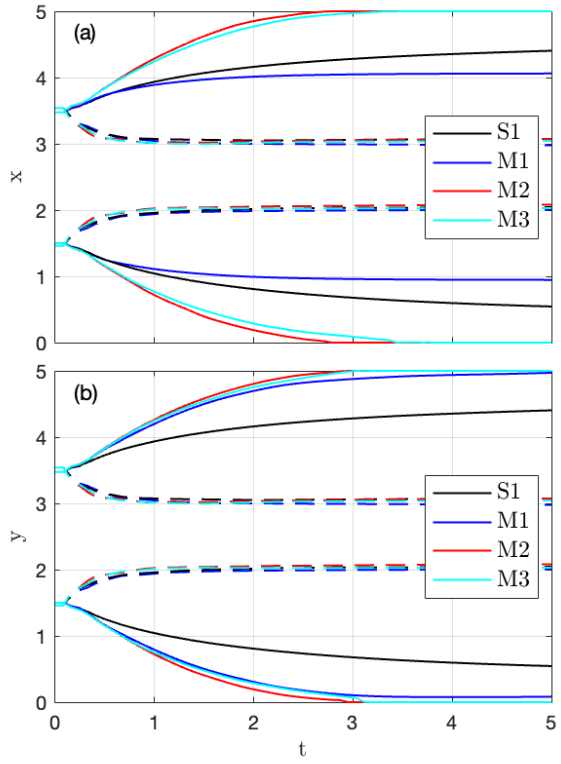

FIG. 12. Temporal evolution and development of fluid (solid lines) and solid (dashed lines) for S1, M1, M2, and M3 along (a) x and (b) y directions.

Similar to figure 3, Figure 11 represents the velocity contours and streamlines for four different cases, S1, M1, M2, and M3 at four different times. Comparing S1 with Menger cases, the Menger channels affect the velocity contours along the channel directions, particularly for the M1 case, which exhibits substantial development for the expelled fluid jet along the y-direction. On the other hand, velocity contours represent a diminishing effect on the expelled fluid jet along the x-axis for M1. Such changes in the hydrodynamics of the expulsion is not observed for the M2 and M3 cases, which indicates that introducing asymmetry in the design of homogeneous materials is effective for developing directional expulsion. Comparing streamlines and flow circulations also introduces interesting findings. Recalling the discussions made earlier on the direction of the streamlines and the development of 8 pairs of circulating flows around the hydrogel cube, one may observe that these circulatory flows are affected in M1, for which the circulations along the y-direction (the main direction of expulsion) is amplified due to a higher momentum generated by the flowing jet. This results in a faster development of lateral circulations towards domain boundaries whilst experiencing a weaker flow. Comparing the development of expelled fluid jets between S1 and Menger cases, it is observed that the streams develop faster and seem to have a stronger momentum for M cases.

Figure 12 illustrates the development of fluid and solid fronts in both x and y directions for S1, M1, M2, and M3 cases. As expected, the magnitude and rate of development for solid fronts do not differ in both directions. On the other hand, it is observed that fluid fronts develop significantly faster for M1, M2, and M3 cases in comparison with S1 case with an exception for M1 along x-direction. The difference is attributed to having a Menger channel along y-direction, thus facilitating the expulsion along y axis and deteriorating the expulsion along other directions. The deterioration effect is large enough to keep the front development along the x-direction behind S1 case. Along the direction of Menger channel, however, the fluid front meets domain boundaries at $t \approx 2.5$ due to the fast expulsion rates, thus no further development is recorded for these cases.

Figure 13 represents the profiles of velocity components i.e., v_x and v_y along x and y directions, respectively. Velocity profiles of all Menger cases are significantly larger than those of the S1 case, with an expected exception for the x velocity of M1. The comparison between the shape and smoothness of velocity profiles inside Menger channels and those of S1 case demonstrates the influence of hydrogel porous structure on affecting the flow regime in their vicinity. It is also interesting to note that the peaks of these profiles are closer to the domain boundaries in comparison with S1 case, which indicate faster jet developments. Subsequently, one may conclude that fluid jets have a larger local Reynolds number.

Figure 14 compares the local Reynolds number for S1, M1, M2, and M3 cases along both x and y directions. Results indicate that the local Reynolds number is approximately two times larger for M cases at early stages of development in comparison with the S1 case. The larger Reynolds number and faster development of fluid fronts for Menger cases suggest that simple heterogeneous designs and asymmetries can generate fast penetrating fluid jets with larger inertial dynamics, which can be incorporated in microfluidic devices where agent release is of importance. Considering the relationship between the peak velocity and Reynolds number, one might further notice that difference between local Reynolds numbers of M cases are approximately two times larger than those for S1, while the maximum velocities have larger difference.

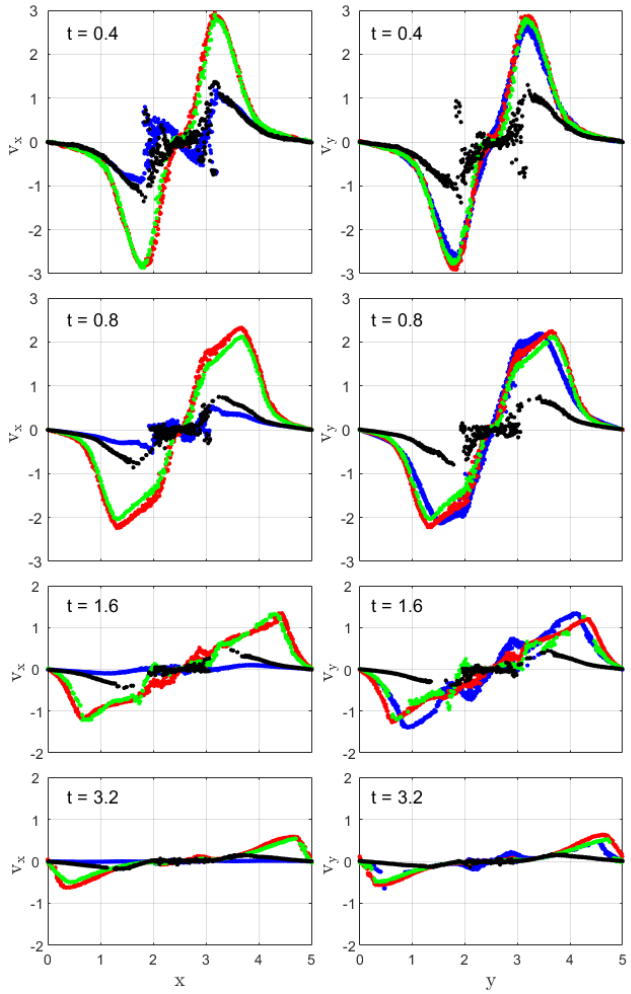

FIG. 13. Velocity profile along the x and y directions passing the centre of the hydrogel at four different times (black at t = 0.4, blue at t = 0.8, red at t = 1.6, and green at t = 3.2) for S1 (black), M1 (blue), M2 (red), and M3 (green) cases.

The matching factor is the size of the fluid jet which are relatively thinner for those along Menger cases compared to those in S1. Careful microfluidics designs of thermo-responsive materials based on the later conclusion may lead to promoted directional release due to the formation of fast developing and concentrated expulsion jets.

Figure 15 represents the relative displacement of particles during the deswelling process for S1, M1, M2, and M3 cases. In all cases, small dark blue colours illustrate the displacement of hydrogel grids during the deswelling which drag fluid particles in their vicinity. Considering the the displacement of fluid particles, however, they are displaced outward almost uniformly through the sides of the hydrogel and inward from the corners for S1. Menger channels facilitate the displacement in the outward direction and provide more directional release by forming fluid jets.

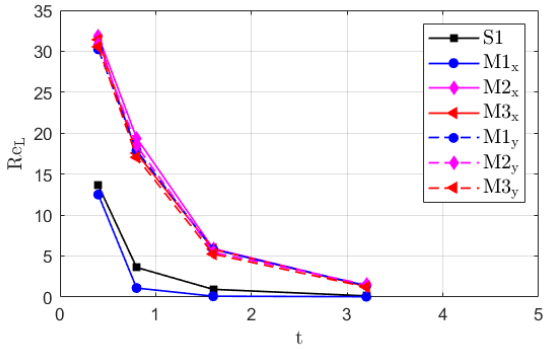

FIG. 14. Local Reynolds number along the x and y directions for S1, M1, M2, and M3 cases.

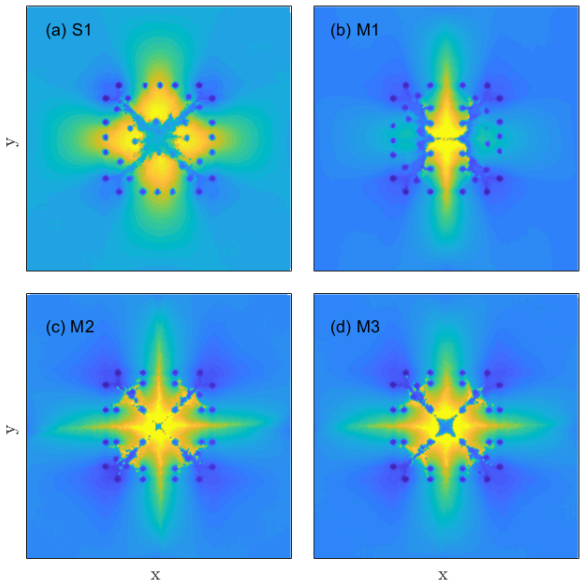

FIG. 15. The heat-map contours for the relative displacement of fluid and solid particles with respect to the hydrogel centre during the deswelling process; the data is shown on a thin slice at z = H/2 ± ϵ.

V. CONCLUDING REMARKS

In this paper, we presented the development of a numerical framework for modelling the dynamics of stimuli-responsive hydrogels during deswelling. The computational framework has a Lagrangian particle-based nature, and is capable of modelling local fluid-solid interactions and explicitly capturing of fluid and solid fronts. The proposed model facilitates the modelling of heterogeneous materials with varying pore sizes and resolves the local fluid-solid interactions. Within the context of modelling stimuli-responsive hydrogels, the model captures the dynamics of the loaded fluid expulsion during

the deswelling process and demonstrates how directional release profiles of expelled fluid can be promotes using design heterogeneity.

Considering the length-scale of the problem and the speed of heat diffusion, we have modelled the deswelling of thermo-responsive hydrogels by imposing an instantaneous change in preferred chain length, and modelling the subsequent interactions between fluid and solid phases. We further employed a grid approach to represent hydrogel beads. We have shown that the introduction of such computational grids does not contribute significantly to the overall hydrodynamics of the hydrogel, but it has a major effect on local hydrodynamics and flow characteristics, especially within the hydrogel structure.

We investigated the effect of polymerisation techniques and realised how elastic modulus and shrinkage ratio affect the overall expulsion profile. Effectively, reducing the shrinkage ratio and elastic modulus similarly results in slower development of fluid front. The shrinkage ratio has the same time-scale for the fluid expulsion, while it changes the amount of the expelled fluid. On the other hand, changing the elastic modulus affects the viscoelastic response of the hydrogel such that reducing the elastic modulus results in a slower front development, while generating a more spread front profile. We have also observed that despite overall dynamics of the microscale thermo-responsive hydrogels are within the Stokes regime, inertial fluid jets may be locally formed during the expulsion, provided shrinkage is rapid enough, and the calculated Reynolds numbers indicate that in this case, inertial effects are present mainly during the early stages of the deswelling along the side faces of a hydrogel cube.

We have also investigated the effect of simple design heterogeneity, in the form of structured mesopores, in promoting the directional release and realised that simple asymmetries affect the shape and development of fluid jets during the expulsion. We have shown that introducing hollow regions (such as Menger channels) in hydrogels increases the local Reynolds number considerably and generates strong penetrative fluid jets. Such simple designs provide useful guidelines for promoting thermo-responsive hydrogels in numerous engineering and biomedical applications such as targeted drug delivery where releasing an agent in a directional pattern is favoured.

VI. AUTHOR CONTRIBUTION

A.R. is responsible for the development of the numerical technique, design of simulations, modelling, pre- and post-processing of the data, scientific discussion, and writing the manuscript. B.A. partially contributed to the writing of the manuscript and pre- and post-processing of the data, as well as scientific discussions. T.D.M.-J. provides research funding, supervised the progress of research, and contributes to the design of simulations, scientific discussions, and the writing of the manuscript. M.S.S. provides funding for accessing HPC facilities and contributed to the design of simulations, scientific discussions, and the writing of the manuscript.

VII. CONFLICT OF INTEREST

Authors declare no conflict of interest.

VIII. ACKNOWLEDGEMENTS

A.R., B.A., and T.D.M.-J. gratefully acknowledge support from the Research Leadership grant, the "Shape-Transforming Active Microfluidics" funded by Leverhulme Trust awarded to T.D.M.-J. B.A. also acknowledges support from the EPSRC for funding via a Ph.D. scholarship (grant no. EP/N509590/1). Further, authors gratefully acknowledge the access to the High-Performance Computing facilities i.e., the French Regional Computing Center of Normandy CRIANN (2022006) and the Gauss Centre for Super-computing e.V. (www.gauss-centre.eu) for funding the access to the GCS Super-computing JUWLES at Julich Supercomputing Centre.

[1] N. Fomina, J. Sankaranarayanan, and A. Almutairi, Photochemical mechanisms of light-triggered release from nanocarriers, Advanced drug delivery reviews **64**, 1005 (2012).

[2] I. Tomatsu, K. Peng, and A. Kros, Photoresponsive hydrogels for biomedical applications, Advanced drug delivery reviews **63**, 1257 (2011).

[3] S. Dai, P. Ravi, and K. C. Tam, ph-responsive polymers: synthesis, properties and applications, Soft Matter **4**, 435 (2008).

[4] G. Kocak, C. Tuncer, and V. Bütün, ph-responsive polymers, Polymer Chemistry **8**, 144 (2017).

[5] Y.-J. Kim and Y. T. Matsunaga, Thermo-responsive polymers and their application as smart biomaterials, Journal of Materials Chemistry B **5**, 4307 (2017).

[6] M. Sponchioni, U. C. Palmiero, and D. Moscatelli, Thermo-responsive polymers: Applications of smart materials in drug delivery and tissue engineering, Materials Science and Engineering: C **102**, 589 (2019).

[7] H. Jia, E. Mailand, J. Zhou, Z. Huang, G. Dietler, J. M. Kolinski, X. Wang, and M. S. Sakar, Universal soft robotic microgripper, Small **15**, 1803870 (2019).

[8] H. Yuk, S. Lin, C. Ma, M. Takaffoli, N. Fang, and X. Zhao, Hydraulic hydrogel actuators and robots optically and sonically camouflaged in water, Nature Com-

munications **8**, 14230 (2017).
[9] M. Prabaharan and J. F. Mano, Stimuli-responsive hydrogels based on polysaccharides incorporated with thermo-responsive polymers as novel biomaterials, Macromolecular Bioscience **6**, 991 (2006).
[10] A. Galperin, T. J. Long, and B. D. Ratner, Degradable, thermo-sensitive poly(n-isopropyl acrylamide)-based scaffolds with controlled porosity for tissue engineering applications, Biomacromolecules **11**, 2583 (2010).
[11] S. Mantha, S. Pillai, P. Khayambashi, A. Upadhyay, Y. Zhang, O. Tao, H. M. Pham, and S. D. Tran, Smart hydrogels in tissue engineering and regenerative medicine, Materials **12**, 3323 (2019).
[12] J. Li and D. Mooney, Designing hydrogels for controlled drug delivery, Nature Reviews Materials **1**, 16071 (2016).
[13] G. Stoychev, N. Puretskiy, and L. Ionov, Self-folding all-polymer thermoresponsive microcapsules, Soft Matter **7**, 3277 (2011).
[14] T. R. Hoare and D. S. Kohane, Hydrogels in drug delivery: Progress and challenges, Polymer **49**, 1993 (2008).
[15] D. Mukherji, C. M. Marques, and K. Kremer, Smart responsive polymers: Fundamentals and design principles, Annual Review of Condensed Matter Physics **11**, 271 (2020).
[16] L. Tang, L. Wang, X. Yang, Y. Feng, Y. Li, and W. Feng, Poly (n-isopropylacrylamide)-based smart hydrogels: Design, properties and applications, Progress in Materials Science **115**, 100702 (2021).
[17] J. F. Mano, Stimuli-responsive polymeric systems for biomedical applications, Advanced Engineering Materials **10**, 515 (2008).
[18] H. Schild, Poly(n-isopropylacrylamide): experiment, theory and application, Progress in Polymer Science **17**, 163 (1992).
[19] M. A. Haq, Y. Su, and D. Wang, Mechanical properties of pnipam based hydrogels: A review, Materials Science and Engineering: C **70**, 842 (2016).
[20] O. Erol, A. Pantula, W. Liu, and D. H. Gracias, Transformer hydrogels: a review, Advanced Materials Technologies **4**, 1900043 (2019).
[21] M. A. Haq, Y. Su, and D. Wang, Mechanical properties of pnipam based hydrogels: A review, Materials Science and Engineering: C **70**, 842 (2017).
[22] Z. Shen, K. Terao, Y. Maki, T. Dobashi, G. Ma, and T. Yamamoto, Synthesis and phase behavior of aqueous poly (n-isopropylacrylamide-co-acrylamide), poly (n-isopropylacrylamide-co-n, n-dimethylacrylamide) and poly (n-isopropylacrylamide-co-2-hydroxyethyl methacrylate), Colloid and Polymer Science **284**, 1001 (2006).
[23] A. S. Hoffman, P. S. Stayton, V. Bulmus, G. Chen, J. Chen, C. Cheung, A. Chilkoti, Z. Ding, L. Dong, R. Fong, *et al.*, Really smart bioconjugates of smart polymers and receptor proteins, Journal of Biomedical Materials Research **52**, 577 (2000).
[24] J. Gernandt, G. Frenning, W. Richtering, and P. Hansson, A model describing the internal structure of core/shell hydrogels, Soft Matter **7**, 10327 (2011).
[25] S. Ashraf, H.-K. Park, H. Park, and S.-H. Lee, Snapshot of phase transition in thermoresponsive hydrogel pnipam: Role in drug delivery and tissue engineering, Macromolecular Research **24**, 297 (2016).
[26] Y. Guan and Y. Zhang, Pnipam microgels for biomedical applications: from dispersed particles to 3d assemblies, Soft Matter **7**, 6375 (2011).
[27] T. Tönsing and C. Oldiges, Molecular dynamic simulation study on structure of water in crosslinked poly (n-isopropylacrylamide) hydrogels, Physical Chemistry Chemical Physics **3**, 5542 (2001).
[28] S. Deshmukh, D. A. Mooney, T. McDermott, S. Kulkarni, and J. D. MacElroy, Molecular modeling of thermoresponsive hydrogels: observation of lower critical solution temperature, Soft Matter **5**, 1514 (2009).
[29] K. K. Bejagam, Y. An, S. Singh, and S. A. Deshmukh, Machine-learning enabled new insights into the coil-to-globule transition of thermosensitive polymers using a coarse-grained model, The journal of physical chemistry letters **9**, 6480 (2018).
[30] A. Narros, C. N. Likos, A. J. Moreno, and B. Capone, Multi-blob coarse graining for ring polymer solutions, Soft Matter **10**, 9601 (2014).
[31] G. D'Adamo, A. Pelissetto, and C. Pierleoni, Coarse-graining strategies in polymer solutions, Soft Matter **8**, 5151 (2012).
[32] S. Nikolov, A. Fernandez-Nieves, and A. Alexeev, Mesoscale modeling of microgel mechanics and kinetics through the swelling transition, Applied Mathematics and Mechanics **39**, 47 (2018).
[33] A. M. Rumyantsev, R. A. Gumerov, and I. I. Potemkin, A polymer microgel at a liquid–liquid interface: theory vs. computer simulations, Soft Matter **12**, 6799 (2016).
[34] J. Walter, J. Sehrt, J. Vrabec, and H. Hasse, Molecular dynamics and experimental study of conformation change of poly (n-isopropylacrylamide) hydrogels in mixtures of water and methanol, The Journal of Physical Chemistry B **116**, 5251 (2012).
[35] M. Alaghemandi and E. Spohr, Molecular dynamics investigation of the thermo-responsive polymer poly (n-isopropylacrylamide), Macromolecular theory and simulations **21**, 106 (2012).
[36] V. Y. Rudyak, A. A. Gavrilov, E. Y. Kozhunova, and A. V. Chertovich, Shell–corona microgels from double interpenetrating networks, Soft Matter **14**, 2777 (2018).
[37] A. Ghavami, H. Kobayashi, and R. G. Winkler, Internal dynamics of microgels: A mesoscale hydrodynamic simulation study, The Journal of chemical physics **145**, 244902 (2016).
[38] H. Masoud and A. Alexeev, Controlled release of nanoparticles and macromolecules from responsive microgel capsules, Acs Nano **6**, 212 (2012).
[39] A. J. Moreno and F. L. Verso, Computational investigation of microgels: synthesis and effect of the microstructure on the deswelling behavior, Soft Matter **14**, 7083 (2018).
[40] S. Seiffert and D. A. Weitz, Controlled fabrication of polymer microgels by polymer-analogous gelation in droplet microfluidics, Soft Matter **6**, 3184 (2010).
[41] N. Gnan, L. Rovigatti, M. Bergman, and E. Zaccarelli, In silico synthesis of microgel particles, Macromolecules **50**, 8777 (2017).
[42] F. Camerin, N. Gnan, L. Rovigatti, and E. Zaccarelli, Modelling realistic microgels in an explicit solvent, Scientific reports **8**, 1 (2018).
[43] M. Hippler, E. Blasco, J. Qu, M. Tanaka, C. Barner-Kowollik, M. Wegener, and M. Bastmeyer, Controlling the shape of 3d microstructures by temperature and light, Nature Communications **10**, 1 (2019).

[44] F.-W. Wang, C.-W. Hsu, and C.-C. Hsieh, Numerical design and experimental realization of a pnipam-based micro thermosensor, ACS applied materials & interfaces **11**, 8591 (2019).

[45] I. Tanasijević, O. Jung, L. Koens, A. Mourran, and E. Lauga, Jet-driven viscous locomotion of confined thermoresponsive microgels, Applied Physics Letters **120**, 104101 (2022).

[46] A. Alexiadis, The discrete multi-hybrid system for the simulation of solid-liquid flows, PloS one **10**, e0124678 (2015).

[47] A. Rahmat, M. Barigou, and A. Alexiadis, Deformation and rupture of compound cells under shear: A discrete multiphysics study, Physics of Fluids **31**, 051903 (2019).

[48] R. A. Gingold and J. J. Monaghan, Smoothed Particle Hydrodynamics: theory and application to non-spherical stars, Monthly Notices of the Royal Astronomical Society **181**, 375 (1977).

[49] R. Löhner, C. Yang, and E. Oñate, On the simulation of flows with violent free surface motion, Computer Methods in Applied Mechanics and Engineering **195**, 5597 (2006).

[50] A. Leroy, D. Violeau, M. Ferrand, L. Fratter, and A. Joly, A new open boundary formulation for incompressible SPH, Computers & Mathematics with Applications **72**, 2417 (2016).

[51] A. Rahmat, N. Tofighi, and M. Yildiz, Numerical simulation of the electrohydrodynamic effects on bubble rising using the SPH method, International Journal of Heat and Fluid Flow **62**, 313 (2016).

[52] R. Saghatchi, A. Rahmat, and M. Yildiz, Electrohydrodynamics of a droplet in a highly confined domain: A numerical study, Physics of Fluids **32**, 123305 (2020).

[53] A. Rahmat, N. Tofighi, M. Shadloo, and M. Yildiz, Numerical simulation of wall bounded and electrically excited Rayleigh-Taylor Instability using incompressible Smoothed Particle Hydrodynamics, Colloids and Surfaces A: Physicochemical and Engineering Aspects **460**, 60 (2014).

[54] M. S. Shadloo and M. Yildiz, Numerical modeling of Kelvin–Helmholtz instability using Smoothed Particle Hydrodynamics, International Journal for Numerical Methods in Engineering **87**, 988 (2011).

[55] A. Rafiee and K. P. Thiagarajan, An SPH projection method for simulating fluid-hypoelastic structure interaction, Computer Methods in Applied Mechanics and Engineering **198**, 2785 (2009).

[56] A. Rahmat, D. Weston, D. Madden, S. Usher, M. Barigou, and A. Alexiadis, Modeling the agglomeration of settling particles in a dewatering process, Physics of Fluids **32**, 123314 (2020).

[57] L. B. Lucy, A numerical approach to the testing of the fission hypothesis, The astronomical journal **82**, 1013 (1977).

[58] J. P. Morris, P. J. Fox, and Y. Zhu, Modeling low reynolds number incompressible flows using sph, Journal of computational physics **136**, 214 (1997).

[59] A. Rahmat and M. Yildiz, A multiphase isph method for simulation of droplet coalescence and electro-coalescence, International Journal of Multiphase Flow **105**, 32 (2018).

[60] R. Fatehi, A. Rahmat, N. Tofighi, M. Yildiz, and M. S. Shadloo, Density-based smoothed particle hydrodynamics methods for incompressible flows, Computers & Fluids **185**, 22 (2019).

[61] M. Ozbulut, N. Tofighi, O. Goren, and M. Yildiz, Investigation of wave characteristics in oscillatory motion of partially filled rectangular tanks, Journal of Fluids Engineering **140**, 041204 (2018).

[62] M. Shadloo, A. Rahmat, and M. Yildiz, A Smoothed Particle Hydrodynamics study on the electrohydrodynamic deformation of a droplet suspended in a neutrally buoyant Newtonian fluid, Computational Mechanics **52**, 693 (2013).

[63] J. J. Monaghan, Simulating free surface flows with SPH, Journal of Computational Physics **110**, 399 (1994).

[64] A. Rahmat, M. Barigou, and A. Alexiadis, Numerical simulation of dissolution of solid particles in fluid flow using the sph method, International Journal of Numerical Methods for Heat & Fluid Flow **30**, 290 (2019).

[65] A. Kilimnik, W. Mao, and A. Alexeev, Inertial migration of deformable capsules in channel flow, Physics of Fluids **23**, 123302 (2011).

[66] B. Lloyd, G. Székely, and M. Harders, Identification of spring parameters for deformable object simulation, IEEE Transactions on Visualization and Computer Graphics **13**, 1081 (2007).

[67] G.-F. Zhao, J. Fang, and J. Zhao, A 3d distinct lattice spring model for elasticity and dynamic failure, International Journal for Numerical and Analytical Methods in Geomechanics **35**, 859 (2011).

[68] C. T. Esmon, Basic mechanisms and pathogenesis of venous thrombosis, Blood reviews **23**, 225 (2009).

[69] M. D. Butler and T. D. Montenegro-Johnson, The swelling and shrinking of spherical thermo-responsive hydrogels, Journal of Fluid Mechanics **947**, A11 (2022).

[70] T. Tanaka and D. J. Fillmore, Kinetics of swelling of gels, The Journal of Chemical Physics **70**, 1214 (1979).

[71] T. Bertrand, J. Peixinho, S. Mukhopadhyay, and C. W. MacMinn, Dynamics of swelling and drying in a spherical gel, Physical Review Applied **6**, 064010 (2016).

[72] R. Fei, J. T. George, J. Park, A. K. Means, and M. A. Grunlan, Ultra-strong thermoresponsive double network hydrogels, Soft Matter **9**, 2912 (2013).

[73] Z. Ayar, M. Shafieian, N. Mahmoodi, O. Sabzevari, and Z. Hassannejad, A rechargeable drug delivery system based on pnipam hydrogel for the local release of curcumin, Journal of Applied Polymer Science **138**, 51167 (2021).

[74] H. Zhang, L. Koens, E. Lauga, A. Mourran, and M. Möller, A light-driven microgel rotor, Small **15**, 1903379 (2019).

[75] C. Maslen, A. Gholamipour-Shirazi, M. D. Butler, J. Kropacek, I. Rehor, and T. Montenegro-Johnson, A new class of single-material, non-reciprocal microactuators, Macromolecular Rapid Communications , 2200842 (2022).

[76] B. Kushwaha, K. Dwivedi, R. S. Ambekar, V. Pal, D. P. Jena, D. R. Mahapatra, and C. S. Tiwary, Mechanical and acoustic behavior of 3d-printed hierarchical mathematical fractal menger sponge, Advanced Engineering Materials **23**, 2001471 (2021).

APPENDIX

LIST OF REFERENCES

[1] M. Alaghemandi and E. Spohr. Molecular dynamics investigation of the thermo-responsive polymer poly(n-isopropylacrylamide). Macromolecular Theory and Simulations, 21(2):106–112, 2012. doi: https://doi.org/10.1002/mats.201100071.

[2] J. C. Athas, C. P. Nguyen, B. C. Zarket, A. Gargava, Z. Nie, and S. R. Raghavan. Enzyme-triggered folding of hydrogels: Toward a mimic of the venus flytrap. ACS Applied Materials & Interfaces, 8(29):19066–19074, 2016. doi: 10.1021/acsami.6b05024.

[3] B. Audoly and Y. Pomeau. Elasticity and Geometry: From Hair Curls to the Non-linear Response of Shells. OUP Oxford, 2010. ISBN 9780198506256. URL `https://books.google.co.uk/books?id=FMQRDAAAQBAJ`.

[4] L. Baraban, R. Streubel, D. Makarov, L. Han, D. Karnaushenko, O. G. Schmidt, and G. Cuniberti. Fuel-free locomotion of janus motors: Magnetically induced thermophoresis. ACS Nano, 7(2):1360–1367, 2013. doi: 10.1021/nn305726m.

[5] G. K. Batchelor. An Introduction to Fluid Dynamics. Cambridge Mathematical Library. Cambridge University Press, 2000. doi: 10.1017/CBO9780511800955.

[6] O. A. Bauchau and J. I. Craig. Euler-Bernoulli beam theory, pages 173–221. Springer Netherlands, Dordrecht, 2009. ISBN 978-90-481-2516-6. doi: 10.1007/978-90-481-2516-6_5. URL `https://doi.org/10.1007/978-90-481-2516-6_5`.

[7] K. K. Bejagam, Y. An, S. Singh, and S. A. Deshmukh. Machine-learning enabled new insights into the coil-to-globule transition of thermosensitive polymers using a coarse-grained model. The Journal of Physical Chemistry Letters, 9(22):6480–6488, 2018. doi: 10.1021/acs.jpclett.8b02956. URL https://doi.org/10.1021/acs.jpclett.8b02956.

[8] H. C. Berg. Motile behavior of bacteria. Physics Today, 53(1):24–29, 2000. doi: 10.1063/1.882934.

[9] N. Bertin, T. A. Spelman, O. Stephan, L. Gredy, M. Bouriau, E. Lauga, and P. Marmottant. Propulsion of bubble-based acoustic microswimmers. Phys. Rev. Applied, 4:064012, Dec 2015. doi: 10.1103/PhysRevApplied.4.064012.

[10] N. Bhattarai, J. Gunn, and M. Zhang. Chitosan-based hydrogels for controlled, localized drug delivery. Advanced Drug Delivery Reviews, 62(1):83–99, 2010. ISSN 0169-409X. doi: https://doi.org/10.1016/j.addr.2009.07.019. URL https://www.sciencedirect.com/science/article/pii/S0169409X09002828. Chitosan-Based Formulations of Drugs, Imaging Agents and Biotherapeutics.

[11] R. Bird, P. Dotson, and N. Johnson. Polymer solution rheology based on a finitely extensible bead—spring chain model. Journal of Non-Newtonian Fluid Mechanics, 7(2):213–235, 1980. ISSN 0377-0257. doi: https://doi.org/10.1016/0377-0257(80)85007-5. URL https://www.sciencedirect.com/science/article/pii/0377025780850075.

[12] J. R. Blake and M. A. Sleigh. Mechanics of ciliary locomotion. Biological Reviews, 49(1):85–125, 1974. doi: https://doi.org/10.1111/j.1469-185X.1974.tb01299.x. URL https://onlinelibrary.wiley.com/doi/abs/10.1111/j.1469-185X.1974.tb01299.x.

[13] P. BOBECK. The public fountains of the city of dijon by henry darcy (1803-1858). In 2005 Salt Lake City Annual Meeting, 2005.

[14] E. L. Bouzarth, A. T. Layton, and Y.-N. Young. Modeling a semi-flexible filament in cellular stokes flow using regularized stokeslets. International Journal for Numerical Methods in Biomedical Engineering, 27(12):2021–2034, 2011. doi: https://doi.org/10.1002/cnm.1454. URL https://onlinelibrary.wiley.com/doi/abs/10.1002/cnm.1454.

[15] J. W. Breitenbach and H. Karlinger. Über quellung von vernetzter polymethacrylsäure. Monatshefte für Chemie und verwandte Teile anderer Wissenschaften, 80(2):312–313, Mar 1949. ISSN 1434-4475. doi: 10.1007/BF00906477. URL https://doi.org/10.1007/BF00906477.

[16] A. Brown and W. Poon. Ionic effects in self-propelled pt-coated janus swimmers. Soft Matter, 10:4016–4027, 2014.

[17] M. D. Butler and T. D. Montenegro-Johnson. The swelling and shrinking of spherical thermo-responsive hydrogels. Journal of Fluid Mechanics, 947:A11, 2022. doi: 10.1017/jfm.2022.641.

[18] G. D. Canio, E. Lauga, and R. E. Goldstein. Spontaneous oscillations of elastic filaments induced by molecular motors. Journal of the Royal Society Interface, 14, 11 2017. ISSN 17425662. doi: 10.1098/rsif.2017.0491.

[19] J. Canny. A computational approach to edge detection. Pattern Analysis and Machine Intelligence, IEEE Transactions on, PAMI-8:679 – 698, 12 1986. doi: 10.1109/TPAMI.1986.4767851.

[20] C. Casagrande, P. Fabre, E. Raphaël, and M. Veyssié. "janus beads": Realization and behaviour at water/oil interfaces. Europhysics Letters, 9(3):251, jun 1989. doi: 10.1209/0295-5075/9/3/011. URL https://dx.doi.org/10.1209/0295-5075/9/3/011.

[21] B. Chakrabarti, Y. Liu, J. LaGrone, R. Cortez, L. Fauci, O. du Roure, D. Saintillan, and A. Lindner. Flexible filaments buckle into helicoidal shapes in strong

compressional flows. Nature Physics, 16(6):689–694, Mar. 2020. ISSN 1745-2481. doi: 10.1038/s41567-020-0843-7. URL http://dx.doi.org/10.1038/s41567-020-0843-7.

[22] X. Chen, N. Shamsudhin, M. Hoop, R. Pieters, E. Siringil, M. Sakar, B. Nelson, and S. Pané. Magnetoelectric micromachines with wirelessly controlled navigation and functionality. Materials Horizons, 3, 12 2015. doi: 10.1039/C5MH00259A.

[23] Y. Cheng, C. Huang, D. Yang, K. Ren, and J. Wei. Bilayer hydrogel mixed composites that respond to multiple stimuli for environmental sensing and underwater actuation. J. Mater. Chem. B, 6:8170–8179, 2018. doi: 10.1039/C8TB02242A.

[24] S. Correa, A. K. Grosskopf, H. Lopez Hernandez, D. Chan, A. C. Yu, L. M. Stapleton, and E. A. Appel. Translational applications of hydrogels. Chemical Reviews, 121(18):11385–11457, 2021. doi: 10.1021/acs.chemrev.0c01177. URL https://doi.org/10.1021/acs.chemrev.0c01177. PMID: 33938724.

[25] R. Cortez. The method of regularized stokeslets. Siam Journal on Scientific Computing, 23, 12 2001. doi: 10.1137/S106482750038146X.

[26] R. Cortez, L. Fauci, and A. Medovikov. The method of regularized stokeslets in three dimensions: Analysis, validation, and application to helical swimming. Physics of Fluids, 17(3):031504, 2005. doi: 10.1063/1.1830486.

[27] R. Cortez, B. Cummins, K. Leiderman, and D. Varela. Computation of three-dimensional brinkman flows using regularized methods. Journal of Computational Physics, 229:7609–7624, 10 2010. doi: 10.1016/j.jcp.2010.06.012.

[28] R. Cortez, M. Hernandez-Viera, and O. Richfield. A model for stokes flow in domains with permeable boundaries. Fluids, 6(11), 2021. ISSN 2311-5521. doi: 10.3390/fluids6110381. URL https://www.mdpi.com/2311-5521/6/11/381.

[29] M. Cosentino Lagomarsino, I. Pagonabarraga, and C. P. Lowe. Hydrodynamic induced deformation and orientation of a microscopic elastic filament. Phys. Rev. Lett., 94:148104, Apr 2005. doi: 10.1103/PhysRevLett.94.148104. URL https://link.aps.org/doi/10.1103/PhysRevLett.94.148104.

[30] P.-G. de Gennes. Soft matter (nobel lecture). Angewandte Chemie International Edition in English, 31(7):842–845, 1992. doi: https://doi.org/10.1002/anie.199208421. URL https://onlinelibrary.wiley.com/doi/abs/10.1002/anie.199208421.

[31] J. A. Delezuk, D. E. Ramírez-Herrera, B. Esteban-Fernández de Ávila, and J. Wang. Chitosan-based water-propelled micromotors with strong antibacterial activity. Nanoscale, 9(6):2195–2200, 2017. ISSN 20403372. doi: 10.1039/c6nr09799e.

[32] B. Delmotte, E. Climent, and F. Plouraboué. A general formulation of bead models applied to flexible fibers and active filaments at low reynolds number. Journal of Computational Physics, 286:14–37, 2015. ISSN 0021-9991. doi: https://doi.org/10.1016/j.jcp.2015.01.026.

[33] S. Deshmukh, Z. Li, G. Kamath, K. Suthar, S. Sankaranarayanan, and D. Mancini. Atomistic insights into solvation dynamics and conformational transformation in thermo-sensitive and non-thermo-sensitive oligomers. Polymer, 54:210–222, 01 2013. doi: 10.1016/j.polymer.2012.11.009.

[34] K. K. Dey, S. Bhandari, D. Bandyopadhyay, S. Basu, and A. Chattopadhyay. The pH taxis of an intelligent catalytic microbot. Small, 9(11):1916–1920, 2013. ISSN 16136810. doi: 10.1002/smll.201202312.

[35] X. Ding, S.-C. S. Lin, B. Kiraly, H. Yue, S. Li, I.-K. Chiang, J. Shi, S. J. Benkovic, and T. J. Huang. On-chip manipulation of single microparticles, cells, and organisms using surface acoustic waves. Proceedings of the National Academy of Sciences, 109 (28):11105–11109, 2012. ISSN 0027-8424. doi: 10.1073/pnas.1209288109.

[36] D.N.Sutherland and C.T.Tan. Sedimentation of a porous sphere. Chemical Engineering Science, 25:1948–1950, 1970.

[37] M. Doi. Soft Matter Physics. Oxford University Press, 06 2013. ISBN 9780199652952. doi: 10.1093/acprof:oso/9780199652952.001.0001. URL https://doi.org/10.1093/acprof:oso/9780199652952.001.0001.

[38] R. Dong, Q. Zhang, W. Gao, A. Pei, and B. Ren. Highly efficient light-driven tio2–au janus micromotors. ACS Nano, 10(1):839–844, 2016. doi: 10.1021/acsnano.5b05940.

[39] R. Dreyfus, J. Baudry, M. Roper, M. Fermigier, H. Stone, and J. Bibette. Microscopic artificial swimmers. Nature, 437:862–5, 11 2005.

[40] J. P. Ebel, J. L. Anderson, and D. C. Prieve. Diffusiophoresis of latex particles in electrolyte gradients. Langmuir, 4(2):396–406, 1988. doi: 10.1021/la00080a024.

[41] O. Erol, A. Pantula, W. Liu, and D. H. Gracias. Transformer hydrogels: A review. Advanced Materials Technologies, 4(4):1900043, 2019. doi: https://doi.org/10.1002/admt.201900043.

[42] B. Esteban-Fernández de Ávila, C. Angell, F. Soto, M. A. Lopez-Ramirez, D. F. Báez, S. Xie, J. Wang, and Y. Chen. Acoustically propelled nanomotors for intracellular sirna delivery. ACS Nano, 10(5):4997–5005, 2016. doi: 10.1021/acsnano.6b01415.

[43] M. Favelukis and G. S. Yablonsky. Catalytic bubble model: Bubble growth with an interfacial chemical reaction. Industrial & Engineering Chemistry Research, 43 (16):4476–4482, 2004.

[44] P. B. Feynman. There's plenty of room at the bottom, 1960.

[45] P. Flory. Principles of Polymer Chemistry. George Fisher Baker non-resident lectureship in chemistry at Cornell University. Cornell University Press, 1953. ISBN 0801401348 9780801401343.

[46] P. J. Flory and J. Rehner. Statistical mechanics of cross-linked polymer networks ii. swelling. The Journal of Chemical Physics, 11(11):521–526, 1943. doi: 10.1063/1.1723792.

[47] S. Fournier-Bidoz, A. C. Arsenault, I. Manners, and G. A. Ozin. Synthetic self-propelled nanorotors. Chem. Commun., pages 441–443, 2005. doi: 10.1039/B414896G.

[48] W. Francis, C. Fay, L. Florea, and D. Diamond. Self-propelled chemotactic ionic liquid droplets. Chemical communications (Cambridge, England), 51(12):2342—2344, February 2015. ISSN 1359-7345. doi: 10.1039/c4cc09214g.

[49] B. M. Friedrich and F. Jülicher. Chemotaxis of sperm cells. Proceedings of the National Academy of Sciences, 104(33):13256–13261, 2007. doi: 10.1073/pnas.0703530104.

[50] H. C. Fu, V. B. Shenoy, and T. R. Powers. Low-reynolds-number swimming in gels. Europhysics Letters, 91(2):24002, aug 2010. doi: 10.1209/0295-5075/91/24002. URL https://dx.doi.org/10.1209/0295-5075/91/24002.

[51] S. Fusco, H. Huang, K. Peyer, C. Peters, M. Haberli, A. Ulbers, A. Spyrogianni, E. Pellicer, J. Sort, S. Pratsinis, B. Nelson, M. Sakar, and S. Pané. Shape-switching microrobots for medical applications: The influence of shape in drug delivery and locomotion. ACS applied materials & interfaces, 7, 03 2015. doi: 10.1021/acsami.5b00181.

[52] M. T. Gallagher and D. J. Smith. Meshfree and efficient modeling of swimming cells. Phys. Rev. Fluids, 3:053101, May 2018. doi: 10.1103/PhysRevFluids.3.053101.

[53] G. Gallino, F. Gallaire, E. Lauga, and S. Michelin. Physics of bubble-propelled microrockets. Advanced Functional Materials, 28(25):1800686, 2018.

[54] G. Gallino, L. Zhu, and F. Gallaire. The hydrodynamics of a micro-rocket propelled by a deformable bubble. Fluids, 4(1), 2019. doi: 10.3390/fluids4010048.

[55] A. Ganguly and A. Gupta. Going in circles: Slender body analysis of a self-propelling bent rod. Phys. Rev. Fluids, 8:014103, Jan 2023. doi: 10.1103/PhysRevFluids.8.014103. URL https://link.aps.org/doi/10.1103/PhysRevFluids.8.014103.

[56] W. Gao and J. Wang. Synthetic micro/nanomotors in drug delivery. Nanoscale, 6: 10486–10494, 2014. doi: 10.1039/C4NR03124E.

[57] W. Gao, S. Sattayasamitsathit, K. M. Manesh, D. Weihs, and J. Wang. Magnetically powered flexible metal nanowire motors. Journal of the American Chemical Society, 132(41):14403–14405, 2010. doi: 10.1021/ja1072349.

[58] W. Gao, M. D'Agostino, V. Garcia-Gradilla, J. Orozco, and J. Wang. Multi-fuel driven janus micromotors. Small, 9(3):467–471, 2013.

[59] W. Gao, M. Liu, L. Liu, H. Zhang, B. Dong, and C. Y. Li. One-step fabrication of multifunctional micromotors. Nanoscale, 7:13918–13923, 2015.

[60] Y. Gao, X. Li, and M. J. Serpe. Stimuli-responsive microgel-based etalons for optical sensing. RSC Adv., 5:44074–44087, 2015. doi: 10.1039/C5RA02306H. URL http://dx.doi.org/10.1039/C5RA02306H.

[61] E. Gauger and H. Stark. Numerical study of a microscopic artificial swimmer. Phys. Rev. E, 74:021907, Aug 2006. doi: 10.1103/PhysRevE.74.021907.

[62] Q. Ge, C. K. Dunn, H. J. Qi, and M. L. Dunn. Active origami by 4d printing. Smart Materials and Structures, 23(9):094007, aug 2014. doi: 10.1088/0964-1726/23/9/094007. URL https://dx.doi.org/10.1088/0964-1726/23/9/094007.

[63] J. Gibbs and Y. Zhao. Autonomously motile catalytic nanomotors by bubble propulsion. Applied Physics Letters, 94:163104–163104, 04 2009.

[64] R. Golestanian, T. B. Liverpool, and A. Ajdari. Propulsion of a molecular machine by asymmetric distribution of reaction products. Phys. Rev. Lett., 94:220801, Jun 2005.

[65] J. Gray and G. J. Hancock. The Propulsion of Sea-Urchin Spermatozoa. Journal of Experimental Biology, 32(4):802–814, 12 1955. ISSN 0022-0949. doi: 10.1242/jeb.32.4.802.

[66] A. L. Hall-McNair, T. D. Montenegro-Johnson, H. Gadêlha, D. J. Smith, and M. T. Gallagher. Efficient implementation of elastohydrodynamics via integral operators. Phys. Rev. Fluids, 4:113101, Nov 2019. doi: 10.1103/PhysRevFluids.4.113101.

[67] M. A. Haq, Y. Su, and D. Wang. Mechanical properties of pnipam based hydrogels: A review. Materials Science and Engineering: C, 70, 09 2016. doi: 10.1016/j.msec.2016.09.081.

[68] A. Hatefi and B. Amsden. Biodegradable injectable in situ forming drug delivery systems. Journal of Controlled Release, 80(1):9–28, 2002. ISSN 0168-3659. doi: https://doi.org/10.1016/S0168-3659(02)00008-1. URL https://www.sciencedirect.com/science/article/pii/S0168365902000081.

[69] F. Hegedűs. Stable bubble oscillations beyond blake's critical threshold. Ultrasonics, 54(4):1113–1121, 2014. ISSN 0041-624X. doi: https://doi.org/10.1016/j.ultras.2014.01.006. URL https://www.sciencedirect.com/science/article/pii/S0041624X14000079.

[70] G. Herrmann and R. W. Bungay. On the Stability of Elastic Systems Subjected to Nonconservative Forces. Journal of Applied Mechanics, 31(3):435–440, 09 1964. ISSN 0021-8936. doi: 10.1115/1.3629660. URL https://doi.org/10.1115/1.3629660.

[71] T. Hino and J. M. Prausnitz. Swelling equilibria for heterogeneous polyacrylamide gels. Journal of Applied Polymer Science, 62(10):1635–1640, 1996. doi: https://doi.

org/10.1002/(SICI)1097-4628(19961205)62:10⟨1635::AID-APP15⟩3.0.CO;2-0. URL https://onlinelibrary.wiley.com/doi/abs/10.1002/%28SICI%291097-4628%2819961205%2962%3A10%3C1635%3A%3AAID-APP15%3E3.0.CO%3B2-0.

[72] M. Hippler, E. Blasco, J. Qu, M. Tanaka, C. Barner-Kowollik, M. Wegener, and M. Bastmeyer. Controlling the shape of 3d microstructures by temperature and light. Nature Communications, 10, 01 2019. doi: 10.1038/s41467-018-08175-w.

[73] D. P. Holmes. Elasticity and stability of shape-shifting structures. Current Opinion in Colloid & Interface Science, 40:118–137, 2019. ISSN 1359-0294. doi: https://doi.org/10.1016/j.cocis.2019.02.008. URL https://www.sciencedirect.com/science/article/pii/S1359029418300839. Particle Systems.

[74] T. Honda, K. Arai, and K. Ishiyama. Micro swimming mechanisms propelled by external magnetic fields. IEEE Transactions on Magnetics, 32(5):5085–5087, 1996. doi: 10.1109/20.539498.

[75] M. Hoop, Y. Shen, X. Chen, F. Mushtaq, L. Iuliano, M. Sakar, A. Petruska, M. Loessner, B. Nelson, and S. Pané. Magnetically driven silver-coated nanocoils for efficient bacterial contact killing. Advanced Functional Materials, 26:n/a–n/a, 12 2015. doi: 10.1002/adfm.201504463.

[76] J. R. Howse, R. A. L. Jones, A. J. Ryan, T. Gough, R. Vafabakhsh, and R. Golestanian. Self-motile colloidal particles: From directed propulsion to random walk. Phys. Rev. Lett., 99:048102, Jul 2007.

[77] A. K. H.P.S, E. Yahya, H. Tajarudin, V. Balakrishnan, and H. Nasution. Insights into the role of biopolymer-based xerogels in biomedical applications. Gels, 8:334, 05 2022. doi: 10.3390/gels8060334.

[78] H. Huang, M. Sakar, A. Petruska, S. Pané, and B. Nelson. Soft micromachines with programmable motility and morphology. Nature Communications, 7:12263, 07 2016. doi: 10.1038/ncomms12263.

[79] T.-Y. Huang, F. Qiu, H.-W. Tung, K. E. Peyer, N. Shamsudhin, J. Pokki, L. Zhang, X.-B. Chen, B. J. Nelson, and M. S. Sakar. Cooperative manipulation and transport of microobjects using multiple helical microcarriers. RSC Adv., 4:26771–26776, 2014. doi: 10.1039/C4RA02260B.

[80] T.-Y. Huang, H. Gu, and B. J. Nelson. Increasingly Intelligent Micromachines. Annu. Rev. Control Robot. Auton. Syst., 2022. doi: 10.1146/annurev-control-042920. URL https://doi.org/10.1146/annurev-control-042920-.

[81] W. Huang, M. Manjare, and Y. Zhao. Catalytic nanoshell micromotors. The Journal of Physical Chemistry C, 117(41):21590–21596, 2013. doi: 10.1021/jp4080288.

[82] J. R. Hutchinson. Shear Coefficients for Timoshenko Beam Theory . Journal of Applied Mechanics, 68(1):87–92, 08 2000. ISSN 0021-8936. doi: 10.1115/1.1349417. URL https://doi.org/10.1115/1.1349417.

[83] M. E. Ibele, Y. Wang, T. R. Kline, T. E. Mallouk, and A. Sen. Hydrazine fuels for bimetallic catalytic microfluidic pumping. Journal of the American Chemical Society, 129(25):7762–7763, 2007. doi: 10.1021/ja0726512. URL https://doi.org/10.1021/ja0726512. PMID: 17550256.

[84] R. F. Ismagilov, A. Schwartz, N. Bowden, and G. M. Whitesides. Autonomous movement and self-assembly. Angewandte Chemie International Edition, 41(4): 652–654, 2002.

[85] B. Jang, E. Gutman, N. Stucki, B. Seitz, P. Wendel Garcia, T. Newton, J. Pokki, O. Ergeneman, S. Pané, Y. Or, and B. Nelson. Undulatory locomotion of magnetic multilink nanoswimmers. Nano letters, 15, 06 2015. doi: 10.1021/acs.nanolett.5b01981.

[86] B. Jang, A. Hong, H. E. Kang, C. Alcantara, S. Charreyron, F. Mushtaq, E. Pellicer, R. Büchel, J. Sort, S. S. Lee, B. J. Nelson, and S. Pané. Multiwavelength light-

responsive au/b-tio2 janus micromotors. ACS Nano, 11(6):6146–6154, 2017. doi: 10.1021/acsnano.7b02177. URL https://doi.org/10.1021/acsnano.7b02177. PMID: 28590716.

[87] B. Jang, M. Ye, A. Hong, X. Wang, X. Liu, D. Bae, J. Puigmartí Luis, and S. Pané. Catalytically propelled micro- and nanoswimmers. Small Science, 3 (11):2300076, 2023. doi: https://doi.org/10.1002/smsc.202300076. URL https://onlinelibrary.wiley.com/doi/abs/10.1002/smsc.202300076.

[88] H.-R. Jiang, N. Yoshinaga, and M. Sano. Active motion of a janus particle by self-thermophoresis in a defocused laser beam. Phys. Rev. Lett., 105:268302, Dec 2010. doi: 10.1103/PhysRevLett.105.268302.

[89] R. E. Johnson. An improved slender-body theory for stokes flow. Journal of Fluid Mechanics, 99(2):411–431, 1980. doi: 10.1017/S0022112080000687.

[90] A. Joseph, C. Contini, D. Cecchin, S. Nyberg, L. Ruiz-Perez, J. Gaitzsch, G. Fullstone, X. Tian, J. Azizi, J. Preston, G. Volpe, and G. Battaglia. Chemotactic synthetic vesicles: Design and applications in blood-brain barrier crossing. Science Advances, 3(8), 2017. doi: 10.1126/sciadv.1700362.

[91] X.-J. Ju, L.-Y. Chu, X.-L. Zhu, L. Hu, H. Song, and W.-M. Chen. Effects of internal microstructures of poly(n-isopropylacrylamide) hydrogels on thermo-responsive volume phase-transition and controlled-release characteristics. Smart Materials and Structures, 15:1767, 10 2006. doi: 10.1088/0964-1726/15/6/031.

[92] B. Jurado-Sánchez, M. Pacheco, R. Maria-Hormigos, and A. Escarpa. Perspectives on Janus micromotors: Materials and applications. Applied Materials Today, 9: 407–418, 2017. ISSN 23529407.

[93] D. Kagan, M. Benchimol, J. Claussen, E. Chuluun-Erdene, S. Esener, and J. Wang. Acoustic droplet vaporization and propulsion of perfluorocarbon-loaded microb-

ullets for targeted tissue penetration and deformation. Angewandte Chemie (International ed. in English), 51:7519–22, 07 2012. doi: 10.1002/anie.201201902.

[94] S. K. Kamarapu, M. Jabbarzadeh, and H. C. Fu. Modeling creeping flows in porous media using regularized stokeslets, 2021.

[95] L. Klouda. Thermoresponsive hydrogels in biomedical applications: A seven-year update. European Journal of Pharmaceutics and Biopharmaceutics, 97:338–349, 2015. ISSN 0939-6411. doi: https://doi.org/10.1016/j.ejpb.2015.05.017. Polymers for Drug Delivery Systems.

[96] L. Klouda and A. G. Mikos. Thermoresponsive hydrogels in biomedical applications. European Journal of Pharmaceutics and Biopharmaceutics, 68(1):34–45, 2008. ISSN 0939-6411. doi: https://doi.org/10.1016/j.ejpb.2007.02.025. Interactive Polymers for Pharmaceutical and Biomedical Applications.

[97] M. C. Koetting, J. T. Peters, S. D. Steichen, and N. A. Peppas. Stimulus-responsive hydrogels: Theory, modern advances, and applications. Materials Science and Engineering: R: Reports, 93:1–49, 2015. ISSN 0927-796X. doi: https://doi.org/10.1016/j.mser.2015.04.001. URL https://www.sciencedirect.com/science/article/pii/S0927796X15000339.

[98] M. Koleoso, X. Feng, Y. Xue, Q. Li, T. Munshi, and X. Chen. Micro/nanoscale magnetic robots for biomedical applications. Materials Today Bio, 8:100085, 2020. ISSN 2590-0064.

[99] W. Kuhn. Reversible dehnung und kontraktion bei änderung der ionisation eines netzwerks polyvalenter fadenmolekülionen. Experientia, 5(8):318–319, Aug 1949. ISSN 0014-4754. doi: 10.1007/BF02172635. URL https://doi.org/10.1007/BF02172635.

[100] J.-C. Kuo, H.-W. Huang, S.-W. Tung, and Y.-J. Yang. A hydrogel-based intravascular microgripper manipulated using magnetic fields. Sensors and Actuators A:

Physical, 211:121–130, 2014. ISSN 0924-4247. doi: https://doi.org/10.1016/j.sna.2014.02.028. URL https://www.sciencedirect.com/science/article/pii/S0924424714000922.

[101] J. P. Lagerwall and G. Scalia. A new era for liquid crystal research: Applications of liquid crystals in soft matter nano-, bio- and microtechnology. Current Applied Physics, 12(6):1387–1412, 2012. ISSN 1567-1739. doi: https://doi.org/10.1016/j.cap.2012.03.019. URL https://www.sciencedirect.com/science/article/pii/S1567173912001113.

[102] J. LaGrone, R. Cortez, and L. Fauci. Elastohydrodynamics of swimming helices: Effects of flexibility and confinement. Phys. Rev. Fluids, 4:033102, Mar 2019. doi: 10.1103/PhysRevFluids.4.033102. URL https://link.aps.org/doi/10.1103/PhysRevFluids.4.033102.

[103] A. Laskar and R. Adhikari. Filament actuation by an active colloid at low reynolds number. New Journal of Physics, 19(3):033021, mar 2017. doi: 10.1088/1367-2630/aa5f80. URL https://dx.doi.org/10.1088/1367-2630/aa5f80.

[104] E. Lauga and T. R. Powers. The hydrodynamics of swimming microorganisms. Reports on Progress in Physics, 72(9):096601, Aug 2009. ISSN 1361-6633. doi: 10.1088/0034-4885/72/9/096601.

[105] K. Leiderman and S. D. Olson. Swimming in a two-dimensional Brinkman fluid: Computational modeling and regularized solutions. Physics of Fluids, 28(2):021902, 02 2016. ISSN 1070-6631. doi: 10.1063/1.4941258. URL https://doi.org/10.1063/1.4941258.

[106] J. Li, T. Li, T. Xu, M. Kiristi, W. Liu, Z. Wu, and J. Wang. Magneto–acoustic hybrid nanomotor. Nano Letters, 15(7):4814–4821, 2015. doi: 10.1021/acs.nanolett.5b01945.

[107] L. Li, H. Manikantan, D. Saintillan, and S. E. Spagnolie. The sedimentation of flexible filaments. Journal of Fluid Mechanics, 735:705–736, 2013. doi: 10.1017/jfm.2013.512.

[108] X. Li, X. Cai, Y. Gao, and M. J. Serpe. Reversible bidirectional bending of hydrogel-based bilayer actuators. J. Mater. Chem. B, 5:2804–2812, 2017. doi: 10.1039/C7TB00426E. URL http://dx.doi.org/10.1039/C7TB00426E.

[109] Y. Li, F. Mou, C. Chen, M. You, Y. Yin, L. Xu, and J. Guan. Light-controlled bubble propulsion of amorphous tio2/au janus micromotors. RSC Adv., 6, 01 2016. doi: 10.1039/C5RA26798F.

[110] J. Lighthill. Flagellar hydrodynamics. SIAM Review, 18(2):161–230, 1976. doi: 10.1137/1018040.

[111] Z. Lin, C. Gao, D. Wang, and Q. He. Bubble-propelled janus gallium/zinc micromotors for the active treatment of bacterial infections. Angewandte Chemie International Edition, 60(16):8750–8754, 2021. doi: https://doi.org/10.1002/anie.202016260. URL https://onlinelibrary.wiley.com/doi/abs/10.1002/anie.202016260.

[112] M. Liu, T. Zentgraf, Y. Liu, G. Bartal, and X. Zhang. Light-driven nanoscale plasmonic motors. Nature nanotechnology, 5:570–3, 08 2010. doi: 10.1038/nnano.2010.128.

[113] Y. Lou, A. Robisson, S. Cai, and Z. Suo. Swellable elastomers under constraint. Journal of Applied Physics, 112(3):034906, 08 2012. ISSN 0021-8979. doi: 10.1063/1.4745878. URL https://doi.org/10.1063/1.4745878.

[114] J. Luan, P. F. Kuijken, W. Chen, D. Wang, L. A. Charleston, and D. A. Wilson. Microfluidic design of streamlined alginate hydrogel micromotors with run and tumble motion patterns. Advanced Science, 10(34):2304995, 2023. doi:

https://doi.org/10.1002/advs.202304995. URL https://onlinelibrary.wiley.com/doi/abs/10.1002/advs.202304995.

[115] K. E. Machin. Wave Propagation along Flagella. Journal of Experimental Biology, 35(4):796–806, 12 1958. ISSN 0022-0949. doi: 10.1242/jeb.35.4.796.

[116] C. Maggi, J. Simmchen, F. Saglimbeni, J. Katuri, M. Dipalo, F. D. Angelis, S. Sanchez, and R. D. Leonardo. Self-assembly of micromachining systems powered by janus micromotors. Small, 12:446–451, 1 2016. ISSN 1613-6829. doi: 10.1002/SMLL.201502391. URL https://onlinelibrary.wiley.com/doi/full/10.1002/smll.201502391https://onlinelibrary.wiley.com/doi/abs/10.1002/smll.201502391https://onlinelibrary.wiley.com/doi/10.1002/smll.201502391.

[117] M. Manghi, X. Schlagberger, and R. R. Netz. Propulsion with a rotating elastic nanorod. Phys. Rev. Lett., 96:068101, Feb 2006. doi: 10.1103/PhysRevLett.96.068101.

[118] M. Manjare, B. Yang, and Y. P. Zhao. Bubble-propelled microjets: Model and experiment. Journal of Physical Chemistry C, 117(9):4657–4665, 2013. ISSN 19327447. doi: 10.1021/jp311977d.

[119] N. Mano and A. Heller. Bioelectrochemical propulsion. Journal of the American Chemical Society, pages 11574–11575, 2005.

[120] B. Marchetti, V. Raspa, A. Lindner, O. D. Roure, L. Bergougnoux, Élisabeth Guazzelli, and C. Duprat. Deformation of a flexible fiber settling in a quiescent viscous fluid. Physical Review Fluids, 3, 10 2018. ISSN 2469990X. doi: 10.1103/PhysRevFluids.3.104102.

[121] A. Martín-Molina and M. Quesada-Pérez. A review of coarse-grained simulations of nanogel and microgel particles. Journal of Molecular Liquids, 280:374–381, 2019.

ISSN 0167-7322. doi: https://doi.org/10.1016/j.molliq.2019.02.030. URL https://www.sciencedirect.com/science/article/pii/S0167732218330186.

[122] C. Maslen, A. Gholamipour-Shirazi, M. D. Butler, J. Kropacek, I. Rehor, and T. Montenegro-Johnson. A new class of single-material, non-reciprocal microactuators. Macromolecular Rapid Communications, 44(6):2200842, 2023. doi: https://doi.org/10.1002/marc.202200842. URL https://onlinelibrary.wiley.com/doi/abs/10.1002/marc.202200842.

[123] O. Maxian. Hydrodynamics of transiently cross-linked actin networks: theory, numerics, and emergent behaviors. New York University, 2023.

[124] J. M. McNeill and T. E. Mallouk. Acoustically powered nano- and microswimmers: From individual to collective behavior. ACS Nanoscience Au, 3(6):424–440, 2023. doi: 10.1021/acsnanoscienceau.3c00038.

[125] M. Medina-Sánchez, V. Magdanz, M. Guix, V. M. Fomin, and O. G. Schmidt. Swimming microrobots: Soft, reconfigurable, and smart. Advanced Functional Materials, 28:1–27, 2018. ISSN 16163028. doi: 10.1002/adfm.201707228.

[126] Y. Mei, G. Huang, A. A. Solovev, E. B. Ureña, I. Mönch, F. Ding, T. Reindl, R. K. Y. Fu, P. K. Chu, and O. G. Schmidt. Versatile approach for integrative and functionalized tubes by strain engineering of nanomembranes on polymers. Advanced Materials, 20(21):4085–4090, 2008. doi: https://doi.org/10.1002/adma.200801589. URL https://onlinelibrary.wiley.com/doi/abs/10.1002/adma.200801589.

[127] P. Mitchell. Self-electrophoretic locomotion in microorganisms: Bacterial flagella as giant ionophores. FEBS Letters, 28(1):1–4, 1972.

[128] T. Montenegro-Johnson, A. Smith, D. Smith, D. Loghin, and J. Blake. Modelling the fluid mechanics of cilia and flagella in reproduction and development. The European physical journal. E, Soft matter, 35:9788, 10 2012. doi: 10.1140/epje/i2012-12111-1.

[129] T. D. Montenegro-Johnson. Microtransformers: Controlled microscale navigation with flexible robots. Phys. Rev. Fluids, 3:062201, Jun 2018.

[130] T. D. Montenegro-Johnson, S. Michelin, and E. Lauga. A regularised singularity approach to phoretic problems. The European Physical Journal E, 38(12), Dec. 2015. ISSN 1292-895X. doi: 10.1140/epje/i2015-15139-7. URL http://dx.doi.org/10.1140/epje/i2015-15139-7.

[131] J. L. Moran and J. D. Posner. Phoretic self-propulsion. Annual Review of Fluid Mechanics, 49(1):511–540, 2017. doi: 10.1146/annurev-fluid-122414-034456.

[132] F. Mou, Y. Li, C. Chen, W. Li, Y. Yin, H. Ma, and J. Guan. Single-component tio2 tubular microengines with motion controlled by light-induced bubbles. Small, 11 (21):2564–2570, 2015. doi: https://doi.org/10.1002/smll.201403372. URL https://onlinelibrary.wiley.com/doi/abs/10.1002/smll.201403372.

[133] Y. Mu, T.-T. Ren, and H.-Q. Yu. Drag coefficient of porous and permeable microbial granules. Environmental science & technology, 42:1718–23, 04 2008. doi: 10.1021/es702708p.

[134] S. R. Nagel. Experimental soft-matter science. Rev. Mod. Phys., 89:025002, Apr 2017. doi: 10.1103/RevModPhys.89.025002. URL https://link.aps.org/doi/10.1103/RevModPhys.89.025002.

[135] A. Najafi and R. Golestanian. Simple swimmer at low reynolds number: Three linked spheres. Phys. Rev. E, 69:062901, Jun 2004. doi: 10.1103/PhysRevE.69.062901.

[136] C. V. Neal, A. L. Hall-McNair, J. Kirkman-Brown, D. J. Smith, and M. T. Gallagher. Doing more with less: The flagellar end piece enhances the propulsive effectiveness of human spermatozoa. Phys. Rev. Fluids, 5:073101, Jul 2020. doi: 10.1103/PhysRevFluids.5.073101.

[137] G. Neale and W. Nader. Practical significance of brinkman's extension of darcy's law: Coupled parallel flows within a channel and a bounding porous medium. The Canadian Journal of Chemical Engineering, 52(4):475–478, 1974. doi: https://doi.org/10.1002/cjce.5450520407. URL https://onlinelibrary.wiley.com/doi/abs/10.1002/cjce.5450520407.

[138] G. Neale, N. Epstein, and W. Nader. Creeping flow relative to permeable spheres. Chemical Engineering Science, 28(10):1865–1874, 1973. ISSN 0009-2509. doi: https://doi.org/10.1016/0009-2509(73)85070-5. URL https://www.sciencedirect.com/science/article/pii/0009250973850705.

[139] A. Nojoomi, H. Arslan, K. Lee, and K. Yum. Bioinspired 3d structures with programmable morphologies and motions. Nature Communications, 9, 09 2018. doi: 10.1038/s41467-018-05569-8.

[140] J. Orozco, L. A. Mercante, R. Pol, and A. Merkoçi. Graphene-based janus micromotors for the dynamic removal of pollutants. J. Mater. Chem. A, 4:3371–3378, 2016. doi: 10.1039/C5TA09850E. URL http://dx.doi.org/10.1039/C5TA09850E.

[141] I.-A. Pavel, A.-I. Bunea, S. David, and S. Gaspar. Nanorods with biocatalytically induced self-electrophoresis. ChemCatChem, 6:n/a–n/a, 03 2014. doi: 10.1002/cctc.201301016.

[142] R. A. Pavlick, S. Sengupta, T. McFadden, H. Zhang, and A. Sen. A polymerization-powered motor. Angewandte Chemie International Edition, 50(40):9374–9377, 2011. doi: https://doi.org/10.1002/anie.201103565.

[143] W. F. Paxton, K. C. Kistler, C. C. Olmeda, A. Sen, S. K. St. Angelo, Y. Cao, T. E. Mallouk, P. E. Lammert, and V. H. Crespi. Catalytic nanomotors: Autonomous movement of striped nanorods. Journal of the American Chemical Society, 126(41):13424–13431, 2004. ISSN 00027863.

[144] C. Peters, M. Hoop, S. Pané, B. J. Nelson, and C. Hierold. Degradable magnetic composites for minimally invasive interventions: Device fabrication, targeted drug delivery, and cytotoxicity tests. Advanced Materials, 28(3):533–538, 2016.

[145] M. S. Plesset and A. Prosperetti. Bubble dynamics and cavitation. Annual Review of Fluid Mechanics, 9(1):145–185, 1977. doi: 10.1146/annurev.fl.09.010177.001045.

[146] F. Plouraboué, E. I. Thiam, B. Delmotte, and E. Climent. Identification of internal properties of fibres and micro-swimmers. Proceedings of the Royal Society A: Mathematical, Physical and Engineering Sciences, 473(2197):20160517, 2017. doi: 10.1098/rspa.2016.0517.

[147] J. Plutnar and M. Pumera. Chemotactic micro- and nanodevices. Angewandte Chemie International Edition, 58(8):2190–2196, 2019. doi: https://doi.org/10.1002/anie.201809101. URL `https://onlinelibrary.wiley.com/doi/abs/10.1002/anie.201809101`.

[148] C. Pozrikidis. Boundary Integral and Singularity Methods for Linearized Viscous Flow. Cambridge Texts in Applied Mathematics. Cambridge University Press, 1992.

[149] C. Pozrikidis. A Practical Guide to Boundary Element Methods with the Software Library BEMLIB. Taylor & Francis, 05 2002. ISBN 9780429139628. doi: 10.1201/9781420035254.

[150] E. M. Purcell. Life at low reynolds number. American Journal of Physics, 45(1):3–11, 1977.

[151] B. Qian, D. Montiel, A. Bregulla, F. Cichos, and H. Yang. Harnessing thermal fluctuations for purposeful activities: the manipulation of single micro-swimmers by adaptive photon nudging. Chem. Sci., 4:1420–1429, 2013. doi: 10.1039/C2SC21263C.

[152] L. Qin, M. J. Banholzer, X. Xu, L. Huang, and C. A. Mirkin. Rational design and synthesis of catalytically driven nanorotors. Journal of the American Chemical Society, 129(48):14870–14871, 2007. doi: 10.1021/ja0772391.

[153] W. Qin, T. Peng, Y. Gao, F. Wang, X. Hu, K. Wang, J. Shi, D. Li, J. Ren, and C. Fan. Catalysis-driven self-thermophoresis of janus plasmonic nanomotors. Angewandte Chemie International Edition, 56(2):515–518, 2017. doi: https://doi.org/10.1002/anie.201609121. URL https://onlinelibrary.wiley.com/doi/abs/10.1002/anie.201609121.

[154] M. Rey, G. Volpe, and G. Volpe. Light, matter, action: Shining light on active matter. ACS Photonics, 10(5):1188–1201, 2023. doi: 10.1021/acsphotonics.3c00140. URL https://doi.org/10.1021/acsphotonics.3c00140.

[155] J. Richardson and W. Zaki. The sedimentation of a suspension of uniform spheres under conditions of viscous flow. Chemical Engineering Science, 3(2):65–73, 1954. ISSN 0009-2509. doi: https://doi.org/10.1016/0009-2509(54)85015-9. URL https://www.sciencedirect.com/science/article/pii/0009250954850159.

[156] S. Sanchez, A. A. Solovev, Y. Mei, and O. G. Schmidt. Dynamics of Biocatalytic Microengines Mediated by Variable Friction Control. Journal of the American Chemical Society, pages 13144–13145, 2010.

[157] E. Sato Matsuo and T. Tanaka. Kinetics of discontinuous volume–phase transition of gels. The Journal of Chemical Physics, 89(3):1695–1703, 1988. doi: 10.1063/1.455115.

[158] S. Sbeih, P. S. Mohanty, M. R. Morrow, and A. Yethiraj. Structural parameters of soft pnipam microgel particles as a function of crosslink density. Journal of Colloid and Interface Science, 552:781–793, 2019. ISSN 0021-9797. doi: https://doi.org/10.1016/j.jcis.2019.05.047. URL https://www.sciencedirect.com/science/article/pii/S0021979719306034.

[159] A. E. SCHEIDEGGER. Physical aspects of permeability, pages 124–151. University of Toronto Press, 1974. ISBN 9781487582395. URL http://www.jstor.org/stable/10.3138/j.ctvfrxmtw.10.

[160] H. Schild. Poly(n-isopropylacrylamide): experiment, theory and application. Progress in Polymer Science, 17(2):163–249, 1992. ISSN 0079-6700. doi: https://doi.org/10.1016/0079-6700(92)90023-R.

[161] P. Sharan, C. Maslen, B. Altunkeyik, I. Rehor, J. Simmchen, and T. Montenegro-Johnson. Fundamental modes of swimming correspond to fundamental modes of shape: Engineering i-, u-, and s-shaped swimmers. Advanced Intelligent Systems, 3:2100068, 07 2021. doi: 10.1002/aisy.202100068.

[162] H. Shen, S. Cai, Z. Wang, Z. Ge, and W. Yang. Magnetically driven microrobots: Recent progress and future development. Materials & Design, 227:111735, 2023. ISSN 0264-1275. doi: https://doi.org/10.1016/j.matdes.2023.111735. URL https://www.sciencedirect.com/science/article/pii/S0264127523001508.

[163] V. V. Singh, B. Jurado-Sánchez, S. Sattayasamitsathit, J. Orozco, J. Li, M. Galarnyk, Y. Fedorak, and J. Wang. Multifunctional silver-exchanged zeolite micromotors for catalytic detoxification of chemical and biological threats. Advanced Functional Materials, 25(14):2147–2155, 2015.

[164] M. Sitti. Miniature devices: Voyage of the microrobots. Nature, 458:1121–2, 05 2009. doi: 10.1038/4581121a.

[165] D. J. Smith, M. T. Gallagher, R. Schuech, and T. D. Montenegro-Johnson. The role of the double-layer potential in regularised stokeslet models of self-propulsion. Fluids, 6(11), 2021. ISSN 2311-5521. doi: 10.3390/fluids6110411.

[166] A. Solovev, Y. Mei, E. Bermudez, G. Huang, and O. Schmidt. Catalytic microtubular jet engines self-propelled by accumulated gas bubbles. Small (Weinheim an der Bergstrasse, Germany), 5:1688–92, 07 2009.

[167] A. A. Solovev, W. Xi, D. H. Gracias, S. M. Harazim, C. Deneke, S. Sanchez, and O. G. Schmidt. Self-propelled nanotools. ACS Nano, 6(2):1751–1756, 2012. ISSN 19360851. doi: 10.1021/nn204762w.

[168] H. Son, E. Byun, Y. J. Yoon, J. Nam, S. H. Song, and C. Yoon. Untethered actuation of hybrid hydrogel gripper via ultrasound. ACS Macro Letters, 9(12): 1766–1772, 2020. doi: 10.1021/acsmacrolett.0c00702. URL https://doi.org/10.1021/acsmacrolett.0c00702. PMID: 35653680.

[169] R. A. Stile, W. R. Burghardt, and K. E. Healy. Synthesis and characterization of injectable poly(n-isopropylacrylamide)-based hydrogels that support tissue formation in vitro. Macromolecules, 32(22):7370–7379, 1999. doi: 10.1021/ma990130w.

[170] G. Stoychev, N. Puretskiy, and L. Ionov. Self-folding all-polymer thermoresponsive microcapsules. Soft Matter, 7:3277–3279, 2011. doi: 10.1039/C1SM05109A. URL http://dx.doi.org/10.1039/C1SM05109A.

[171] D. Sutherland and I. Goodarz-Nia. Floc simulation: The effect of collision sequence. Chemical Engineering Science, 26(12):2071–2085, 1971. ISSN 0009-2509. doi: https://doi.org/10.1016/0009-2509(71)80045-3. URL https://www.sciencedirect.com/science/article/pii/0009250971800453.

[172] T. Tanaka and D. J. Fillmore. Kinetics of swelling of gels. The Journal of Chemical Physics, 70(3):1214–1218, 1979. doi: 10.1063/1.437602.

[173] G. I. Taylor. Film notes for low-reynolds number flow. National Committee for Fluid Mechanics, 1967.

[174] T. Tomari and M. Doi. Swelling dynamics of a gel undergoing volume transition. Journal of the Physical Society of Japan, 63(6):2093–2101, 1994. doi: 10.1143/JPSJ.63.2093. URL https://doi.org/10.1143/JPSJ.63.2093.

[175] T. Tomari and M. Doi. Hysteresis and incubation in the dynamics of volume transition of spherical gels. Macromolecules, 28(24):8334–8343, 1995. doi: 10.1021/ma00128a050. URL https://doi.org/10.1021/ma00128a050.

[176] A.-K. Tornberg and M. Shelley. Simulating the dynamics and interactions of flexible fibers in stokes flows. Journal of Computational Physics, 196:8–40, 05 2004. doi: 10.1016/j.jcp.2003.10.017.

[177] V. A. Turek, R. Chikkaraddy, S. Cormier, B. Stockham, T. Ding, U. F. Keyser, and J. J. Baumberg. Thermo-responsive actuation of a dna origami flexor. Advanced Functional Materials, 28(25):1706410, 2018. doi: https://doi.org/10.1002/adfm.201706410. URL https://onlinelibrary.wiley.com/doi/abs/10.1002/adfm.201706410.

[178] J. Tyrrell, D. J. Smith, and R. J. Dyson. Regularized stokeslet rings: An efficient method for axisymmetric stokes flow with application to the growing pollen tube. Phys. Rev. Fluids, 4:063102, Jun 2019. doi: 10.1103/PhysRevFluids.4.063102. URL https://link.aps.org/doi/10.1103/PhysRevFluids.4.063102.

[179] M. Valdez-Garduño, M. Leal-Estrada, E. S. Oliveros-Mata, D. I. Sandoval-Bojorquez, F. Soto, J. Wang, and V. Garcia-Gradilla. Density asymmetry driven propulsion of ultrasound-powered janus micromotors. Advanced Functional Materials, 30(50):2004043, 2020. doi: https://doi.org/10.1002/adfm.202004043. URL https://onlinelibrary.wiley.com/doi/abs/10.1002/adfm.202004043.

[180] S. Wang and N. Wu. Selecting the swimming mechanisms of colloidal particles: Bubble propulsion versus self-diffusiophoresis. Langmuir, 30(12):3477–3486, 2014.

[181] W. Wang. Open questions of chemically powered nano- and micromotors. Journal of the American Chemical Society, 145(50):27185–27197, 2023. doi: 10.1021/jacs.3c09223. URL https://doi.org/10.1021/jacs.3c09223. PMID: 38063192.

[182] W. Wang, L. A. Castro, M. Hoyos, and T. E. Mallouk. Autonomous motion of metallic microrods propelled by ultrasound. ACS Nano, 6(7):6122–6132, 2012. doi: 10.1021/nn301312z.

[183] W. Wang, S. Li, L. Mair, S. Ahmed, T. J. Huang, and T. E. Mallouk. Acoustic propulsion of nanorod motors inside living cells. Angewandte Chemie International Edition, 53(12):3201–3204, 2014. doi: https://doi.org/10.1002/anie.201309629. URL https://onlinelibrary.wiley.com/doi/abs/10.1002/anie.201309629.

[184] W. Wang, Y. He, H. Liu, Q. Guo, Z. Ge, and W. Yang. Bubble-based microrobot: Recent progress and future perspective. Sensors and Actuators A: Physical, 360:114567, 2023. ISSN 0924-4247. doi: https://doi.org/10.1016/j.sna.2023.114567. URL https://www.sciencedirect.com/science/article/pii/S0924424723004168.

[185] Y. Wang, R. M. Hernandez, D. J. Bartlett, J. M. Bingham, T. R. Kline, A. Sen, T. E. Mallouk, R. V. June, I. Final, and F. August. Bipolar Electrochemical Mechanism for the Propulsion of Catalytic Nanomotors in Hydrogen Peroxide Solutions †. Langmuir, 22(25):10451–10456, 2006. doi: 10.1021/la0615950.

[186] J. B. Waterbury, J. M. Willey, D. G. Franks, F. W. Valois, and S. W. Watson. A cyanobacterium capable of swimming motility. Science, 230(4721):74–76, 1985. doi: 10.1126/science.230.4721.74.

[187] S. Whitaker. Flow in porous media i: A theoretical derivation of darcy's law. Transport in Porous Media, 1:3–25, 03 1986. doi: 10.1007/BF01036523.

[188] B. Williams, S. Anand, J. Rajagopalan, and M. Saif. A self-propelled biohybrid swimmer at low reynolds number. Nature communications, 5:3081, 01 2014. doi: 10.1038/ncomms4081.

[189] T. A. Witten. Insights from soft condensed matter. Rev. Mod. Phys., 71:S367–S373,

Mar 1999. doi: 10.1103/RevModPhys.71.S367. URL https://link.aps.org/doi/10.1103/RevModPhys.71.S367.

[190] J. K. Wróbel, R. Cortez, and L. Fauci. Modeling viscoelastic networks in Stokes flow. Physics of Fluids, 26(11):113102, 11 2014. ISSN 1070-6631. doi: 10.1063/1.4900941. URL https://doi.org/10.1063/1.4900941.

[191] Z. Wu, B. Esteban-Fernández de Ávila, A. Martín, C. Christianson, W. Gao, S. K. Thamphiwatana, A. Escarpa, Q. He, L. Zhang, and J. Wang. Rbc micromotors carrying multiple cargos towards potential theranostic applications. Nanoscale, 7: 13680–13686, 2015. doi: 10.1039/C5NR03730A.

[192] Z. Wu, T. Si, W. Gao, X. Lin, J. Wang, and Q. He. Superfast near-infrared light-driven polymer multilayer rockets. Small, 12(5):577–582, 2016. doi: https://doi.org/10.1002/smll.201502605.

[193] P. D. Yeh and A. Alexeev. Mesoscale modelling of environmentally responsive hydrogels: emerging applications. Chem. Commun., 51:10083–10095, 2015. doi: 10.1039/C5CC01027F. URL http://dx.doi.org/10.1039/C5CC01027F.

[194] K. B. Yesin, K. Vollmers, and B. J. Nelson. Modeling and control of untethered biomicrorobots in a fluidic environment using electromagnetic fields. The International Journal of Robotics Research, 25(5-6):527–536, 2006. doi: 10.1177/0278364906065389. URL https://doi.org/10.1177/0278364906065389.

[195] P. Zahedi, R. Saleh, R. Moreno-Atanasio, and K. Yousefi. Influence of fluid properties on bubble formation, detachment, rising and collapse; investigation using volume of fluid method. Korean Journal of Chemical Engineering, 31:1349–1361, 2014. ISSN 02561115. doi: 10.1007/s11814-014-0063-x.

[196] J. Zhang, X. Zheng, H. Cui, and Z. Silber-Li. The self-propulsion of the spherical Pt-SiO2 Janus micro-motor. Micromachines, 8(4), 2017. ISSN 2072666X. doi: 10.3390/mi8040123.

[197] L. Zhang, J. J. Abbott, L. Dong, B. E. Kratochvil, D. Bell, and B. J. Nelson. Artificial bacterial flagella: Fabrication and magnetic control. Applied Physics Letters, 94(6):064107, 2009. doi: 10.1063/1.3079655.

[198] B. Zhao, E. Lauga, and L. Koens. Method of regularized stokeslets: Flow analysis and improvement of convergence. Phys. Rev. Fluids, 4:084104, Aug 2019. doi: 10.1103/PhysRevFluids.4.084104. URL https://link.aps.org/doi/10.1103/PhysRevFluids.4.084104.

[199] G.-F. Zhao, J. Fang, and J. Zhao. A 3d distinct lattice spring model for elasticity and dynamic failure. International Journal for Numerical and Analytical Methods in Geomechanics, 35(8):859–885, 2011. doi: https://doi.org/10.1002/nag.930. URL https://onlinelibrary.wiley.com/doi/abs/10.1002/nag.930.

[200] S.-F. Zhao and G.-F. Zhao. Implementation of a high order lattice spring model for elasticity. International Journal of Solids and Structures, 49(18):2568–2581, 2012. ISSN 0020-7683. doi: https://doi.org/10.1016/j.ijsolstr.2012.05.015. URL https://www.sciencedirect.com/science/article/pii/S002076831200217X.

[201] D. Zhou, Y. Gao, J. Yang, Y. C. Li, G. Shao, G. Zhang, T. Li, and L. Li. Light-ultrasound driven collective "firework" behavior of nanomotors. Advanced Science, 5(7):1800122, 2018. doi: https://doi.org/10.1002/advs.201800122. URL https://onlinelibrary.wiley.com/doi/abs/10.1002/advs.201800122.

[202] Y. Zhou, M. Layani, W. Shancheng, P. Hu, K. Yujie, and S. Magdassi. Fully printed flexible smart hybrid hydrogels. Advanced Functional Materials, 28:1705365, 02 2018. doi: 10.1002/adfm.201705365.